Measuring Excitations of a Strongly Interacting Superfluid Fermi Gas

Dissertation
zur
Erlangung des Doktorgrades (Dr. rer. nat.)
der
Mathematisch-Naturwissenschaftlichen Fakultät
der
Rheinischen Friedrich-Wilhelms-Universität Bonn

vorgelegt von
Andreas Kell
aus
Berlin

Bonn, April 2022

Angefertigt mit Genehmigung der Mathematisch-Naturwissenschaftlichen Fakultät
der Rheinischen Friedrich-Wilhelms-Universität Bonn

Gutachter: Prof. Dr. Michael Köhl
Gutachter: Prof. Dr. Sebastian Hofferberth

Tag der Promotion: 05.07.2022
Erscheinungsjahr: 2022

Abstract

This thesis investigates experimentally the superfluid phase of strongly interacting ultracold Fermi gases. The diluteness of the considered gases of neutral atoms ensures that their interaction can be described by a single interaction parameter leading to universal behavior, which can be relevant for entirely different physical systems. The interactions are tunable by a magnetic offset field, which enables the exploration of the so called "BEC-BCS" crossover. This crossover is a smooth connection from a weakly attractive superfluid, which has similarities to a superconductor and is described by Bardeen-Cooper-Schrieffer (BCS) theory, across a strongly interacting regime with remarkably stable superfluidity, to a weakly repulsive Bose-Einstein condensate (BEC) of molecules.

The critical temperature of superfluid systems is a crucial property and in the case of high temperature superconductivity, a better understanding of the critical temperature could have a practical impact. Nevertheless, previous measurements of the critical temperature of the superfluid phase transition across the BEC-BCS crossover show large deviations from theoretical predictions, especially towards the BEC side of the strongly interacting regime. The deviations can be attributed to difficulties in measuring the temperature of strongly interacting gases. This problem is addressed here by employing a more careful thermometry, based on the low density regions of the trapped sample, taking interaction effects into account. Additionally, by measuring the density of the gas at the trap center, the dependence of the critical temperature on compression effects is examined, which allows a comparison between the critical temperature of a trapped and a homogeneous gas.

The superfluid state is typically detected by observing a bimodal density distribution in time-of-flight, caused by a macroscopic occupation of low momentum paired states, which can be distinguished from a thermal background. However, on the BCS side the pairs break up during time-of-flight, which is usually mitigated with a rapid ramp of the magnetic field towards the BEC side to project the pairs onto more robust molecules. Here, analysis methods based on machine learning are described, which do not require the rapid ramp but can detect superfluidity directly from time-of-flight images.

Recently, the excitations of Fermi gases in the BEC-BCS crossover have been explored experimentally in quite some detail, except for the Higgs amplitude mode, which is difficult to excite and to detect. It directly couples to the interaction, but in order to excite the Higgs amplitude mode the interaction has to be changed on a timescale similar to the Fermi time of typically a few microseconds, which poses technical challenges. Here, the construction of a new fast magnetic coil is described, which allows the manipulation of the interaction on a timescale faster than the Fermi time and enables the implementation of two different theoretically proposed excitation schemes of the Higgs amplitude mode.

The first method is an interaction quench, which leads to subsequent oscillation of the order parameter. Indeed, an experimental signature of these oscillations is found, but the low signal-to-noise ratio requires a careful analysis.

The second method, interaction modulation, provides an excitation scheme with a narrow frequency resolution and reveals a resonance at the Higgs frequency. The mode can be distinguished from the background consisting of the pair breaking continuum and the dissociation of Feshbach molecules on the BEC side.

Parts of this thesis have been published in the following articles

[1] T. Harrison, M. Link, A. Behrle, K. Gao, A. Kell, J. Kombe, J.-S. Bernier, C. Kollath, and M. Köhl, *Decay and revival of a transient trapped Fermi condensate*, Phys. Rev. Research **3**, 023205 (2021), https://doi.org/10.1103/PhysRevResearch.3.023205.

[2] A. Kell, M. Link, M. Breyer, A. Hoffmann, M. Köhl, and K. Gao, *A compact and fast magnetic coil for the manipulation of quantum gases with Feshbach resonances*, Review of Scientific Instruments **92**, 093202 (2021), https://doi.org/10.1063/5.0049518.

Acknowledgments

First of all, I would like to thank Michael Köhl for his trust and for giving me the opportunity to work on this experiment. I have always considered his advice very encouraging and helpful.

I would like to thank Alexandra Behrle and Timothy Harrison for building the experimental apparatus from scratch, Kuiyi Gao for his contributions to the early experiment, as well as his supervision later on, and Martin Link who joined for the first large investigation of the experiment, before my time as a doctoral student. Thanks to them we had access to a reliable experimental apparatus, which is the basis for the investigations of this thesis. It was nice to join a joyful team and I happily remember team activities like mud races, VR adventures, eating century eggs or baiting colleagues to CrossFit workouts. I thank Benjamin Rauf for his time at the project and for sharing his fascination for optical lattices, combs and clocks. I thank Moritz Breyer, Daniel Eberz and the new lab mascot who are currently running the experiment. I really enjoyed the great atmosphere in the team and appreciate the good ideas and hard work which went into the projects. I also thank Valentin Jonas, who joined the experiment for his Bachelor's and Master's thesis, for interesting discussions and his cleverness in problem solving.

I would like to thank Christoph Linse, Max Zawierucha, Justas Andrijauskas and Till Leuteritz for having built important elements of the experiment before I joined the team.

I thank Johannes Kombe, Jean-Sébastien Bernier and Corinna Kollath for improving the theoretical understanding of our projects.

I want to thank Akos Hoffmann who saved us from several problems in the lab, especially related to electronics. By designing the quench and modulation circuits for a fast magnetic coil, he contributed significantly to the projects of this thesis

I would like to thank Tina Naggert, Nana El Mellal and Janek Fleper for help with administrative tasks.

I also thank Jan Drewes, Jeffrey Chan, Marcel Gall, Nicola Wurz, Nick Klemmer, Janek Fleper, Jens Samland and Andrea Bergschneider from the Fermi experiment, Jonas Schmitz, Felix Rönchen and Tobias Kree from the Fairy experiment, Hendrick-Marten Meyer, Kilian Kluge, Pascal Kobel, Vidhya Nair, Ralf Berner and Santosh from the Ion experiment, Thorsten Langerfeld, Anica Hamer, Steffen Gohlke, Luisa Tolle, Andreas von Haaren, Moritz Scharfstädt, Pia Fürtjes and Leon Reiffert for being great colleagues. Additionally, I thank the colleagues from the time before I became doctoral student who originally inspired me to join and stay in this group, Eugenio Cocchi, Luke Miller, Ferdinand Brennecke, Jonathan Silver, Leonardo Carcagni and especially Daniel Pertot, Robert Maiwald and Tim Ballance.

This thesis would not have been possible without a good coffee supply organized by Marcell and Daniel. I want to thank Martin and Steffen for organizing regular contributions to the group meeting.

I thank Moritz Breyer, Daniel Eberz, Valentin Jonas, Sebastian Ciupka and Nicolas Felten for proofreading.

I am grateful for the support from my parents and my two siblings and I am grateful for the friends who accompanied me during this time. I want to thank my roommates Nicola and Sebastian for the fun time and interesting discussions and I want to mention Tobi, Sophie, Johanna, David, Nicolas and Aki for helping me to keep my motivation at a high level. I have to admit that this is an incomplete list and I am grateful for several things which I have not expressed here explicitly.

Contents

1 Introduction

Discovery of Superfluids Research on superfluid systems originates in the discovery of superconductivity by Onnes in 1908, when he observed the vanishing of the electrical resistance of mercury cooled to temperatures below 4.2 K [3]. Superconductivity can be seen as a superfluid state of an electron gas [4]. Additionally, in order to achieve these cold temperatures, he was using liquefied Helium-4 and observed an anomaly of its density at about 2.2 K, which has later been identified as a phase transition to a superfluid state, for which the viscosity of the liquid drops significantly [5, 6].

In 1938 a connection was drawn between the superfluidity of bosonic Helium-4 and the concept of a BEC [7], which describes the macroscopic occupation of the single particle ground state for a Bose gas at low temperature [8]. This can explain superfluidity because a BEC does only allow excitations above a critical velocity [9]. For superconductivity, a similar explanation was considered, that fermionic electrons might form a "pair condensate in momentum space" [4]. Finally, conventional superconductivity was explained by BCS theory [10, 11], which indeed relies on pairing of momentum states, so called "Cooper pairs". The pairing is possible by a weak attractive interaction between electrons of opposite spin, which is mediated by phonons and can overcome the screened Coulomb interaction. However, it has been argued that these pairs, which have a characteristic size larger than the inter-particle distance, cannot be described as composite bosons, which would indicate that BEC and BCS states are two different phenomena [4].

Nevertheless, it was shown later that by varying interaction and density the Cooper pairs can smoothly be transformed to tightly bound molecules, which follow bosonic statistics and can form a BEC [12, 13]. From this perspective, a BEC can be seen as a special case of an interacting Fermi gas and the evolution between the two regimes is called the "BEC-BCS crossover" [4].

Ultracold Quantum Gases In 1975 it was proposed to use laser light to cool a dilute gas [14] and subsequently several techniques were developed to trap and cool atoms by employing their interactions with laser light and magnetic fields [15–17]. This lead to the first realization and observation of a BEC from a bosonic gas [18–20]. An advantage of ultracold quantum gases is the possibility to precisely tune important parameters of the system. For example, atom number and temperature can be varied. Additionally, it turned out that in certain cases also the interaction between the atoms can be tuned by changing an external magnetic field, which is based on the phenomenon of Feshbach resonances [21, 22].

After the success with Bose gases, research was also conducted on Fermi gases. Cooling of fermions is in principle more difficult because the Pauli exclusion principle prevents effective thermalization of cold and identical fermions. Therefore, the fermions are prepared in more than one internal state or they are mixed with a bosonic gas. With the help of Feshbach resonances, molecules were produced from fermionic gases [23, 24], which finally lead to the creation of molecular BECs [25–27]. Note that while molecules were also created from Bose gases, for molecules consisting of fermions longer lifetimes have been achieved [4].

As mentioned before, tuning interactions of a Fermi gas allows the exploration of the BEC-BCS crossover. Superfluidity towards the BCS side requires lower temperatures and its observation is more challenging. On the BEC side the condensation is seen by a bimodal momentum

distribution, which is measured in time-of-flight and consists of a broad thermal distribution and a sharp peak of condensed low-momentum molecules. On the BCS side, however, the pairing does not survive time-of-flight. Instead, a rapid magnetic ramp is performed, which projects the Cooper pairs onto deeply bound molecules, thus recovering the bimodal distribution [28, 29].

Universal Behavior The considered Fermi gases are so dilute that the range of interactions is small compared to the average inter-particle distance. This justifies to ignore the actual range of the interactions and to describe them as a contact interaction [30]. For strong interactions, this leads to universal behavior which depends on a single parameter describing the strength of the interaction [31].

A special case is the so called "unitarity limit", in which the interaction takes a maximum value and the inter-particle distance becomes the only relevant length scale at zero temperature, implying universal laws for physical quantities [32]. This means that the system has a scale invariance which, for example, leads to a proportionality between pressure and energy density of the gas, even at finite temperature [33], as well as a vanishing bulk viscosity [34].

This universality connects the unitary Fermi gas to other physical systems like neutron matter in the crust of neutron stars, although non-universal effects play a role at higher neutron densities [35]. The superfluid critical temperature of strongly interacting Fermi gases is comparable to that of a BEC but higher than the critical temperature of a weakly interacting Fermi gas. Consequently, if the critical temperature is appropriately scaled to take the diluteness of the gas into account[1], it is a magnitude larger than for high temperature superconductors and several magnitudes larger than for fermionic helium-3 or conventional superconductors [36].

Another universality stems from the critical behavior near the superfluid phase transition [37]. According to Ginzburg-Landau theory, the free energy can be expanded in the superfluid order parameter [38], which results in a free energy landscape below the critical temperature resembling a "Mexican hat" [39], as shown in figure 1.1. The phase transition causes symmetry-breaking connected to the complex phase of the order parameter which implies the existence of a massless phase mode according to the Goldstone theorem [40]. Additionally, an amplitude mode can occur in certain cases. The phase mode is also called Nambu-Goldstone mode and the amplitude mode is also called Higgs amplitude mode [39].

When considering dynamics of the order parameter, the equations of motion are not fully determined by the mexican hat potential, but additional dynamic terms can appear, depending on the symmetries of the system [39]. It can be shown that Lorentz invariance or particle-hole symmetry imply a stable amplitude mode, whereas the absence of such a symmetry can lead to a fast decay of the amplitude mode into phase modes [39]. In particle physics, a connection between the phase modes and the W and Z bosons can be drawn [39], as well as between the amplitude mode and the Higgs boson [39]. Note that in this case W and Z bosons are not massless due to a coupling to gauge fields according to the Higgs-Anderson mechanism. The Higgs amplitude mode also appears in superconductors. Here the electric charge of the electrons leads to an elevated energy of the phase modes by the Higgs-Anderson mechanism and prevents the decay of the Higgs amplitude mode into phase modes [41]. The absence of particle-hole symmetry in Bose gases prevents the observation of a Higgs amplitude mode (an exception is a superfluid Bose gas in a lattice close to the Mott insulator transition, where particle-hole symmetry can be restored) [39]. Weakly interacting Fermi gases, however, feature particle-hole symmetry, which enables a well-defined Higgs amplitude mode [42].

[1] Consistent with the universal relations, the critical temperature is scaled by the Fermi energy, which is a scale for the density of the system, but also depends on the particle mass, so that the Fermi energy of a superconductor can be much larger than that of e.g. helium-3.

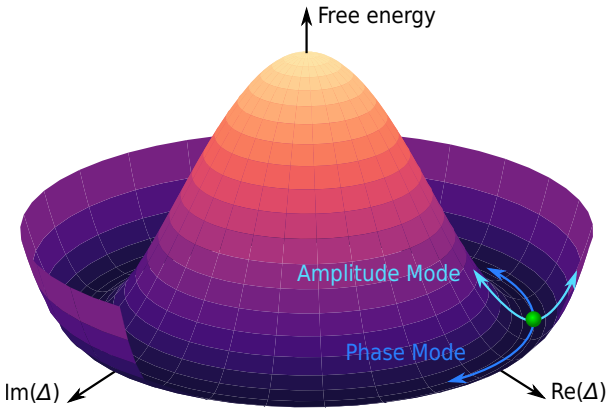

Figure 1.1: Sketch of free energy landscape below superfluid phase transition The free energy is a function of the order parameter $\Delta = |\Delta|e^{i\varphi}$ and in the ground state a particular value of the phase φ is chosen, which breaks the symmetry of the system. The geometry suggests the occurrence of phase and amplitude modes but additional conditions must be fulfilled for the latter.

Excitations The excitation spectrum of a superfluid Fermi gas is very important because the phenomenon of superfluidity relies on the property that no excitation below a critical velocity is possible. This can directly be measured via the heating rate of a gas which is stirred by a laser beam at a certain velocity [43]. It is shown that the critical velocity is limited on the BEC side by the sound velocity corresponding to the Bogoliubov-Anderson mode, which has a linear dispersion relation at low momenta. Towards the BCS side, the critical velocity is limited by pair breaking.

The Bogoliubov-Anderson mode, at low energies, can be identified as the Nambu-Goldstone phase mode mentioned above. It has also been measured with Bragg spectroscopy [44]. Recently, this measurement was also performed with variable momentum to map out the pair breaking continuum and the dispersion of the Bogoliubov-Anderson mode [45]. The Higgs amplitude mode has been measured spectroscopically with a method based on RF dressing [46]. However, predictions about its damping mechanisms have not been verified experimentally yet.

Superfluid Phase Diagram As already mentioned, the critical temperature of the superfluid phase has a similar order of magnitude in the strongly interacting regime as towards the BEC side, while it is substantially reduced towards the BCS side. This qualitative behavior is sketched in figure 1.2, resulting in a phase diagram which depends on the interaction and temperature of the gas.

The dependence of the critical temperature on interaction is well understood theoretically in the weakly interacting BCS regime based on a correction of BCS theory [48]. Similarly, the critical temperature in the BEC limit is well understood for the homogeneous and trapped gas [49, 50], although the variation of calculated results for the first order correction from interactions was initially quite large [51]. The results on the BEC side are also confirmed by measurements of the critical temperature of a trapped weakly interacting Bose gas [52]. There are several theoretical models for the critical temperature over the whole crossover [53, 54], which roughly agree with each other and with Monte-Carlo results [55]. However, some differences remain, for example a maximum critical temperature in the strongly interacting regime towards the BEC side is predicted but there is no agreement on the prominence and exact location of this maximum.

Shortly after the creation of molecular BECs from Fermi gases, the critical temperature of the whole crossover was measured [28, 29]. However, the focus of these early studies was the detection of superfluidity, rather than a precise thermometry. Superfluidity was detected

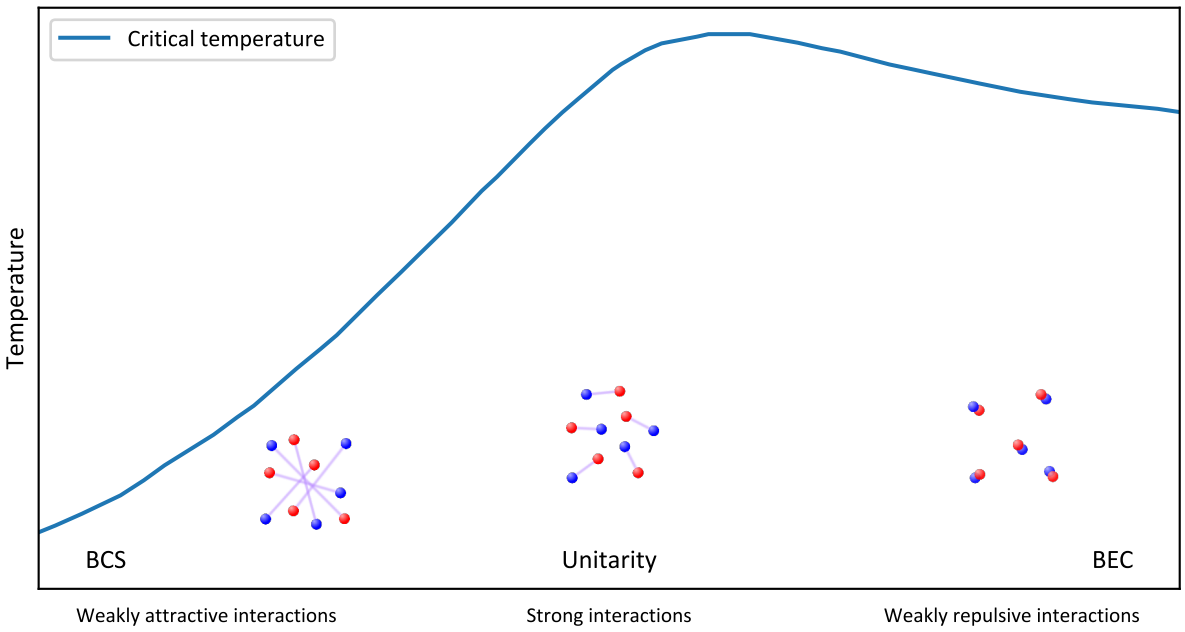

Figure 1.2: Sketch of phase diagram of the BEC-BCS crossover The area below the critical temperature corresponds to the superfluid phase. The pairing in the BEC regime, at unitarity and in the BCS regime is illustrated, emphasizing the different characteristic pair size relative to the average particle distance. The curve of the critical temperature is based on data from ref. [47] for a homogeneous gas, see figure 2.3 for a quantitative and more detailed version of this figure.

from a bimodal momentum distribution after a rapid magnetic ramp (as mentioned above). The thermometry was based on fits after time-of-flight, which is not reliable for interacting gases [4]. Additionally, the thermometry involved adiabatic ramps of the magnetic field, although they can have a significant effect on the temperature of the sample. Consequently, large deviations from theoretical predictions [47] of the critical temperature of a harmonically trapped gas on the BEC side were seen. In a later study the thermometry was considered more carefully [56], but the usage of two different thermometry methods leads to some ambiguity of the results. Further measurements of the critical temperature were typically only performed at unitarity [57–61].

In this thesis a new measurement of the critical temperature is presented. The thermometry is based on the in-trap density distribution in the low density regions, where interaction effects do not play a large role. Nevertheless, systematic effects from interactions are identified, which are especially important on the BEC side, and are taken into account with a virial expansion of the thermodynamic potential [62]. By measuring the density in the trap center, it is possible to distinguish between the critical temperature of a trapped gas and a homogeneous gas. This enables the comparison of the results to a larger number of theoretical calculations.

While the superfluid transition is detected in the same way as the previous studies by employing the rapid ramp technique, an independent method based on machine learning is additionally used, which demonstrates the possibility to infer the superfluid phase transition from simple images in time-of-flight without a rapid ramp. It has previously been demonstrated, mostly based on theoretically generated data, that machine learning can be used to infer phase transitions [63] and recently this was also performed for experimental data [64].

Interaction Quenches The abrupt change of a parameter of a quantum gas can be used to probe nonequilibrium physics, like the creation of nonequilibrated steady states [65]. But this

can also be used to learn about the excitation spectrum of the equilibrium state. For example, collective trap modes have been excited by a sudden change of the trap potential [66, 67]. However, in order to effectively excite a mode of the system, the parameters of the system have to be changed fast compared to the timescale connected to the mode. In the case of trap modes, the trap potential has to be changed on a timescale which is comparable or faster than the trap period.

This thesis describes interaction quenches for which the interaction parameter is changed significantly faster than the trap dynamics. First, the interaction is changed faster than the quasi-particle excitation time of the superfluid, in order to examine how the superfluid state adapts to a new interaction value, which directly influences the pairing of the equilibrium state. The interaction quench is experimentally realized with a fast RF population transfer from strongly to weakly interacting states of the atoms.

Secondly, to perform even faster quenches, a new dedicated magnetic quench coil is designed and implemented. It enables interaction quenches faster than the Fermi time, which is the fastest relevant timescale of the system. It has been theoretically suggested that such interaction quenches can excite oscillations of the order parameter [68] identified as the Higgs amplitude mode of the system. It is expected that even after the application of a rapid ramp these oscillations are still visible [69].

Interaction Modulation The new fast magnetic coil is also capable to probe the Higgs amplitude mode spectroscopically by applying an oscillating magnetic field at the Higgs frequency in the kilohertz regime. This is the implementation of another suggested excitation method of ref. [69] and it is expected that the mode can be detected with a higher signal-to-noise ratio than after an interaction quench because the system is only probed in a very narrow frequency range. The magnetic interaction modulation is spectroscopically more narrow than the previous excitation method of the Higgs amplitude mode in a strongly interacting Fermi gas in ref. [46] because that method based on RF dressing has a dependence of the modulation frequency on the addressed momentum state.

Magnetic interaction modulation was already employed to examine Feshbach molecules and pair breaking of a Fermi gas in the BEC-BCS crossover [70]. Those results are reproduced here to allow a distinction between the different excitation modes, but also some new details are found.

Structure of Thesis

The main results of this thesis are the improved measurement of the critical temperature of the superfluid phase transition of the BEC-BCS crossover and the investigation of excitations caused by interaction quenches or interaction modulation, most notably the observation of the Higgs amplitude mode.

- *Chapter 2* briefly reviews the theory of ultracold Fermi gases in the BEC-BCS crossover and provides the most basic predictions for the critical temperature and an overview of the excitations of the system. Additionally, density distributions of trapped gases are considered, including interaction effects at low density, which become relevant for the thermometry.

- *Chapter 3* describes the experimental apparatus and the preparation of quantum degenerate samples, but in particular detail, the new fast magnetic coil is explained, which enables the interaction quench and modulation experiments.

- As preparation for the actual investigations, *chapter 4* details several measurement techniques, including absorption imaging, the rapid ramp technique for superfluidity detection and the characterization of the trap potential. Additionally, various analysis methods are discussed. At first the inverse Abel transformation is presented, which allows a conversion of measured column density into three-dimensional density by exploiting the symmetry of the trap. Then the thermometry is explained, which uses the density distribution and takes weak interaction effects into account. Finally, some basic machine learning concepts of deep learning are discussed, which are later used for an alternative method to detect the superfluid transition.

- The first investigation, presented in *chapter 5*, examines the phase diagram of the superfluid transition in the BEC-BCS crossover. One part is the detection of superfluidity based on the rapid ramp technique or, alternatively, based on machine learning techniques. The other part is a reliable thermometry in order to determine the critical temperature of the transition.

- In *chapter 6* excitations of the superfluid and nonequilibrium induced by interaction quenches are probed. At first a quench based on an RF transfer is performed, which is fast compared to the quasi-particle excitation time. Then a quench realized with a ramp of the magnetic field faster than the Fermi time of the system is performed to investigate the excitation of the Higgs amplitude mode.

- Finally, in *chapter 7* interaction modulation is employed as a spectroscopic method to measure the Higgs amplitude mode. Additionally, excitations from pair breaking and Feshbach molecule dissociation are examined.

- The results are summarized and discussed in *chapter 8*.

2 Ultracold Fermi Gases and the BEC-BCS Crossover

This chapter describes the basic theory of ultracold Fermi gases, which is relevant for the investigations of this thesis. Sometimes specific properties of ^{6}Li are explained, which is the isotope used in the experiments.

At first one of the most useful properties of experimentally studied Fermi gases is explained, the ability to precisely control the interactions of the gas via an external magnetic field, and how these interactions influence the state of the gas.

The interaction can be tuned continuously from weak attractive interactions towards a strongly interacting regime and further to a regime, where the atoms form molecules with weak repulsive interactions. For weak attractive interactions and zero temperature, it follows from Bardeen-Cooper-Schrieffer (BCS) theory that the gas is superfluid. For weak repulsive interactions, the bosonic molecules can be described with the theory of Bose-Einstein condensation (BEC). Interestingly, tuning the interaction from weakly repulsive to strongly interacting to weakly attractive results in a continuous crossover of the superfluid state, which is called the BEC-BCS crossover. Of particular interest here are the excitation spectrum of the gas at different interactions and how the gas behaves at finite temperature.

The microscopic theory of the BEC-BCS crossover is complemented with a description of the gas by macroscopic thermodynamics. It is discussed how the interactions of the gas can be described with thermodynamic variables and especially how they influence the density distribution of the gas.

Finally, effects of the trapping potential are evaluated, which lead to inhomogeneous density distributions, modify the critical temperature of the superfluid transition and give rise to characteristic collective excitations.

2.1 Overview

In a macroscopic description, the thermodynamic state of a gas in equilibrium is given by only a few variables, e.g. pressure (or volume), temperature (or entropy), particle number (or chemical potential) and a measure for its interaction. Such a state corresponds to an ensemble of microscopic states. For a classical gas, a microstate can be characterized by the velocities of the individual particles, but for an ultracold gas this picture has to be refined. “Ultracold” stands for temperatures at which the description of the constituents as particles breaks down and wave-like properties become relevant, which requires a quantum mechanical description. Formally, the transition to this so called “degenerate” regime is given, when the thermal wavelength [36]

$$\lambda_T = \frac{h}{\sqrt{2\pi m k_\mathrm{B} T}}\,, \tag{2.1}$$

which is a typical length scale for the de Broglie wavelengths of the particles with mass m at the given temperature T (also using the Boltzmann constant k_B and Planck constant h), becomes larger than the average inter-particle distance.

In this regime the statistics of the microstates has to take into account whether the particles of the gas are indistinguishable. Indistinguishable particles are described by a collective wavefunction, which must be either symmetric or antisymmetric for the exchange of two particles depending on their spin. Particles with integer spin are bosons, for them the total wavefunction is symmetric and the indistinguishability enhances the probability of multiple occupation of the same single particle state. Particles with half-integer spin are fermions, for them the total wavefunction is antisymmetric, which implies the Pauli exclusion principle, that the same single particle state cannot be occupied by more than one fermion.

In this thesis exclusively Fermi gases with a balanced mixture of two pseudo-spin states $\sigma \in \{\downarrow, \uparrow\}$ are considered. Therefore, the average inter-particle distance for one spin state can be characterized by the density n_σ per spin state[1].

In an ideal (i.e. non-interacting) Fermi gas at zero temperature, all states are occupied in ascending order of energy and the maximum energy of an occupied state is called the Fermi energy. It is an important energy scale of the system and is directly connected to the density of the gas. For a homogeneous gas of fermions it is given as [4]

$$E_\mathrm{F} = \frac{\hbar^2}{2m} \left(6\pi^2 n_\sigma\right)^{2/3} . \tag{2.2}$$

Similarly, Fermi momentum and Fermi temperature are defined as

$$E_\mathrm{F} =: \frac{\hbar^2 k_\mathrm{F}^2}{2m} =: T_\mathrm{F} k_\mathrm{B} \tag{2.3}$$

and provide important scales, which are often also used as a reference for the properties of a gas at finite temperature and finite interactions. Note that it is sometimes useful to think of the Fermi momentum

$$k_\mathrm{F} = \left(6\pi^2 n_\sigma\right)^{1/3} \tag{2.4}$$

as a measure, which is proportional to the inverse average inter-particle distance.

Typical Orders of Magnitude The Fermi energy is usually about $E_\mathrm{F} \approx 1\,\mu\mathrm{K} \times k_\mathrm{B} \approx 20\,\mathrm{kHz} \times h$, while chemical potential and temperature might be hundreds of nanokelvins or less. The extent of the cloud is about 100 µm and the density consists of a few up to hundreds of atoms per $\mu\mathrm{m}^3$, corresponding to an average particle distance of 0.1 µm to 1 µm, while the thermal wavelength can become a few micrometer large (2.3 µm for ^{6}Li at 100 nK).

2.2 Interactions

In ultracold gases several conditions are met which simplify the description of interactions. The interaction potential between two atoms has a typical range r_0 and can be neglected for larger distances $r \gg r_0$. The contribution to the scattering potential with the largest range is well described by a Van-der-Waals potential $V_\mathrm{VdW}(r) = -C_6/r^6$, which can be associated to the typical length scale $r_0 = 1/2\left(mC_6/\hbar^2\right)^{1/4}$ [71]. For lithium the constant $C_6 \approx 1393 \times a_\mathrm{B}^4 \hbar^2/m_\mathrm{e}$ has been calculated [71, 72], referenced to the Bohr radius a_B and electron mass m_e, and results in a length scale $r_0 \approx 31 a_\mathrm{B} \approx 1.7\,\mathrm{nm}$.

Other important length scales are the thermal wavelength λ_T and the mean atom distance expressed by the inverse Fermi momentum k_F^{-1}. The considered samples are dilute and ultracold, so that the interaction range is much smaller than the inter-particle distance and smaller than

[1] In the literature n sometimes refers to the total density or the density per spin state, the index can help to make it clear, that n_σ refers to the density per spin state.

the thermal wavelength [36] (this can also be seen from the typical orders of magnitude, provided above)

$$r_0 \ll k_\mathrm{F}^{-1} \tag{2.5}$$
$$r_0 \ll \lambda_T \,. \tag{2.6}$$

At low enough temperatures, where equation (2.6) is fulfilled, only s-wave scattering must be considered. The reason is, that for a given interaction range r_0 and a maximum thermal velocity v_T of the atoms, the maximum angular momentum mv_Tr_0 which could be involved in a scattering event would be lower than $\hbar$. The temperature T_p below which p-wave scattering freezes out can accordingly be calculated as $T_p = \hbar^2/\left(mr_0^2k_\mathrm{B}\right)$ and is 6 mK for the case of ^{6}Li [4]. However, this already exceeds the temperature in the MOT (can be as low as 140 µK as discussed in section 3.2.2), which is only the initial cooling stage of our experiment.

For identical fermions, s-wave collisions are also forbidden because the total wavefunction has to be antisymmetric, which makes a spin polarized fermionic gas a good implementation of an ideal Fermi gas [4].

The remaining case, the collision between two fermions of different internal state, can be evaluated by solving the Schödinger equation (ignoring the weak magnetic interaction between the different spin states) of the reduced system, with relative coordinate $\boldsymbol{r} = \boldsymbol{r}_2 - \boldsymbol{r}_1$ (given the fermion positions $\boldsymbol{r}_1$ and $\boldsymbol{r}_2$) and reduced mass $m_r = m/2$ [4]

$$\left(\nabla^2 + \boldsymbol{k}^2\right)\Psi_{\boldsymbol{k}}(\boldsymbol{r}) = \frac{m_r V(\boldsymbol{r})}{\hbar^2}\Psi_{\boldsymbol{k}}(\boldsymbol{r})\,. \tag{2.7}$$

Here $\Psi_{\boldsymbol{k}}$ is the wave function describing the reduced system and $V(\boldsymbol{r})$ is the scattering potential.

According to equation (2.5) the average distance of the free particles is much larger than the range of the potential, which means that the essential physics is captured by describing the scattering problem in the asymptotic limit $r \gg r_0$. In this limit the equation is solved with an ansatz which combines an incoming planar wave with an outgoing wave weighted by a scattering amplitude $f(\boldsymbol{k}', \boldsymbol{k})$

$$\Psi_{\boldsymbol{k}}(r) \propto \exp(ikr) + f(\boldsymbol{k}', \boldsymbol{k})\exp(ikr)/r\,. \tag{2.8}$$

By restricting the result to isotropic s-wave scattering via a partial wave decomposition and by performing an expansion for small momentum $k \ll 1/r_0$ the scattering amplitude can be written as [4]

$$f_0(k) = \frac{1}{a^{-1} - k^2 r_\mathrm{eff}/2 - ik}\,, \tag{2.9}$$

i.e. the scattering amplitude only depends on two newly introduced parameters with units of length, the scattering length a and the effective range r_eff.

The effects of the interactions are often described as "universal" because they do not depend on the details of the scattering potential at $r < r_0$, but can be well described by only the scattering length a and the inter-particle distance characterized by k_F^{-1}. The effective range can then be seen as a correction to the universal behavior, which does depend on the details of the potential, but depending on the atomic species the contribution of r_eff can be very small. As discussed in the next section, this is the case for ^{6}Li [4], therefore r_eff is omitted in the following.

The cross section follows directly from the optical theorem as

$$\sigma = \frac{4\pi}{a^{-2} + k^2}\,. \tag{2.10}$$

For small scattering lengths $k|a| \ll 1$, the cross section $\sigma = 4\pi a^2$ can be interpreted as the scattering of hard spheres with radius $|a|$ [73], while for very large scattering lengths $k|a| \gg 1$ one gets the largest possible, "unitarity limited" cross-section $\sigma = 4\pi/k^2$ [4].

The asymptotic wavefunction described by a does not depend on the details of the scattering potential, therefore it is useful to replace it by a simple pseudo-potential. A common choice is the contact potential

$$V(\boldsymbol{r}) = V_0 \delta(\boldsymbol{r}) \,, \tag{2.11}$$

which uses the Dirac delta function $\delta(\boldsymbol{r})$ and therefore only has a finite value V_0 at $\boldsymbol{r} = 0$. But this leads to an artificial problem of "ultraviolet divergences", where integrals in the following equations would diverge, because this potential would lead to a finite coupling of very high momentum states, whereas a realistic potential vanishes for $k \gg 1/r_0$. The problem is solved with a renormalization technique, which connects V_0 to the scattering length with [53, 74]

$$\frac{m}{4\pi\hbar^2 a} = \frac{1}{V_0} + \frac{m}{\hbar^2} \sum_{\boldsymbol{k}} \frac{1}{k^2} \,. \tag{2.12}$$

Note that here the sum on the right hand side does not converge, which is compensated by letting $V_0 \to -0$ [53]. Equation (2.11) can be used to describe the interactions in a Hamiltonian, while equation (2.12) has to be used to finally translate the coupling V_0 into the scattering length a, which is the physical quantity which characterizes the interaction.

2.2.1 Feshbach Resonances

The scattering length of the interaction between two hyperfine states is not necessarily a constant value, but it can be tuned via the magnetic field in certain cases, by employing (Fano-) Feshbach resonances [71].

Considering the reduced system of two atoms, there are different ways how the quantum numbers of their hyperfine states can be combined, which are called the channels of the collision [71]. For alkali atoms, the spin of the valence electrons of both atoms can be combined to a singlet or triplet state, which differ in energy depending on the distance as illustrated in figure 2.1. In the case of ^{6}Li, at large distance and for the available energy at low temperatures, only the triplet state is energetically accessible and is called an open channel, while non-accessible channels (the singlet state) are called closed channels of the collision. The scattering potential associated with the closed channel features a bound state with similar energy as the open channel and this bound state can mix with the continuum of the open channel and strongly affect the scattering properties.

If such a bound state energy can be tuned by a magnetic field relative to the energy of the open channel by exploiting the Zeeman effect, one gets a magnetically tunable interaction. In the case of ^{6}Li, it is quite natural that the energy of open and closed channel have a different dependence on the magnetic field because they correspond to singlet and triplet state. The functional dependence of the scattering length on the magnetic field has a resonant shape and can be approximated close to resonance as [71, 75]

$$a = a_{\mathrm{bg}} \left(1 - \frac{\Delta B}{B - B_0} \right) \,, \tag{2.13}$$

introducing the background scattering length a_{bg}, the width ΔB of the resonance and its resonance position B_0.

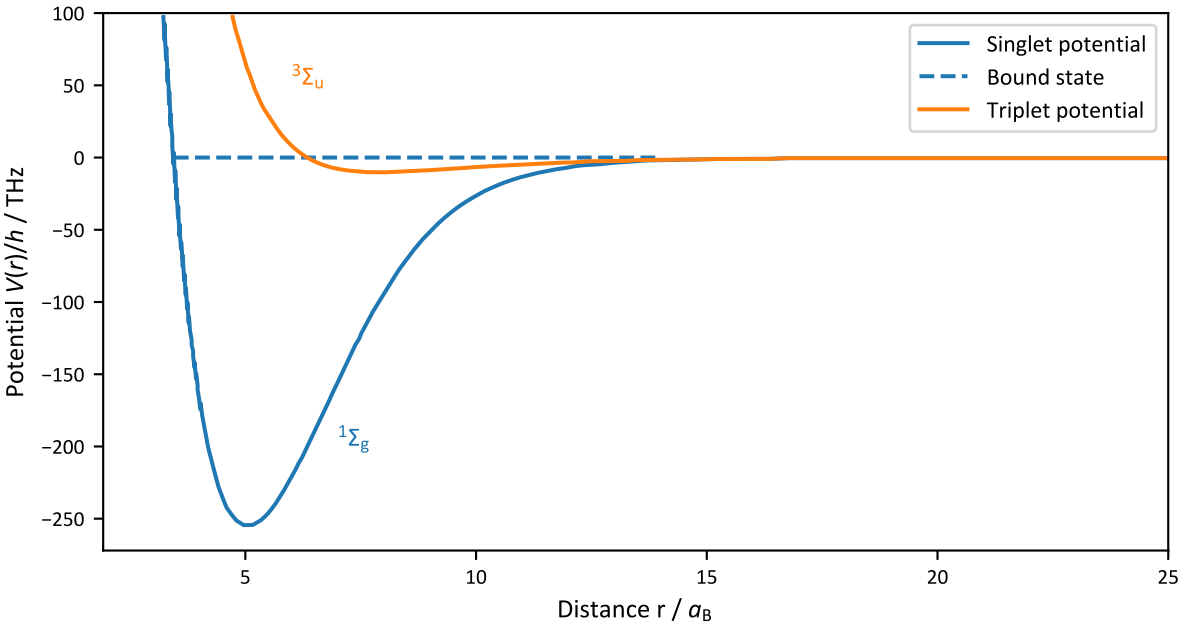

Figure 2.1: Molecular potentials of $^6Li_2$ Adapted from ref. [71]; The singlet state $^1\Sigma_g$ (closed channel) features a bound state close to the continuum energy of the triplet state $^3\Sigma_u$ (open channel), which causes the large background scattering lengths and broad Feshbach resonances of ^{6}Li. More precisely, there are two relevant, almost degenerate bound states and the open channel can be realized with different hyperfine states of the atoms, but this cannot be resolved on the scale of this figure [71].

Narrow and Broad Feshbach Resonances Feshbach resonances are categorized into broad and narrow resonances [71]. For a broad resonance the occupation of the closed channel can be neglected over a wide range of magnetic fields around the resonance position, while for a narrow resonance the occupation of the closed channel has to be considered and the physics becomes non-universal. "Narrow" and "broad" often also coincide with a smaller or larger ΔB, which allows a more precise interaction tuning in the case of a broad resonance, although there are exceptions.

^{6}Li has three particularly broad Feshbach resonances. The commonly used Feshbach resonances between the lowest three hyperfine-states of lithium are shown in figure 2.2.

Bound State Near a Feshbach resonance on the side of positive scattering length a two-body bound state exists with energy [71]

$$\epsilon_B = -\hbar^2/(2m_r a^2) = -\hbar^2/(ma^2)\,. \tag{2.14}$$

For a broad Feshbach resonance, its associated length scale a is much larger than the range of the potential r_0, which is a hint for universal behavior, not depending on the details of the scattering potential. Due to this large length scale, it is sometimes called a "halo state" [71]. I will also refer to it as "Feshbach molecule", although this term can sometimes also describe more deeply bound states, which are not relevant here.

Indeed, the binding energy can be expressed universally only in terms of the Fermi energy and interaction parameter $1/(k_F a)$

$$\epsilon_B/E_F = \frac{-2}{(k_F a)^2}\,. \tag{2.15}$$

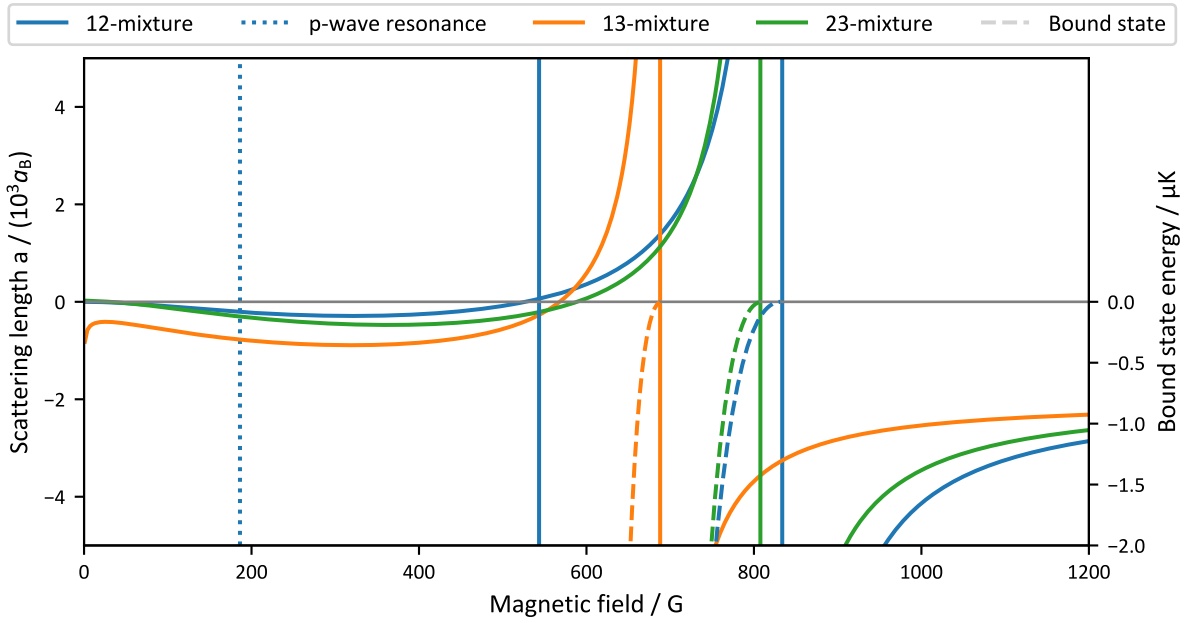

Figure 2.2: Broad Feshbach resonances of ^{6}Li The data is provided by ref. [76]. For the 12-mixture also the positions of a narrow [77] and a p-wave resonance [78] are shown.

Effective Range The effective range of the scattering potential near the Feshbach resonance, as introduced in equation (2.9), describes a deviation from universal behavior and is given by [62]

$$r_{\mathrm{eff}} = -2R_* \left(1 - \frac{a_{\mathrm{bg}}}{a}\right)^2 + \frac{4b}{\sqrt{\pi}} - \frac{2b^2}{a}\,, \tag{2.16}$$

with $R \approx 0.0269\,\mathrm{nm}$ and $b \approx 2.1\,\mathrm{nm}$ for the 12-resonance of ^{6}Li. In ref. [4] it is discussed that the deviation from universal behavior can be neglected if $k_{\mathrm{F}} \ll r_{\mathrm{eff}}$, which is well fulfilled over a large range of magnetic fields around the Feshbach resonance and is consistent to measurements which have found a rather small occupation of the closed channel bound state [79].

2.3 Qualitative Description of BEC-BCS Crossover

Here we consider a gas of fermions in a balanced mixture of two different spin states and a tunable contact interaction between fermions of opposite spin, as discussed in the previous section. Tuning the interaction results in a crossover of different pairing phenomena and a variable transition temperature from a superfluid to a normal state, which is illustrated in figure 2.3 and is qualitatively described in the following, based on refs. [4, 30, 36].

For weak attractive interactions and low temperatures, the gas enters a superfluid state which features Cooper pairs as described by BCS theory (see section 2.4). Although Cooper pairs are the mixture of only two opposite momentum states, Cooper pairing is a many-body effect, which is only possible due to the presence of the Fermi surface (occupation of all single-particle energy levels up to the Fermi energy, which leads to suppressed scattering due to the Pauli exclusion principle). Pairing and the superfluid transition coincide, i.e. the temperature T^* below which pairing occurs is equal to the critical temperature of superfluidity T_{c}.

For stronger interactions, the pair size decreases and at maximum interaction it becomes similar to the average particle distance. This point is called unitarity. At zero temperature the only relevant length scale of the system is the average particle distance, which results in

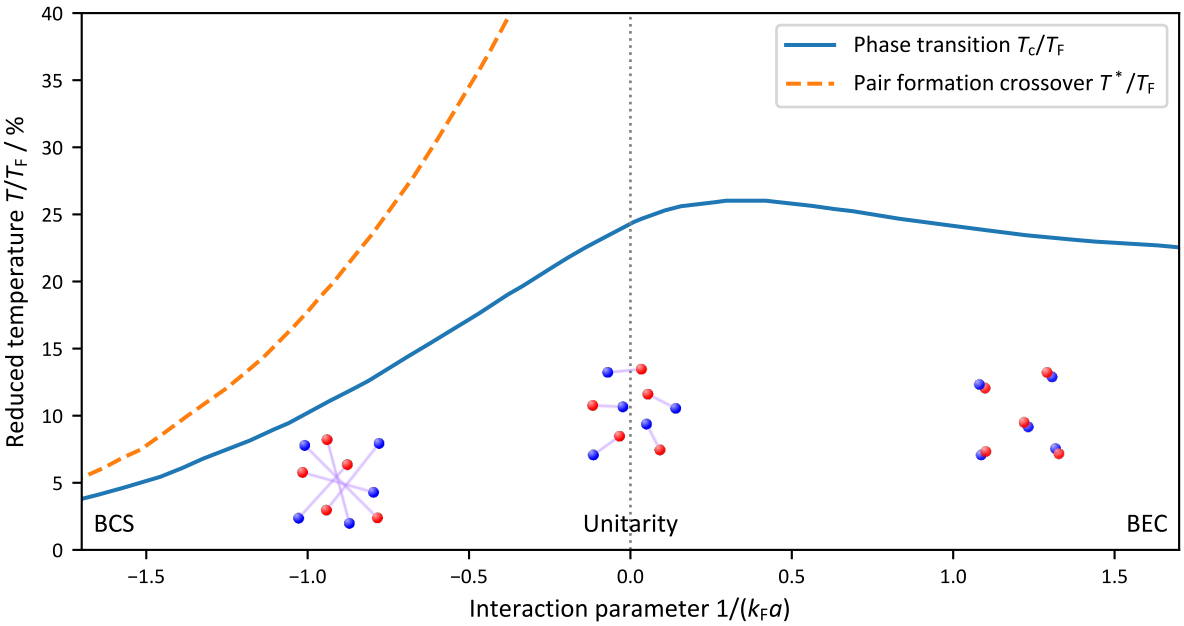

Figure 2.3: Phase diagram of the BEC-BCS crossover Figure is inspired by ref. [30] and data is from ref. [47], although there is no consensus yet about the exact curves as discussed in chapter 5. Illustrated are long range Cooper pairing on the BCS side, pairing with similar range as inter-particle distance at unitarity and a gas of Feshbach molecules on the BEC side.

scale-invariance and gives rise to universal[2] behavior of thermodynamics.

At the maximum interaction strength Feshbach molecules emerge, a bound state of two fermions which would even exist without considering many-body contributions to the pairing. By further tuning, a regime of decreasing weakly repulsive interactions can be reached. The repulsive interaction applies to the scattering of single fermions, but also the residual interaction between two Feshbach molecules is repulsive. The Feshbach molecules become more deeply bound and form a BEC at low temperatures.

Note that although a two-body bound state appears and the statistics of the gas changes from fermionic to composite-bosonic, the thermodynamic properties change smoothly and it is considered a crossover and not a phase transition. The thermodynamics can be described universally in terms of the interaction parameter $1/(k_F a)$ [30].

2.4 BCS Theory

General Hamiltonian We consider a Fermi gas with two different spin states $\sigma \in \{\uparrow, \downarrow\}$ and with interactions described by the Hamiltonian [4]

$$\hat{H} = \sum_{\boldsymbol{k},\sigma} \epsilon_{\boldsymbol{k}} \hat{c}^\dagger_{\boldsymbol{k},\sigma} \hat{c}_{\boldsymbol{k},\sigma} + \sum_{\substack{\boldsymbol{k}_1,\boldsymbol{k}_2,\boldsymbol{q},\\ \sigma_1,\sigma_2}} \tilde{V}_{\boldsymbol{q}} \hat{c}^\dagger_{\boldsymbol{k}_1+\boldsymbol{q},\sigma_1} \hat{c}^\dagger_{\boldsymbol{k}_2-\boldsymbol{q},\sigma_2} \hat{c}_{\boldsymbol{k}_2,\sigma_2} \hat{c}_{\boldsymbol{k}_1,\sigma_1} \,, \tag{2.17}$$

with the dispersion relation $\epsilon_{\boldsymbol{k}} = \frac{\hbar^2 k^2}{2m}$ for fermions with mass m. $\hat{c}_{\boldsymbol{k},\sigma}$ is the particle annihilation operator of a fermion with wave vector $\boldsymbol{k}$ and spin σ and $\tilde{V}_{\boldsymbol{q}}$ is the fourier component of the interaction potential corresponding to a momentum transfer $\boldsymbol{q}$.

[2] Here "universal" means, that at unitarity the scattering length is not a relevant length scale anymore [32], while in the context of broad Feshbach resonances a wider range of interactions is called "universal" because the interaction is only described by the scattering length rather than the details of the scattering potential [71].

Simplifications According to BCS theory [4, 10, 11] there are multiple steps to simplify this Hamiltonian:

- consider only interactions between particles with **opposite spin** (good approximation for low temperatures because of the Pauli exclusion principle)
- assume the potential to be **independent of the momentum transfer** $\tilde{V}_{\boldsymbol{q}} = V_0$, which is a good approximation for contact potentials and low temperatures where the considered momenta are smaller than the inverse range of the potential $k \ll r_0^{-1}$. Then V_0 can be seen as the coupling strength from the pseudo-potential in equation (2.11) and the sum over all momentum states requires the renormalization from equation (2.12). This also connects the interaction described here to the scattering length, which is known for our system from the Feshbach resonances.
- consider only interactions between particles with **opposite momentum**

The last point is the implication of one of the key ideas of BCS theory, the **Cooper pair instability**. Considering the presence of the Fermi sea, where all momentum states up to the Fermi momentum are occupied, scattering will mainly occur for states close to the Fermi surface, because deeper states cannot bring up enough energy to reach unoccupied target states for the scattering. Momentum states close to the Fermi surface, can scatter to other momentum states at the Fermi surface, without violating energy conservation or the Pauli exclusion principle, but the number of possible final states is further restricted by momentum conservation. But if the considered states have opposite momentum, they can scatter to all pairs of final momentum states which have also opposite momentum, which means that this process should dominate over the scattering of other momentum state combinations.

Additionally, the problem is handled as **grand canonical ensemble**, which fixes the average atom number[3] N with the chemical potential μ as Lagrange multiplier. For this, $\mu\hat{N}$ is subtracted from the Hamiltonian, where the atom number operator is given as

$$\hat{N} = \sum_{\boldsymbol{k},\sigma} \hat{c}^\dagger_{\boldsymbol{k},\sigma} \hat{c}_{\boldsymbol{k},\sigma} \,. \tag{2.18}$$

The chemical potential is absorbed into the particle dispersion $\xi_{\boldsymbol{k}} := \epsilon_{\boldsymbol{k}} - \mu$.

After implementing these simplifications, the Hamiltonian reads

$$\hat{H} - \mu\hat{N} = \sum_{\boldsymbol{k},\sigma} \xi_{\boldsymbol{k}} \hat{c}^\dagger_{\boldsymbol{k},\sigma} \hat{c}_{\boldsymbol{k},\sigma} + V_0 \sum_{\boldsymbol{k},\boldsymbol{q}} \hat{c}^\dagger_{\boldsymbol{k}+\boldsymbol{q},\uparrow} \hat{c}^\dagger_{-\boldsymbol{k}-\boldsymbol{q},\downarrow} \hat{c}_{-\boldsymbol{k},\downarrow} \hat{c}_{\boldsymbol{k},\uparrow} \,. \tag{2.19}$$

Mean-Field Theory A mean-field approach is used for the pair annihilation operator $\hat{b}_{\boldsymbol{k}} := \hat{c}_{-\boldsymbol{k},\uparrow}\hat{c}_{\boldsymbol{k},\downarrow}$ by splitting it into the expectation value and fluctuations $\hat{b}_{\boldsymbol{k}} = \left\langle \hat{b}_{\boldsymbol{k}} \right\rangle + \delta\hat{b}_{\boldsymbol{k}}$, with $\delta\hat{b}_{\boldsymbol{k}} = \hat{c}_{-\boldsymbol{k},\uparrow}\hat{c}_{\boldsymbol{k},\downarrow} - \left\langle \hat{b}_{\boldsymbol{k}} \right\rangle$. By neglecting all terms which are quadratic in the fluctuations, the interaction term of the Hamiltonian simplifies, reducing the maximum number of consecutive operators from four to two. Additionally, the **pairing field**

$$\Delta := -V_0 \sum_k \left\langle \hat{b}_{\boldsymbol{k}} \right\rangle \tag{2.20}$$

is introduced, which changes the BCS Hamiltonian to

$$\hat{H} - \mu\hat{N} = -|\Delta|^2/V_0 + \sum_{\boldsymbol{k}} \xi_{\boldsymbol{k}} \left(\hat{c}^\dagger_{\boldsymbol{k},\uparrow}\hat{c}_{\boldsymbol{k},\uparrow} + \hat{c}^\dagger_{\boldsymbol{k},\downarrow}\hat{c}_{\boldsymbol{k},\downarrow} \right) - \left(\Delta^* \hat{c}_{-\boldsymbol{k},\downarrow}\hat{c}_{\boldsymbol{k},\uparrow} + \Delta \hat{c}^\dagger_{\boldsymbol{k},\uparrow}\hat{c}^\dagger_{-\boldsymbol{k},\downarrow} \right) . \tag{2.21}$$

[3] For better compatibility to the references, N corresponds to the atom number of both spin states, but the results will be expressed in terms of E_F and k_F, which refer to N_σ via e.g. equation (2.2).

Since only opposite momenta are coupled, the Hamiltonian separates into 2x2 matrices for each momentum state $\boldsymbol{k}$

$$\hat{H} - \mu\hat{N} = -|\Delta|^2/V_0 + \sum_{\boldsymbol{k}} \begin{pmatrix} \hat{c}^\dagger_{\boldsymbol{k},\uparrow} & \hat{c}_{-\boldsymbol{k},\downarrow} \end{pmatrix} \begin{pmatrix} \xi_{\boldsymbol{k}} & \Delta \\ \Delta^* & -\xi_{\boldsymbol{k}} \end{pmatrix} \begin{pmatrix} \hat{c}_{\boldsymbol{k},\uparrow} \\ \hat{c}^\dagger_{-\boldsymbol{k},\downarrow} \end{pmatrix} + \sum_{\boldsymbol{k}} \xi_{\boldsymbol{k}} \,. \tag{2.22}$$

Note that in the last step the fermionic cummutation relation of the particle annihilation operators $\hat{c}^\dagger_{\boldsymbol{k},\downarrow}\hat{c}_{\boldsymbol{k},\downarrow} = 1 - \hat{c}_{\boldsymbol{k},\downarrow}\hat{c}^\dagger_{\boldsymbol{k},\downarrow}$ was used.

Bogoliubov Transformation The Hamiltonian can be diagonalized with the Bogoliubov transformation by introducing new **annihilation/creation operators for quasi-particle excitations**

$$\begin{pmatrix} \hat{\gamma}_{\boldsymbol{k},\uparrow} \\ \hat{\gamma}^\dagger_{-\boldsymbol{k},\downarrow} \end{pmatrix} := \begin{pmatrix} u_{\boldsymbol{k}}\hat{c}_{\boldsymbol{k}\uparrow} - v_{\boldsymbol{k}}\hat{c}^\dagger_{-\boldsymbol{k},\downarrow} \\ u_{\boldsymbol{k}}\hat{c}^\dagger_{-\boldsymbol{k}\downarrow} + v_{\boldsymbol{k}}\hat{c}_{\boldsymbol{k},\uparrow} \end{pmatrix} , \tag{2.23}$$

with

$$\begin{aligned} u^2_{\boldsymbol{k}} &= \frac{1}{2}\left[1 + \frac{\xi_{\boldsymbol{k}}}{E_{\boldsymbol{k}}}\right] , \\ v^2_{\boldsymbol{k}} &= \frac{1}{2}\left[1 - \frac{\xi_{\boldsymbol{k}}}{E_{\boldsymbol{k}}}\right] , \end{aligned} \tag{2.24}$$

and the dispersion relation of the quasi-particles

$$E_{\boldsymbol{k}} = \sqrt{\xi^2_{\boldsymbol{k}} + \Delta^2} \,. \tag{2.25}$$

Finally, the diagonalized Hamiltonian is given as

$$\hat{H} - \mu\hat{N} = -\Delta^2/V_0 + \sum_{\boldsymbol{k}} \xi_{\boldsymbol{k}} + \sum_{\boldsymbol{k}} E_{\boldsymbol{k}} \left(\hat{\gamma}^\dagger_{\boldsymbol{k},\uparrow}\hat{\gamma}_{\boldsymbol{k},\uparrow} + \hat{\gamma}^\dagger_{-\boldsymbol{k},\downarrow}\hat{\gamma}_{-\boldsymbol{k},\downarrow}\right) . \tag{2.26}$$

The first two terms describes the groundstate energy from the pairing and the single particle dispersion and the last term represents quasi-particle excitations with the energy spectrum $E_{\boldsymbol{k}}$.

BCS Ground State Formally, the ground state $|\Psi_{\mathrm{BCS}}\rangle$ is found by minimizing the free energy $H - \mu N$. From equation (2.26) it becomes clear, that the minimum is given if no quasi-particle excitation is present, i.e. $\hat{\gamma}_{\boldsymbol{k},\sigma}|\Psi_{\mathrm{BCS}}\rangle = 0$. Based on equation (2.23), this allows the construction of the ground state from the vacuum state $|0\rangle$ as

$$|\Psi_{\mathrm{BCS}}\rangle = \prod_{\boldsymbol{k}} \left(u_{\boldsymbol{k}} + v_{\boldsymbol{k}}\hat{c}^\dagger_{\boldsymbol{k}\uparrow}\hat{c}^\dagger_{-\boldsymbol{k}\downarrow}\right)|0\rangle \ . \tag{2.27}$$

This leads to the interpretation of $u_{\boldsymbol{k}}$ and $v_{\boldsymbol{k}}$ as the amplitude for the non-occupation and occupation of the corresponding momentum states. Interestingly, one can interpret the wave function of the Cooper pairs as

$$\left\langle \hat{c}^\dagger_{\boldsymbol{k}\uparrow}\hat{c}^\dagger_{-\boldsymbol{k}\downarrow} \right\rangle = u_{\boldsymbol{k}}v_{\boldsymbol{k}} \,. \tag{2.28}$$

These quantities are shown in figure 2.4. Indeed, far on the BCS side $|v_{\boldsymbol{k}}|^2$ features a Fermi edge, which is only slightly washed-out by cooper pairing close to the Fermi momentum. Towards unitarity and BEC side the Fermi surface vanishes and pairing occurs for a wider range of momenta.

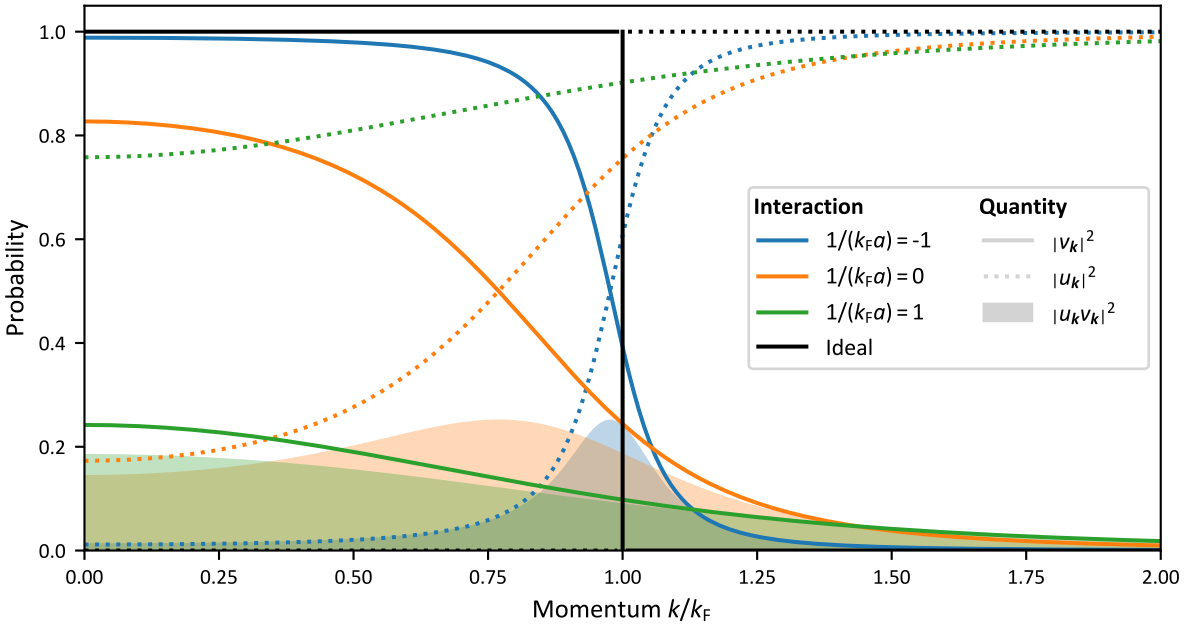

Figure 2.4: Interpretation of coefficients of Bogoliubov transformation Occupation ($|v_{\boldsymbol{k}}|^2$) and non-occupation ($|u_{\boldsymbol{k}}|^2$) of momentum states and Cooper pairing ($|u_{\boldsymbol{k}}v_{\boldsymbol{k}}|^2$) are compared for different interactions.

Gap Equation and Number Equation The result still has two free parameters: The chemical potential μ, which fixes the atom number and the interaction V_0, which is closely connected to the pairing field Δ. Note that Δ is also called the "gap" because it corresponds to the lowest excitation energy of a quasi-particle, as can be seen from equation (2.25) and will be discussed later. Since $u_{\boldsymbol{k}}$ and $v_{\boldsymbol{k}}$ depend on μ and Δ, one still has to evaluate these two constraints. They lead to the gap equation, by evaluating the average in equation (2.20) for the BCS ground state

$$\Delta = -V_0 \sum_{\boldsymbol{k}} u_{\boldsymbol{k}} v_{\boldsymbol{k}} \tag{2.29}$$

$$\Rightarrow -\frac{1}{V_0} = \sum_{\boldsymbol{k}} \frac{1}{2E_{\boldsymbol{k}}} \,. \tag{2.30}$$

Similarly, one finds the number equation by evaluating the mean of the number operator in equation (2.18) for the BCS ground state

$$N = 2 \sum_{\boldsymbol{k}} |v_{\boldsymbol{k}}|^2 \,. \tag{2.31}$$

Ultraviolet Divergence Note that the sum on the right hand side of equation (2.30) does not converge for a three-dimensional system, because $E_{\boldsymbol{k}} \propto k^2$ for large momentum states. As discussed in section 2.2, this problem is an artifact from the choice of the pseudo-potential and is mitigated by replacing V_0 with the scattering length according to equation (2.12), which modifies the gap equation to

$$-\frac{m}{4\pi\hbar^2 a} = \sum_{\boldsymbol{k}} \left(\frac{1}{2E_{\boldsymbol{k}}} - \frac{1}{2\epsilon_{\boldsymbol{k}}} \right) \,. \tag{2.32}$$

Thermodynamic Limit In the thermodynamic limit, one can consider the continuous versions of the gap equation and number equation

$$-\frac{m}{4\pi\hbar^2 a} = \int \frac{\mathrm{d}^3\boldsymbol{k}}{(2\pi)^3}\left(\frac{1}{2E_{\boldsymbol{k}}} - \frac{1}{2\epsilon_{\boldsymbol{k}}}\right) \tag{2.33}$$

$$N = 2\int \frac{\mathrm{d}^3\boldsymbol{k}}{(2\pi)^3}|v_{\boldsymbol{k}}|^2 \,. \tag{2.34}$$

Analytic Solution The standard strategy is to solve these equations numerically, but there is also an analytic solution, expressed by complete elliptic integrals [74]. This is nowadays probably the more convenient[4] solution and has been used here to calculate gap and chemical potential in the crossover region, shown in figure 2.5.

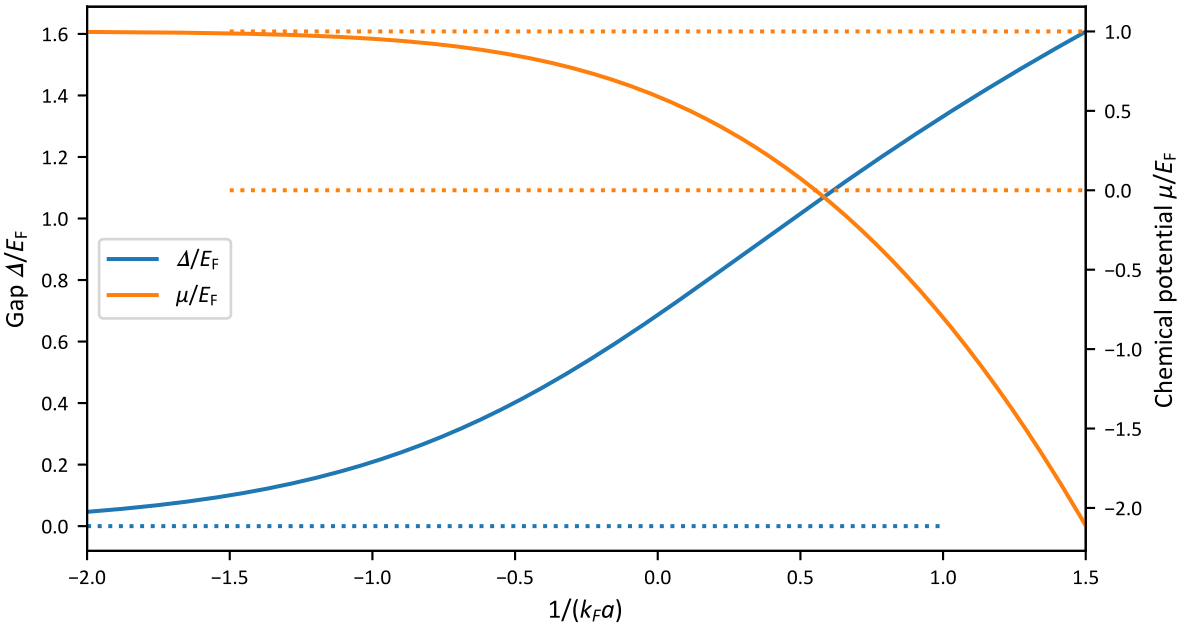

Figure 2.5: Analytic BCS solution for gap and chemical potential in the BEC-BCS crossover The auxiliary lines demonstrate that the gap is substantially suppressed towards the BCS side and that the chemical potential is equal to the Fermi energy on the BCS side and becomes negative towards the BEC side.

BCS Limit In the limit of weakly attractive interactions $1/(k_\mathrm{F}a) \ll 0$, the solutions for gap and chemical potential reduce to [4]

$$\mu = E_\mathrm{F} \tag{2.35}$$

$$\Delta = \mu\frac{8}{e^2}e^{-\pi/(2k_\mathrm{F}|a|)} \,. \tag{2.36}$$

It has been shown that density fluctuations, which are neglected in the mean-field treatment above, lead to a density mediated interaction [4, 48]. The effectively weakened attractive interaction reduces the superfluid gap by roughly 55 %

$$\Delta = \mu\left(\frac{2}{e}\right)^{7/3} e^{-\pi/(2k_\mathrm{F}|a|)} \,. \tag{2.37}$$

This beyond mean-field result is called Gor'kov and Melik-Barkhudarov (GMB) correction.

[4] One has to consider different definitions of the argument of the complete elliptic integrals, see appendix A.1.

Validity in BEC Regime Several assumptions of BCS theory suggest that it is only applicable to the BCS limit of weak attractive interactions, for example the mean-field approach, the Cooper pair stability which is based on the Fermi sea or the use of fermionic operators. But interestingly, it can also be used to describe the BEC side of the crossover. For example, it is possible to define pair creation operators which approximately fulfill bosonic commutator relations in the BEC limit. This results in a "formally identical" ground state as for the Gross-Pitaevskii equation, which would be used for an ideal bosonic system [4]. Next it will be discussed, that also the pair-breaking excitation spectrum on the BEC side can reasonably be predicted by BCS theory.

2.4.1 Excitation Spectrum

Pair-Breaking The quasi-particle excitation spectrum is described by $E_{\boldsymbol{k}}$ in equation (2.25) and is visualized in figure 2.6. This kind of excitation is also called the "pair-breaking continuum". Far on the BEC side, the lowest excitation is at the Fermi momentum with a finite

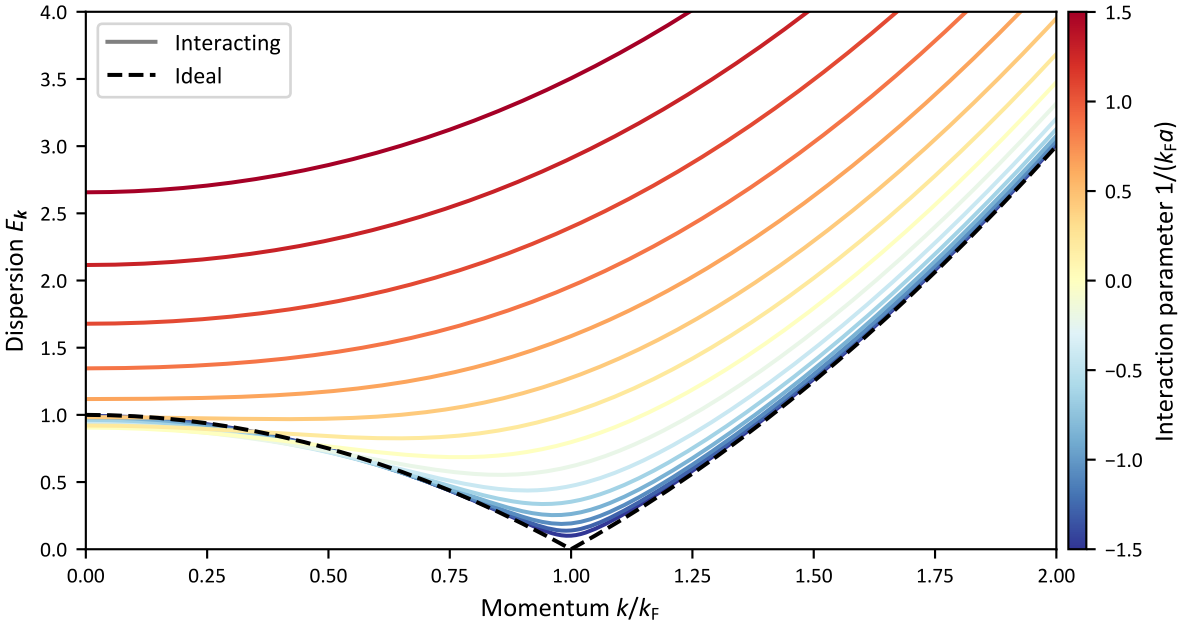

Figure 2.6: Quasi particle excitation spectrum in BEC-BCS crossover The results are calculated within BCS theory from equation (2.25) and are compared to the results for an ideal Fermi gas.

energy Δ. Since arbitrarily small excitations are not possible, the state is superfluid and Δ is identified as the **superfluid gap**.

Note that the excitation of a single quasi-particle does not conserve particle number [4]. To preserve the particle number, at least two quasi-particle excitations are required, which leads to a minimum excitation energy of 2Δ.

Towards the BEC side, at a certain point where μ becomes negative, the lowest excitation is instead at zero momentum and its energy from equation (2.25) can be approximated as $2\sqrt{\mu^2 + \Delta^2} \approx 2|\mu| + \Delta^2/|\mu|$ (Again, the factor 2 is needed for particle number conservation). Interestingly, it can be shown that the second summand can be interpreted as the mean-field experienced by two fermions in a molecular gas [4].

Sound Mode On the BEC side there are collective excitations with linear dispersion at low energy and momentum, which can be interpreted as sound waves [4]. This mode does not

appear in the BCS theory presented above but a more careful analysis, which includes density fluctuations, shows that the mode also exists on the BCS side and it is called the Bogoliubov-Anderson mode.

Superfluidity According to the Landau criterion for superfluidity, a finite minimum excitation energy implies superfluidity, where the critical velocity at which superfluidity breaks down on the BEC side is given by [4]

$$v_c = \min\left(\frac{E_{\boldsymbol{k}}}{\hbar \boldsymbol{k}}\right) = \frac{\Delta}{\hbar k_F} . \tag{2.38}$$

The system is also superfluid on the BEC side but the critical velocity is limited by the sound velocity of the Bogoliubov-Anderson mode.

Collective Excitations It has been shown that phase transitions with symmetry breaking are generally connected to the emergence of a massless excitation mode [39, 40]. Symmetry breaking in this context means, that there is a continuous transformation, which changes the ground state of the system, but not the Hamiltonian [40].

In BCS theory, the gap Δ can be identified as the order parameter of the system [4] and below the phase transition the U(1) symmetry of the phase of Δ is broken [39].This suggests the existence of a massless excitation connected to phase fluctuations of the superfluid order parameter and is identified as the Bogoliubov-Anderson mode [44], mentioned above.

Additionally, fluctuations of the amplitude of the order parameter could give rise to an amplitude mode, which has many similarities to the Higgs mode in particle physics [39]. But whether there is a stable amplitude mode or whether it decays rapidly into phase modes depends on additional symmetries of the system. It has been shown that in particle physics one gets a defined mode due to Lorentz invariance. In a superconductor the decay to phase modes is prevented by the coupling of the phase modes to the electomagnetic field via the Anderson-Higgs mechanism. For a neutral BCS type superfluid, particle-hole symmetry guarantees the observability of the Higgs mode. But particle-hole symmetry is only given on the BCS side and vanishes towards the BEC side.

2.4.2 Gap and Condensate Fraction

In equation (2.20) Δ was introduced as the pairing field. Later it was also identified as the superfluid gap and it was stated that it corresponds to the superfluid order parameter.

In the experiment, a direct measurement of Δ is not easy. Instead, a closely related quantity is targeted, the **condensate fraction**, i.e. the number of condensed pairs relative to the number of fermions. The number of condensed pairs is given by [80]

$$N_0 = \sum_{\boldsymbol{k}} \left| \left\langle \hat{b}_{\boldsymbol{k}} \right\rangle \right|^2 , \tag{2.39}$$

which is very similar to the definition of Δ in equation (2.20) but note that any complex phase of the pairing drops out. It should be stressed that the density of condensed pairs is a different quantity than the superfluid density, which becomes unity at zero temperature, whereas the density of condensed pairs can have lower values at zero temperature depending on the interaction [4].

The condensate fraction is directly connected to the long-range order of the system [4, 81]. It can be seen as a signature of the superfluid state [4]. Additionally, the sensitivity of the condensate fraction on the temperature is exploited in the experiments and a dependence of the condensate fraction on the amplitude of the order parameter is assumed. The measurement of the condensate fraction is based on the rapid ramp technique, which is discussed in section 4.2.

2.4.3 Critical Temperature

On the BCS side one can modify gap and number equation in the following way to get a description of the system at the critical temperature [4] of the phase transition between superfluid and normal state.

- Consider the occupation of quasi-particles according to the Fermi-Dirac distribution for the gap equation
- Set the value of the gap to zero
- Describe the occupation of momentum states by the Fermi-Dirac distribution and assume $\mu \gg k_\mathrm{B}T$

This allows to solve the gap equation for the critical temperature and results in $T_\mathrm{C,BCS} = \frac{\mathrm{e}^\gamma}{\pi}\Delta_0$, using Euler's constant $\mathrm{e}^\gamma \approx 1.78$ and the zero temperature gap Δ_0 according to equation (2.36) for the BCS result or according to equation (2.37) to include the GMB correction, which gives

$$T_\mathrm{c,BCS}/T_\mathrm{F} = \frac{\mathrm{e}^\gamma}{\pi}\frac{8}{e^2}e^{-\pi/(2k_\mathrm{F}|a|)} \tag{2.40}$$

$$T_\mathrm{c,BCS+GMB}/T_\mathrm{F} = \frac{\mathrm{e}^\gamma}{\pi}\left(\frac{2}{e}\right)^{7/3}e^{-\pi/(2k_\mathrm{F}|a|)}\,. \tag{2.41}$$

Far on the BEC side at low temperatures, the gas can be described as a condensate of bosonic molecules, which have twice the mass of the fermions $m_b = 2m$ and their density corresponds to the density of one spin component n_σ [4]. This results in a critical temperature [80]

$$T_\mathrm{c,BEC,0} = \frac{n_\sigma^{2/3}\hbar^2}{m_b}\left(\frac{\sqrt{2}\pi^2}{\Gamma(3/2)\zeta(3/2)}\right)^{2/3} \approx 1.66\frac{\hbar^2 n_\sigma^{2/3}}{m}\,, \tag{2.42}$$

using the gamma function Γ and Riemann zeta function ζ. The result can directly be compared to the Fermi temperature (see equation (2.2))

$$T_\mathrm{c,BEC,0}/T_\mathrm{F} \approx 21.8\,\%\,. \tag{2.43}$$

For interactions, there is no correction of T_c from mean-field theory, but the leading order correction is caused by density fluctuations and yields [52]

$$T_\mathrm{c,BEC} = T_\mathrm{c,BEC,0}\left(1 + c_1 a_\mathrm{dd}/\lambda_0\right)\,, \tag{2.44}$$

with $c_1 \approx 1.3$, the residual scattering length of the molecules $a_\mathrm{dd} \approx 0.60a$ [36] and the thermal wavelength λ_0 according to equation (2.1), but evaluated at temperature[5] $T_\mathrm{c,BEC,0}$. In the BEC-BCS crossover the interaction is usually described with the interaction parameter $1/(k_\mathrm{F}a)$ instead, so it is useful to calculate

$$\frac{a}{\lambda_0} = \frac{k_\mathrm{F}a}{2\sqrt{(6\zeta(3))^{1/3}\,\pi}} \approx 0.20k_\mathrm{F}a\,. \tag{2.45}$$

[5] To emphasize this, it is written as λ_0, instead of λ_T.

2.5 Thermodynamics of a Gas

2.5.1 Partition Function and Thermodynamic Potential

To recover the thermodynamics of the gas, a straightforward way is to calculate the grand canonical partition function [82, 83]

$$Z := \mathrm{Tr}\left(\mathrm{e}^{-\beta\left(\hat{H}-\mu\hat{N}\right)}\right) = \sum_{N,i} \mathrm{e}^{-\beta(\epsilon_i-\mu N)}\,, \tag{2.46}$$

which will incorporate the different statistics of the particles. Here $\beta = 1/(k_\mathrm{B}T)$ is the inverse temperature and ϵ_i the single particle energy of a state i. On one hand, the partition function gives access to the grand canonical potential

$$\Omega = -k_\mathrm{B}T \ln Z\,, \tag{2.47}$$

from which thermodynamic properties can be derived via differentiation. On the other hand, it allows to calculate expectation values of operators via

$$\left\langle \hat{O} \right\rangle = Z^{-1}\,\mathrm{Tr}\left(\mathrm{e}^{-\beta\left(\hat{H}-\mu\hat{N}\right)}\hat{O}\right). \tag{2.48}$$

For example, of special interest is the distribution function $f(\epsilon_i)$, which calculates the average occupation of the state i and reduces to [82, 84]

$$f(\epsilon_i) = \frac{-1}{\beta}\frac{\partial}{\partial\epsilon_i}\ln Z\,. \tag{2.49}$$

For a Bose gas, when calculating the partition function, the summation over all possible occupation numbers leads to a geometric series, resulting in

$$Z_\mathrm{B} = \prod_{i=1}^{\infty} \frac{1}{1-\mathrm{e}^{-\beta(\epsilon_i-\mu)}} \tag{2.50}$$

$$\Rightarrow \Omega_\mathrm{B} = k_\mathrm{B}T \sum_{i=1}^{\infty} \ln\left(1-\mathrm{e}^{-\beta(\epsilon_i-\mu)}\right), \tag{2.51}$$

$$f_\mathrm{B}(\epsilon_i) = \frac{1}{\mathrm{e}^{\beta(\epsilon_i-\mu)}-1}\,. \tag{2.52}$$

For a Fermi gas only occupation numbers 0 and 1 are considered due to the Pauli exclusion principle, which results in a different partition function

$$Z_\mathrm{F} = \prod_{i=1}^{\infty} \frac{1}{1+\mathrm{e}^{-\beta(\epsilon_i-\mu)}} \tag{2.53}$$

$$\Rightarrow \Omega_\mathrm{F} = -k_\mathrm{B}T \sum_{i=1}^{\infty} \ln\left(1+\mathrm{e}^{-\beta(\epsilon_i-\mu)}\right), \tag{2.54}$$

$$f_\mathrm{F}(\epsilon_i) = \frac{1}{\mathrm{e}^{\beta(\epsilon_i-\mu)}+1}\,. \tag{2.55}$$

At high temperatures, the chemical potential behaves as $\beta\mu \to -\infty$ and both gases can be approximated as a Boltzmann gas with

$$f_\mathrm{Boltzmann}(\epsilon_i) = \mathrm{e}^{\beta(\epsilon_i-\mu)}\,. \tag{2.56}$$

The different distribution functions are compared in figure 2.7. Note that in order to prevent unphysical negative values for the Bose distribution function, the chemical potential for an ideal Bose gas is restricted to $\mu \leq 0$.

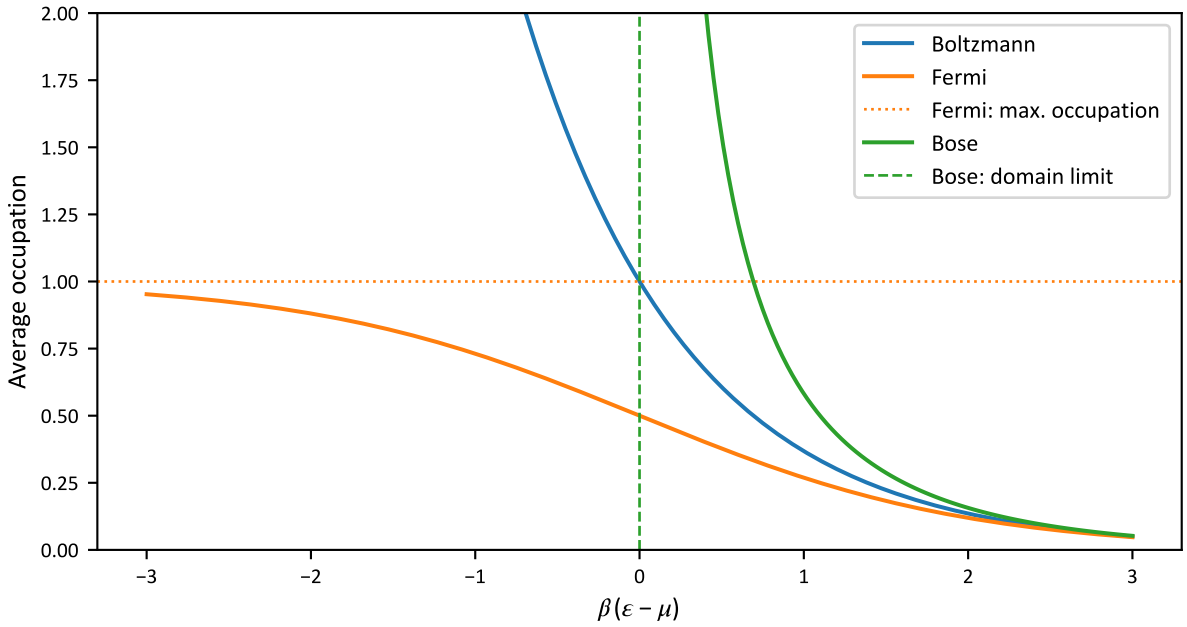

Figure 2.7: Distribution function for Fermi, Bose and Boltzmann statistics It is indicated that the maximum occupation number for indistinguishable fermions is 1 and that the Bose distribution function is only defined for $\beta(\epsilon - \mu) > 0$.

Energy Spectrum and Density of States To apply above equations to an actual system, one has to choose an appropriate energy spectrum $\{\epsilon_i\}$ [83]. The sums over energy states can often be approximated by integrals, which are weighted by the density of states $\rho(\epsilon)$. For example a homogeneous gas in a 3D volume V with periodic boundary conditions and dispersion

$$\epsilon_{\boldsymbol{k}} = \frac{\hbar^2 k^2}{2m} \tag{2.57}$$

has the density of states [80]

$$\rho(\epsilon) = \frac{V m^{3/2}}{\sqrt{2}\pi^2\hbar^3}\epsilon^{1/2}\,. \tag{2.58}$$

This can be used to calculate the density of the gas from the grand canonical potential, which yields [4]

$$n_\sigma = -\frac{1}{V}\frac{\partial\Omega}{\partial\mu} = \pm\frac{1}{\lambda_\mathrm{T}^3}\,\mathrm{Li}_{3/2}(\pm e^{\beta\mu})\,, \tag{2.59}$$

using the polylogarithm Li_n (upper sign for bosons, lower sign for fermions). Alternatively, this can also be determined from the distribution function $n_\sigma = \sum_{i=1}^{\infty} f(\epsilon_i)$.

In the low density and high temperature limit, i.e. $\beta\mu \ll 0$, one recovers the density distribution of the Boltzmann gas by using $\lim_{|z|\to 0}\mathrm{Li}_n(z) = z$

$$n_\sigma(\boldsymbol{r}) = \frac{1}{\lambda_\mathrm{T}^3}e^{\beta\mu}\,. \tag{2.60}$$

The different behavior of the density functions is compared in figure 2.8. Interestingly, one finds a maximum density n_c for the Bose gas, which is an artifact of approximating sums over states by integrals. A more careful analysis shows that the calculation does not properly account for a macroscopic occupation of the single particle ground state, which becomes relevant at roughly this density and is the effect of Bose-Einstein condensation [84].

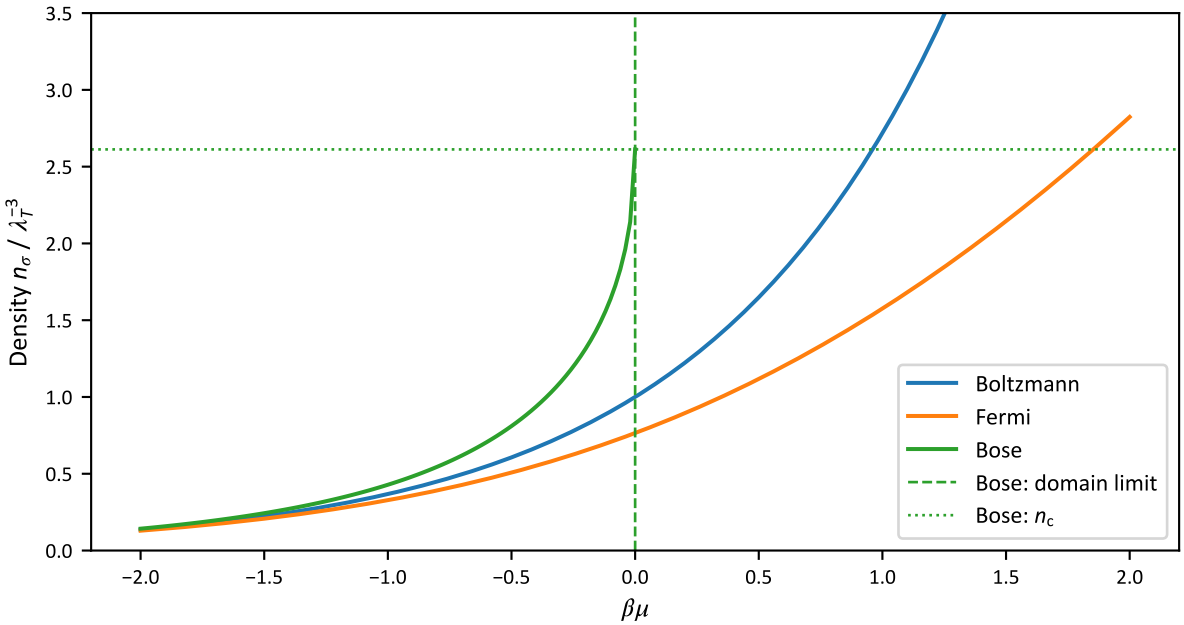

Figure 2.8: Density of ideal Bose, ideal Fermi and Boltzmann gas For the Bose gas the critical density n_c is indicated and the domain of permitted chemical potential $\mu < 0$.

2.5.2 Local Density Approximation

For gases in an inhomogeneous trapping potential, the thermodynamic properties can have a spatial dependence. Local density approximation (LDA) assumes that the local properties can be deduced from an equivalent homogeneous system with same temperature and a local chemical potential [4, 36]

$$\mu(\boldsymbol{r}) := \mu_0 - V(\boldsymbol{r})\,. \tag{2.61}$$

For a classical gas it seems reasonable that the system in a grand canonical ensemble can be subdivided into many smaller ensembles with almost constant potential. But for a quantum gas, where long range correlations might be important, this seems less intuitive. Nevertheless the applicability of LDA has been confirmed for many systems by experiment and numerical calculations [33]. As an example, for a bosonic two-dimensional gas in an optical lattice the local density relation is closely related to the fluctuation-dissipation theorem, which has been confirmed in ref. [85] by measuring local density fluctuations.

For example the density distribution of a trapped gas within LDA is given by applying equation (2.61) to equation (2.59)

$$n_\sigma(\boldsymbol{r}) = \pm\frac{1}{\lambda_\mathrm{T}^3}\,\mathrm{Li}_{3/2}\left(\pm e^{\beta(\mu_0 - V(\boldsymbol{r}))}\right). \tag{2.62}$$

2.5.3 Virial Expansion

Calculating the density distribution of a gas at finite temperature with finite interactions is not trivial, but in the "virial regime"[6] $\beta\mu \ll 0$, thermodynamic quantities can be approximated with an expansion in the fugacity $z := e^{\beta\mu}$.

The second coefficient of the expansion was already calculated 1937 [86], but recently there were more efforts to calculate the higher order coefficients [62]. The virial expansion is calculated

[6] This regime is called "Boltzmann limit" in ref. [32], but can be called "virial regime" [61] to indicate that more orders of the expansion than only the first are significant.

by expanding the grand partition function from equation (2.46) into partition functions of clusters, which consider only few particles [87]. This leads to the form

$$\Omega = -k_\mathrm{B} T V \lambda_T^{-3} \sum_{n=1} b_n z^n \,, \tag{2.63}$$

with the virial coefficients b_n and volume[7] V. This allows the calculation of the density n_σ

$$n_\sigma = -\frac{1}{V}\frac{\partial \Omega}{\partial \mu} = \lambda_T^{-3} \sum_{n=1} n b_n z^n \,, \tag{2.64}$$

where the derivative of the fugacity $\frac{\partial z}{\partial \mu} = \beta^{-1} z$ was used.

For the ideal Fermi gas, the coefficients of the virial expansion are given by [88]

$$b_n^{(0)} = (-1)^{n+1} n^{-5/2} \,, \tag{2.65}$$

which leads to the density distributions shown in figure 2.9. Here it is easy to calculate the

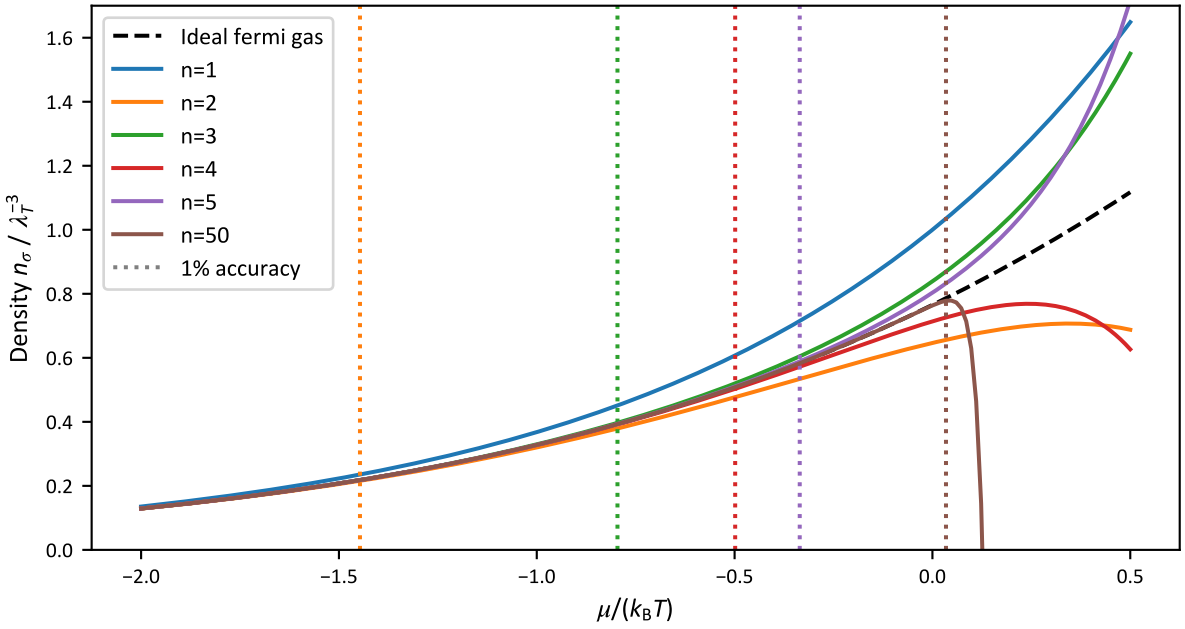

Figure 2.9: Density distribution of the ideal Fermi gas compared to the non-interacting virial expansion The density scaled by λ_T^{-3} does not depend on actual temperature, but only on the ratio $\mu/(k_\mathrm{B}T)$. The degree of the virial expansion is denoted by n. The vertical lines show up to which point the virial expansion is accurate on a 1 % level.

virial expansion up to arbitrary order, which shows that the accuracy further improves for $\mu/(k_\mathrm{B}T) < 0$, but quickly becomes invalid for $\mu/(k_\mathrm{B}T) > 0$.

Calculating virial coefficients for finite interactions can be challenging. The first virial coefficient is trivial $b_1 = 1$. For higher coefficients usually the difference to the ideal coefficients is specified $\Delta b_n = b_n - b_n^{(0)}$. The second order is still well understood and is given by [86, 89]

$$\Delta b_2 = \begin{cases} \frac{e^{x^2}}{\sqrt{2}} \left[1 - \mathrm{erf}(|x|)\right] & \text{if } x < 0, \\ \sqrt{2} e^{\beta |\epsilon_\mathrm{B}|} - \frac{e^{x^2}}{\sqrt{2}} \left[1 - \mathrm{erf}(x)\right] & \text{if } x \geq 0. \end{cases} \tag{2.66}$$

[7] Unfortunately, the letter "V" denotes several quantities but has always a function argument if it describes a potential $V(r)$, has always an index if it describes the coupling of interactions V_0 and otherwise it denotes the Volume. Similarly, the order of the virial expansion n is distinguished from the density n_σ by the index.

with $x = \lambda_T / \left(\sqrt{2\pi} a\right)$. In the universal strongly interacting regime, $e^{\beta|\epsilon_B|}$ can be replaced by x^2.

Higher, up to fifth order coefficients are calculated in ref. [88] for unitarity and towards BCS side. Around unitarity, the third order coefficient is calculated in ref. [90] and for a larger range in ref. [87].

Combining the results from refs. [86, 88, 90], one knows the virial coefficients up to third order on the BEC side and up to fifth order at unitarity and BCS side, as presented in figure 2.10.

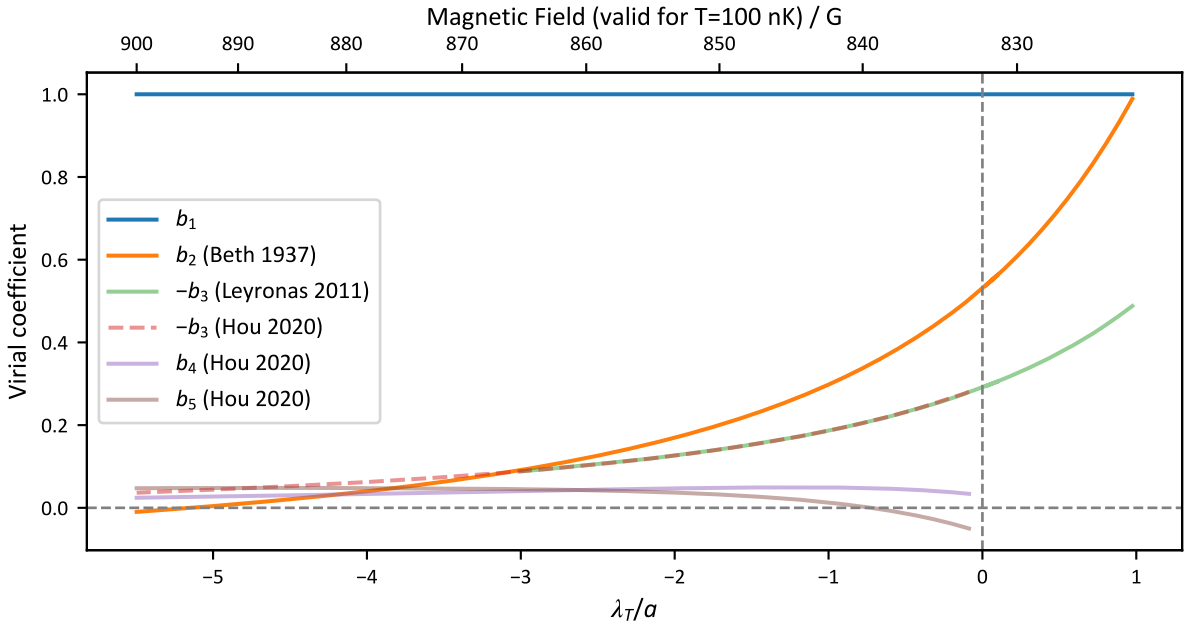

Figure 2.10: Virial coefficients Data is based on ref. [86] ("Beth 1937"), ref. [90] ("Leyronas 2011") and ref. [88] ("Hou 2020").

Towards the BEC side, the value for the coefficients increases drastically. Large coefficients $b_n \gg 1$ are problematic for an expansion, but decisive for the convergence is not the size of the coefficients b_n, but how fast the whole terms $b_n z^n$ decrease. From equation (2.66) one can understand that b_2 scales as $e^{\beta|\epsilon_B|}$, but the expectation is that the chemical potential of the fermions scales as the bound state energy ϵ_B and therefore the fugacity $z = e^{\beta\mu}$ should roughly scale with the inverse factor as b_2 when the bound state energy increases.

This inspires to specify the large coefficients on the BEC side relative to $e^{\beta|\epsilon_B|}$, as shown in figure 2.11. By construction, this leads to a vanishing b_1 and converging b_2, but indeed this reveals that b_3 has also a similar scaling, which is consistent with a converging series. Due to the smaller fugacity on the BEC side, the expansion should even converge faster for higher order terms of z^n.

The calculated virial coefficients from ref. [87] are not presented in a temperature independent form, which makes it a bit more difficult to implement them. Inspired by ref. [88], Δb_3 can be seen as a function of Δb_2, which mostly removes the temperature dependence, but a small additional temperature dependence remains. Instead, on the BEC side the dependence between Δb_3 and Δb_2 can be well approximated by a linear function, as demonstrated in the inset of figure 2.11 for the coefficients from ref. [90], which allows the extrapolation of the third order virial coefficient shown in the main plot.

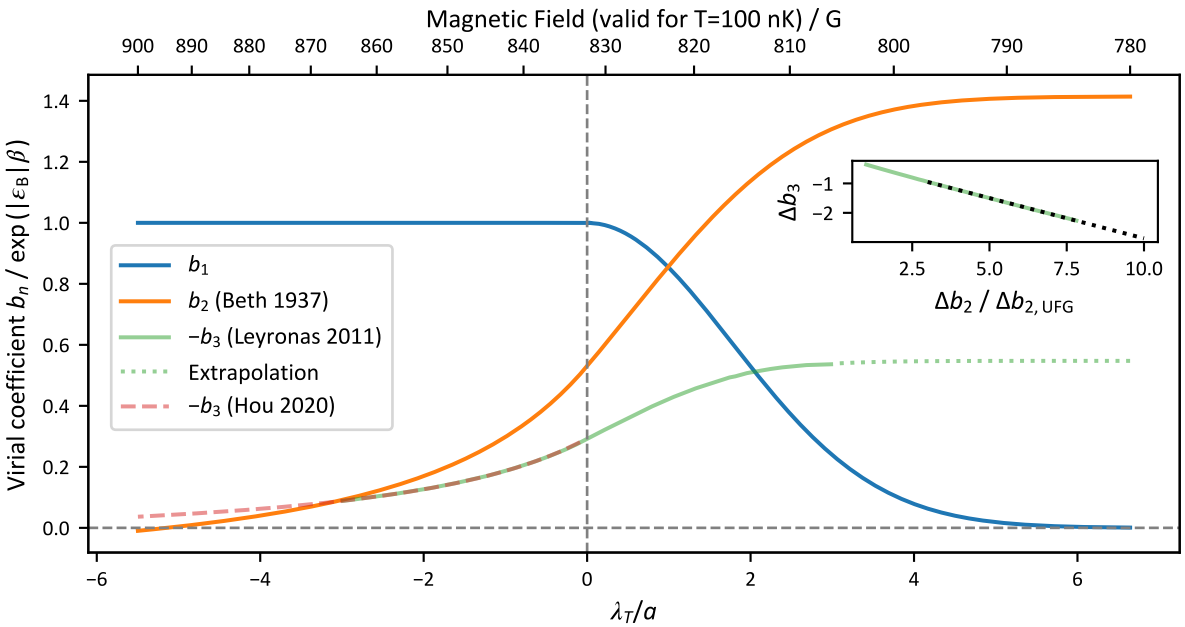

Figure 2.11: Virial coefficients scaled on BEC side Data is based on ref. [86] ("Beth 1937"), ref. [90] ("Leyronas 2011") and ref. [88] ("Hou 2020"). On the BEC side the coefficients are referenced to $e^{\beta|\epsilon_B|}$, which captures the most dramatic scaling of the coefficients and leads to converging values for $\lambda_T/a \gg 1$. The third order coefficient is extrapolated further to the BEC side by exploiting the quite linear dependence of Δb_3 on the second order coefficient (More precisely, on $\Delta b_2/\Delta b_{2,\mathrm{UFG}}$ with $\Delta b_{2,\mathrm{UFG}}$ referring to the value of Δb_2 at unitarity) shown in the inset, based on the data from ref. [90].

2.5.4 Contact

Macroscopically, within the canonical ensemble, the thermodynamics of a gas in equilibrium is characterized by the conjugate variables pressure P and volume V, as well as temperature T and entropy S. In the grand canonical ensemble, additionally density n and chemical potential μ are used. It has been shown that the interaction can be handled in a similar manner: By identifying the conjugate variable of the inverse scattering length a as the contact C, one has a new quantity which describes important properties of the gas [91, 92].

For example, it can be used to describe the change in energy during an adiabatic sweep of the interaction, which is called the "adiabatic sweep theorem" [93]

$$\frac{\mathrm{d}E}{\mathrm{d}(-1/a)} = \frac{\hbar^2 V C}{4\pi m}. \tag{2.67}$$

But this equation can also be generalized for faster sweeps and for a sudden change of the scattering length from a_0 to a_1, the energy changes by

$$\Delta E = \frac{\hbar^2 V C_0}{4\pi m}\left(\frac{1}{a_0} - \frac{1}{a_1}\right). \tag{2.68}$$

Intuitively, the contact can be interpreted as the "density of pairs at short distances" [62] and has several additional experimental signatures, including the shape of the momentum distribution at large momentum and the shape of the frequency response in RF spectroscopy at large frequencies.

2.6 Effects of Harmonic Traps

In experiments it is common to trap the atoms in a potential which can be approximated by a harmonic potential

$$V(\boldsymbol{r}) = \frac{1}{2} m \left(\boldsymbol{\omega} \cdot \boldsymbol{r}\right)^2 , \tag{2.69}$$

with trap frequencies $\boldsymbol{\omega} = \left(\omega_x, \omega_y, \omega_z\right)$.

The Fermi energy of a harmonically trapped gas is [36]

$$E_\mathrm{F} = \left(6N_\sigma\right)^{1/3} \hbar\bar{\omega}. \tag{2.70}$$

and depends on the atom number per spin N_σ and the geometric mean of the trap frequencies $\bar{\omega}$. Note that for a zero temperature Fermi gas the central density in the trap is the same as for a homogeneous gas with the same Fermi energy.

2.6.1 Zero Temperature Density Distributions

Within LDA the density distribution of a zero temperature **ideal Fermi gas** can be described by a Thomas-Fermi profile [36]

$$n_\sigma(\boldsymbol{r}) = \frac{8}{\pi^2} \frac{N_\sigma}{R_x R_y R_z} \left[1 - \frac{x^2}{R_x^2} - \frac{y^2}{R_y^2} - \frac{z^2}{R_z^2}\right]^{3/2} , \tag{2.71}$$

with the Thomas-Fermi radius in direction $i \in \{x, y, z\}$ given as

$$R_i = a_\mathrm{ho} \left(48N_\sigma\right)^{1/6} \bar{\omega}/\omega_i \, , \tag{2.72}$$

using the characteristic length of the potential, the harmonic-oscillator length $a_\mathrm{ho} = \sqrt{\hbar/\left(m\bar{\omega}\right)}$.

Similar density profiles can in principle be calculated for a zero temperature interacting gas, using LDA with equation (2.61), but additionally the relationship between density and chemical potential must be known. See ref. [36] e.g. for the first order interaction correction of the Fermi gas on the BCS side.

For the zero temperature **unitary gas**, universality dictates the proportionality of chemical potential and Fermi energy (which then also fixes the density)

$$\mu = \xi E_\mathrm{F} \, . \tag{2.73}$$

For the proportionality factor, the Bertsch parameter ξ, several measurements and theoretical calculations exist. Here I use $\xi = 0.376$ [61], which is also close to recent Monte-Carlo data [94]. Then the density profile has the same form as equation (2.72), but with rescaled Thomas-Fermi radii [36]

$$R_i = \xi^{1/4} a_\mathrm{ho} \left(48N_\sigma\right)^{1/6} \bar{\omega}/\omega_i \, , \tag{2.74}$$

Similar profiles can be calculated for the weakly interacting BEC side [36].

2.6.2 Anharmonic Traps

If the trap potential $V(\boldsymbol{r})$ deviates from a harmonic trap, the Fermi energy E_F can be calculated from the density distribution $n_0(\epsilon_\mathrm{F}\left(\boldsymbol{r}\right))$ of a zero temperature ideal Fermi gas, where $\epsilon_\mathrm{F}(\boldsymbol{r}) = E_\mathrm{F} - V(\boldsymbol{r})$ is the local Fermi energy within LDA. This exploits $\mu = E_\mathrm{F}$ for the zero temperature ideal Fermi gas and from equation (2.2) follows

$$n_0(\epsilon_\mathrm{F}) = \begin{cases} \frac{1}{6\pi^2} \left(\frac{2m\epsilon_\mathrm{F}}{\hbar^2}\right)^{3/2} & \text{if } \epsilon_\mathrm{F} > 0, \\ 0 & \text{otherwise.} \end{cases} \tag{2.75}$$

Then the Fermi energy can be recovered from the atom number by solving numerically

$$N = \int n_0(\epsilon_\mathrm{F}(\boldsymbol{r}))\,\mathrm{d}\boldsymbol{r} \tag{2.76}$$

for E_F. Note that naturally the integral must be restricted to positions $\boldsymbol{r}$ within the trap.

2.6.3 Critical Temperature

Far on the BEC side, the dependence of the critical temperature on the interaction differs from the homogeneous case, where interactions increase T_c, as discussed in section 2.4.3. For the trapped gas, the dominant effect stems from the reduction of the central density by repulsive interactions, which reduces T_c and results in [49]

$$T^\mathrm{t}_\mathrm{c,BEC} = T_\mathrm{c,BEC,0}\left(1 + c^\mathrm{t}_1 \frac{a}{\lambda_0}\right), \tag{2.77}$$

with $c^\mathrm{t}_1 \approx -3.426$.

This result has also been calculated for the next order [50]

$$T^\mathrm{t}_\mathrm{c,BEC} = T_\mathrm{c,BEC,0}\left[1 + c^\mathrm{t}_1 \frac{a}{\lambda_0} + \left(c^{\mathrm{t}\prime}_2 \ln\frac{a}{\lambda_0} + c^{\mathrm{t}\prime\prime}_2\right)\left(\frac{a}{\lambda_0}\right)^2\right], \tag{2.78}$$

with $c^{\mathrm{t}\prime}_2 = -\frac{32\pi\zeta(2)}{3\zeta(3)} \approx 45.9$ and $c^{\mathrm{t}\prime\prime}_2 \approx -155.0$. The second order gives a positive contribution if $a/\lambda_0 > \exp(-c''_2/c'_2) \approx 0.74$ or $1/(k_\mathrm{F}a) > 3.7$.

Far on the BCS side, however, one expects a similar reduced critical temperature $T_\mathrm{c}/T_\mathrm{F}$ for the trapped gas as for the homogeneous gas because compression effects are suppressed by the Pauli exclusion principle so that the Fermi energy E_F is very similar to the local Fermi energy at the trap center.

2.6.4 Collective Modes

The trap geometry gives rise to additional collective modes of the system, which are at a similar order of magnitude as the trap frequencies. For example, the monopole ("breathing") mode of a unitary Fermi gas has been examined [57], but also the quadrupole mode [67] and scissors mode [95] in the BEC-BCS crossover, which demonstrates hydrodynamic behavior in the superfluid region and collisionless behavior at high temperature.

3 Experimental Setup

This chapter describes the experimental apparatus, which prepares degenerate samples of ^{6}Li by sympathetic cooling with ^{23}Na. Since it has already been detailed in the previous theses related to this experiment by Timothy Harrison [96], Alexandra Behrle [97] and Martin Link [98], I will only briefly describe the most relevant parts of the experiment. For the new fast magnetic coil, a more detailed characterization is presented.

3.1 Laser Systems and Atomic Transitions - A Rough Overview

Lasers are used for manipulation of ^{6}Li and ^{23}Na atoms, either close to resonance of their D2 lines for laser cooling, optical pumping and imaging, or far detuned to create optical dipole potentials.

The lithium laser system at a wavelength of 671 nm is based on home-built external cavity diode lasers and tapered amplifiers. The first laser is locked to a spectroscopy cell [99] and provides the light for the magneto-optical trap (first trapping stage, explained in section 3.2.2). A second laser, which is referenced to the first laser with an offset lock, provides the light for Zeeman slower and optical pumping (deceleration of the atom beam from the oven and transfer between hyperfine states, both also explained in section 3.2.2). To allow imaging at high magnetic field, where the imaging transition is shifted due to the Zeeman effect, the laser frequency is ramped before the imaging by hundreds of megahertz, by changing the offset lock. A home-built interference filter laser has been added recently, to drive Raman transitions [100].

The sodium laser light at a wavelength of 589 nm is created by frequency doubling of a 1178 nm diode laser (DL Pro by Toptica) in a home-built bow-tie cavity [97] and amplified by a Raman fiber amplifier (by MPB). The frequency is locked to a lithium spectroscopy cell [101].

Additionally, exploiting the dipole interaction of atoms with far detuned lasers, a repulsive laser at 532 nm is used (Sprout-G-15 by Lighthouse Photonics) in the magnetic trap, and an attractive laser at 1070 nm (50 W Ytterbium Fiber Laser by IPG) for the optical dipole trap [102]. A laser at 1064 nm (Mephisto MOPA 55 W by Coherent) will be used in the future to realize an optical lattice [103], and the implementation of tweezer traps at 780 nm has been prepared [104].

Atomic Energy Levels ^{6}Li and ^{23}Na are alkalis and thus, have a hydrogen-like level structure. Here only the transitions of the D2 line are relevant, which are shown in figure 3.1 for both species.

Experiments with ^{6}Li are performed at magnetic fields up to about 1000 G, which is already far in the Paschen-Back regime of the hyperfine structure, as demonstrated by the Breit-Rabi diagram in figure 3.2. It is common to denote the hyperfine states of the ground states as $|1\rangle$, $|2\rangle$, ..., $|6\rangle$ in ascending order of energy. RF transitions between the states can be calculated as the difference of the shown energy levels, while the imaging transitions are calculated in a similar way, by also considering the energy levels of the excited state.

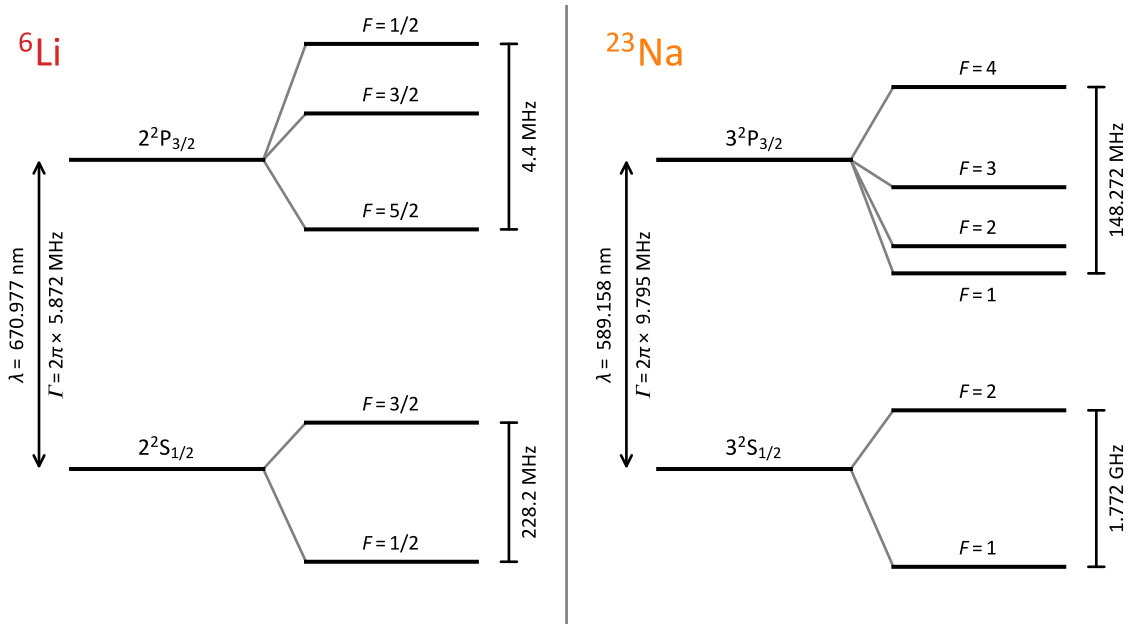

Figure 3.1: D2 line of ^{6}Li and ^{23}Na and its hyperfine splitting Not to scale; Note that for ^{6}Li the hyperfine splitting of the excited state cannot be resolved, because it is smaller than the natural linewidth. The D1 line is 10 GHz below the D2 line for ^{6}Li and 516 GHz below for ^{23}Na. ^{6}Li data is taken from ref. [105] and ^{23}Na data from ref. [106].

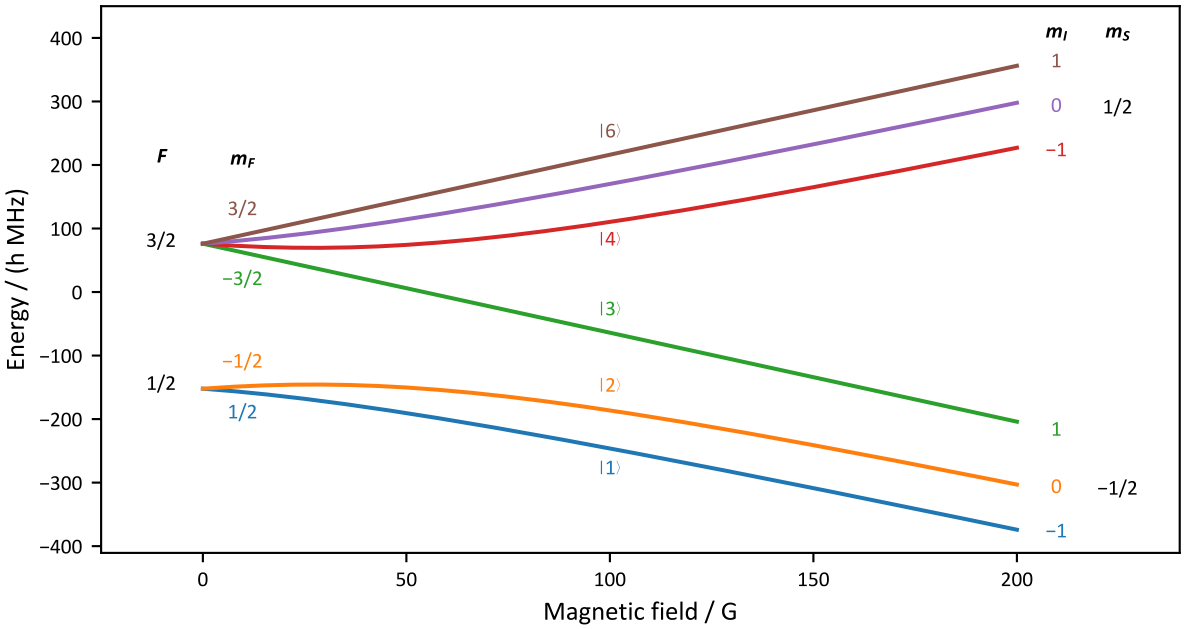

Figure 3.2: Breit-Rabi diagram of the ground state $2^2S_{1/2}$ of ^{6}Li At low fields the quantum numbers of the $|F, m_F\rangle$ basis are specified and at high fields the ones of the $|m_I, m_S\rangle$ basis ($m_J = m_S$ since $L = 0$). The measurements are typically performed at even higher fields of about 500 G to 1000 G, far in the Paschen-Bach regime of the hyperfine splitting. For varying magnetic fields, the states in the eigenbasis of the Hamiltonian are denoted as $|1\rangle$ to $|6\rangle$. My calculation is inspired by ref. [105].

Optical Dipole Potentials Far detuned laser beams interact with an induced electric dipole moment of the atoms, which creates an energy offset proportional to the laser intensity I, according to the AC-Stark effect [107]. The proportionality factor η has to be calculated and depends on the species and the laser wavelength but in our case only negligibly on the state, magnetic field and polarization.

If the atom is approximated as a two-level system with transition frequency ω_{atom} and linewidth Γ, and by using the rotating-wave approximation $|\Delta| \ll \omega_{\mathrm{atom}}$ for laser detuning $\Delta = \omega_{\mathrm{laser}} - \omega_{\mathrm{atom}}$, the energy shift of the ground state is given by [107]

$$U_{\mathrm{dipole}} = \frac{3\pi c^2}{2\omega_{\mathrm{atom}}^3}\frac{\Gamma}{\Delta} I\,, \tag{3.79}$$

while the scattering rate of photons is given by

$$\Gamma_{\mathrm{scatter}} = \frac{3\pi c^2}{2\hbar\omega_{\mathrm{atom}}^3}\left(\frac{\Gamma}{\Delta}\right)^2 I\,. \tag{3.80}$$

The idea behind far detuned dipole traps is that the scattering of photons, which can lead to heating of the atomic sample, is suppressed quadratically for large detuning, while the reduced trap depth can be compensated for by linearly increasing the laser power. Red detuned lasers ($\Delta < 0$) create attractive potentials and blue detuned lasers ($\Delta > 0$) create repulsive potentials.

In practice, the rotating-wave approximation and the multi-level structure of the atom can have a noticeable effect and the full calculation for the energy shift of $|g_i\rangle$ reads[1]

$$\Delta E_i = -I\frac{3\pi c^2}{2}\sum_j \left[\frac{\Gamma_{ij}}{\omega_{\mathrm{atom},ij}^3}\left(\frac{1}{\omega_{\mathrm{atom},ij} - \omega_{\mathrm{laser}}} + \frac{1}{\omega_{\mathrm{atom},ij} + \omega_{\mathrm{laser}}}\right)\right]\,, \tag{3.81}$$

where the linewidth associated to the transition to each excited energy-level $|e_j\rangle$ can be calculated from the dipole matrix element $\langle e_j|\mu|g_i\rangle$

$$\Gamma_{ij} = \frac{\omega_{\mathrm{atom},ij}^3}{3\pi\epsilon_0\hbar c^3}\left|\langle e_j|\mu|g_i\rangle\right|^2\,. \tag{3.82}$$

The prefactors for the relevant species and laser wavelengths are detailed in table 3.1. We

Table 3.1: Prefactors of dipole potential The prefactors $\eta = U_{\mathrm{dipole}}/I$ for the relevant wavelengths and species of the experiment are calculated from equation (3.81), considering the (first) D1 and D2 line. If additionally the transitions for $2^2\mathrm{S}_{1/2} \rightarrow 3^2\mathrm{P}_{3/2}$ are considered, the correction of η for ^{6}Li at 1070 nm is only ∼0.1 %.

Wavelength / nm	$\eta_{^6\mathrm{Li}}/k_\mathrm{B}$ / nKW^{-1}mm^2	$\eta_{^{23}\mathrm{Na}}/k_\mathrm{B}$ / nKW^{-1}mm^2
532	61.7	159.3
589	122.4	
671		−158
780	−140.2	−84.19
1064	−60.51	−52.13
1070	−60.07	−51.87

use a laser at 1070 nm as an attractive potential for ^{6}Li and a laser at 532 nm as a repulsive potential for both species. Other specified wavelengths will be used in the future for additional optical dipole potentials.

[1] This is consistent to equation 18 in ref. [107], but keeping more terms. The additional approximation $\Gamma \ll |\omega_{\mathrm{atom},ij} - \omega_{\mathrm{laser}}|$ is also exploited here, but is well fulfilled for the considered wavelengths.

3.2 Preparation of a Degenerate Fermi Gas

To give an overview, the experimental sequence to prepare a degenerate ^{6}Li sample can be divided coarsely into three different phases, which will be explained in later subsections: The Magneto-Optical-Trap (MOT) phase, the magnetic trap phase and the dipole trap phase. In the MOT phase ^{6}Li and ^{23}Na are both emitted from the oven, simultaneously decelerated with a Zeeman slower and caught in a MOT, where they can be cooled down to about the limit of the Doppler temperature. In the Magnetic trap ^{23}Na is evaporatively cooled to a few microkelvins, which also cools ^{6}Li sympathetically, but does not significantly decrease the number of ^{6}Li atoms. Finally, in the dipole trap phase ^{6}Li is cooled evaporatively until degeneracy, using two different hyperfine states, which provide good thermalization during the cooling process.

The procedure until the end of the magnetic trap is similar as described in ref. [108].

3.2.1 Vacuum System

The vacuum chamber can be subdivided into the oven section, the Zeeman slower and the experiment section. The design of the vacuum system is shown in figure 3.3.

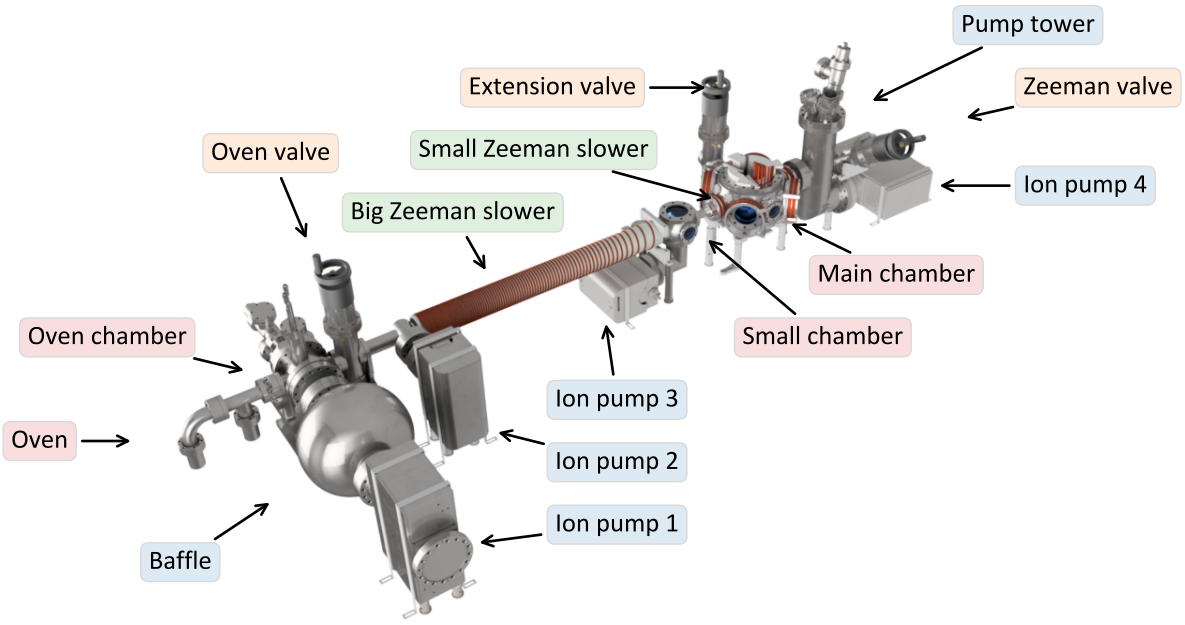

Figure 3.3: CAD design of vacuum system In addition to the pumps annotated above, there are three titanium sublimation pumps connected to the oven chamber, close to *ion pump 3* and to the pump tower. The oven is usually wrapped with heating elements and aluminum foil for thermal insulation and the Big Zeeman slower is usually covered with a water-cooled heat-sink.

Due to the atom vapor emitted from the oven, the oven chamber has only a moderate vacuum of $\sim 5 \times 10^{-7}$ mBar, while the experiment chamber has to support ultra high vacuum of $\sim 5 \times 10^{-11}$ mBar to enable reasonable life times of the atoms in the shallow optical trap. This is realized with several ion pumps and differential pumping stages.

Ion pump 1 is directly connected to the oven chamber, with a baffle in between, which protects the ion pump by blocking the direct path with a plate, on which vapor deposits. Before and after *ion pump 2* and along the Zeeman slower, differential pumping is realized with small tubes, which limit the amount of gas which can flow between the different sections of the

vacuum chamber (this is estimated in ref. [97]). This reduces the pressure to 2×10^{-9} mBar at *ion pump 2* and to 2×10^{-10} mBar at *ion pump 3*.

The ion pumps are continuously monitored and their electric current is used as an estimate for the pressure. A pressure gauge in the pumping tower close to the main chamber is currently not in use, because in the past deterioration of the pressure has been observed, while it was in operation. Additionally, there are titanium sublimation pumps, which are only used occasionally to keep the pressure at low values.

At the end of the vacuum system, opposite to the oven, is the entrance window for the Zeeman slower beams. The window is heated to prevent deposits from the atom beam. There is a valve which can separate the window from the main chamber if it were necessary to replace or clean the window.

The oven has to be refilled with sodium roughly every two years. Lithium has not been replaced yet, but is predicted to be exhausted soon. The oven chamber can be separated from the Zeeman slower section with a valve, which allows to open and clean the oven chamber and to refill sodium without compromising the ultra high vacuum in the main chamber. Afterward only the oven section of the vacuum system is baked-out. The oven chamber has windows to observe the initial fluorescence of the atom beam, it has a connection for the turbo-pump and features a titanium sublimation pump.

A small chamber between the two parts of the Zeeman slower features optical access. It is intended for transverse cooling of the atomic beams, which is not implemented because the loading rate into the MOT is already sufficiently high. Instead, it is currently used to monitor the fluorescence of the Zeeman slower beams, which has proven a good indicator for when a refill of the oven becomes necessary. The main chamber features an extension valve, where the experiment could be extended in the future.

The basic geometry of the main chamber is presented in figure 3.4. The MOT is positioned close to the entrance of the atomic beam, from where the atoms are transported magnetically over a distance of about 30 mm to the position of the magnetic trap. This position coincides with the final atom position in the dipole trap and allows to use the same magnetic coils for the magnetic trap as for the generation of the Feshbach field. The final atom position is 3 mm below the top window because the usage of an objective with high numerical aperture is planned for the future.

3.2.2 Magneto-Optical Trap Phase

The first phase of the experiment is the loading of the Magneto-Optical Trap (MOT) and involves the simultaneous slowing of both species coming from the oven with a Zeeman slower and capturing them in the dual-species MOT. Some special techniques during and at the end of the MOT phase are also discussed in this subsection, including a dark-spot MOT and optical molasses for ^{23}Na, a compressed MOT (CMOT) for ^{6}Li and finally the optical pumping for both species and their magnetic transport to the magnetic trap.

Oven The dual species oven has separate reservoirs for lithium and sodium, the design is based on ref. [109], which features different cups for the species to enable an individual adjustment of the fluxes. The temperatures are 330 °C for sodium, 400 °C for lithium, while the mixing nozzle at 475 °C and final nozzle at 490 °C are hotter to prevent clogging.

The atoms from the oven are emitted into the oven chamber which contains the “cold cup”, a water-cooled plate with a hole, which together with the final nozzle of the oven defines the collimation of the atomic beam. Atoms with deviating flight path mostly stick at the surface of the cold cup which keeps the oven chamber clean.

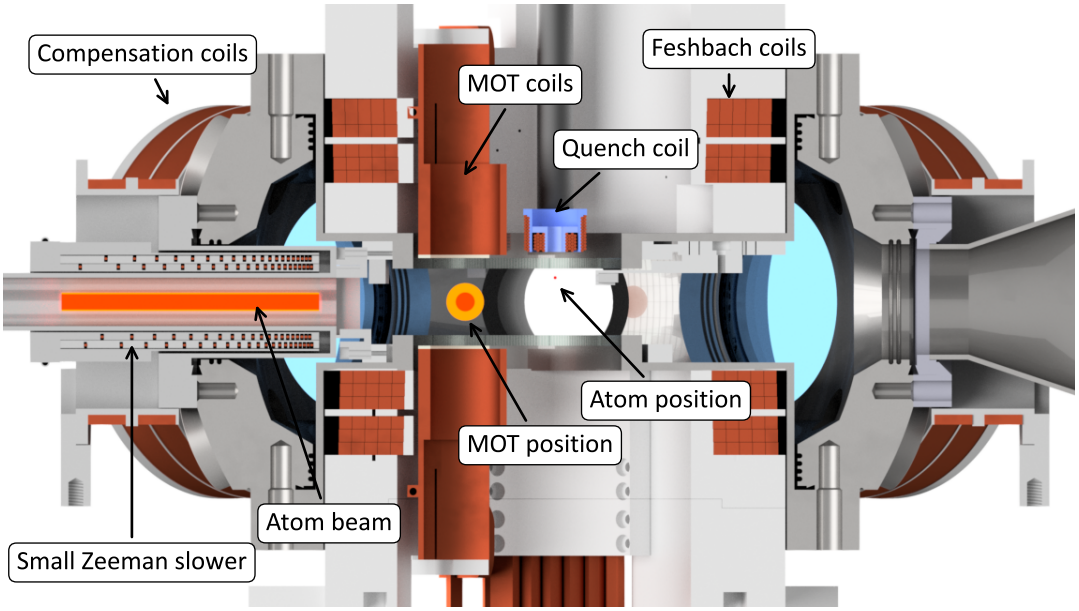

Figure 3.4: CAD design of main chamber Atom beam (in region of small Zeeman slower), MOT position and final atom position are marked and various coils are shown. Note that the MOT coils are not included in the CAD model but only their enclosing passive cooling shield.

During the loading phase the atomic beam progresses forward towards the Zeeman slower, but for the rest of the sequence when no atoms are loaded, the beam can be intercepted with a shutter. Currently the shutter is not in use because in the past there was the problem that sodium from the cold cup was deposited in the bearing of the shutter and it got stuck. A new shutter has already been designed [100] and will be exchanged during the next sodium refill.

The consumption of ^{6}Li and ^{23}Na is estimated by calculating the atom flux from the measured oven temperature, which determines their partial pressures. The estimated consumption for recent years is shown in figure 3.5. The estimation for ^{23}Na seems to be quite accurate: It has been refilled several times already and the amount of refilled ^{23}Na roughly matches the estimated amount of consumption. Our estimation for ^{6}Li is wrong. It has never been refilled yet and the estimated consumption already surpasses the initial amount of 5 g by more than a factor of two.

Zeeman Slower The atomic beam containing both species is slowed down and longitudinally cooled in a Zeeman slower of a similar design as described in ref. [110]. A Zeeman slower consists of a counter-propagating laser beam, which is red detuned to a closed atomic transition, and a spatially varied magnetic field, which shifts the atomic transition into resonance with the laser and compensates the Doppler shift during the deceleration. A cooling effect appears because slower atoms are decelerated less, which compresses the longitudinal velocity distribution. The variation of the magnetic field is realized with magnetic coils which have a variable pitch.

The initial velocity of the atoms given by the temperature of the oven is 740 m/s for ^{23}Na and 1450 m/s for ^{6}Li (most probable speed according to the Maxwell-Boltzmann distribution). The parameters of the Zeeman slower are optimized for ^{23}Na, for which a larger atom number is needed later for the sympathetic cooling. The calculated capture velocities are 1250 m/s for ^{23}Na and 1800 m/s for ^{6}Li [96] (atoms with velocity above the capture velocity are barely decelerated, see e.g. ref. [100]).

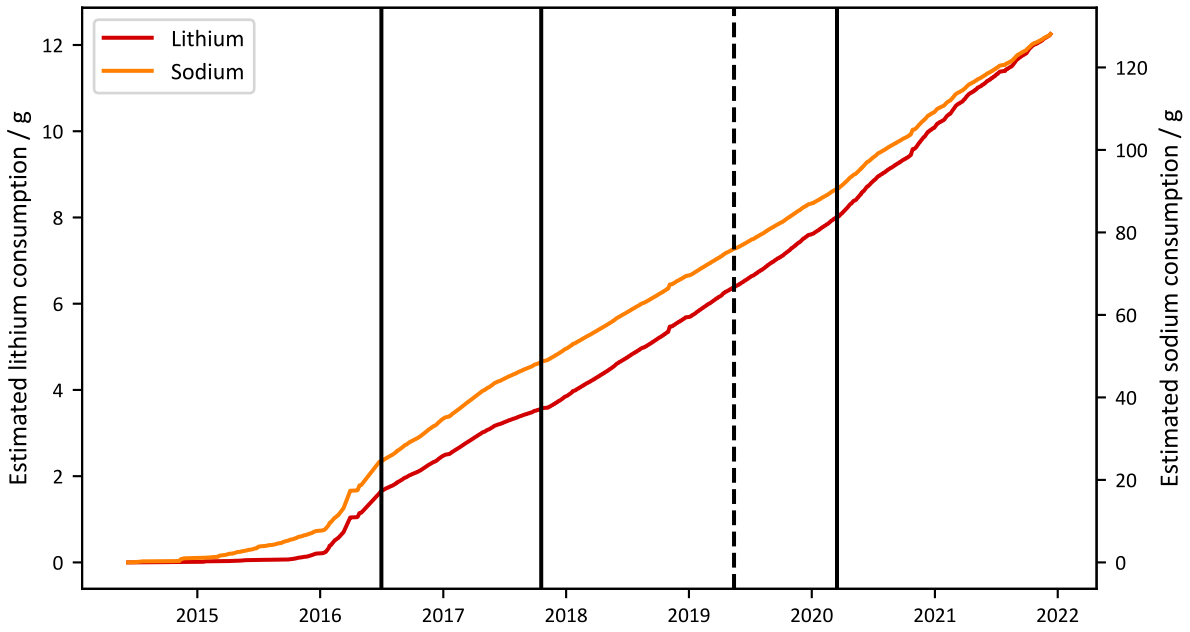

Figure 3.5: Estimated consumption of ^{6}Li and ^{23}Na Estimation of ^{6}Li is too large by more than a factor of two but accurate for ^{23}Na. In 2016 and 2020 25 g of ^{23}Na were refilled and in 2017 50 g were refilled. In 2019 the cold cup was clogged, which was resolved by heating the cold cup without opening the vacuum chamber.

The Zeeman slower consists of two parts, the "big" and "small Zeeman slower", with a zero-crossing of the magnetic field in between which changes the transition addressed by the laser beam. The advantage of such a "spin-flip Zeeman slower" design is that a lower maximum magnetic field is required. Also, the slowed atoms behind the Zeeman slower are not resonant to the laser beam as would be for a single decreasing field slower. Still, the magnetic field at the end of the slower is relatively small, which reduces the influence on the MOT and allows a smaller distance to the MOT. See refs. [97, 111] for a more detailed discussion of the Zeeman slower design.

At the zero-crossing of the magnetic field the quantization axis of the hyperfine states is flipped. The addressed transitions are $3^2\mathrm{S}_{1/2}\,|F=2\rangle \rightarrow 3^2\mathrm{P}_{3/2}\,|F=3\rangle$ for ^{23}Na and $2^2\mathrm{S}_{1/2}\,|F=3/2\rangle \rightarrow 2^2\mathrm{P}_{3/2}\,|F=5/2\rangle$ for ^{6}Li with extreme values for m_F depending on the direction of the quantization axis. The specified states are valid for small magnetic field, while along the Zeeman slower admixtures of other states could become relevant. Without a complete analysis of all involved states and their magnetic field dependence, the empiric observation is that by adding some repumper light the efficiency of the Zeeman slower can be increased [96].

The influence of the magnetic field from the small Zeeman slower on the MOT is reduced with a compensation coil, which is ramped down simultaneously with the Zeeman slower at the end of the MOT phase.

The Big Zeeman slower runs at a current of 400 A, which leads to significant heating. The wires are hollow and water cooled. Additionally, it is enclosed in a water cooled heat-sink. Still, the heating does not allow a continuous operation and limits the minimum sequence duration to ∼20 s, depending on the duty cycle of the Zeeman slower. Mitigations have been explored in ref. [100].

Magneto-Optical Trap The atoms of both species are captured and cooled down in a Magneto-optical trap (MOT) [111]. The optical part of a MOT consists of three perpendicular pairs of

counter-propagating red detuned laser beams, which on itself would constitute an optical molasses: The Doppler effect creates a deceleration, which is stronger for faster atoms (up to a certain velocity), because their transition frequency is shifted closer to resonance with the counter propagating lasers.

Additionally, a MOT comprises a magnetic quadrupole field, which changes the atomic resonances via the Zeeman effect and leads to a spatially dependent force. The beams require σ^- polarization and the lithium light addresses the $2^2\mathrm{S}_{1/2}\,|F = 3/2, m_F = -3/2\rangle \rightarrow 2^2\mathrm{P}_{3/2}\,|F = 5/2, m_F = -5/2\rangle$ transition and the sodium light addresses the $3^2\mathrm{S}_{1/2}\,|F = 2, m_F = -2\rangle \rightarrow 3^2\mathrm{P}_{3/2}\,|F = 3, m_F = -3\rangle$ transition[2].

Together, these two effects create a force which is approximately (assuming small Zeeman shift and small Doppler detuning) proportional to velocity and center displacement of an atom [111].

The MOT is realized in the main chamber close to the entrance port of the Zeeman slower, as can be seen in figure 3.4. The magnetic field is generated with the small MOT coil pair and the sodium and lithium beams are aligned to the MOT position from all six directions.

The presence of the sodium MOT reduces the efficiency of the lithium MOT due to light assisted collisions. This can be mitigated by displacing the MOT positions by adjusting the power-balance of the MOT beams [108]. But this is not done, because it can affect the loading efficiency into the small magnetic trap [97].

To achieve high ^{23}Na numbers, a dark spot MOT is implemented by applying almost no repumper light to the center of the MOT, so that a large fraction of the atoms stays in a dark state, which reduces repulsive forces from reabsorption of photons and enables larger densities [112].

The minimum temperature achievable in the MOT is limited by the Doppler temperature [111]

$$T_\mathrm{D} = \frac{1}{2}\frac{\hbar\Gamma}{k_\mathrm{B}}\,, \tag{3.83}$$

which is a consequence of the random nature of single photon scattering events and is 240 µK for ^{23}Na and 140 µK for ^{6}Li.

Lithium Compressed MOT and Sodium Molasses At the end of the MOT phase, after the Zeeman slower has already ramped down and while the sodium MOT is continued, a compressed MOT (CMOT) [113, 114] is performed for lithium to further increase its phase-space density. This is done by adjusting detuning and power of the MOT beams.

Finally, the MOT coils are turned off and for ^{23}Na an optical molasses is performed to further decrease the temperature. The estimated temperature of lithium after the CMOT is 290(30) µK and of sodium after the molasses is 125(8) µK [97]. The molasses time is limited to 2 ms, as for larger expansion times lithium would not be captured efficiently by the subsequent magnetic trap.

Although the CMOT increases the achieved atom number in the magnetic trap by a factor of three, the power ramp does currently not use the optimum parameters described in the literature. The reason is that the power ramp of the MOT beams, which is realized by reducing the electric current of a tapered amplifier, proved problematic, because changing the current by too much changes the mode of the amplifier and leads to an oscillatory behavior instead

[2] I consider the quantization axis in radial direction, i.e. in opposite direction for e.g. positive and negative z positions. A different convention is to choose a fixed quantization axis in Cartesian coordinates, but then one has to consider additional states with opposite m_F values and denote the laser beams with opposite polarization, matching to the transition they drive, although they have the same handedness, see discussion in ref. [111].

of a linear ramp. Realizing the power ramp by other means in the future might improve the CMOT and allow for a slightly longer duration of the sodium molasses.

Optical Pumping, Small Magnetic Trap and Magnetic Transport In order to achieve lower temperatures, the atoms have to be loaded into a trap where the heating by scattering photons is reduced, which can be realized with a magnetic trap.

A magnetic trap exploits the magnetic moment $\boldsymbol{\mu}$ of the atoms, which leads to a spatially dependent potential energy [111]

$$V(\boldsymbol{r}) = -\boldsymbol{\mu} \cdot \boldsymbol{B}(\boldsymbol{r})\,. \tag{3.84}$$

It is realized by a magnetic field landscape $\boldsymbol{B}(\boldsymbol{r})$ with a minimum magnetic field $|\boldsymbol{B}(0)|$ at the center. This implies that not all hyperfine states can be trapped but only "low-field seeker" states which have a negative magnetic moment relative to the magnetic field direction. An additional constraint, especially when trapping two different species, is to use "maximum stretched states" with extreme values of m_F chosen in such a way that no spin-exchange collisions are possible. It proved effective to choose the $2^2\mathrm{S}_{1/2}\,|F = 3/2, m_F = 3/2\rangle$ state for ^{6}Li and the $3^2\mathrm{S}_{1/2}\,|F = 2, m_F = 2\rangle$ state for ^{23}Na [108].

At first a small magnetic bias field is ramped up quickly to define a quantization axis for the states. Then optical pump light is applied to transfer all atoms into the target states. For ^{6}Li the optical pump light addresses the $2^2\mathrm{S}_{1/2}\,|F = 3/2\rangle \rightarrow 2^2\mathrm{P}_{3/2}$ transitions and the repumper the $2^2\mathrm{S}_{1/2}\,|F = 1/2\rangle \rightarrow 2^2\mathrm{P}_{3/2}$ transitions. For ^{23}Na the $3^2\mathrm{S}_{1/2}\,|F = 2\rangle \rightarrow 3^2\mathrm{P}_{3/2}\,|F = 2\rangle$ transition is used for optical pumping and $3^2\mathrm{S}_{1/2}\,|F = 1\rangle \rightarrow 3^2\mathrm{P}_{3/2}\,|F = 2\rangle$ as a repumper. By choosing σ^+ polarization for the beams, the atom population accumulates in dark states with maximum m_F.

Recently, a degraded efficiency in the preparation of the sodium repumper beam lead to instabilities of the optical pumping. Usually, various laser beams in our setup are split up with polarizing beam splitters and the polarization of the beam defines the power of each beam. By adding a liquid crystal waveplate (Compensated Half-Wave Liquid Crystal Retarder by Thorlabs) to the setup, it has become possible to quickly redistribute the power from different paths, which resolves this issue by increasing the margins for the alignment of the optics. The same approach also allows us to increase the maximum power of the imaging beam.

The atoms are recaptured by a small magnetic trap, which is realized by the MOT coils. Then they are transferred to the proper magnetic trap via magnetic transport over a distance of roughly 30 mm, which involves optimized magnetic field ramps of compensation coils and both magnetic traps to allow for a gentle transport of the atoms.

3.2.3 Plugged Magnetic Trap

The magnetic trap is realized by a quadrupole field from the Feshbach coils. That means that there is a vanishing magnetic field at the trap center, which would be problematic, because this allows Majorana-losses in this region, i.e. spin flips which can cause heating and atom loss [96]. To avoid this, a blue detuned repulsive laser beam ("Plug beam") is tightly focused onto the trap center.

^{23}Na is evaporatively cooled by transferring atoms into an untrapped "high-field seeking" state via RF transfer. By addressing the $|F = 2, m_F = 2\rangle \rightarrow |F = 1, m_F = 1\rangle$ transition, which requires a frequency of $1771.6\,\mathrm{MHz} + 1.4\,\mathrm{MHzG}^{-1} \cdot B$ depending on the absolute magnetic field B [96], higher energy atoms can selectively be removed from the trap. During the cooling process the frequency is adjusted to the decreasing temperature with a linear ramp from 1.9 GHz to 1.774 GHz for a duration of 5 s. Meanwhile, ^{6}Li is sympathetically cooled without much atom loss.

3.2.4 Dipole Trap

The atoms are loaded into the crossed dipole trap, which has its center in close proximity to the magnetic trap, by ramping up the dipole beam to full power and subsequently ramping the magnetic trap down. The dipole trap uses far red detuned laser beams at 1070 nm to create an optical dipole potential with strongly suppressed scattering of photons as discussed in section 3.1. It consists of two collimated beams, the horizontal dipole beam and the vertical dipole beam. The top window is highly reflective at this wavelength and reflects the vertical beam back onto itself, but no optical lattice is formed due to the short coherence length of the laser. The horizontal dipole beam intersects the vertical dipole beam at the atom position.

With this dipole potential it is possible to confine the hyperfine states $|1\rangle$, $|2\rangle$ or $|3\rangle$, which are not trappable in the magnetic trap. The loaded $|6\rangle$ state is transferred by Landau-Zener sweeps using RF. First it is transferred to the $|1\rangle$ state, next it is converted to a 50:50 mixture of state $|1\rangle$ and $|2\rangle$. Some experiments use a mixture of $|1\rangle$ and $|3\rangle$, which is realized with an additional transfer from $|2\rangle$ to $|3\rangle$.

The spin mixture enables the last evaporative cooling step, since collisions between different hyperfine states are not suppressed by the Pauli exclusion principle. To further increase the thermalization rate, the Feshbach field is tuned close to resonance. It is generated with the same magnetic coils which are used for the magnetic trap. In order to generate a homogeneous magnetic field, instead of a quadrupole field, IGBTs in an H-bridge configuration are switched. Evaporative cooling is realized by reducing the laser powers and therefore the trap depth.

At the end of the evaporation the trap depth is low enough for gravity to play a role, which might slightly improve the efficiency of the final evaporation, because in a tilted trap the trap depth can be reduced while the trap frequencies are barely affected [115]. After the evaporation it is possible to reduce the effect of gravity be recompressing the dipole trap or by compensating gravity with a magnetic gradient (The magnetic moments of the lower states of ^{6}Li at high field are very similar, which hinders Stern-Gerlach experiments, but enables simple gravity compensation).

Finally, a balanced mixture of more than 1×10^6 atoms per spin state at a temperature of roughly $0.07T_\mathrm{F}$ is achieved [96, 97].

3.2.5 Cool-Down and Demagnetization

While the preparation of the degenerate atomic sample takes typically 11 s, an additional cool-down time of ∼10 s is required for sufficient cooling of the coils, especially the Zeeman slower, which was already discussed above.

Close to the chamber only non-magnetic materials are used, but some magnetization effects can still be observed. To remove systematic drifts of the magnetization, a ramp to the maximum magnetic field and back is performed at the end of each experimental cycle.

3.2.6 Additional Trap Configurations

From the dipole trap the atoms can be loaded to further trap geometries. Already implemented is a repulsive TEM01 beam [103], as suggested by refs. [116, 117], using the same laser as for the optical plug of the magnetic trap. The TEM01 beam compresses the cloud in vertical direction and the transition to the quasi-2D regime has already been observed, following [118], but further experiments are yet to be done.

Additionally, a repulsive beam for a box potential has been realized, similar to ref. [119], and the implementation of optical tweezers has been prepared [104].

3.3 Quench Coil

The fast quench and modulation of the magnetic field studied in this thesis is enabled by the construction of a fast magnetic coil. Its design is described in ref. [2], but in this section a few additional details are presented.

3.3.1 Problem, Constraints and Goals

The goal is to perform a quench of the magnetic field, which changes the interaction of the system by a significant amount faster than the smallest timescale of the system, which is given by the Fermi time $\tau_F = \hbar/E_F$ with a typical value of roughly 5 µs to 10 µs for our samples.

The interaction is usually tuned via the magnetic field using Feshbach resonances, as described in section 2.2.1. With the dedicated Feshbach coils of the experiment the time to change the magnetic field is characterized in figure 3.6 to be roughly[3] $\tau_{90\,\%\to10\,\%} = 310\,\mu s$. This already requires the use of MOSFETs to quickly switch off the current and to discharge the power supply, as will be discussed in section 4.2, because the regulation of the power supply would be slower. The actual timing of the MOSFETs as well as initial and final field might have an influence on the value of $\tau_{90\,\%\to10\,\%}$.

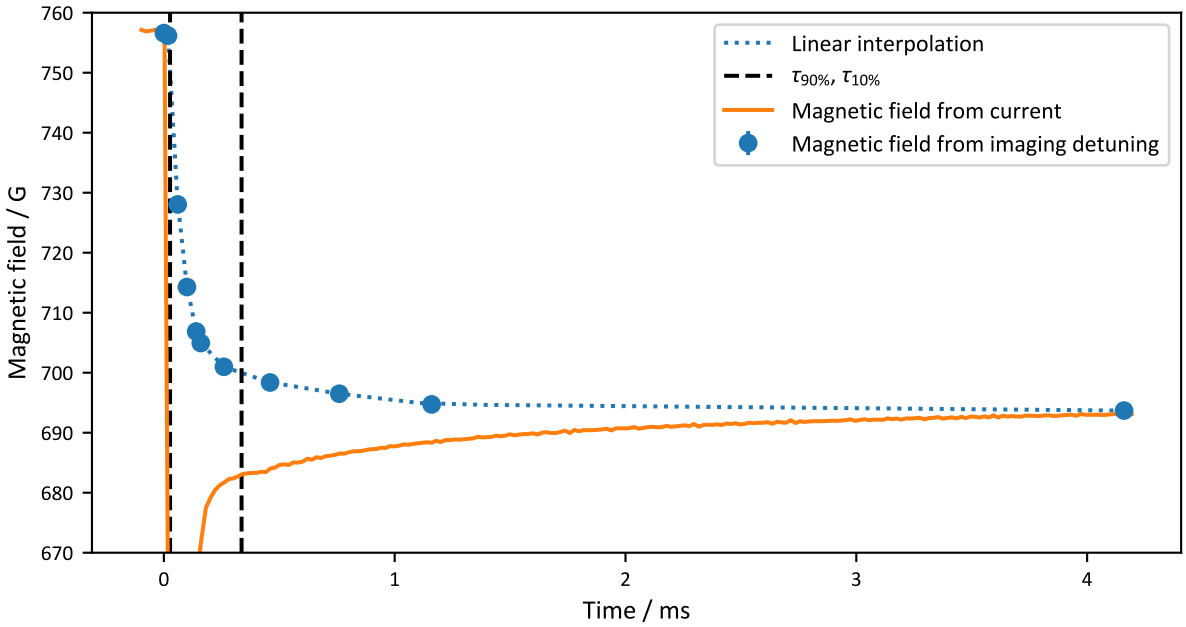

Figure 3.6: Magnetic field during a quench employing the Feshbach coils The actual magnetic field at the atom position is measured via the imaging detuning of the atomic resonance. This is compared to a measurement of the current in the coils. The large initial deviation shows that the current is indeed suppressed very quickly (achieved by using MOSFETs, see text), but the magnetic field lags behind due to eddy currents. $\tau_{90\,\%\to10\,\%}$ is determined from a linear interpolation to the detuning data.

The current in the coils is suppressed much faster than the quoted timescale, but the magnetic field persists for a longer time due to eddy currents, probably in the vacuum chamber or gaskets. Therefore, it is ruled out to beat the Fermi time by quenching with these coils.

The idea is to build a new dedicated quench coil with low enough self-inductance, which creates an additional offset field which can be switched off quickly, and with low mutual-

[3] An exponential fit yields a decay time of $\tau = 86(9)\,\mu s$, which would correspond to $\tau_{90\,\%\to10\,\%} = \ln(9)\tau = 189(21)\,\mu s$, but the actual decay slows down compared to the exponential dependence and results in the higher number quoted in the text. An earlier measurement yielded $\tau = 77(7)\,\mu s$.

inductance to avoid eddy currents in the chamber and other nearby conducting materials. The self-inductance of an idealized coil is given as [120]

$$L = \frac{\mu_0 \pi N^2 R^2}{l} \cdot k_L \,, \tag{3.85}$$

i.e. it is quadratic in the winding number N and the radius R and inversely proportional to its length l. The geometry factor k_L depends on the ratio R/l and is not important at this point.

The magnetic field of a single wire loop close to its symmetry axis z can be approximated as [121]

$$B(z) = \frac{\mu_0 I R^2}{2\left(R^2 + z^2\right)^{3/2}} \,. \tag{3.86}$$

From the denominator one can see, that the "range" of the magnetic field of the coil is on the same order of magnitude as its radius.

This suggests to build a small coil with not too many windings, to keep the self-inductance low and to reduce eddy currents in nearby conductors by having a shorter range of the magnetic field. But in order to generate a reasonable magnetic field at the position of the atoms, this would require the coil to be in close proximity.

Putting the coil directly next to the atoms within the vacuum chamber is not an option, because this would obstruct the optical access, complicate the alignment procedure of the coil relative to the atoms and be troublesome to implement into the existing apparatus. So the closest viable position is directly above the top window whose upper surface has a distance of ∼6.5 mm to the atoms.

This poses additional geometric constraints (see figure 3.7 for an illustration of a possible placement of the coil): First, it has to be considered that the optical path of the vertical imaging systems has to pass through the quench coil. Assuming that its axis should be aligned with the atoms, this sets a lower bound of ∼5 mm to the inner diameter of the coil to avoid too much clipping of the imaging beam. Secondly, since MOT and final atom position have a distance of roughly 30 mm, the distance to the MOT coils, which are also very close to the windows, gives the constraint on the outer diameter of the new coil. According to the CAD model of the experiment, the new coil would touch the heat-sink of the MOT coil if it had an outer diameter of 32 mm, but after testing the first prototypes it became clear that this deviates from the actual setup and that an alignment to the atoms is not possible for an outer diameter larger than 22 mm.

Vertically, the final atom position is not in the center of the vacuum chamber but closer to the upper window to enable a high NA imaging system in the future. Traditionally, one would use a pair of coils which is centered around the atom position to prevent gradients of the magnetic field at the atom position, but this would mean that the distance between the atoms and the coils would be at least 23 mm (which is the distance between the atom position and the lower surface of the bottom window). Also, the placement and alignment of the lower coil would be challenging because the access below the chamber has become difficult due to optics, posts and connections of other coils.

3.3.2 Design of Coil and Circuit

To meet these constraints, a compact coil is developed, which is positioned only above the atoms without a second coil below the chamber. To avoid magnetic gradients at the atom position, the coil comprises an inner and an outer coil with opposite current direction, which cancel the gradient at a certain distance whereas a magnetic field remains. Using a different current direction for inner and outer coil also reduces the inductance of the combined coil, as will be shown.

The coil is wound on 3D printed plastic mounts out of polylactide (PLA), which allows fast prototyping and avoids eddy currents. Temperatures above the glass temperature of 60 °C [122] should be avoided, but we want to avoid high temperatures close to the top window in any case. 3D printable plastics like polyetherimide, which withstand much higher temperatures, are available but require slightly more advanced printers.

The inner coil and outer coil have each 22 windings. The outer diameter is 22 mm and the inner diameter is 6 mm. The design of the coil is shown in figure 3.7.

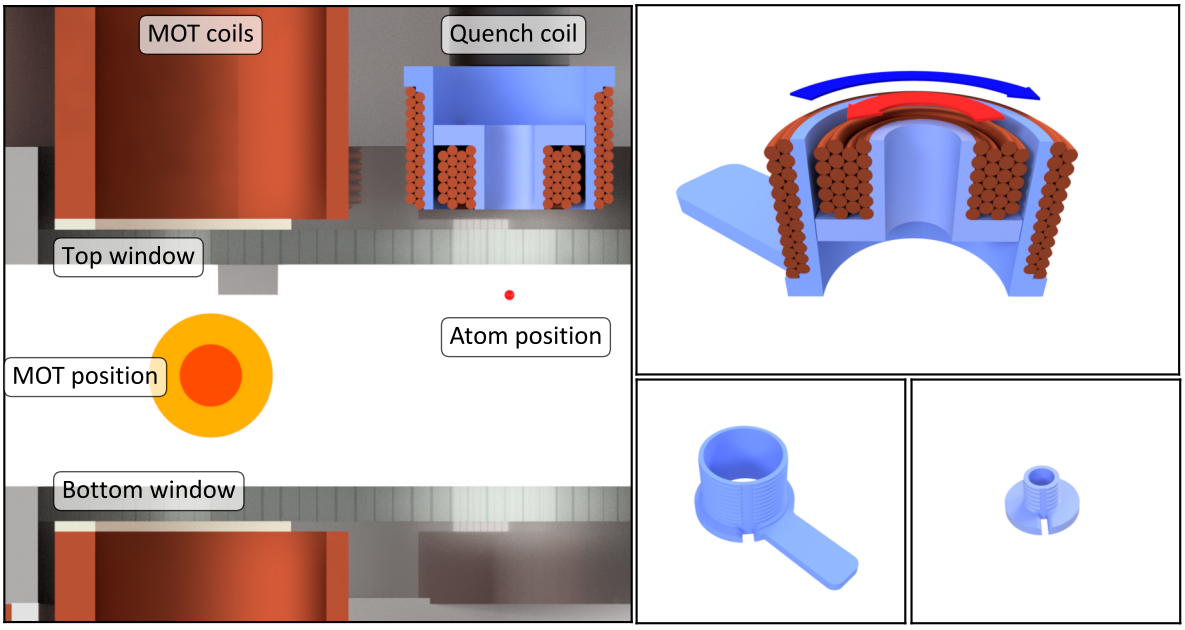

Figure 3.7: Design of quench coil The placement of the quench coil relative to the MOT coils and top window is shown **(left)**. Note that for the MOT coils only the outer heat-sink is displayed. The inner and outer plastic mounts are presented **(right)** and how they are combined with the wires of the coil (wires are simplified). The arrows indicate the opposite direction of current.

The challenge of quickly changing the current through an inductor is that it can induce quite large voltages $U = L\dot{I}$. The current is supplied by a programmable power supply (S280 S6-40 by Delta Electronika) in constant voltage mode, but changing the setpoint of the current would be relatively slow. Instead, a dedicated circuit shown in figure 3.8 is used, with a MOSFET which suddenly switches the current off. If this happens too fast, the voltage induced by the quench coil would be higher than the voltage rating of 200 V of the MOSFET (IXFN140N20P by IXYS). This is mitigated with an RLC-circuit, where $R_{10} = 10\,\Omega$ and $C_6 = 600\,\text{nF}$ are chosen in combination with the inductance of the quench coil L to realize a slightly overdamped oscillation which is as fast as possible without exceeding that voltage limit.

3.3.3 Characterization

Magnetic Field

In the experiment the magnetic field from the Feshbach coils along the z-axis (symmetry axis of the Feshbach coils and quench coil) is much stronger ($> 500\,\text{G}$) than the field of the quench coil ($< 50\,\text{G}$). Therefore, the x and y component of the quench coil field do not play a significant role after the vector addition with the Feshbach field and only the z component is considered. The quench coil is modeled as a collection of solenoids and the magnetic field is calculated

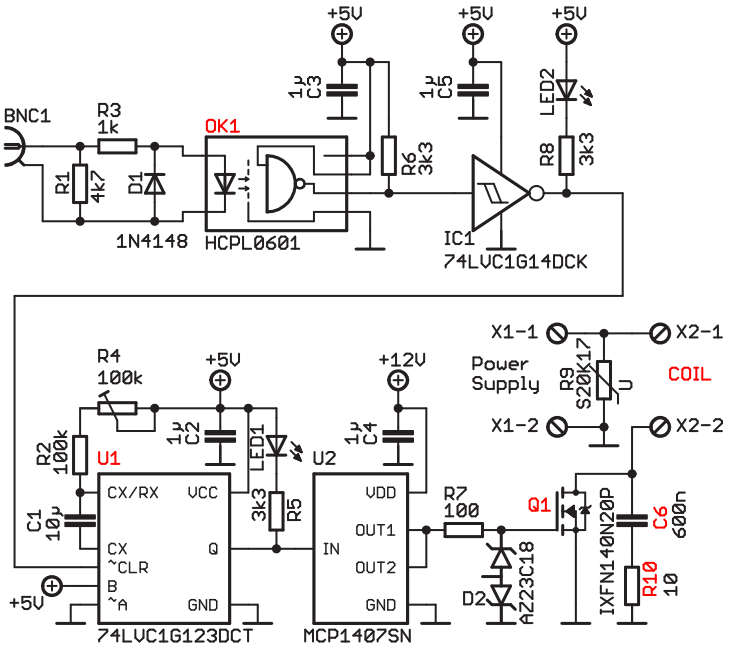

Figure 3.8: Quench Circuit When the MOSFET (Q1) switches off, the coil together with the resistor (R10) and capacitor (C6) form an RLC circuit, which fixes the timescale on which the current through the coil is switched off. It has to be slow enough to not exceed the voltage limit of the MOSFET. An optocoupler (OK1) isolates the input signal. A monostable multivibrator (U1) is used to limit the duration during which the coil is on, to prevent overheating (in addition to a separate temperature interlock). Design and simulation of the circuit have been done by Dr. Akos Hoffmann.

numerically with the Biot-Savart law [121]

$$\mathrm{d}\boldsymbol{B} = \frac{\mu_0}{4\pi} I \frac{\mathrm{d}\boldsymbol{l} \times \boldsymbol{r}}{r^3}\,, \tag{3.87}$$

by integrating the contributions $\mathrm{d}\boldsymbol{B}$ to the magnetic field at position $\boldsymbol{r}$ over all wire elements $\mathrm{d}\boldsymbol{l}$ with current I.

At a distance z_0 the gradient from the inner coil is canceled by the gradient from the outer coil, which is the optimum position for the atoms. A curvature of the magnetic field is present and is negative in the z direction (reduced magnetic field for misalignment along z) and positive in radial direction (increased magnetic field for misalignment along x or y).

The z-component of the magnetic field of the quench coil is measured on a bench with a hall probe (DTM-151 Digital Teslameter by Group3) at a constant current of 5 A. The axis of the coil is determined by searching the minimum field in the xy-plane at a distance which would roughly correspond to the distance of the atoms to the coil. Finally, the designed atom position is narrowed down by maximizing the magnetic field by varying the z position. From there the magnetic field is measured while varying the position along the principle directions, and the result is presented in figure 3.9.

The measurement is compared with the calculated magnetic field from our model and a fit is performed to account for an offset in the position and small deviations in the actual radius of the coils from the designed values. The fitted model predicts an optimum distance between atoms and quench coil of $z_0 = 8.2\,\mathrm{mm}$ and a magnetic field at that position of $B_z = 0.98\,\mathrm{G/A}$. With no misalignment, the gradient of the magnetic field is zero by design, but a curvature is present which is calculated as $\partial_z^2 B_z = -5.2\,\mathrm{Gcm}^{-2}/\mathrm{A}$ and $\partial_r^2 B_z = -2.6\,\mathrm{Gcm}^{-2}/\mathrm{A}$.

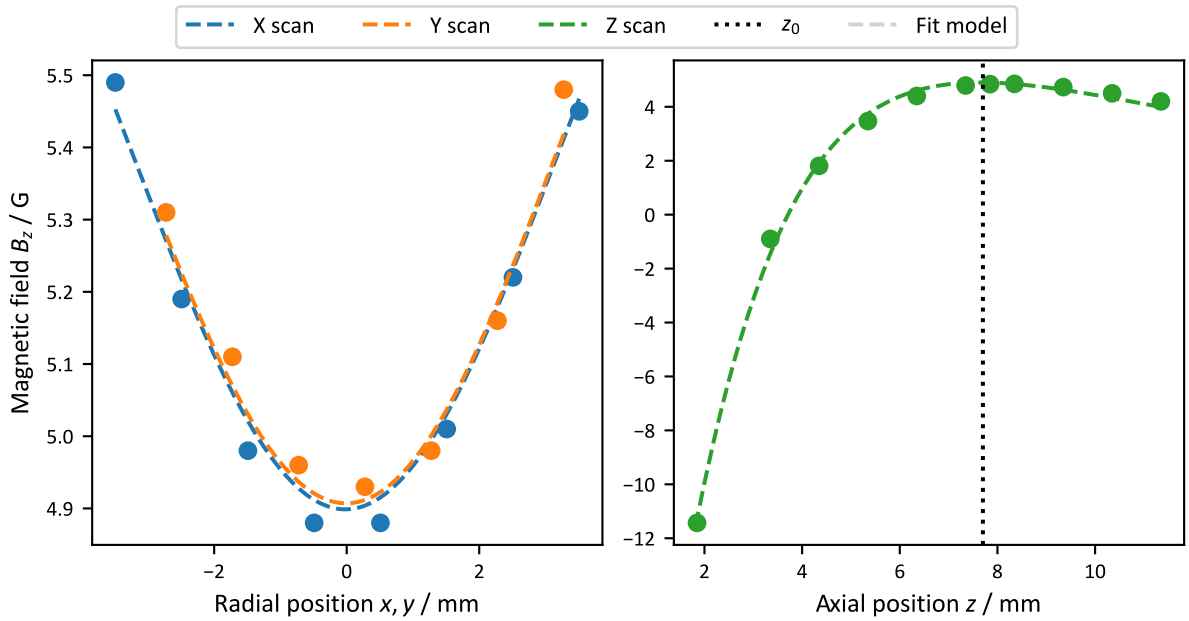

Figure 3.9: Magnetic field of quench coil The data was measured at $I = 5\,\mathrm{A}$ along radial **(left)** and axial **(right)** direction. It is compared to a model of the quench coil based on Biot-Savart calculations, after fitting parameters for alignment and deviation of coil radii. The fit result is used to choose the absolute values for the radial and axial positions to match $x = y = 0$ to the symmetry axis of the coil and to match z to the axial distance between atoms and quench coil.

Alignment The general alignment strategy, after the quench coil is roughly at the correct position, is to find the minimum magnetic field in the xy-plane and the maximum magnetic field in z direction.

This can be achieved by mapping out the magnetic field for different positions of the quench coil, which is mounted on a 3D translation stage. The magnetic field is measured via the imaging detuning of the atoms or via an RF transition for higher precision. The alignment should be done very carefully because the quench coil is very close to the top window of the vacuum chamber. Initially, it was measured that at a position of $z_{\mathrm{translation}} = 19.75\,\mathrm{mm}$ on the vertical scale of the translation stage the quench coil is at the closest possible position to the atoms (smaller values of $z_{\mathrm{translation}}$ are further away) and starts to touch the thin RF coils, which are wrapped in Kapton tape and lie directly above the top window.

Mapping out the magnetic field is quite tedious because each determined magnetic field value is based on several measurements for the imaging detuning or RF spectroscopy. In practice it was sometimes more convenient to look at the atom number, which is reduced for a misaligned quench coil, because its gradient weakens the trap. Another useful strategy is to switch the quench coil on only during time-of-flight and to minimize the deflection of the atoms caused by the gradient of the Feshbach coil. Here it is useful to apply an additional magnetic gradient which cancels gravity for the ^{6}Li atoms, so that at the optimum position of the quench coil the center-of-mass of the cloud does barely move during time-of-flight.

The design of the quench coil requires a compromise between the magnetic field which can be reached for a given current and the distance between the quench coil and the optimum atom position. It turned out that in the latest iteration of the quench coil we were too greedy and it was not possible to move the quench coil close enough to the atom position to cancel the magnetic gradient completely. Figure 3.10 shows the measurement of the magnetic field for different distances between the closest position of the quench coil and its actual position

$z := 19.75\,\text{mm} - z_{\text{translation}}$. In the measured region the measured magnetic field fits well to a quadratic function, as expected when the quench coil is close to its optimum position, which justifies to slightly extrapolate the fit function to negative z. This reveals that the optimum position for the quench coil would be reached at $z_0 = -0.22(4)\,\text{mm}$, which is out of reach for us. Instead the remaining gradient at $z = 0$ is $B'_z(z = 0) = -1.6(5)\,\text{G/cm}$. In principle, it would be possible to create a few more prototypes of the quench coil until the gradient is perfectly canceled. However, we decided that we are satisfied with the result because the remaining gradient can be compensated easily. In the case of a quench experiment, we are usually interested on dynamics on a faster timescale than that of the sloshing of the atomic cloud which is caused by a sudden change of the gradient.

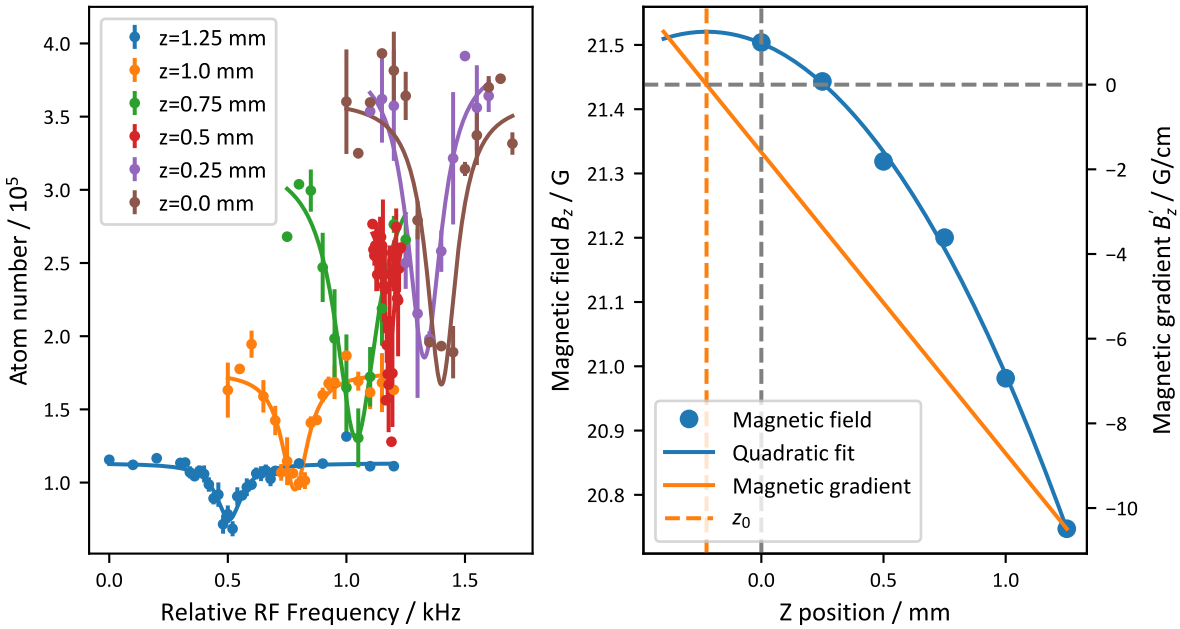

Figure 3.10: Measurement of magnetic field and gradient for vertical misalignment of the quench coil The signal of the RF spectroscopy is shown for various vertical positions z of the quench coil **(left)**. For larger misalignment the background atom number is reduced because the trap is weakened by the stronger gradient of the quench coil. The measurement at $z = 0.5\,\text{mm}$ is performed with less RF power but with longer duration, achieving a higher resolution. The extracted magnetic field **(right)** has a quadratic dependence on the position and reveals the gradient free position z_0.

The magnetic field is measured via RF spectroscopy on the $|1\rangle \rightarrow |2\rangle$ transition of the ground state of ^{6}Li at a Feshbach field of 913 G. The dependence of the resonance frequency on the magnetic field is known from Breit-Rabi calculations, but this is also confirmed by repeating the measurement instead for the already calibrated Feshbach coils, which gives consistent results.

Magnetic Field Calibration After alignment, the magnetic field of the quench coil as a function of the set current is calibrated via the detuning of the imaging transition of the atoms, as demonstrated in figure 3.11. The set current is controlled via an analog signal from 0 V to 5 V to the power supply, which supports currents up to 40 A, but this has to be done carefully, because the analog input already saturates at a slightly lower voltage than 5 V. A linear-constant fit reveals a maximum magnetic field of 35.0(3) G and a dependence on the current of 0.874(8) G/A.

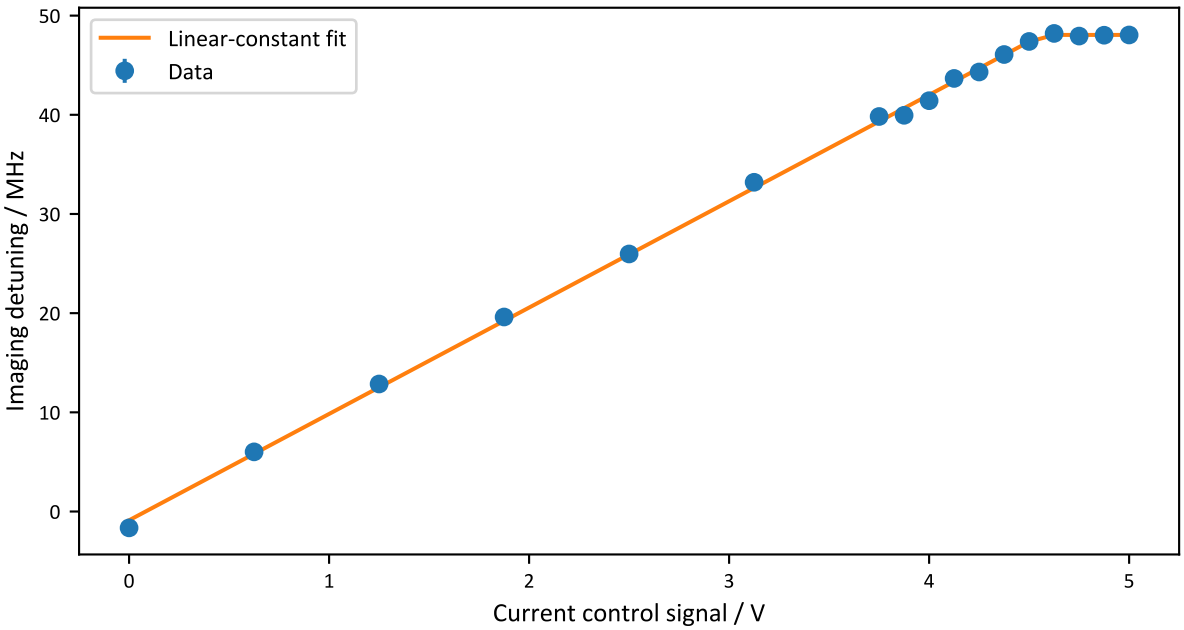

Figure 3.11: Calibrating magnetic field of quench coil with atomic resonance The current varies from 0 A to 40 A, but the maximum current is already reached below the maximum set value of 5 V.

Calculated Inductance

The inductance of a coil, approximated as a solenoid shape of current sheets, which are infinitesimally thin and have no gaps, has already been presented with equation (3.85), but here it is necessary to consider the geometry factor k_L, sometimes called Nagaoka factor, more carefully. It depends on the ratio of the coil diameter and coil length $2R/l$. For a long coil with $l \gg 2R$, k_L approaches 1. But here we consider coils with $l < 2R$, so that it is useful to calculate [120] (also see ref. [123] for very comprehensible explanations)

$$k_L = \frac{4}{3\pi\sqrt{m'}} \left(\frac{m'}{m} \left(K(m) - E(m) \right) + E(m) - \sqrt{m} \right) , \tag{3.88}$$

which depends on the complete elliptic integrals $E(m)$ and $K(m)$ and

$$m = \frac{R^2}{R^2 + l^2} \qquad \text{and} \qquad m' = \frac{l^2}{R^2 + l^2} . \tag{3.89}$$

See appendix A.1 for the definitions of the complete elliptic integrals and a comment about different conventions in the literature. Traditionally, it was a bit tedious to calculate this factor because the term $\frac{m'}{m}\left(K(m) - E(m)\right)$ can get close to zero and lead to numeric instabilities for small m, but I checked that this is not a problem for the implementation of complete elliptic integrals in *python/scipy* as long as $m > 10^{-5}$, which means that calculating k_L is very straightforward.

Calculating the inductance of the quench coil is still a bit more complicated because it consists of several layers of windings. Some of them have opposite current direction and the mutual inductance between these layers has to be considered. For simplicity, each winding i is considered as a circular wire loop with radius R_i and wire diameter d_w. Then the mutual inductance between two parallel and coaxial wire loops i, j is [123]

$$M_{ij} = -\mu_0 \sqrt{R_i R_j} \left(\left(\sqrt{m_{ij}} - \frac{2}{\sqrt{m_{ij}}} \right) K(m_{ij}) + \frac{2}{\sqrt{m_{ij}}} E(m_{ij}) \right) , \tag{3.90}$$

with the vacuum permeability μ_0, with

$$m_{ij} = \frac{4R_iR_j}{(R_i + R_j)^2 + x_{ij}^2} \tag{3.91}$$

and with the distance x_{ij} between the wire loops. The self inductance of one wire loop can be calculated with the same formula as for the mutual inductance $L_i = M_{ii}$, by setting the distance to $x_{ii} = d_w e^{-1/4}/2$.

Finally, the total inductance of the coil is calculated by summation over all windings

$$L = \sum_{i,j} s_{ij} M_{ij} \,, \tag{3.92}$$

with a prefactor $s_{ij} = +1$ if the wire loops have the same current direction and $s_{ij} = -1$ otherwise. Note that this sum includes the self inductance M_{ii} of the wire loops and that the mutual inductance M_{ij} for each pair i, j is implicitly counted twice if $i \neq j$, because $M_{ij} = M_{ji}$. This is consistent with the situation where two different coils with self inductance L_1 and L_2 and mutual inductance M are wired together and the total inductance is given as

$$L = L_1 + L_2 \pm 2M \,, \tag{3.93}$$

where the upper sign is used when the current direction for both coils is the same.

For the parameters of the quench coil the calculation gives an inductance of 6.2 µH. The separate results for only the inner, only the outer and the combined coil with same current direction are given in table 3.2.

Measuring the Inductance with Signal Generator and Oscilloscope The inductance of the coil is measured with a very simple circuit, in which a signal generator is connected in series with a resistor $R = 50\,\Omega$ and the coil, for which the impedance is described by

$$Z_{\text{coil}} = R_{\text{coil}} + \omega L_{\text{coil}} \,. \tag{3.94}$$

An oscilloscope measures the voltage V_{coil} parallel to the coil and the voltage V_{R} parallel to the resistor for several frequency settings. Together, this gives the impedance of the coil $Z_{\text{coil}} = V_{\text{coil}}/I = V_{\text{coil}}/\left(V_{\text{R}}/R\right)$.

Figure 3.12 shows that the impedance is in a linear regime at least in the range from 10 kHz to 100 kHz, so the inductance is given by the slope because the last term of equation (3.94) becomes dominant. The measurement is done for the inductance of the inner coil L_1 and the inductance of the outer coil L_2, separately, and also for the configuration that the current runs in the same orientation through both coils (L_{same}) and for the actual configuration of the quench coil, where the current runs in different orientations through both coils (L_{reverse}).

It is remarkable that the total inductance of the quench coil is lower than the inductance of only the outer coil by 21 % and lower than the inductance of the configuration with both coils running current in the same orientation by 57 %. Equation (3.93) suggests a mutual inductance of $M = \left(L_{\text{same}} - L_{\text{reverse}}\right)/4 = 2.3\,\mu\text{H}$ and demonstrates the consistency of the measured values (note that $2\left(L_1 + L_2\right) \approx L_{\text{same}} + L_{\text{reverse}}$).

The measured values are also presented in table 3.2 and are very close to the calculated values. Deviations can be explained by the idealized model used in the calculations and imprecise winding of the coils.

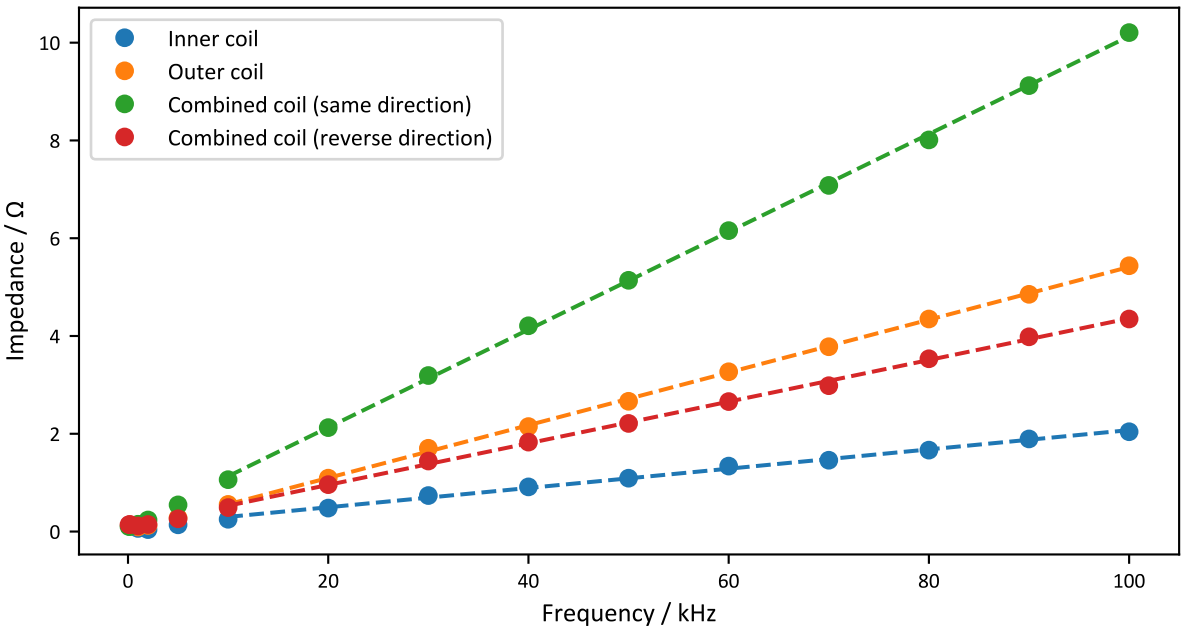

Figure 3.12: Impedance of quench coil versus frequency for determination of inductance The inner and outer coil are measured separately, as well as combined with different polarity.

Table 3.2: Measured and calculated inductance of the quench coil in different combinations of inner and outer coil The actually used configuration is the combined coil with reverse direction of inner and outer coil.

Coil	Measured inductance / µH	Calculated inductance / µH
Inner coil	3.14(6)	3.4
Outer coil	8.58(6)	7.5
Combined coil (same direction)	15.9(1)	16
Combined coil (reverse direction)	6.78(9)	6.2
$M = (L_{\text{same}} - L_{\text{reverse}})/4$	2.28(4)	2.3

Heating

To keep the design of the quench coil simple without the need of an active cooling system, it is only used in short time intervals before an interaction quench. Typically, the quench coil is on during 0.5 s, which corresponds to a duty cycle of 2 % compared to a usual sequence length of 25 s. Still, the quench coil should be ramped adiabatically and usually there is an additional hold time before the quench to guarantee that the sample is well thermalized, which limits the shortest possible operation time of the quench coil to a few hundred milliseconds.

During the operation time of the quench coil, the current is not at its maximum value all the time. For example, a realistic scenario would be a ramp time of 300 ms and a hold time of 200 ms for a total sequence length of 25.3 s. The duty cycle of 2.0 % only describes the on-off time of the coil. Instead, one could give an effective duty cycle of ∼1.1 %, which is calculated from a quadratic mean of the actual current ramps (anticipating a linear dependence of temperature on electric power) and indicates that a duty cycle of 1.1 % with the current always at the maximum value would lead to similar heating as for the given current ramps. Figure 3.13 shows the thermalization of the coil for different current settings. The temperature is measured with temperature sensors (PT100 element, DM-301 by Labfacility), which are glued to the

outside of the coil (The readings of both sensors agree very well and for the measurements here both values are averaged). An exponential fit suggests a thermalization time of 5.09(2) min.

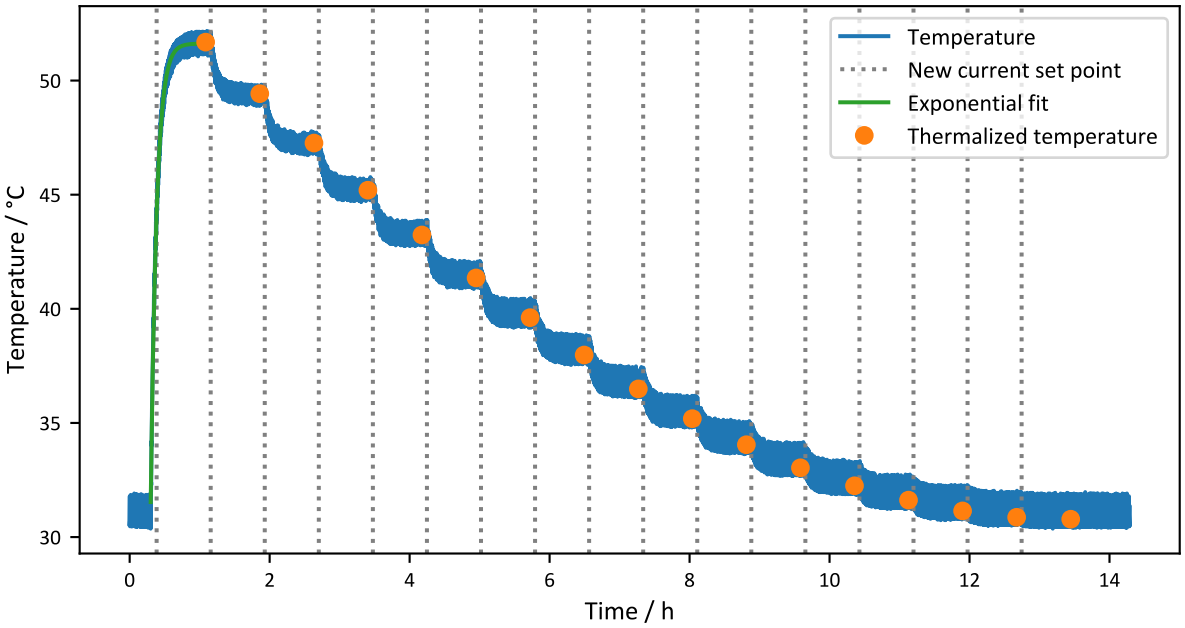

Figure 3.13: Heating of quench coil for a realistic sequence The current setpoint is varied in steps from 32 A to 0 A and a wait time is added for thermalization, which is characterized by an exponential fit for the first setpoint. The temperatures are measured every 4 s and temperature changes within a sequence lead to the relatively broad band of measured temperature values. Thermalized temperature values are extracted by averaging over the last twenty sequences for each current setting.

The extracted temperature after thermalization is shown in figure 3.14 as a function of the current or the electric power. The latter is calculated from the resistance of the coil $R_{\mathrm{QC}} = 82(2)\,\mathrm{m\Omega}$, which is determined from the voltage of 0.41 V measured with a DMM parallel to the coil at a DC current of 5 A. A four point measurement is used, which ignores any voltage drop at the contact between DMM and coil (This setup is realized by placing the contact points between DMM and coil further inside compared to the separate contact points between coil and current source). The temperature of the coil is quite linear to the averaged electric power in the considered range with a slope of 23.2(2) °C/W. Similar as in ref. [124] this quantity can be interpreted as the thermal resistance of the coil (they achieve much lower values by using water cooling).

When performing quench experiments, the current setpoint is not varied for the same dataset and the sequence is run for a few minutes before taking the data. This prevents thermal drifts of the coil during the measurement.

The temperature properties are sufficient for the current investigations, but are the limiting factors if an operation at higher current or duty cycle were desired. My expectation is that a significant part of the cooling at the moment takes place via heat flow through the electrical contacts of the coil, since the mount is realized without metal parts. This suggests that the passive cooling of the coil can still be improved. A preliminary test of a similar coil prototype, but with an aluminimum heat-sink, realized a thermal resistance of 3.74(2) °C/W, which would enable more than twice the current or six times the duty cycle. However, this slightly complicates the mount of the coil because it should be constructed in a way which minimizes eddy currents.

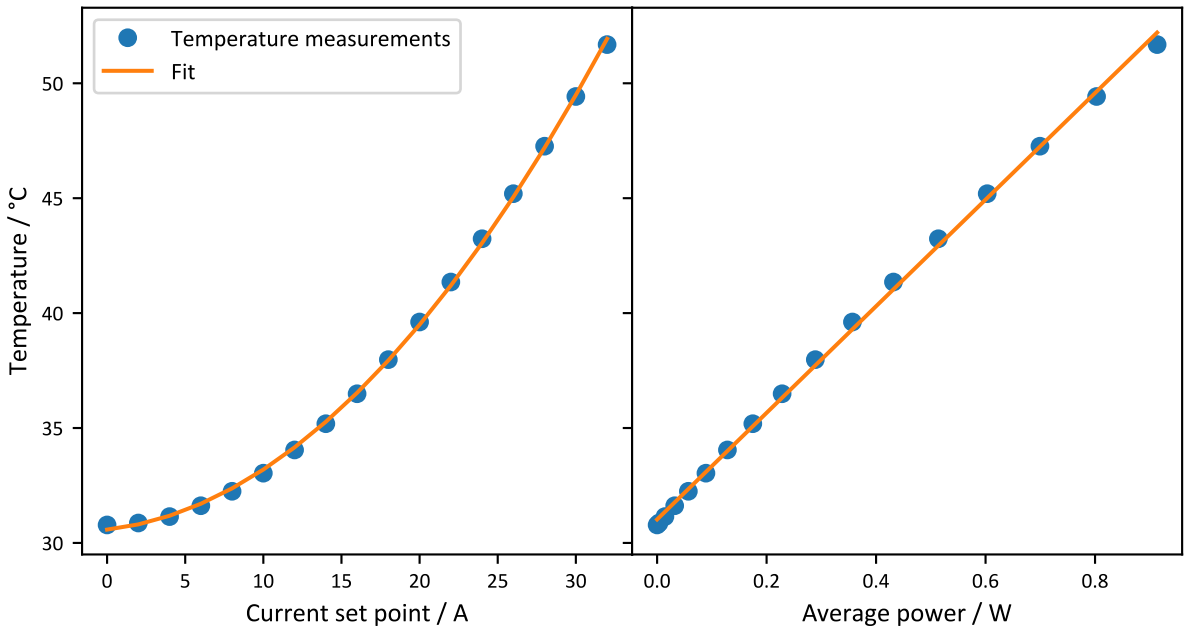

Figure 3.14: Heating of quench coil The temperature is plotted versus the current setpoint **(left)** and versus the average electric power, which takes the effective duty cycle into account **(right)**.

Switching Time

In a test setup the timing of the quench coil is measured with a small pick-up coil, which is positioned close to the quench coil and connected to an oscilloscope. The pick-up coil only consists of a few windings and can be considered as an open circuit because of the large input resistance of the oscilloscope, which means that the influence of the pick-up coil on the measured timing is negligible. The voltage impulses induced after suddenly switching off the coil are shown in figure 3.15 for different scenarios: At first the signal is measured for the free standing quench coil. Then this is compared to the signal when some flanges or gaskets are brought to close proximity to simulate the environment of the experiment. According to Faraday's law of induction, the measured voltage is proportional to the change of magnetic field $\dot{B}$ [121]. Therefore, the magnetic field can be reconstructed up to a proportionality constant and is also shown in the figure by integrating the signal. It is demonstrated that putting various conducting objects in close proximity of the coil does only slightly change the decay time of the magnetic field.

The timing is characterized by reading off the time interval $\tau_{10\,\%\to 90\,\%}$ in which the integrated signal changes from 10 % to 90 % of its maximum value, which is given in table 3.3. The measurements indicate a timing of 2.1 µs to 2.3 µs, which is slightly increased to ∼3 µs when the quench coil is integrated in the real experiment, as confirmed by a measurement based on the imaging detuning of the atoms.

Field stability The rms noise level of the current from the power supply of the quench coil is 15 mA, which would correspond to a relative noise level of 4×10^{-4} compared to the full current from that power supply. It leads to a magnetic field fluctuation of 13 mG. Compared to the typical Feshbach fields of the experiment, this corresponds to a relative noise level of $\sim 2 \times 10^{-5}$.

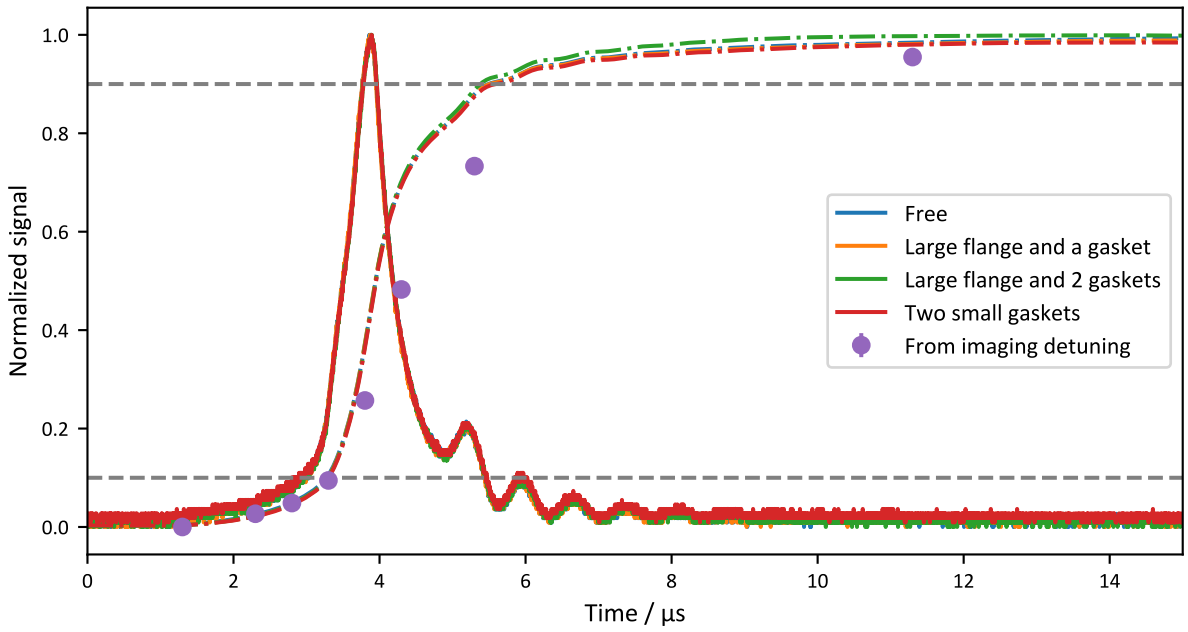

Figure 3.15: Switching time of quench coil measured with a pick-up coil $\tau_{10\,\%\to 90\,\%}$ is determined from the integrated signal. After implementation of the coil into the experiment, the timing is verified with a measurement of the imaging detuning during a field quench, which results in only a slightly increased switching time.

Table 3.3: Switching time of quench coil for different scenarios The first four measurements are done in a test setup and show that the presence of gaskets do not significantly increase the switching time. After implementation of the coil into the experimental apparatus a small decrease of the switching time is observed, which is directly determined from the atoms by measuring their imaging detuning.

Situation	10 % to 90 % decay time / µs
Free	2.2
Large flange and a gasket	2.2
Large flange and 2 gaskets	2.1
Two small gaskets	2.3
In experimental apparatus	∼3

3.3.4 Modulation of the Magnetic Field

The "quench coil" can not only be used for a fast change of the magnetic field by switching it off. An alternative use case is a fast modulation of the magnetic field, which is interesting because a fast modulation of the interaction lead to certain kinds of excitations of a superfluid gas, investigated in chapter 7.

For this purpose the quench circuit from figure 3.8 is replaced by an amplifier, for which the core functionality is described by the circuit shown in figure 3.16.

It is connected to a power supply in constant voltage mode and to the quench coil. The input signal is generated by a programmable arbitrary function generator (AFG-2225 by GW Instek). The amplifier is designed for an output current of up to 10 A (bipolar, i.e. 20 A peak-to-peak) and for frequencies up to 40 kHz, but higher frequencies are possible at a reduced maximum amplitude. While initially we did not know the best parameters of the modulation, in retrospect a smaller amplitude and a higher frequency range seems more useful.

The bandwidth of the amplifier has been simulated in *LTSpice* and is shown in figure 3.17 for

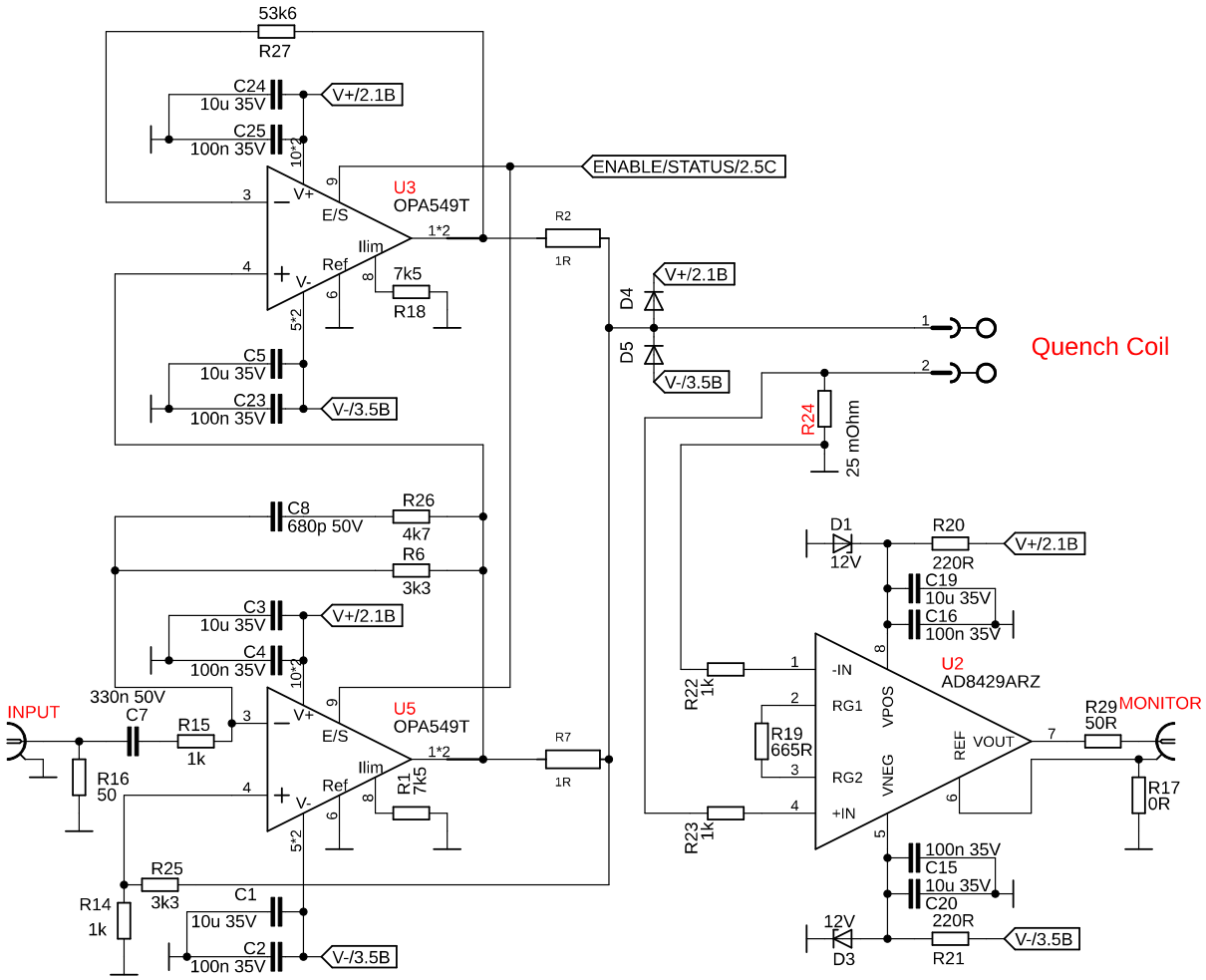

Figure 3.16: Amplifier circuit for magnetic field modulation (excerpt) The main amplification stage consists of the amplifiers (U3) and (U5). A current monitor is realized with the instrumentation amplifier (U2), measuring the voltage parallel to the power resistor (R24) with a gain of ten. The duration for which the amplifier is enabled is limited to prevent an accidental overheating of the coil, similar to the circuit in figure 3.8, but not shown here. Design and simulation of the circuit have been done by Dr. Akos Hoffmann.

several assumed values for the inductance of the quench coil. A calibration of the modulation amplitude, which is described in the following, can be used to compare the simulated bandwidth. At high frequencies the bandwidth of the amplifier drops faster than expected for the low inductance of the quench coil. It is possible that the connections to the quench coil lead to an additional inductance or parts of the circuit which are not considered in the simulation have an effect.

Characterization of Magnetic Field Modulation

In a first step, the current monitor of the amplifier is used to calibrate the amplitude of the current in the quench coil. It has a sensitivity of 0.25 V/A and we operate it far below its bandwidth limit of 4 MHz. While scanning frequency and amplitude of the input signal generated by the signal generator, the output of the monitor is recorded and presented in figure 3.18. The measured amplitude is very linear for a low input amplitude, but for larger amplitudes at some point a quadratic description is required to get featureless fit residuals. At a certain input amplitude, depending on the frequency, a strongly non-linear behavior is observed, because the

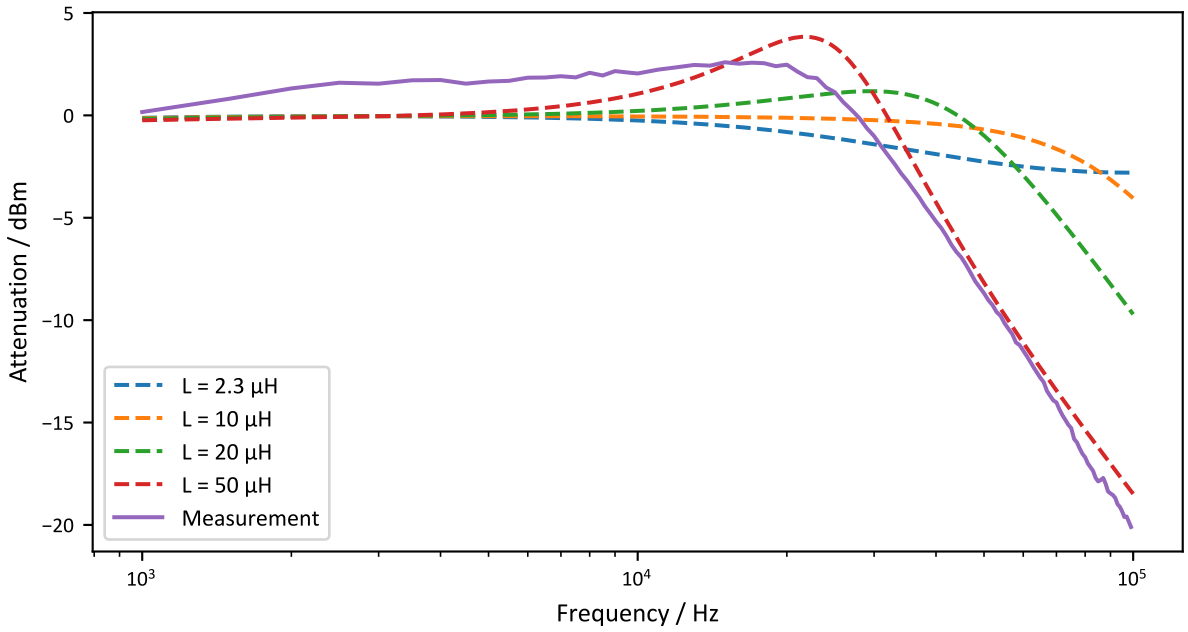

Figure 3.17: Simulated and measured bandwidth of the amplifier for magnetic field modulation

amplifier gets saturated. The limit for the maximum amplitude of the input signal, which avoids this region, is shown in the inset of figure 3.18. The measured voltage of the current monitor can be converted to the amplitude of the magnetic field modulation by using the sensitivity of the current monitor and the known relation between magnetic field and current through the quench coil, which has been characterized before in the DC case.

As a validation, the magnetic field is directly measured with the atoms via the imaging detuning for a short imaging pulse of 1 µs, which is significantly lower than the period of the oscillations with frequencies of up to $\nu_{\mathrm{mod}} = 120\,\mathrm{kHz}$. Using the known dependence of the imaging detuning on the magnetic field, the amplitude of the magnetic field modulation can be reconstructed. This can be compared with the result from the current monitor and figure 3.19 displays the ratio of the amplitude from the imaging detuning to the amplitude measured with the monitor.

It turns out that the magnetic field measurement from the imaging detuning is systematically lower than the measurement using the current monitor. The expectation is, that the imaging detuning is the more accurate measurement of the magnetic field, while a measurement which only considers the current in the quench coil might neglect additional contributions from eddy currents. Fortunately, the ratio between the measurements has a simple linear dependence, which can be used to determine a frequency dependent correction factor for the measurement from the current monitor.

Note that the measurement with the current monitor is very simple, while the measurement via the imaging detuning takes a lot of time. As an example, the inset of figure 3.19 shows a measurement of the amplitude via imaging detuning. For one datapoint, which measures the magnetic field, usually 11 absorption images are taken at different imaging detunings. While the example has some more datapoints, at least 10 datapoints should be measured to allow a reasonable fit for the extraction of the amplitude. At a sequence length of ∼25 s, the measurement of a single amplitude then takes roughly 45 min.

The final calibration is therefore based on the current monitor, but taking the frequency dependent correction factor into account, which is determined via the imaging detuning. In the

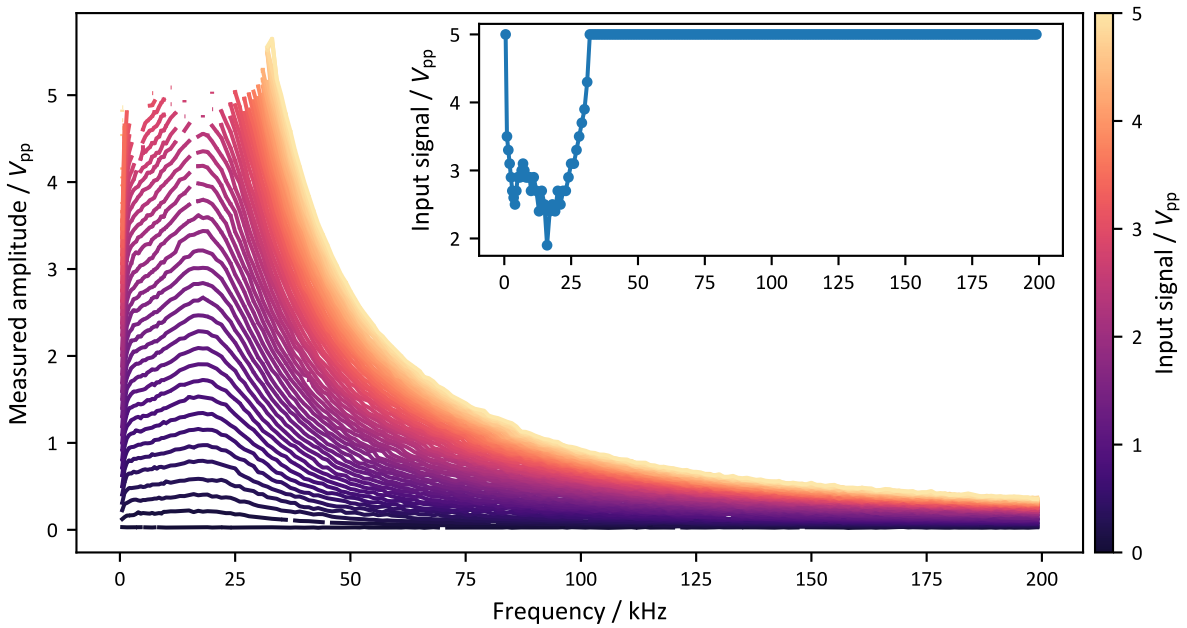

Figure 3.18: Amplitude calibration via current monitor At large amplitudes the amplifier becomes saturated and the output deviates from a sinusoidal modulation. This causes failed fits and missing datapoints, which is visible in the graphs when the measured amplitudes get close to 5 Vpp. The inset shows the maximum allowed input amplitude to stay in the linear regime. The inset uses the same x-axis as the main plot.

linear regime of the amplifier this leads to the calibration factor shown in figure 3.20.

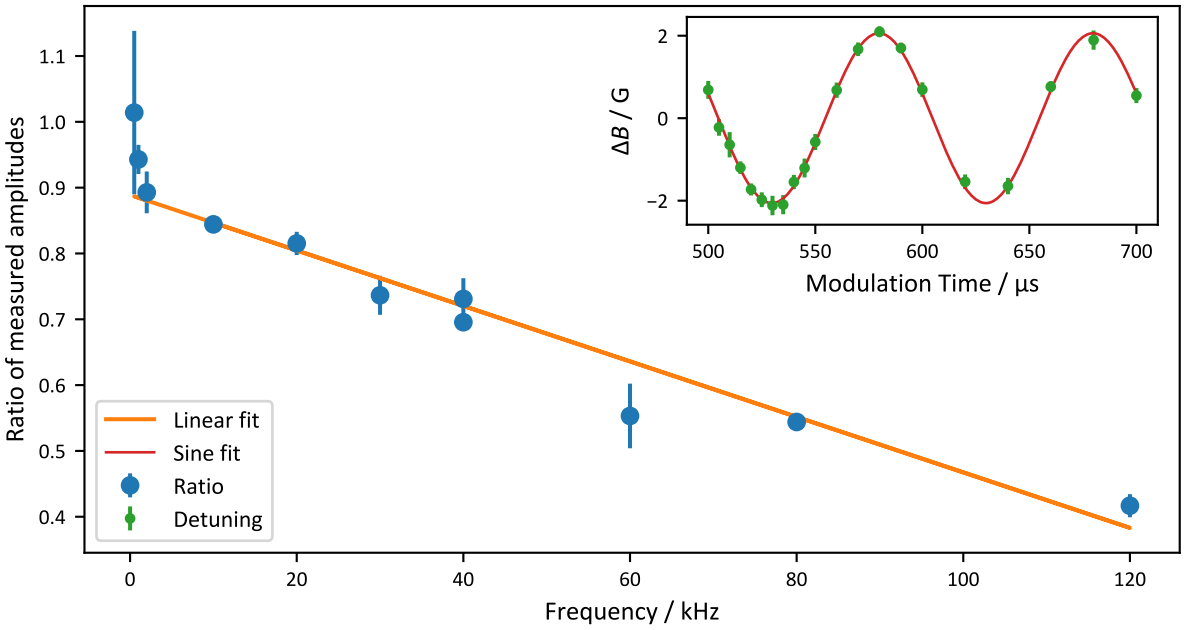

Figure 3.19: Comparison of calibration with current monitor and imaging detuning The imaging detuning leads to systematically lower amplitudes, but the ratio has a clear linear dependence which can be used to correct the result of the current monitor. The inset provides an example of an amplitude measurement via imaging detuning: For different times the magnetic field is measured by determining the imaging detuning of a short imaging pulse and the results are fitted with a sine function to extract the amplitude.

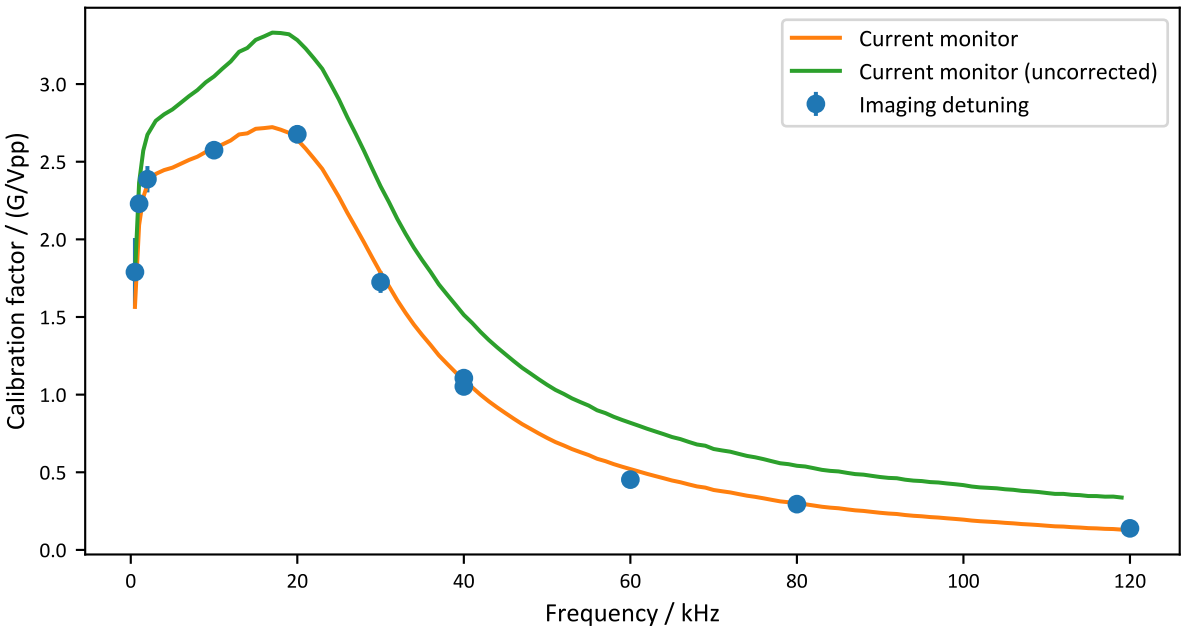

Figure 3.20: Calibration factor versus modulation frequency The calibration factor describes the resulting amplitude of the magnetic field for a given amplitude of the input voltage in the linear regime of the amplifier. The corrected values from the current amplifier are by construction consistent with the values based on the imaging detuning measurements.

4 Measurement and Analysis Methods

This chapter describes several methods being used in the investigations of subsequent chapters. On the experimental side this includes absorption imaging, the rapid ramp, which is used to measure condensate fraction, and the characterization of the trapping potential. As analysis tools, the inverse Abel transformation, which is used to convert column density to 3D density, the thermometry and machine learning techniques are explained.

4.1 Imaging of Atomic Samples

4.1.1 Imaging Systems

The experimental apparatus has several imaging systems, which are aligned to the final atom position. Their properties are summarized in table 4.1. The resolution limit is calculated according to the Rayleigh criterion [125] and the depth of focus according to the equation from ref. [126][1]. The two main imaging systems are aligned along the vertical z direction. For *Andor0* the imaging beam propagates downward and it is mainly used for time-of-flight images, while for *Andor1* the imaging beam propagates upward and it is mainly used for in-trap images.

Table 4.1: Summary of imaging systems for the final atom position and their properties For *Andor2* the magnification differs in horizontal and vertical direction due to an astigmatism, as discussed in the text, so two different values are specified. *Alta0* is made by Apogee Imaging Systems and the other cameras are made by Andor from Oxford Instruments. The effective pixel size constitutes the size at the atom position, which corresponds to one pixel. Similarly, the effective sensor size constitutes the size at the atom position, which corresponds to the whole CCD sensor.

(Internal) name	Andor0	Andor1	Andor2	Alta0
Camera Model	iXon Ultra 897	iXon Ultra 897	iXon Ultra 888	Alta U1
Imaging direction	z	z	y'	x'
Magnification	4.2	6.5	(8.4, 4.5)	1.2
Pixel size	16 µm	16 µm	13 µm	9 µm
Effective pixel size	3.8 µm	2.4 µm	(1.6, 2.9) µm	7.7 µm
Last lens f	120 mm	50 mm	120 mm	200 mm
Last lens D	25.4 mm	25.4 mm	25.4 mm	25.4 mm
Numerical aperture	0.11	0.25	0.11	0.063
Resolution limit	3.9 µm	1.6 µm	3.9 µm	6.4 µm
Depth of Focus	60 µm	10 µm	60 µm	166 µm
Pixel count	512 px	512 px	1024 px	(768, 512) px
Effective sensor size	1.9 mm	1.3 mm	(1.6, 3.0) mm	(5.9, 3.9) mm

Astigmatism of Andor2 For the horizontal imaging system *Andor2*, an astigmatism has been found. It turned out that the optimum camera positions which produce a good focus in either horizontal or vertical direction differ by more than a centimeter. To compensate this, a

[1] With an additional factor 2, to describe the full height over which the focus is acceptable.

cylindrical lens has been put into the beam path, but this has the effect that the image on the camera has an aspect ratio, i.e. the magnification differs horizontally and vertically.

The astigmatism could be caused by dichroic mirrors, which are placed at 45° to the optical axis or by an inclined beam relative to the optics. However, one major contribution probably stems from the lens closest to the atoms: In the past this achromatic lens caused clipping of the MOT beam, which lead to significant lower atom numbers. To mitigate this, a few millimeter on one side of the lens were cut away, which might have caused the astigmatism for example by slightly affecting the alignment of the lenses of the achromat or by introducing mechanical stress. For the other imaging systems no astigmatism is observed.

In table 4.1 both magnifications are specified. The vertical magnification of *Andor2* and the magnfication of *Alta0* is calibrated to gravity, by observing the center-of-mass of a cloud during free fall. To calibrate the horizontal magnification of *Andor2*, an atomic cloud with known aspect ratio is imaged. ^{23}Na in the final magnetic trap has initially an aspect ratio of two because the vertical magnetic gradient is twice as strong as the horizontal one. After sufficiently long time-of-flight, the aspect ratio converges to a value of 1, reflecting the isotropic momentum distribution of a thermal gas.

The calibration measurement is shown in figure 4.1. For *Alta0* the aspect ratio of the cloud is as expected because there is no significant astigmatism in the imaging system. For *Andor2* the aspect ratio deviates and the ratio between the aspect ratio measured with both imaging systems corresponds to the ratio of horizontal and vertical magnification of *Andor2*. Initially the ratio is 1.86, but it changes slightly during time-of-flight, which might be due to residual magnetic fields or an imaging artifact, when the cloud moves out-of-focus.

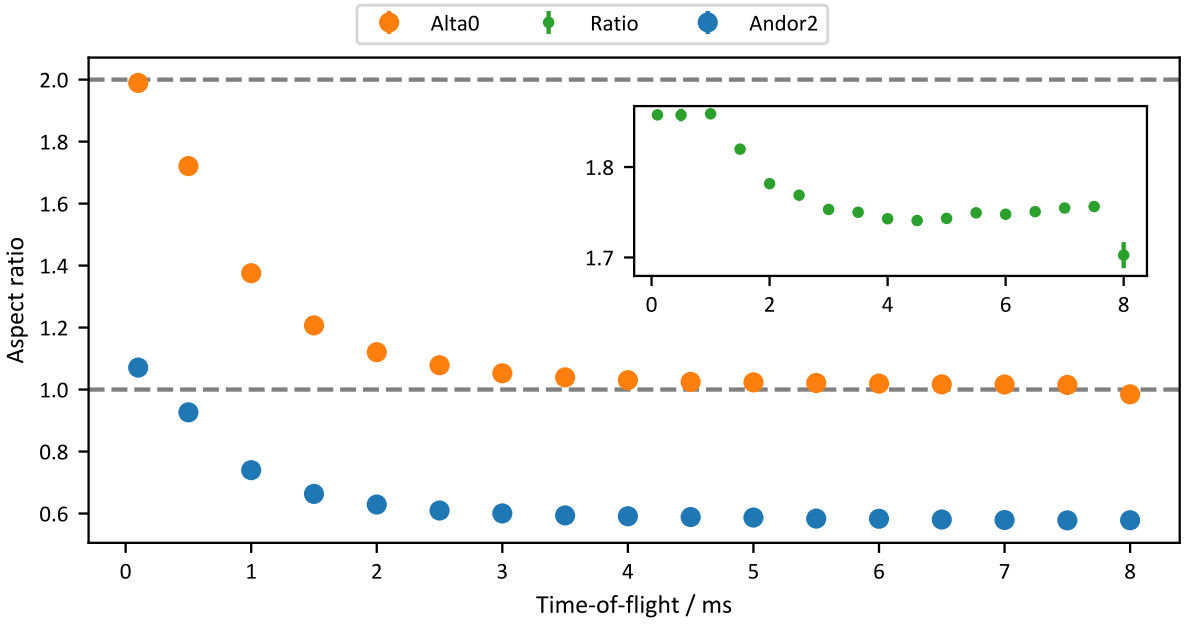

Figure 4.1: Aspect ratio of a ^{23}Na cloud in the magnetic trap during time-of-flight imaged with *Andor2* and *Alta0* The inset has the same x-axis as the main plot. It shows the ratio between the values of both cameras and the initial value is used to calibrate the magnification of *Andor2* in horizontal direction, which differs from the magnification in vertical direction due to an astigmatism in the imaging system.

4.1.2 Absorption Imaging and High Intensity Calibration

Overview

Absorption imaging is a reliable way to measure the column density of the atomic cloud along the line-of-sight of the camera. The idea is that the attenuation of a resonant imaging beam depends exponentially on the column density, i.e. the density integrated along the line-of-sight (Beer-Lambert law). By measuring the intensity of the imaging beam with a laser, once with the atoms and once without the atoms as a reference for the initial intensity of the beam, the column density can be determined.

In practice, certain constraints for the imaging intensity and duration have to be obeyed. First, the imaging pulse accelerates the atoms and causes a doppler shift of the imaging transition, which will eventually go out of resonance with the laser. Secondly, the accelerated atoms will leave the depth-of-focus of the camera at some point. Thirdly, the density can spread further than the imaging resolution by a random walk caused by the scattered photons.

Additionally, for high intensities the saturation of the transition has to be considered, which increases the transparency of the sample. While this makes the interpretation of the signal more complicated, it can also be helpful to image very dense clouds, because less imaging intensity is needed until a detectable signal can penetrate the cloud.

Imperfections of the polarization or non-ideal level-structures can reduce the ideal cross section and increase the effective saturation intensity, which has to be taken into account by a correction factor α. It has turned out, that this correction factor depends on the density of the sample, which has been attributed to local multiple scattering, but this dependence can be calibrated. Another calibration is necessary to convert the counts of the camera into intensity, because a comparison with the ideal saturation intensity of the imaging transition is required.

The calibration of α is based on a study with ^{87}Rb [127], but they do not report a dependence of the correction factor on the density on the sample. An alternative calibration of the effective saturation intensity, which does not rely on a measurement with a power meter, is described in ref. [128], but they have a constant correction factor $\alpha \approx 1$ for the optical densities which they consider. A similar calibration is also described in ref. [129] but for two-dimensional samples with relatively low optical density and they also report no variation of α.

The calibration procedure has also been described in several theses from our group but also for low optical densities where the factor is constant [130, 131]. At our experiment the dependence of α on the optical density has been already described [96, 97] and a more simple heuristic parametrization of that dependence has been shown [98], but the exact way how this is used to recover the corrected column density is new and will be described here. A similar dependence of α on the optical density is shown in ref. [132] but for a two-dimensional system.

Modified Beer-Lambert Law

In order to measure the attenuation of the imaging beam by the atoms, the intensity I_{atom} attenuated by the atoms is measured and compared with the intensity I_{light} when no atoms are present.

At low intensity I (compared to the saturation intensity I^{sat}), the resonant cross section $\sigma_0 = \frac{3\lambda^2}{2\pi}$ is set by the wavelength of the imaging transition λ [111]. The attenuation of the imaging beam along its propagation direction is described by the differential equation

$$\frac{\mathrm{d}I}{\mathrm{d}z} = -n\sigma_0 I\,, \tag{4.95}$$

leading to the Beer-Lambert law [111], which connects the column density $n_{\mathrm{col}} := \int_{-\infty}^{\infty} n\,\mathrm{d}z$ to

the optical density OD_0 (here the index "0" always denotes the low intensity limit)

$$n_{\mathrm{col}}\sigma_0 = -\ln\left(I_{\mathrm{atom},0}/I_{\mathrm{light},0}\right) =: OD_0\,. \tag{4.96}$$

In practice, the effective cross section $\sigma_{0,\mathrm{eff}}$ is reduced e.g. due to imperfect polarization or non-ideal level-structure and one introduces the calibration factor $\alpha := \sigma_0/\sigma_{0,eff}$, which also implies an increased effective saturation intensity $I_{\mathrm{eff}}^{\mathrm{sat}} = \alpha I^{\mathrm{sat}}$.

At higher imaging intensity the saturation of the imaging transition has to be considered

$$\sigma_{\mathrm{eff}} = \sigma_{0,\mathrm{eff}}/(1 + I/I_{\mathrm{eff}}^{\mathrm{sat}})\,. \tag{4.97}$$

This leads to an additional dependence $\sigma(I)$ in equation (4.95), which replaces σ_0, leading to a modified Beer-Lambert law [127]

$$n_{\mathrm{col}}\sigma_0 = -\alpha\ln\left(\frac{I_{\mathrm{atom}}}{I_{\mathrm{light}}}\right) + \frac{I_{\mathrm{light}} - I_{\mathrm{atom}}}{I^{\mathrm{sat}}}\,. \tag{4.98}$$

The intensities are determined from the counts on the CCD camera of the raw atom image $C_{\mathrm{raw,atom}}$ and the raw light image $C_{\mathrm{raw,light}}$. Additionally, a dark image C_{dark} considers the offset from dark counts, read-out noise and background light and is subtracted from the raw images, which gives $C_{\mathrm{atom}} = C_{\mathrm{raw,atom}} - C_{\mathrm{dark}}$ and $C_{\mathrm{light}} = C_{\mathrm{raw,light}} - C_{\mathrm{dark}}$. The ideal saturation intensity I^{sat} for the imaging transition is known and can be converted to a count rate $\dot{C}^{\mathrm{sat}}$ after the CCD chip has been calibrated with a power meter and the imaging magnification has been calibrated. Then the modified Beer-Lambert law can directly be expressed in terms of the measured camera counts during the imaging pulse duration τ [130]

$$n_{\mathrm{col}}\sigma_0 = -\alpha\ln\left(\frac{C_{\mathrm{atom}}}{C_{\mathrm{light}}}\right) + \frac{C_{\mathrm{light}} - C_{\mathrm{atom}}}{\dot{C}^{\mathrm{sat}}\tau}\,. \tag{4.99}$$

Calibration of CCD

A power calibration of the CCD chip of the camera is required, in order to determine the count rate $\dot{C}^{\mathrm{sat}}$, which corresponds to the known saturation intensity for the ^{6}Li D2 line of $2.54\,\mathrm{mW/cm^2}$ [105]. The total counts on the camera C_{total} are proportional to the power of the imaging beam P_{total} and the duration of the imaging pulse τ. By introducing a calibration factor m, the total counts on the camera are given by $C_{\mathrm{total}} = m\tau P_{\mathrm{total}}$. Similarly, the counts of a single pixel C_{pixel} and corresponding power P_{pixel}, i.e. the power corresponding to the part of the imaging beam imaged by that pixel, are related by the same calibration factor $C_{\mathrm{pixel}} = m\tau P_{\mathrm{pixel}}$.

Additionally, in order to relate the counts of a pixel to the corresponding beam intensity I_{pixel}, the magnification of the imaging system must be known, from which the effective pixel size w at the atom position can be deduced. This leads to

$$I_{\mathrm{pixel}} = P_{\mathrm{pixel}}/w^2 = \frac{C_{\mathrm{pixel}}}{m\tau w^2}\,. \tag{4.100}$$

The power of the imaging beam is measured before and after the experiment chamber with a power meter (Nova by Ophir Optronics Solutions) to get a reasonable accurate estimate. The ratio of total counts and imaging beam power is shown in figure 4.2 as a function of the imaging pulse time τ_{set}, defined by the sequence of the experiment. By applying a linear fit, the calibration factor m is determined. Additionally, a finite and positive x-axis intersect τ_{offset} is found, which can be explained with the finite rise time of the AOMs, which switch the imaging beam on and off. This offset has to be considered for the effective imaging duration τ, which is done by setting $\tau = \tau_{\mathrm{set}} - \tau_{\mathrm{offset}}$.

The result for the saturation count rate with *Andor1* for the D2 line is $\dot{C}^{\mathrm{sat}} = 323(9)\,\mu\mathrm{s}^{-1}$ and the offset of the imaging pulse is $\tau_{\mathrm{offset}} = 336(5)\,\mathrm{ns}$.

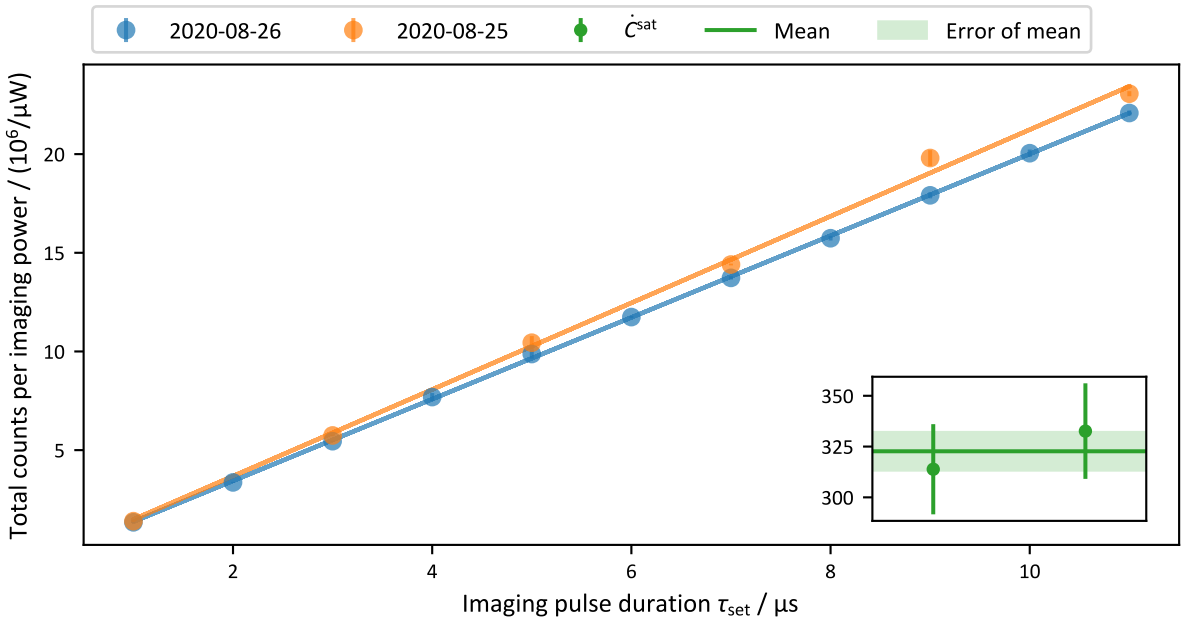

Figure 4.2: Calibration of the CCD of *Andor1* Shown are two different measurements, which result in a consistent value for $\dot{C}^{sat}$, as demonstrated in the inset. The x-axis of the inset has no special meaning, except for the measurement number, and is omitted, the y-axis shows $\dot{C}^{sat}$ in counts per microsecond.

Calibration of Effective Saturation Intensity

For the calibration of α, an atomic sample which has been prepared at identical experimental parameters is imaged repeatedly with varying imaging parameters (pulse duration and imaging intensity). The imaging parameters are varied in random order to prevent systematic errors from drifts of the atom number. A Gaussian profile is fitted to the uncalibrated optical density images and the pixels are divided into elliptic bins of equal column density. For each bin, equation (4.99) is interpreted as a linear function $D = -\alpha L + OD_0$ with slope $-\alpha$ and ideal low intensity optical density OD_0 as x axis intercept and relates the difference term $D := \frac{C_{\text{light}} - C_{\text{atom}}}{\dot{C}^{sat}\tau}$ to the logarithmic term $L := -\ln\left(\frac{C_{\text{atom}}}{C_{\text{light}}}\right)$. The resulting linear fits are shown in figure 4.3.

From slope and intercept of the fits, α and OD_0 are determined for each bin. One observes a dependence between the two values, α increases for larger optical densities as shown in figure 4.4. Results for *Andor0* and *Andor1* are displayed. Both imaging systems use different imaging beams, which might have a different quality of the polarization and lead to a different result. For *Andor0*, α is constant for low optical densities and then increases linearly, which is similar to the behavior described in ref. [132].

Application of Calibration

In general it is not trivial, to apply the correction factor α, because it is a function of the yet unknown optical density OD_0. It is feasible to determine α as a function of the effective optical density L for a given constant count rate, as in demonstrated in ref. [96], where $\alpha(L)$ is described as a polynomial function and used to find the corrected optical density $OD_0 \approx \alpha(L) \cdot L$ (ignoring the difference term at low intensity).

However, it could be desirable to change the count rate to improve the signal-to-noise ratio. Especially for large optical densities it is necessary to increase the imaging intensity, so that enough photons can still reach the camera. In this case, the difference term should also be

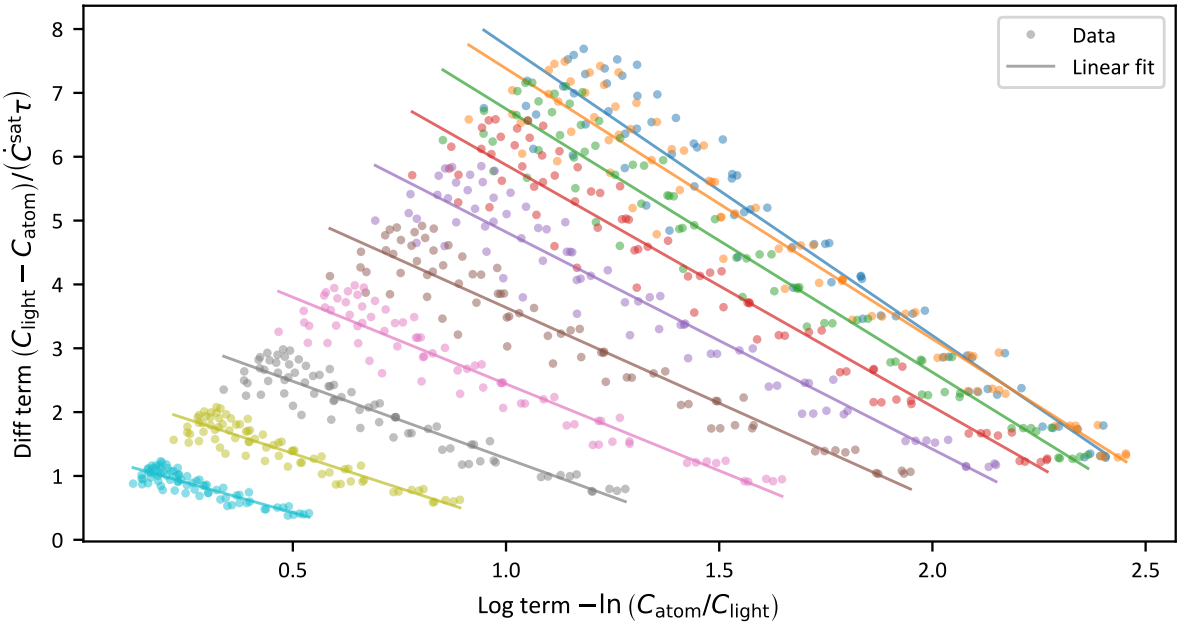

Figure 4.3: Difference and logarithmic term of modified Beer-Lambert law for bins of equal column density for varying imaging parameters For a better overview and better separation of data from different bins only a subset of the bins are shown. For stronger imaging intensity, the logarithmic term decreases, while the difference term increases. From slope and x axis intercept α and OD_0 can be determined. A different imaging duration should not have an effect on the position of the datapoints in this diagram, but in practice one can see a small reduction of the logarithmic term and for high intensity also a reduction of the difference term (This is the main reason for the spread of the datapoints, sometimes points arrange in a short line of five datapoints, corresponding to the five different imaging durations used in the measurement).

included. Fortunately, for a simple dependence of α on OD_0 it is not difficult to solve this generally. By using *Mathematica* it is shown that for $\alpha = a + b\max(0, OD_0 - c)$ and $OD_0 = -\alpha L + D$, where a, b, c are parameters determined from the calibration, the corrected value of the optical density is

$$OD_0 = \begin{cases} D - aL & \text{if } c + aL > D, \\ (D - aL + bcL)/(1 + bL) & \text{otherwise.} \end{cases} \tag{4.101}$$

Observation of Power Broadening

I also want to briefly show the effect of power broadening at high imaging intensities, which can in principle be an alternative way to determine α by measuring the effective saturation intensity. This has been investigated in ref. [128] by measuring the transferred momentum from the imaging beam to the atoms with a secondary imaging system.

Here, instead, just the apparent atom number is measured for varying imaging intensity and detuning. The measurement is performed for a large atomic cloud with not too high optical density to avoid systematic errors from refractive effects and depletion of the imaging beam intensity.

Power broadening describes an increased linewidth [111]

$$\Gamma' = \Gamma\sqrt{1 + s_{\text{eff}}}, \tag{4.102}$$

due to a reduced response on resonance for large saturation s. Indeed, a larger linewidth is measured for increased intensity of the imaging beam, as shown in figure 4.5. A fit to the

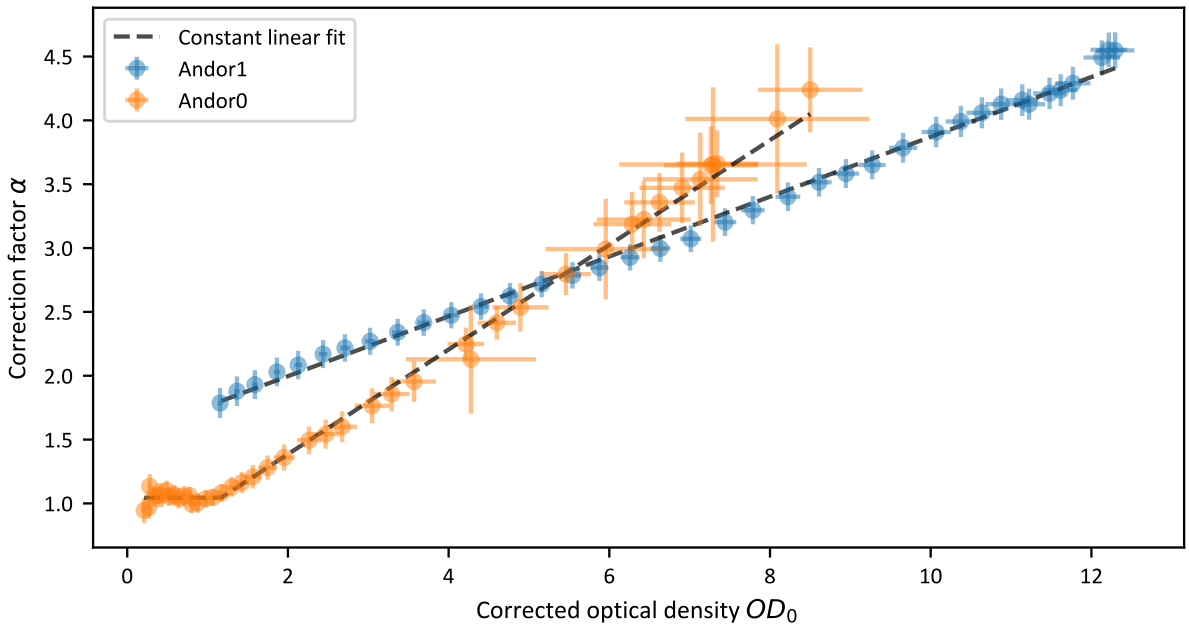

Figure 4.4: Dependence of the correction factor on the optical density

measured linewidths shows good agreement to the unbroadened linewidth $\Gamma = 5.8724\,\mathrm{MHz}$ [105], but this gives a large statistical error due to a strong correlation between Γ and $\dot{C}^{\mathrm{sat}}$. By fixing Γ at the literature value yields a fitted value of $\dot{C}^{\mathrm{sat}}_{\mathrm{eff}} = 466(19)\,\mu\mathrm{s}^{-1}$, which corresponds to a correction factor of $\alpha \approx 1.4$, but a comparison to the previous results would require a more careful analysis, which considers the dependence of α on OD_0.

Constraints on Imaging Parameters

The momentum transfer of scattered photons during imaging poses constraints on the imaging pulse duration τ, dependent on the intensity of the imaging beam. This is especially important for a lightweight atom as ^{6}Li. The atoms are accelerated along the propagation axis of the imaging beam. Additionally, they perform a random-walk caused by the emission of photons into random directions. The measurement is affected if the Doppler shift of the accelerated atoms is not negligible compared to the linewidth of the imaging transition ("Doppler limit") or if the atoms have moved by a distance which is not negligible compared to the depth-of-focus of the imaging system ("depth-of-focus limit") or if the lateral spread from the random walk is not negligible compared to the imaging resolution ("random walk limit").

Doppler and depth-of-focus are discussed in several theses of our groups, see e.g. ref. [133]. The random walk limit is described in ref. [134], which additionally considers the minimum intensity required to achieve a reasonable signal-to-noise ratio (not discussed here).

Assuming resonant imaging light with saturation $s = I/I^{\mathrm{sat}}$, the acceleration of the atoms is given as [111]

$$a = \frac{\hbar k}{m}\frac{\Gamma}{2}\frac{s}{1+s}\,, \tag{4.103}$$

which determines the velocity $v = a\tau$ and traveled distance $d = a\tau^2/2$ after the imaging pulse duration τ.

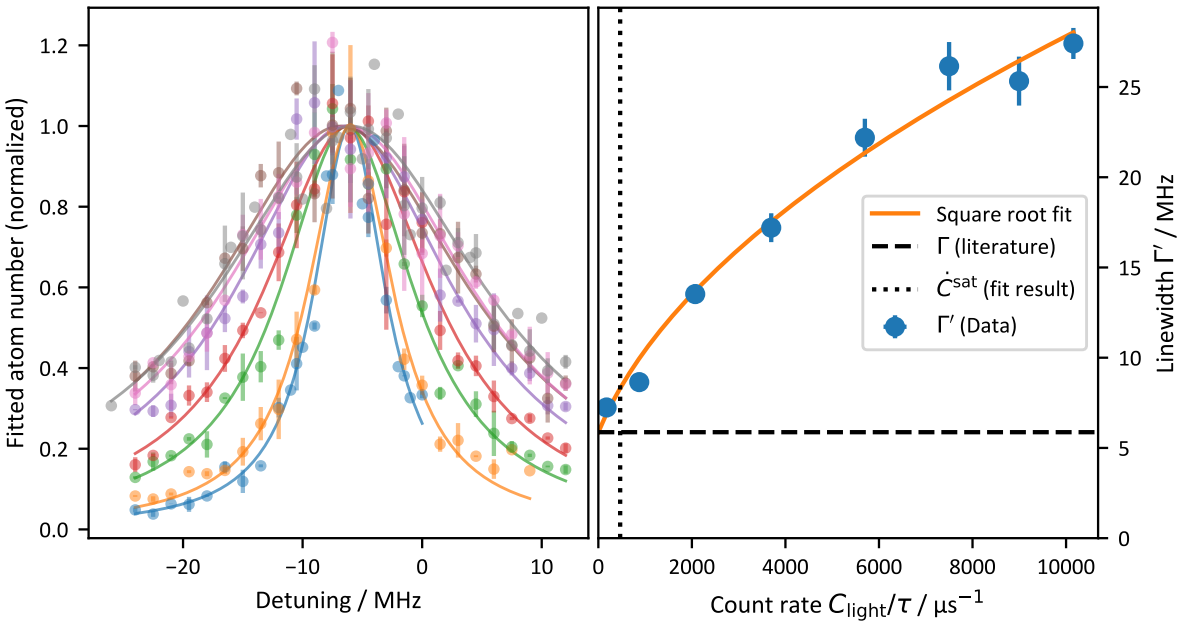

Figure 4.5: Determination of effective saturation count rate from power broadening For different imaging intensities the apparent atom number is measured as function of the detuning **(left)**. Using the extracted linewidths a fit to equation (4.102) ("Square root fit") allows the extraction of the effective saturation count rate $\dot{C}^{\text{sat}}$ **(right)**. Γ is set to the literature value [105], leaving $\dot{C}^{\text{sat}}$ as the only fit parameter.

Doppler Limit The Doppler shift has to be smaller than the power broadened linewidth

$$\begin{aligned} kv &< \Gamma\sqrt{1+s} \\ \Leftrightarrow \tau &< \frac{(1+s)^{3/2}}{s}\frac{2m}{\hbar k^2}\,. \end{aligned} \tag{4.104}$$

Note that ref. [134] uses a stricter condition, by comparing the Doppler shift to half of the linewidth. But in practice a "resonant laser" will be blue detuned at the beginning and red detuned at the end of the imaging pulse, justifying the comparison with the full linewidth, which is consistent to e.g. ref. [98].

Depth of Field Limit For not too large numerical apertures, the depth-of field is given by $d_{\text{dof}} \approx \lambda/NA^2$ [133][2], which yields the constraint

$$\begin{aligned} d = \frac{\hbar k\Gamma}{4m}\frac{s}{1+s}\tau^2 &< \frac{\lambda}{NA^2} = d_{\text{dof}} \\ \Rightarrow \tau &< \sqrt{\frac{8m\pi}{\hbar\Gamma NA^2k^2}\frac{1+s}{s}}\,. \end{aligned} \tag{4.105}$$

Random Walk Limit The random walk limit is the point where the lateral spread of the atoms becomes larger than the resolution of the imaging system d_{rw}, which might either be limited by the resolution of the optical system or the effective pixel size of the camera. The condition reads [134]

$$\tau < 3\left(\frac{m\lambda}{2h}d_{\text{rw}}\sqrt{\frac{1+s}{\Gamma s}}\right)^{2/3}\,. \tag{4.106}$$

[2]For *Andor1* the deviation compared to the formula of ref. [126] is only ∼2 %.

The constraints are shown in figure 4.6 and compared to the parameters used for the high intensity calibration.

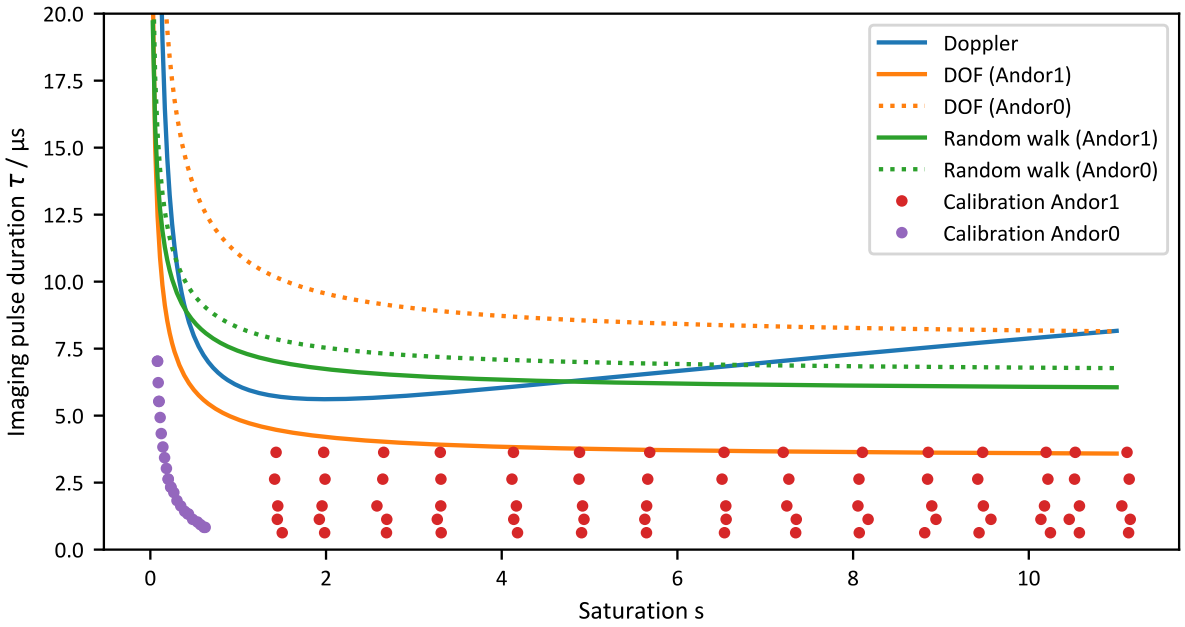

Figure 4.6: Constraints on imaging pulse duration and intensity The limits are compared to parameters used for the high intensity calibration.

4.2 Rapid Ramp

The "rapid ramp" is a method to detect the condensate fraction of the gas and has been explored by refs. [28, 29]. Measuring the condensate fraction far on the BEC side is not complicated, because the molecules which are part of the condensate occupy very low momentum states, which can be differentiated from the momentum distribution of the thermal background. More specific, the momentum distribution is measured in time-of-flight and the condensate fraction can be extracted by fitting a bimodal distribution.

On the BCS side the measurement is more difficult because Cooper pairing modifies the momentum distribution only slightly around the Fermi momentum. The idea of the rapid ramp technique, as sketched in figure 4.7, is to apply a magnetic field ramp towards the BEC side close to the zero-crossing of the Feshbach resonance. The ramp must be fast enough to project the Cooper pairs onto low momentum Feshbach molecules, but should not be too fast, to allow an adiabatic evolution towards deeper bound molecules after the projection. The field close to the zero-crossing of the Feshbach resonance ensures that the momentum distribution is not distorted by interaction effects during the time-of-flight. Finally, the field is ramped back to a point where molecules are not deeply bound and can be imaged easily and the condensate fraction is extracted via a bimodal fit. Note that the conversion efficiency of Cooper pairs to low momentum molecules could depend on the initial field and the magnetic ramp speed and is usually not known precisely, which means that the measured condensate fraction can deviate from the actual condensate fraction of the initial state.

Experimental Implementation of the Rapid Ramp In our implementation of the rapid ramp, the magnetic field is ramped directly after the dipole trap is switched off. A fast sweep of the magnetic field is difficult to implement due to the relatively large inductance of the Feshbach

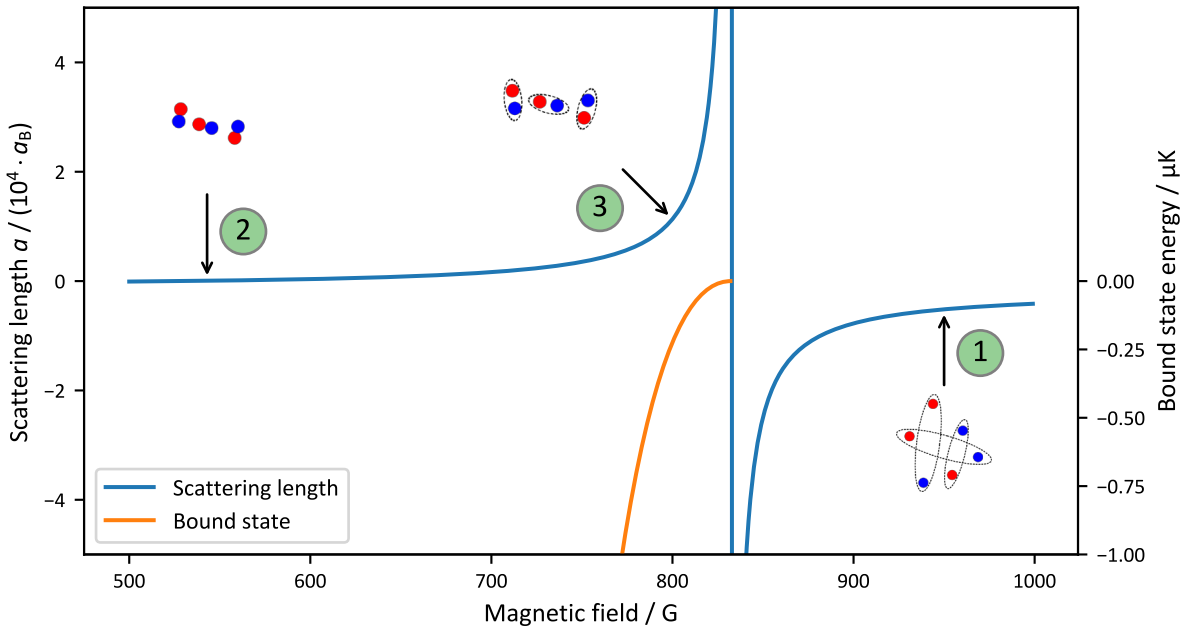

Figure 4.7: Sketch of rapid ramp technique The Cooper pairs of the initial state **(1)** are projected with a rapid magnetic ramp onto deeply bound non-interacting molecules **(2)**. Towards the end of the time-of-flight the magnetic field is ramped back to a field where the molecules can be imaged **(3)**.

coils and due to the possibility of eddy currents e.g. in the experimental chamber (see section 3.3, especially figure 3.6, for an example of the magnetic field during the first part of a rapid ramp). To achieve a ramp speed of about 80 µs, the H-bridge (IGBT Module 2MBI900VXA-120P-50 by Fuji Electric) is switched off for a time $\tau_{\text{off}} = 5\,\mu\text{s}$ to 50 µs and high voltages induced by the coils are removed with varistors. Additionally, the charge from the power supply is reduced by shorting the contacts with an IGBT (1MBI600U4B-120 by Fuji Electric) for a time $\tau_{\text{discharge}} = 150\,\mu\text{s}$ to 250 µs. The shape of the current ramp is mainly determined by these two time intervals, rather than the setpoints of the current regulation of the power supply, which is too slow on these timescales.

The time-of-flight duration is 15 ms, which is close to $T/4$ for the typical magnetic fields, where $T/4$ stands for a quarter of the trap period of the remaining potential during time-of-flight and is the time after which the measured density distribution resembles the momentum distribution of the original gas [135], or in this case the momentum distribution of the projected pairs. The remaining potential is caused by the curvature of the magnetic Feshbach field and is only confining in radial direction. Shortly before the absorption image is taken, the magnetic field is ramped to the imaging field using the normal ramp of the power supply.

For each initial magnetic field, the two time intervals τ_{off} and $\tau_{\text{discharge}}$ have to be optimized by measuring the current during the ramp. From time to time it is necessary to check if the calibration is still valid or if it has to be reoptimized. Recently the rapid ramp was used at many different initial fields, which allows an empiric understanding how to choose the optimum values for the time intervals. Figure 4.8 shows the results of several manual optimizations and it turns out that the optimum off time depends linearly on the difference between target and initial field ΔB

$$\tau_{\text{off}} = \Delta B \cdot a_{\text{off}} + b_{\text{off}}\,, \tag{4.107}$$

with $a_{\text{off}} = 0.157(3)\,\mu\text{s/G}$ and $b_{\text{off}} = -5.1(8)\,\mu\text{s}$. The optimum discharge time has an exponential dependence on ΔB

$$\tau_{\text{off}} = a_{\text{discharge}}\left[1 - \exp\left(-\Delta B / b_{\text{discharge}}\right)\right]\,, \tag{4.108}$$

with $a_{\text{discharge}} = 262(2)\,\mu\text{s}$ and $b_{\text{discharge}} = 101(2)\,\text{G}$. This should simplify the optimization process of the rapid ramp in the future.

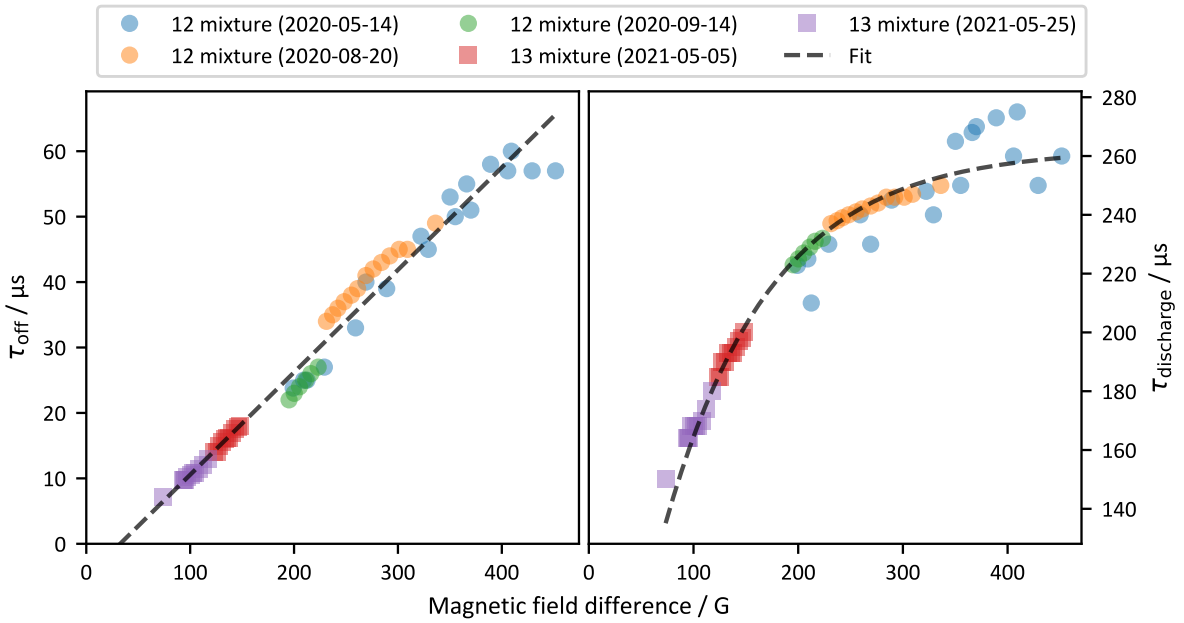

Figure 4.8: Dependence of optimum rapid ramp parameters on the difference between initial and target magnetic field Shown are the off time **(left)** and the discharge time **(right)** together with empiric fits described in the text.

4.3 Interpreting Column Density

Measurements are usually taken in the form of absorption images. They represent the optical density OD_0 of the atomic sample, which is directly connected to the column density n_{col} of the atomic gas along the line-of-sight of the camera

$$\int_{-\infty}^{\infty} n_\sigma \,\mathrm{d}z =: n_{\text{col}} = OD_0/\sigma_{0,\text{eff}}\,. \tag{4.109}$$

In general, it is not easy to convert n_{col} into the physically more interesting three-dimensional density n_σ, but depending on the trap geometry there are different strategies available.

For a harmonically trapped gas one can recover the 3D density by employing the Gibbs-Duham relation within LDA, which implies for constant temperature that the pressure is the integral of the density over the local chemical potential. The procedure consists of integrating n_{col} along one measured direction and differentiating the result along the other direction [33].

For axially symmetric trap geometries $V(\rho, z)$, n_σ can be calculated with the inverse Abel transformation [33, 61]. This is also possible, if the trap potential is not strictly axially symmetric but requires a stretching factor to become axially symmetric, i.e. if it can be expressed by variables for height z and "radius" $\rho = \sqrt{(x/s_x)^2 + (y/s_y)^2}$, with stretch factors s_x and s_y. This is the method which is used in this thesis, in order to be less affected by anharmonicities of the trap.

4.3.1 Inverse Abel Transformation

Assuming that the 3D density n_σ is radially symmetric along the z axis and that the column density n_{col} is considered for a camera with line-of-sight along the y axis, the density can be recovered with the inverse Abel transformation [61]:

$$n_\sigma(\rho, z) = -\frac{s_x}{s_y}\frac{1}{\pi}\int_\rho^\infty \frac{\mathrm{d}x}{\sqrt{x^2-\rho^2}}\frac{\partial n_{\mathrm{col}}}{\partial x}(x, z) \tag{4.110}$$

Behavior and Caveats of the Inverse Abel Transformation

The inverse Abel transformation yields exact results if it is applied analytically, but for discrete and noisy data and imperfections of the symmetry it can lead to dramatic deviations from the correct result. Therefore, some observations are detailed here, how the transformation can be applied carefully, by applying it to a Gaussian density distribution as a toy model.

Toy Model A Gaussian density distribution $n_\sigma(x, y) = \exp(-(x^2+y^2)/(2\sigma^2))$ with standard deviation σ is chosen[3], which is cylindrically symmetric around the z axis. The z dependence is omitted for simplicity. A Gaussian distribution can be an acceptable approximation of the density of the atomic gas in many cases, but here it also has the advantage that the column density n_{col} along the y axis can easily be calculated as $n_{\mathrm{col},0}(x) = \int_{-\infty}^{\infty} n_\sigma(x, y)\,\mathrm{d}x = \exp(-x^2/(2\sigma^2))\sqrt{2\pi}\sigma$.

Discrete Data In order to apply the inverse Abel transformation on discrete data, a simple approach would be to replace the integral in equation (4.110) by a sum using the trapezoidal rule for approximating integrals. But this is problematic because the first factor of the integrand diverges for $x \to \rho$ and if consequently the first term of the sum is omitted, the reconstructed density differs dramatically from the original density as is demonstrated in figure 4.9.

In ref. [136] it is suggested to perform a variable substitution $\tau := \sqrt{x^2-\rho^2}$ in equation (4.110), which avoids divergences at $x = \rho > 0$, but it is demonstrated that for a simulated density distribution this still leads to deviations of 8 % at the cloud center and can be reduced to 4 % by using super-sampling.

Here a more accurate method is presented. The derivative of the column density is locally, over the range of a pixel, approximated by a linear function $n'_{\mathrm{col}}(x) =: ax + b$, which is then used to calculate part of the integral in equation (4.110) analytically, which results in

$$\int_k^{k+1} \frac{ax+b}{\sqrt{x^2-\rho^2}}\,\mathrm{d}x = \begin{cases} a & \text{if } r = k = b = 0, \\ a + (b-ak)\ln(1+1/k) & \text{if } r = 0 \wedge k > r, \\ h(a, b, r, k) & \text{if } r > 0 \wedge k > r, \end{cases} \tag{4.111}$$

where $h(a, b, r, k)$ is not a nice expression but can be easily determined with a CAS as

$$h(a, b, r, k) = -a\sqrt{k^2-r^2} + a s_{k,r} + \frac{ak-b}{2}\left[l_+(k, r) - l_-(k, r) + l_+(k+1, r) - l_-(k+1, r)\right], \tag{4.112}$$

with $l_\pm(x, r) := \ln\left(x \pm \sqrt{x^2-r^2}\right)$. Note that b must vanish in the center $r = k = 0$ for the integral to diverge, which is used as a constraint when determining a and b for the discrete intervals. Applying this method to the toy model gives a quite accurate reconstruction of the original density distribution, which is also shown in figure 4.9.

[3] There is no connection to the index of n_σ, which refers to the considered spin state. The index is kept for a better consistency, although it is not very relevant here.

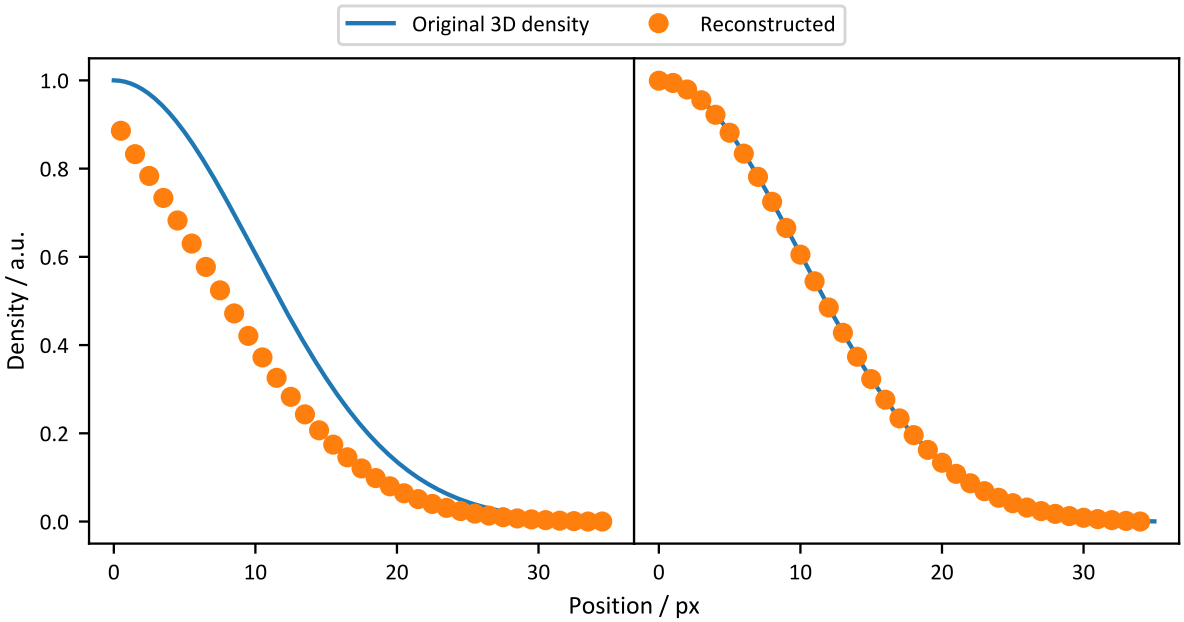

Figure 4.9: Application of the inverse Abel transformation on discrete data The naive approach **(left)**, which directly approximates the integral by a sum, fails to recover the original density. The more careful approach **(right)** uses linear interpolation of the column density and step-wise analytical integration.

Misalignment between Symmetry Axis and Pixels For simplicity it is tempting to consider the position of the symmetry axis to coincide with the position of a camera pixel. But figure 4.10 demonstrates that if there is a misalignment of up to $\pm 0.5\,\mathrm{px}$, this already has a large effect on the recovered density profile in the center of the cloud.

This effect is simply compensated, by considering the offset for the integral boundaries of equation (4.111), which gives an improved reconstruction as shown in figure 4.10.

Noise Since the inverse Abel transformation relies on derivatives which are approximated by differences of discrete datapoints, it is very susceptible for noisy data. Figure 4.11 shows that already a noise level of $1\,\%$ leads to an amplified noise level of the reconstructed density, especially in the center.

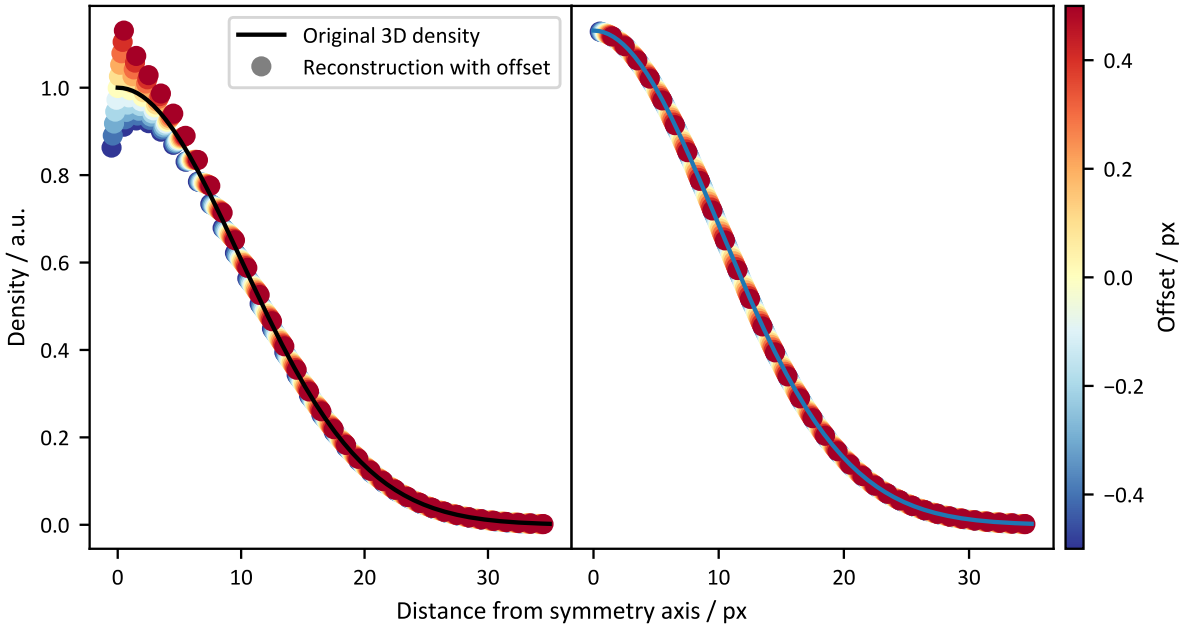

Figure 4.10: Offset between the symmetry axis and the pixel grid The influence of the offset on the reconstructed density distribution **(left)** leads to a systematic error in the trap center. However, a known offset can be compensated **(right)**.

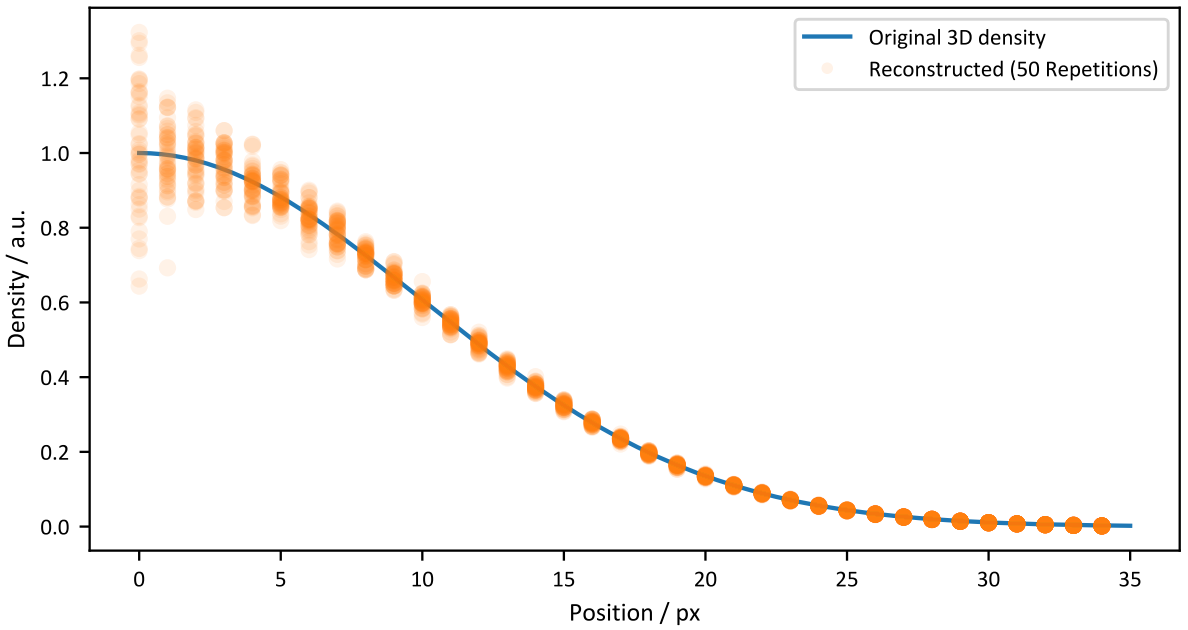

Figure 4.11: Effect of noisy data A noise level of 1 % is added to the column density of the toy model before the reconstruction, which is repeated 50 times. This reveals that especially the reconstruction of the central density is prone to noisy data.

4.4 Thermometry

This section describes how thermometry of a strongly interacting Fermi gas is performed. At first some approaches which can be found in the literature are discussed and why thermometry for an ultracold and strongly interacting Fermi gas is challenging. Then several methods which have been employed in our experiment are described in more detail.

4.4.1 Overview

It has often been noted in the literature that a reliable thermometry of a strongly interacting gas is difficult. "There is no model-independent method" [137] or a "model-independent thermometry is notoriously difficult" [60], "a general difficulty" [138], it "generally is a very difficult task" [139], "one of the major" [140] or "formidable challenges" [56] and "is not well understood" [58].

For hot and weakly interacting gases, thermometry is usually performed by measuring the expansion speed of the cloud after switching the trapping potential off. The density distribution after time-of-flight reveals the momentum distribution of the gas, if one considers the initial size of the cloud or if it is negligible. Alternatively, one can let the cloud expand into a harmonic potential, then the density distribution resembles the momentum distribution if the time-of-flight corresponds to a quarter of the trap period [135]. For the different scenarios there are fit functions available, which can extract the temperature [4].

For imbalanced gases, thermometry is also straightforward but must be performed with the in-trap density distribution. At low temperatures there appears a phase separation and in the outer region the gas of majority atoms can be considered as an ideal gas, which allows the extraction of the temperature with Thomas-Fermi fits [141].

For balanced strongly interacting samples, the thermometry based on time-of-flight images is problematic. First, the interaction energy is released when the trapping potential is switched off, which leads to an increased kinetic energy and a modified momentum distribution. Secondly, the idea of the $T/4$ measurement described above is only valid for a "quadratic structure of the Hamiltonian", which means that interactions distort the measured profiles [135]. Thirdly, the original momentum distribution is already affected by interaction effects in a non-trivial way. For example, a fit function would need to consider the effect of the contact and its temperature dependence on the momentum distribution [93].

For a two-dimensional gas these problems can be circumvented by a fast axial expansion, which decreases the interaction without modifying the radial momentum distributions [135].

Ref. [142] suggests to use the cloud size as an empirical thermometer, which gives access to the potential energy of the gas and is connected to the total energy via the virial theorem. For a unitary gas, universality implies a strict relationship between the total energy relative to its ground state energy E/E_0 and the reduced temperature T/T_F, but this relationship has to be calibrated by using another thermometry method. Also, this method is not suitable for low temperatures, because at some point the size of the cloud depends mainly on the Fermi energy or atom number, instead of the temperature [4].

If interaction effects during time-of-flight are ignored, one can still fit the cloud to a Thomas-Fermi distribution as in the non-interacting case. This yields an empiric temperature $\tilde{T}$, which has to be calibrated to take the interaction effects into account [58]. Note that the fits for this thermometry can be affected by features in the profiles caused by interactions, as discussed in ref. [4] for in-trap density distributions. For an in-trap density distribution it is possible that the wings are still in a normal state, while there is already a superfluid forming in the center of the trap. Such a separation of different phases is not given in momentum space because the momentum distributions of normal and superfluid components can overlap. This complicates

the interpretation of the empiric temperature.

4.4.2 Adiabatic Interaction Ramp to Weakly-Interacting Regime

The problem of thermometry in the strongly interacting regime can in principle be circumvented by an adiabatic interaction ramp into the weakly interacting regime [137, 143]. Far on the BCS side the temperature can be determined via the interaction at which superfluidity vanishes. This can for example be detected via vanishing condensate fraction using the rapid ramp technique. Based on BCS theory with GMB correction, the temperature can be calculated as the critical temperature at that interaction, as described in section 2.4.3. Far on the BEC side, the temperature can directly be determined from condensate fraction and atom number.

Note that an adiabatic ramp from BCS to BEC side can be slightly problematic due to the vanishing bound state energy at unitarity, which prevents a strict adiabatic ramp in finite time. Another problem is that the adiabatic ramp does not keep the temperature unaffected [144], rather it keeps the entropy constant. So instead, one can measure entropy in the weakly interacting regime, then one can either measure physical properties as a function of entropy or one has to use additional theory to convert the entropy to temperature.

The change in temperature during the adiabatic ramp is governed by the adiabatic sweep theorem and is connected to the contact of the gas (see section 2.5.4). So if the contact is known, the temperature change can be calculated. The contact has been measured for varying interactions in the BEC-BCS crossover [145] and for varying temperature at unitarity [146, 147]. Unfortunately, the full dependence on both parameters would be required.

These points show that a thermometry, which is only based on adiabatic sweeps towards the weakly interacting regime, is not optimal for us, but can be used for additional checks.

4.4.3 Bosonic Cloud as Thermometer

One promising option to measure the temperature of a strongly interacting gas is to thermalize it with a weakly-interacting gas and use it as a thermometer. In ref. [148] the thermomtry of a ^{6}Li gas far on the BCS side was demonstrated by using the condensate fraction of a ^{41}K BEC to calculate the temperature. The temperature can also be extracted from the thermal wings after expansion and leads to consistent results, although this is less precise for the probed regime. They use a small fraction of ^{41}K atoms relative to ^{6}Li and they have a large mass ratio, which allows to measure a large temperature range without influencing the ^{6}Li temperature too much. A "moderate" interspecies scattering length ensures that thermalization is possible, but avoids other interaction effects and losses. They argue that this method should also work at unitarity but might lead to problems towards the BEC side due to atom loss [139].

We did consider to use a similar scheme for our thermometry. One option would be to use bosonic ^{7}Li as thermometer, which has been demonstrated in ref. [60]. But this would require changes of the laser system to allow the preparation of cold ^{7}Li. Another possibility could be to use ^{23}Na as thermometer, which is very convenient because we already use it in our system for sympathetic cooling. Unfortunately, we have not found experimental parameters for which the thermalization is faster than the atom losses, as discussed in ref. [98].

4.4.4 Density Distribution at the Surface of the Cloud

Boltzmann Thermometry Based on Optical Density At the "surface" of the atomic sample, i.e. at large radial distance from the cloud center, the density is at some point small enough to justify the description as a Boltzmann gas [33]. Assuming a harmonic potential along the line-of-sight $V(x, y, z) = 0.5m\omega_z^2 z^2 + V(x, y)$, the resulting optical density retains the exponential

decay of the density versus potential

$$OD_0 = \sigma_0 n_{\mathrm{col}} \propto \sigma_0 \int_{-\infty}^{\infty} e^{\beta(\mu - V(z))} \mathrm{d}z \propto \int_{-\infty}^{\infty} e^{\beta(-0.5 m \omega_z^2 z^2 - V(x,y))} \mathrm{d}z \propto e^{-\beta V(x,y)} \,. \tag{4.113}$$

By measuring the decay constant $\beta = 1/(k_{\mathrm{B}}T)$, the temperature can be determined if the trap potential $V(x, y) = V(x, y, 0)$ is known accurately.

But some caveats have to be considered. At large radius anharmonicities of the trap become more dominant, so that e.g. a Gaussian trap potential does not split up into $V(x, y, z) = V(x)+V(y, z)$ as assumed above, resulting in a more complicated behavior than the exponential decay, so that the inverse temperature β cannot be extracted without further assumptions. Also, if the density is not low enough, Bose and Fermi statistics and interaction effects become relevant and modify the dependence of the density on the potential, leading to systematic errors.

Thermometry Based on 3D Density and Virial Expansion To include the effects of Bose or Fermi statistics, one can use Fermi and Bose fits. For intermediary interactions, one can use virial expansion, to allow fit ranges up to higher densities. For these fits the absolute value of the density is important, which requires the conversion of the measured column density to 3D density using the inverse Abel transformation, as described in section 2.5.3.

A fit to the density distribution based on the virial expansion has two fit parameters, the (global) chemical potential μ_0 and the temperature T. The fit region has to be restricted to low densities, where the condition $\mu(\boldsymbol{r})/(k_{\mathrm{B}}T) \ll 0$ for the virial expansion within LDA is fulfilled. The coefficients of the virial expansion are calculated from the fit parameter T and the scattering length a, which is known for a given magnetic field B, using the knowledge about the Feshbach resonance from section 2.2.1.

A thermometry based on the virial expansion has already been realized previously, for example, by ref. [149] with an expansion up to second order.

Comparison As an example, both thermometries are compared in figure 4.12. At first the thermometry based on the optical density is demonstrated. To reduce noise, the optical density is averaged along equipotential lines and plotted against the potential, which reveals the exponential decay described above, where the decay constant corresponds to the inverse temperature β if the density is low enough to assume the equation of state of a Boltzmann gas.

The optical density can be converted to 3D density, using the inverse Abel transformation, as explored in section 4.3.1. This allows the application of more appropriate fit functions and a fit based on the third order virial theorem is demonstrated.

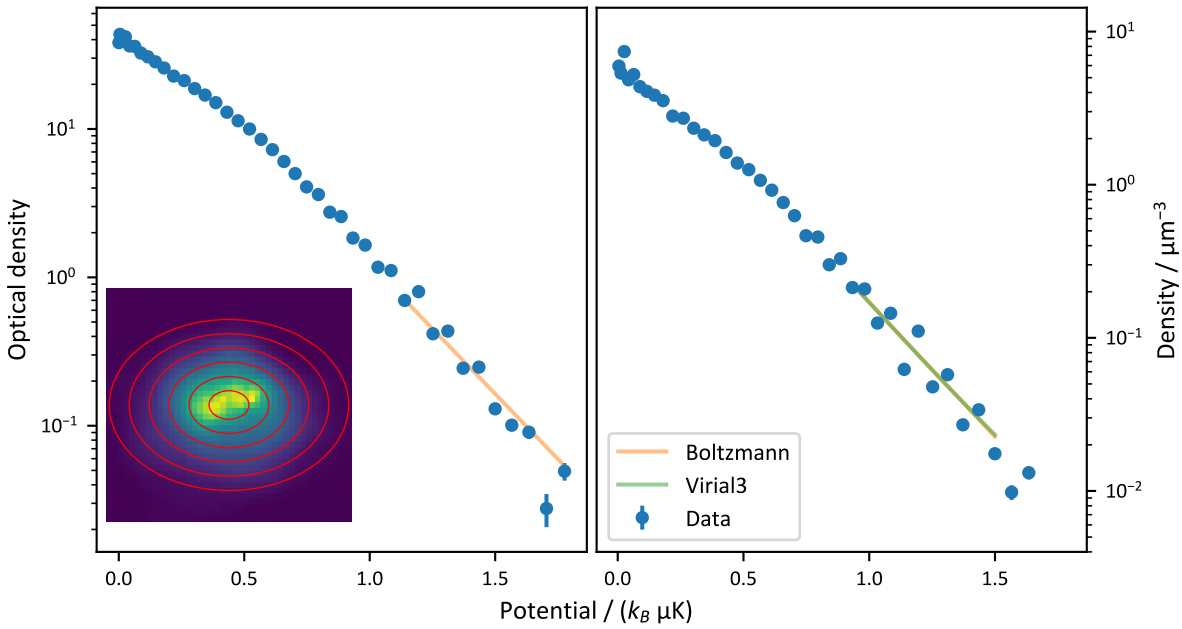

Figure 4.12: Exemplary thermometry Shown are a thermometry based on the optical density and a Boltzmann fit **(left)**, as well as a thermometry based on the 3D density and a fit using the third order virial expansion **(right)**. The data is taken at 836 G and a small amount of heating has been applied. The absorption image is shown in the inset and equipotential lines are indicated, which are used for radial averaging.

4.5 Characterization of the Trap

The potential of the final trap configuration, in which the experiment is performed, is composed of different contributions

$$U_{\text{trap}} = U_{\text{optic}} + U_{\text{magnetic}} + U_{\text{gravity}} \,. \tag{4.114}$$

The main part U_{optic} stems from the optical dipole trap. Additionally, the magnetic field curvature creates an additional potential U_{magnetic}, sometimes including a gradient for gravity compensation. Finally, also the gravitational potential U_{gravity} has to be considered.

Gravity Potential The potential from gravity is given by

$$U_{\text{gravity}} = gmz \,, \tag{4.115}$$

with vertical position z and gravity of earth g.

Magnetic Potential The magnetic field from the Feshbach coils has its strongest component along the vertical axis (z-direction), which defines the quantization axis for the atomic states, whereas magnetic field components along the other directions only have a negligible contribution to the trap potential. This also means that only gradients and curvatures of the z component of the magnetic field have a significant influence on the potential. In ref. [96] it is shown that the magnetic field of our Feshbach coils can be approximated by a Taylor expansion up to second order[4]

$$B_z = B_0 + B'' \cdot (-x'^2 - y'^2 + 2z^2) \,, \tag{4.116}$$

[4]In order to be consistent with our internal notation, the trap is described with the horizontal coordinates x' and y' and the vertical coordinate z, whereas x and y would be used for another coordinate system which is not relevant here.

with simulated values $B_0/I = 1.893\,\mathrm{GA}^{-1}$ and $B''/I = 0.0106\,\mathrm{Gcm}^{-2}\mathrm{A}^{-1}$ at current I.

The magnitude of the magnetic field is not directly relevant for the trapping potential, because it only creates an energy offset, instead it is important how the magnetic field changes over the extent of the atomic cloud, therefore the corresponding potential for an atom with magnetic moment μ can be described as

$$U_{\mathrm{magnetic}} = \mu \cdot (B_z - B_0) = \mu B'' \cdot (-x'^2 - y'^2 + 2z^2)\ . \tag{4.117}$$

The magnetic moment of a hyperfine state corresponds to its slope in the Breit-Rabi diagram, which is shown in figure 3.2 for ^{6}Li. But since the experiments are performed in the Paschen-Back regime, the magnetic moment is dominated by the magnetic moment of the valence electron, i.e. it correponds roughly to the Bohr magneton or $\mu \approx \pm h \times 1.4\,\mathrm{MHz/G}$. For the lower three states, which are commonly used in the experiment, the negative sign is valid, which implies a confining potential in horizontal direction and an anti-confining potential in vertical direction.

Optical Potential The optical potential is a dipole trap, which comprises two far red detuned laser beams at a wavelength of 1070 nm. The horizontal dipole trap beam passes the experiment chamber along the x' axis in a single pass. The vertical dipole trap beam propagates upwards along the z axis and hits the atomic cloud 3 mm below the top window, but is then reflected at the top window back onto itself and passes the atomic cloud a second time. The coherence length of the laser is short enough to guarantee that no optical lattice is created by the vertical beam.

Both beams are not tightly focussed and can be considered as collimated beams over the extent of the atomic cloud. Their waist $w_0 > 50\,\mu\mathrm{m}$ corresponds to a rayleigh range of $z_\mathrm{R} = \pi w_0^2/\lambda > 7\,\mathrm{mm}$, which is large compared to typical atom cloud sizes on the order of $\sim$100 µm. Consequently, only the radial intensity profile of the dipole beams has to be considered.

By describing the dipole trap beams as Gaussian beams, the potential is given by

$$\begin{aligned} U_{\mathrm{dipole}} = {} & \eta \frac{2P_\mathrm{H}}{\pi w_{\mathrm{H},y'} w_{\mathrm{H},z}} \exp\!\left(-2y'^2/w_{\mathrm{H},y'}^2 - 2z^2/w_{\mathrm{H},z}^2\right) \\ & + \eta \frac{2P_\mathrm{V}}{\pi w_{\mathrm{V},x'} w_{\mathrm{V},y'}} \exp\!\left(-2x'^2/w_{\mathrm{V},x'}^2 - 2y'^2/w_{\mathrm{V},y'}^2\right), \end{aligned} \tag{4.118}$$

with beam power $P_\mathrm{H/V}$ and beam waists $w_{\mathrm{H/V},i}$ in direction $i \in \{x', y', z\}$. P_V includes the power of the reflected beam. The prefactor η is introduced in section 3.1.

Relative Alignment In the description of the trapping potential presented above the origin is centered to the laser beams and to the magnetic field saddle point. In practice, this requires a good alignment of the laser beams relative to each other and to the saddle point of the magnetic field. The dipole trap beams can be moved precisely via piezo-motorized mirrors (Picomotor Mount 8821 by New Focus) and the center of the magnetic field can in principle be moved vertically by applying a magnetic field gradient. A horizontal shift of the magnetic field center is currently not possible. Note that a gradient in horizontal direction would not suffice, but rather a magnetic field with finite $\partial_{x'} B_z$ or $\partial_{y'} B_z$ were required.

The alignment is probed by quickly reducing the power of one of the dipole beams. If there is relative misalignment, this causes a sloshing of the atoms and the beam positions have to be adjusted until the sloshing vanishes. If the vertical beam is moved, one also has to check if the back-reflection at the top window still coincides with the original beam, which can be done quite precisely by coupling the beam back into the fiber by which it is transported to

the experiment. This has to be done at low power and requires to rotate an optical isolator into transmission mode. In this case the back reflection and sloshing have to be optimized iteratively.

4.5.1 Characterization of Dipole Trap

Overview For the measurements in the subsequent chapters it is important to know the trap potential precisely. The main contribution of the final trap stems from the dipole trap, which is also the most challenging to characterize. This section discusses several methods which are used to get a good understanding of the trap.

For an atomic cloud which is much smaller than the waists of the dipole trap beams, one does not have to consider their Gaussian profiles, but can instead assume a harmonic potential. In this case, the characterization is not difficult, because the trap potential is fully constrained by its trap frequencies measured by exciting the dipole mode of the gas with small amplitude. However, for the investigations described in this thesis, some deviations from a harmonic potential have been observed. This is especially important for the thermometry based on the in-trap density distribution at the surface of the cloud, because the assumed trap potential directly affects the outcome of the thermometry. At the surface of the cloud, i.e. at large distance from the trap center, the largest deviations from the harmonic potential are expected.

In contrast to a magnetic potential, which can in principle be mapped out using RF transitions, the dipole potential acts on all ground state atoms in the same way, ruling out spectroscopic methods for the characterization of the trap. Actually, the excited states are shifted in the opposite direction [107], which would in principle allow to measure the energy shift from the trap directly, but the linewidth of D1 and D2 line are roughly 6 MHz, while the typical trap depth is around 1 µK, which corresponds to a maximum energy shift of 42 kHz, which is too small to resolve directly.

In a first step the relative intensity distributions of the dipole beams are determined by directly imaging the beams onto the cameras, which are usually used for absorption imaging of the atoms. This is not completely reliable, because the beam passes through optics which are not designed for the wavelength of the beams.

The power of the beams is calibrated with a power meter, but this has a large error from the power measurement directly and also because the power can only be measured close to the experiment chamber and not at the position of the atoms. Knowing the power of the beams and the trap frequencies along the principle axes, one still requires one additional constraint to know all relevant beam parameters. In this case, the aspect ratio of the horizontal beam is measured separately, which allows the calculation of the beam parameters and results in a good description of the trap potential.

Alternatively, a straightforward approach to measure the anharmonicity of the trap is to excite the dipole mode with larger amplitude. If the amplitude is large enough so that the cloud can probe the regions of anharmonicity, this affects the measured oscillation frequencies. This effect is measured and a small numeric simulation shows how to calculate the beam waists from the data. Unfortunately, the result is not realistic, it deviates from the previous result and it would require a beam power which is clearly not compatible with the power measurements. This is an indication that the model to describe the the dipole potential with Gaussian beams is not appropriate.

Finally, this problem is overcome by calibrating the trapping potential directly from the observed density distribution for a gas with known equation of state.

Direct Imaging on Camera The beam waists are measured with the cameras, which are focused onto the atom position. The vertical dipole beam is imaged with *Andor1*, using the

Table 4.2: Measured parameters of horizontal and vertical dipole beam The values for the beam waists and central intensity are compared for the various methods described in the text.

Parameter	Camera	Dipole Mode	Equation system	Full model
$w_{\mathrm{H},y'}$	115 µm		107 µm	104(2) µm
$w_{\mathrm{H},z}$	63 µm	44 µm	62 µm	61.2(7) µm
$I_{\mathrm{H}}/\mathrm{W/mm^2}$		15 $\mathrm{W/mm^2}$	29.5 $\mathrm{W/mm^2}$	30.5(6) $\mathrm{W/mm^2}$
$w_{\mathrm{V},x'}$	149 µm	145 µm	111 µm	112(1) µm
$w_{\mathrm{V},y'}$	152 µm		140 µm	142(4) µm
$I_{\mathrm{V}}/\mathrm{W/mm^2}$		62 $\mathrm{W/mm^2}$	35.6 $\mathrm{W/mm^2}$	34.7(8) $\mathrm{W/mm^2}$

small amount of light which is transmitted by the high-reflection coated top window and using the imaging optics, which are designed for lithium wavelengths. The horizontal dipole beam has been imaged with *Alta0*, using the small amount of light which is transmitted by a dichroic mirror, which reflects most of the dipole beam to a beam dump. The measured waists are given in the first column of table 4.2. They should give a good idea of the actual beam waists, although the measurement is not very reliable because of the use of optics which are not design to transmit the light at 1070 nm.

Power Calibration of Dipole Beams For various constant power settings of the dipole beam laser power, the power is measured with a power meter close to the chamber and compared with the value of the regulating photodiode. The calibrations are shown in figure 4.13 and give

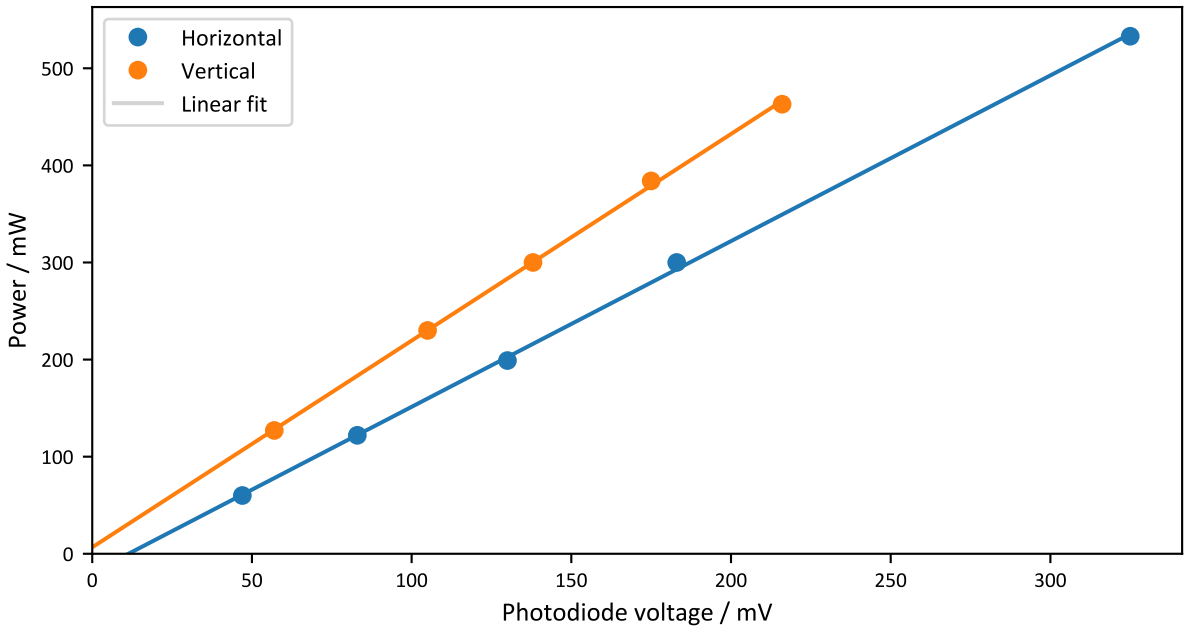

Figure 4.13: Power calibration of dipole trap beams The power of the beams, measured with a power meter close to the experimental chamber, is calibrated to the voltage of the regulating photodiode.

the linear dependence of laser power $P_{\mathrm{H/V}}$ on the voltage of the regulating photodiode $U_{\mathrm{H/V}}$

$$P_{\mathrm{H/V}} = m_{\mathrm{H/V}} \cdot U_{\mathrm{H/V}} + n_{\mathrm{H/V}}\,, \tag{4.119}$$

with the parameters in table 4.3.

Table 4.3: Fit results of power calibration for dipole trap beams Parameters are defined by equation (4.119).

Parameter	Value
m_H	1.7 mW/mV
n_H	−19 mW
m_V	2.1 mW/mV
n_V	6.7 mW

Numeric Study of Dipole Mode in Gaussian Potential Measuring the frequency of the dipole mode of an atomic gas is a reliable method to determine the trap frequencies. The result is unaffected by interaction effects of the atoms, because this does not affect the center-of-mass movement of the cloud.

However, the atomic cloud should be small compared to the length scale of the trap potential, otherwise the probed potential is a convolution of the trap potential with the density distribution of the cloud. While this effect can be taken into account for a static density distribution, in practice the density distribution changes its form during the oscillation, which would complicate the calculation.

A second condition is that the amplitude of the dipole oscillations should be small enough to stay in the harmonic region of the trap, otherwise the observed oscillation frequencies are affected by the anharmonicities of the potential.

Here we consider the dipole mode of a small cloud but with oscillation amplitudes which are large enough to probe the anharmonicities of the trap potential, which is considered to be Gaussian. The deviation from the harmonic trap frequencies is used as a probe to fully characterize the Gaussian potential.

The dipole mode oscillation of the center-of-mass of the cloud at large amplitudes is not described by a simple sine function, because the time spent at maximum elongation is increased compared to an oscillation in a harmonic potential, whereas the movement close to the trap center is not affected. This makes it challenging to model this analytically and instead a numeric approach is chosen.

Only considering one dimension, the trap potential is given as

$$V(x) = -V_0 \exp(-2x^2/w^2)\,, \tag{4.120}$$

for trap depth V_0 and waist w. A second-order Taylor series expansion at $x = 0$ and comparison to a harmonic potential $V_\mathrm{harmonic} = 0.5m\,(2\pi\nu_\mathrm{center}x)^2$ with mass m and trap frequency ν_center yields a trap frequency

$$\nu_\mathrm{center} = \frac{1}{\pi w}\sqrt{\frac{V_0}{m}}\,, \tag{4.121}$$

which is valid for small oscillation amplitudes.

The acceleration of an atom in the Gaussian potential is

$$\ddot{x} = \frac{-\partial_x V(x)}{m} = \frac{-4V_0 x \exp(-2x^2/w^2)}{mw^2} \tag{4.122}$$

This differential equation is solved numerically for realistic parameters, assuming a trap depth of $V_0/k_\mathrm{B} = 1\,\mu\mathrm{K}$ and a waist of $w = 100\,\mu\mathrm{m}$ and varying initial amplitudes A. The result is fitted with a sine function, which does not match well to the actual movement for large amplitudes, but is sufficient to reliably extract the apparent trap frequency, as shown in figure 4.14. This procedure is repeated for different waists w but also for different central trap frequencies ν_center.

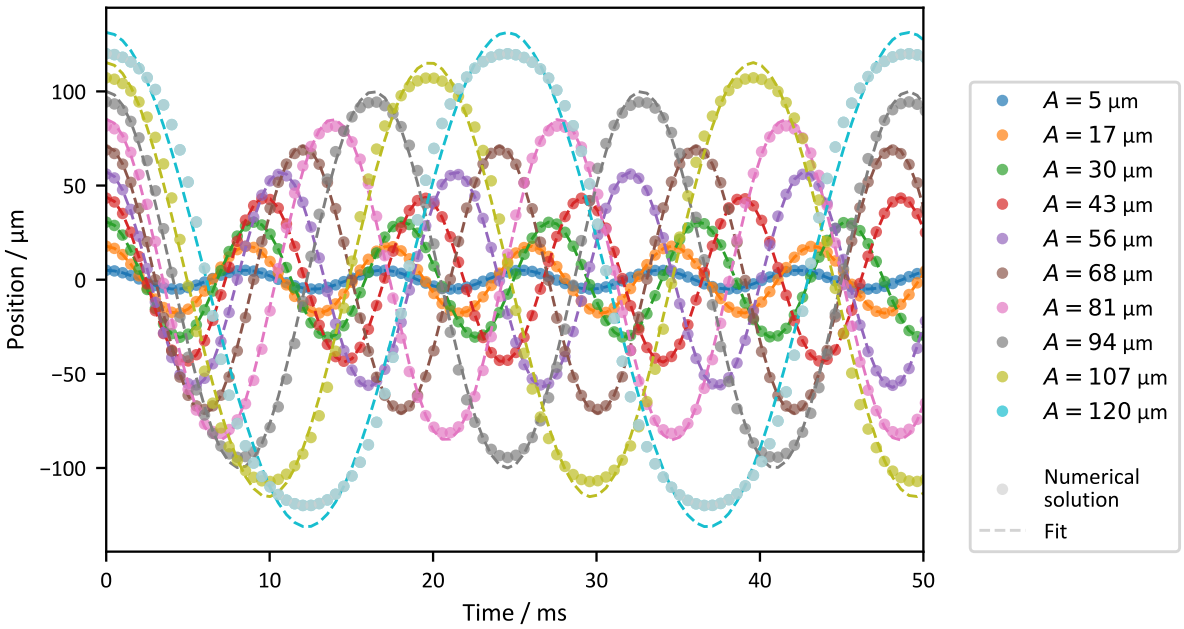

Figure 4.14: Simulated dipole mode oscillations of a small cloud in a Gaussian trap potential Apparent trap frequencies are reduced in an anharmonic trap for large amplitudes and are extracted by fitting a sine function, which works well despite the poor fit at large amplitudes. Simulation and fits are performed for a larger time interval than shown. Chosen values for trap depth and beam waist are $V_0/k_\mathrm{B} = 1\,\mu\mathrm{K}$ and $w = 100\,\mu\mathrm{m}$.

Indeed, the trap frequency is reduced for larger amplitudes and this reduction is slower for larger waists, but if the trap frequency is plotted against A/w, the curves all fall on top of each other, as shown in figure 4.15. Empirically, one finds that this dependence is well described by

$$\nu = \nu_\mathrm{center} \exp\left(\frac{-2A^2}{(w\gamma)^2}\right), \tag{4.123}$$

with $\gamma = 1.651(4)$ found by a fit to the results of the simulation.

This relation only has two free parameters, the waist w and the central trap frequency ν_center, which together also determine the trap depth via equation (4.121). This makes it well suited as a fit function applied to measured data, as soon as a reduction of trap frequency due to anharmonicity is observed.

The same problem has also been discussed in ref. [66] using an analytic approach but considering the anharmonicity only to the lowest order.

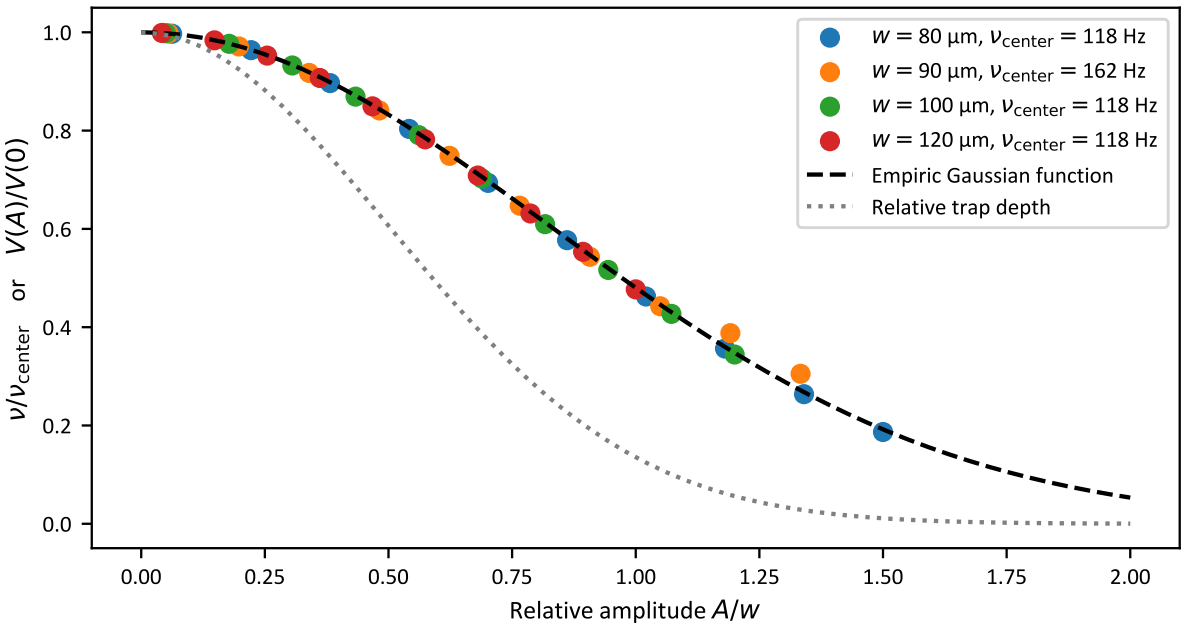

Figure 4.15: Reduction of simulated trap frequencies for large oscillation amplitudes in a Gaussian potential The data only depends on the relative amplitude A/w and is described by a simple empiric function, given in the main text. A comparison shows that the trap frequency $\nu(A)$ diminishes slower compared to the trap depth $V(A)$, although the functional shape is the same.

Measurement of Trap Frequencies via Dipole Mode To perform the measurement, a small atomic cloud is prepared and slowly displaced by a magnetic gradient along one of the principle axes. After quickly switching off the gradient, the cloud accelerates back to the trap center and the dipole mode is excited.

In a harmonic trap one can measure the trap frequencies for different axes at the same time because the movement along the principle axes separates. In general, this is not the case and for large amplitudes in a Gaussian trap the movement along one axis can affect the movement along another axis. Therefore, the magnetic gradient is applied in a way to only excite an oscillation along one principle axis. The gradient is generated by the quench coil, which is slightly misaligned relative to the atoms to generate the gradient.

Figure 4.16 shows examplatory the measurement of the dipole mode along the x' direction. The amplitude of the oscillation cannot be increased further because for stronger gradients the cloud starts to fragment into several parts and for even stronger gradients the atoms are lost. For large amplitudes the oscillation is damped. Therefore, amplitude A and frequency ν are extracted by fitting the data to a decaying sine function

$$f(t) = A\exp(-(t-t_0)/\tau)\sin\left(2\pi\sqrt{\nu^2 - 1/(2\pi\tau)^2}t + \phi_0\right) + x_0\,, \tag{4.124}$$

with additional fit parameters for the damping time τ, initial phase ϕ_0 and equilibrium position x_0. Since the amplitude of the oscillation is damped, it is not appropriate to choose the initial amplitude, but instead the amplitude at the center t_0 of the measured time interval is extracted.

The dependence of the oscillation frequency on the initial amplitude is shown in figure 4.17 for all three principle axes. The resulting beam waists and trap depths of this characterisation are shown in table 4.4. A beam waist for the y' direction cannot be determined, because the confinement in y' direction stems from both dipole beams, which can have different waists. This means that one additional constraints must be used, for example the power calibration of a beam can be used or a measurement of the aspect ratio of a beam.

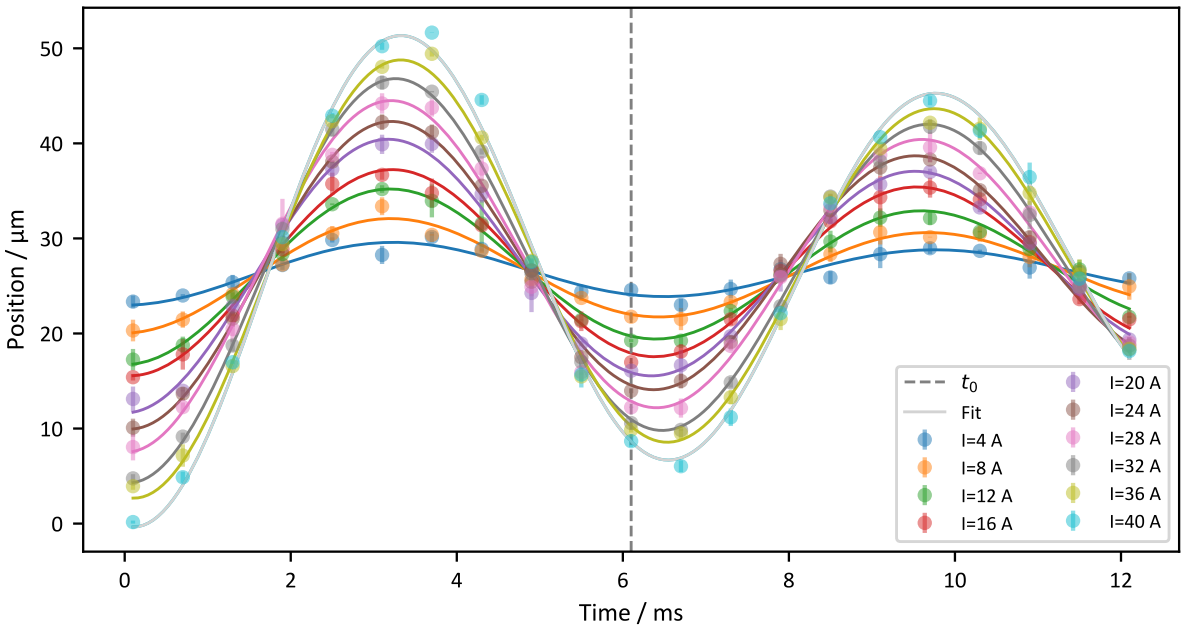

Figure 4.16: Measured dipole oscillations for different amplitudes The initial displacement of the cloud along the x' direction is realized by the magnetic gradient of the misaligned quench coil and varied via the applied current, which is specified in the legend. The oscillation frequencies and initial amplitudes are extracted via a fit to a decaying sine function.

Unfortunately, it turns out that the result from this method does not lead to consistent result and therefore the derivation of the beam waists in y' direction is omitted. One explanation for this could be, that the damping leads to systematic errors, which are not considered in the numeric model. But also deviations of the dipole beams from a Gaussian profile are a possible explanation.

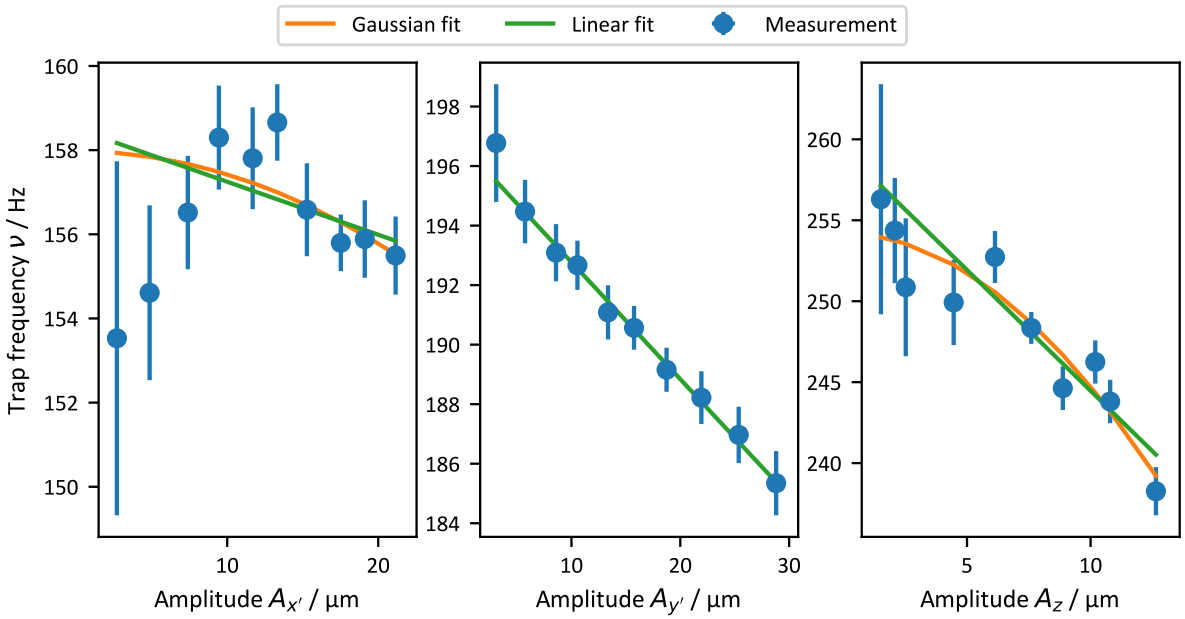

Figure 4.17: Measured trap frequencies for different amplitudes of the dipole mode for the three principal axes The data is fitted to a linear function and to the Gaussian function from equation (4.123), except for the y' direction, for which the trap frequency has contributions from both dipole trap beams and cannot be described with that model.

Table 4.4: Parameters of the fits from figure 4.17

Parameter	Value
$\nu_{\mathrm{center},x'}$	158.0(8) Hz
$w_{x'}$	145(38) µm
$m_{x'}$	−0.13(9) Hz/µm
$n_{x'}$	159(1) Hz
$m_{y'}$	−0.39(1) Hz/µm
$n_{y'}$	196.7(2) Hz
$\nu_{\mathrm{center},z}$	254(1) Hz
w_z	44(3) µm
m_z	−1.5(2) Hz/µm
n_z	259(2) Hz

Trap Characterization Based on Power Calibration Assuming for now that the damping causes the inconsistencies, in the following only the central frequencies are used. Together with the power calibration already 5 of 6 parameters of the two dipole beams (trap depth and two waists per beam) are constrained. As additional input the measured aspect ratio $A_{\mathrm{H},y',z} \approx 1.74$ of the atomic cloud with only the horizontal beam is used, which gives a system of six equations

$$P_{\mathrm{H}} = \frac{1}{2} I_{\mathrm{H}} \pi w_{\mathrm{H},y'} w_{\mathrm{H},z} \tag{4.125}$$

$$P_{\mathrm{V}} = \frac{1}{2} I_{\mathrm{V}} \pi w_{\mathrm{V},x'} w_{\mathrm{V},y'} \tag{4.126}$$

$$\nu_{x'} = \frac{1}{\pi w_{\mathrm{V},x'}} \sqrt{\frac{\eta I_{\mathrm{V}}}{m}} \tag{4.127}$$

$$\nu_{y'} = \sqrt{\frac{\eta I_{\mathrm{H}}}{m\pi^2 w_{\mathrm{H},y'}} + \frac{\eta I_{\mathrm{V}}}{m\pi^2 w_{\mathrm{V},y'}}} \tag{4.128}$$

$$\nu_{z} = \frac{1}{\pi w_{\mathrm{H},z}} \sqrt{\frac{\eta I_{\mathrm{H}}}{m}} \tag{4.129}$$

$$A_{\mathrm{H},y',z} = w_{\mathrm{H},y'} / w_{\mathrm{H},z} \,. \tag{4.130}$$

The parameters on the left hand sides have all been measured. The power of the dipole beams has been calibrated and is calculated from the setpoints $U_{\mathrm{H}} = 0.19\,\mathrm{V}$ and $U_{\mathrm{V}} = 0.20\,\mathrm{V}$ using equation (4.119) and the parameters from table 4.3. For the trap frequencies the values $\nu_{\mathrm{center},x'}$, $n_{y'}$ and $\nu_{\mathrm{center},z}$ from figure 4.17 are used. The equation system is solved and the results for beam waists and intensities are added to table 4.2.

Optimization of Full Trap Model In the last paragraph, only the contributions to the trap from the dipole beams are considered, but at the final trap settings the trap frequencies are also slightly affected by gravity and magnetic curvature, as indicated in equation (4.114). To take this into account, the full trap is modeled and numerically optimized by changing the beam waists and powers until the derived trap frequencies and the aspect ratio agree to the measured values. The result is a small correction to the previous values and is given in the last column of table 4.2. The specified error is a very rough estimation: Assuming a 2 % error on the measured trap frequencies and the aspect ratio, these values are randomly varied before they are fed into the numeric optimization, which is repeated 50 times and the estimates are calculated as standard deviation of the optimized parameters.

Trap Characterization from Density via Equation of State The previous approaches assume that the beams have a perfect Gaussian profile. But the trap potential can also be calibrated without that assumption by comparing the in-trap density distribution of a gas with a known equation of state. At unitarity the equation of state has been measured [61] and by preparing the gas just at the phase transition, temperature and chemical potential of the gas are also known relative to the local Fermi energy at the trap center. Ref. [61] quotes a critical temperature of $T_{\mathrm{c}}/T_{\mathrm{F}} = 0.167(13)$ and a chemical potential very close to the transition of $\mu/E_{\mathrm{F}} = 0.42(1)$.

This procedure requires access to the 3D density of the gas, which is determined via the inverse Abel transformation, as described in section 4.3.1. To reduce noise, the optical density is first averaged over elliptical bins, similar as in section 4.4.4. The last two steps assume that the trap potential has a symmetry which results in elliptic equipotential lines in the $x'y'$-plane over the considered volume.

Figure 4.18 shows the density of a unitary gas prepared just at the superfluid transition, as confirmed with the rapid ramp technique. Anticipating a relative smooth relationship between

the logarithm of the density and the potential, the data is shown on a logarithmic scale against the squared radius and a cubic spline is fitted to the data to reduce fluctuations from noise. The

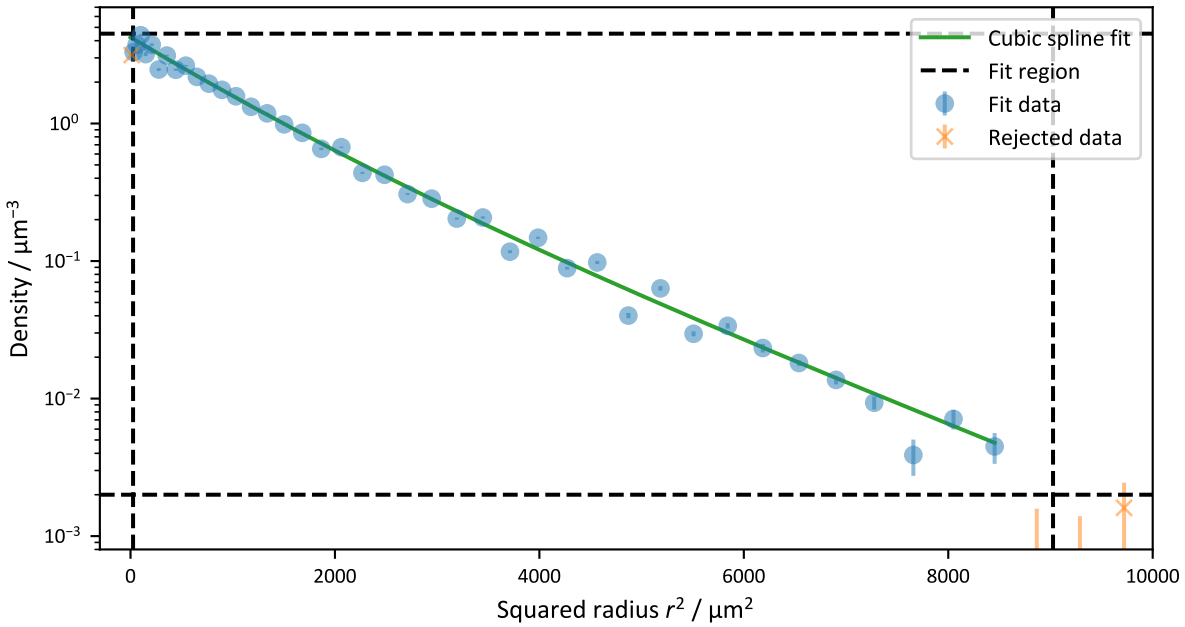

Figure 4.18: Density versus radius squared a spline is fitted to the data to extrapolate towards the trap center at $r = 0$ and is used as a low noise description of the density from which the potential will be calculated via the unitary equation of state. The fit region is chosen to rejected noisy data at large radius, where the density becomes too low and close to the trap center, where the density becomes unreliable due to the properties of the inverse Abel transformation. The quadratic scale on the x-axis and logarithmic scale on the y-axis is chosen to achieve a relationship between the two quantities which is as trivial as possible and the spline fit is also performed to the data in this representation.

spline is used to extrapolate the density towards the trap center, which gives $n_{\mathrm{center}} \approx 4.24\,\mu\mathrm{m}^{-3}$ and translates to a local Fermi energy at the trap center of $E_{\mathrm{F}} \approx k_{\mathrm{B}} \times 1.60\,\mu\mathrm{K}$ a temperature of $T_{\mathrm{c}} \approx 0.27\,\mu\mathrm{K}$ and a chemical potential of $\mu_{\mathrm{c}} \approx k_{\mathrm{B}} \times 0.67\,\mu\mathrm{K}$.

At first it is interesting to see how well the thermometry works for the current model of the trap. For this purpose, for several small intervals of the potential, a fit to the equation of state is performed, which results in a value for temperature and global chemical potential. Additionally, the virial expansion at unitarity up to second and up to third order is used. The latter is our standard thermometry method for different magnetic fields where the full equation of state is not known.

The results are presented in figure 4.19. The temperature from the unitary fit does not deviate too much from the expected temperature, but is underestimated in the trap center and far outside, whereas it is overestimated at intermediate potential. Starting at a potential of about $k_{\mathrm{B}} \times 0.8\,\mu\mathrm{K}$ the results from the virial fits becomes consistent with the fit to the unitary equation of state, which demonstrates that we can reach the region where the thermometry only based on the virial expansion becomes reliable. Nevertheless, one has to state clearly that at potential values above $1.1\,\mu\mathrm{K}$ the resulting temperature decreases steadily and it becomes ambiguous which temperature values are reliable. Similarly, for the chemical potential, the results from the unitary fit agree roughly to the expected chemical potential, but for large potential values the curve bends upwards and it becomes ambiguous which values should be chosen.

With known temperature and global chemical potential, the equation of state dictates a strict relationship between density and local chemical potential, which can be used to correct

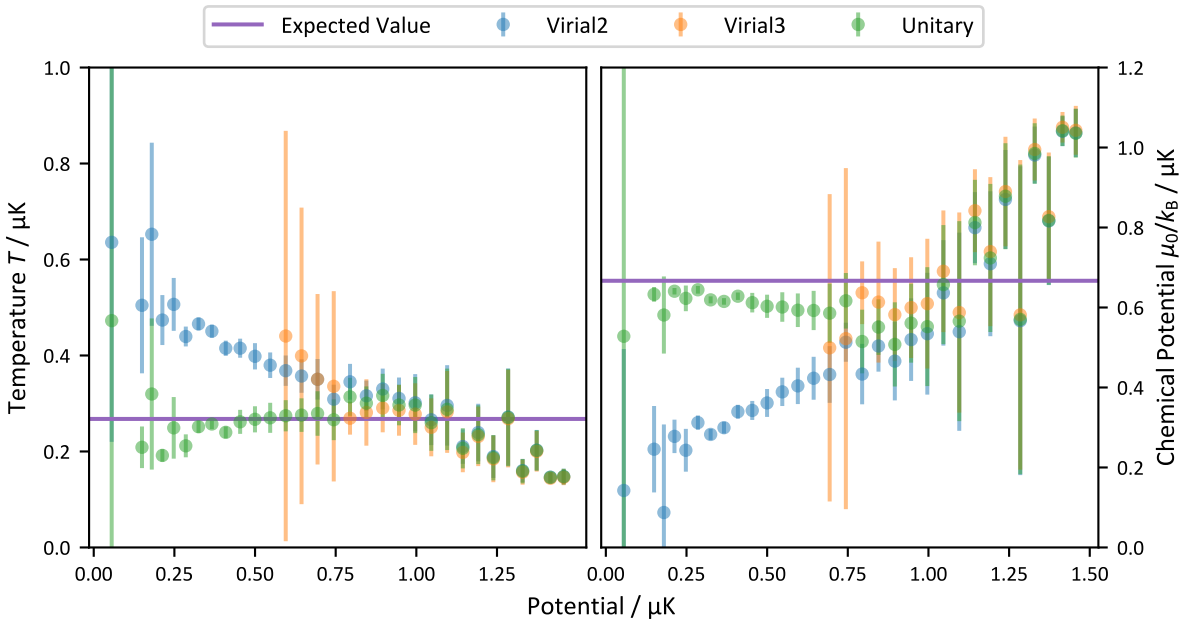

Figure 4.19: Thermometry result for a unitary gas at the superfluid transition using the current uncorrected trap model The thermometry is performed by fitting the data to seven consecutive datapoints in order to probe the reliability of the potential locally. The data is fitted to second and third order virial expansion and to the unitary equation of state, only the last one is reliable towards the trap center but the virial fits agree above a certain potential. The expected value for temperature and chemical potential is known because the gas is prepared just at the superfluid transition so that temperature and chemical potential can be deduced from the central density.

the potential. We use the unitary equation of state by interpolating the data from ref. [61] and extend it towards low densities via the virial expansion. The inverse function, which would calculate local chemical potential from density at a given temperature, is not calculated explicitly but solved numerically. Then from the local density approximation $\mu(r) = \mu_0 - V(r)$ the potential $V(r)$ is reconstructed, which yields the corrected trap potential, which is shown in figure 4.20 and compared to the previous model of the trap.

Finally, as a consistency check, the same procedure which generated figure 4.19 is repeated on the new, corrected trapping potential, which results in figure 4.21. Note that the precise agreement between expected temperature and chemical potential with the fit to the unitary equation of state is not surprising, but is by design of the reconstruction process of the corrected potential. A comparison between the thermometry based on the unitary equation of state and the thermometry based on the virial expansion demonstrates how the latter result converges to the expected value above a certain potential. This is also the case for the chemical potential, although the results become quite noisy at large potential values. However, it is natural that the chemical potential, which fixes the atom number of the gas, cannot be determined very precisely far from the center of the trap.

Note that by using the equation of state at unitarity, further measurements will by construction get a consistent temperature to the known transition temperature at unitarity. One can overcome this by using the equation of state of an ideal gas, which will be implemented soon.

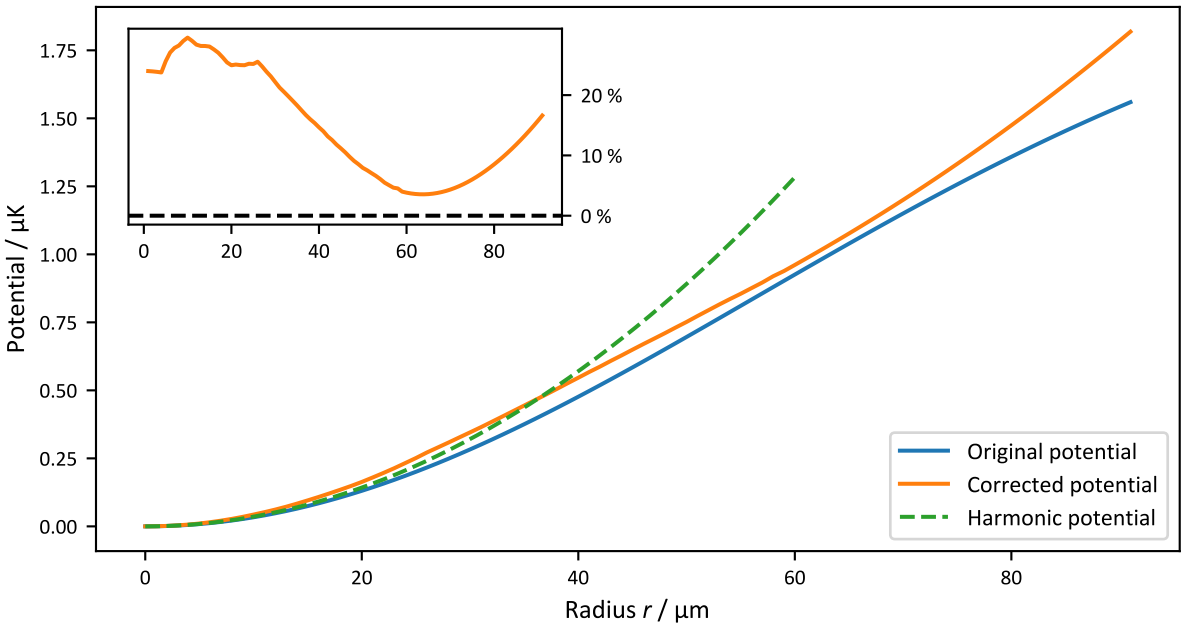

Figure 4.20: Corrected trap potential in comparison to previous trap model and harmonic potential The inset shows the relative deviation of the corrected trap potential from the original trap model on the y-axis. It uses the same x-axis as the main plot.

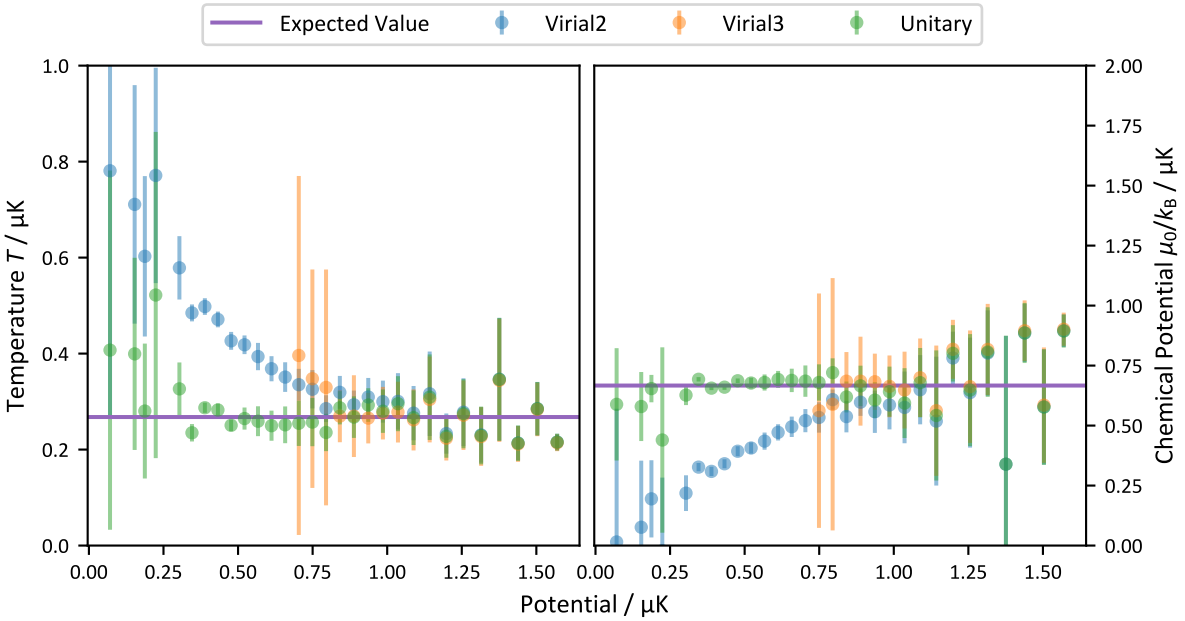

Figure 4.21: Thermometry result for a unitary gas at the superfluid transition based on the corrected trap potential This is meant as a check for the successful reconstruction of the potential, as the good agreement to the expected temperature and chemical potential is by design of the reconstruction process of the corrected potential.

4.6 Machine Learning

In chapter 5 and chapter 6 machine learning tools are used to extract data from absorption images. The first use case is to determine the condensate fraction of an atomic sample from time-of-flight images, which requires training on example images for which the condensate fraction is already known. The second use case is to find a low dimensional representation of time-of-flight images over a wide parameter space, which can be used to determine a phase transition. The techniques are already described in detail in ref. [98], so I will only briefly describe the principles on which they are based on.

4.6.1 Overview

There are many different tasks for which machine learning is used, like classification, regression or denoising and there are many different approaches for machine learning, like principle component analysis, support vector machines or decision trees [150].

Here we focus on deep learning, which is based on the idea that very complicated functions can be reduced to multiple sequential layers, which each implement a very simple nonlinear function [151]. This is typically realized with artificial neural networks, composed of artificial neurons, which resemble their biological counterpart to a certain degree, because they have many input signals, which are weighted and lead in a nonlinear way to an output signal [152][5].

Early work on neural networks includes a first mathematical description in 1943 [153] and the implementation of an electric neural network with adjustable weights in 1957 [154]. In 1969 it was proven that a single layer of neurons is not sufficient to learn certain functions [155], like the XOR function. However, this limitation can be overcome by using multiple layers. Later backpropagation was developed, an efficient learning algorithm for the adjustment of the parameters of a neural network [156]. In 2012 it was demonstrated that deep neural network are a competitive solution for image classification [157]. See refs. [152, 158, 159] for a more detailed historical overview.

4.6.2 Neural Networks

A neural network is a network of neurons and can have various geometries. Here we only consider feedforward neural networks, in which the neurons are grouped into several layers, starting with the input layer, followed by a certain number of "hidden" layers and finally the output layer.

Neuron

A neuron has several inputs x_i and as trainable parameters it has a weight w_i for each input and a bias b. The first operation of the neuron is a weighted sum of the input values plus the bias. The weighted sum can also be interpreted as a scalar product of the input vector $\boldsymbol{x}$ and the vector of the weights $\boldsymbol{w}$ [158]

$$z = \boldsymbol{w} \cdot \boldsymbol{x} + b\,. \tag{4.131}$$

In a second step, the output (or "activation") of the neuron is calculated by applying a nonlinear activation function ϕ

$$a = \phi(z)\,. \tag{4.132}$$

Typical activation functions are tanh, a sigmoid or the so called Rectified Linear Unit (ReLU) and are displayed in figure 4.22. Intuitively, one gets a large output if the weighted sum over the inputs is larger than the threshold $-b$, i.e. if $z > 0$.

[5] In the following only artificial neural networks and neurons are relevant and the term "artificial" is omitted.

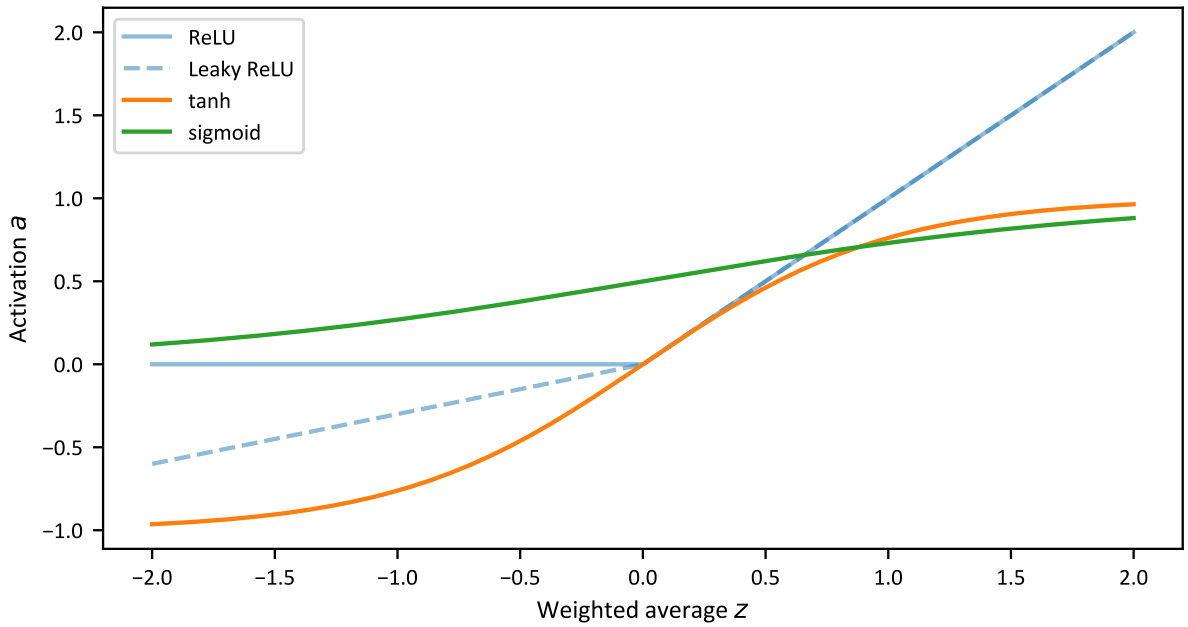

Figure 4.22: Typical activation functions of a neuron

Dense Layer

A dense or fully connected layer consists of a number of neurons, whose inputs are connected to each output of the previous layer. As an extension of the single neuron, the weights can be represented as a matrix W and the inputs and biases as a vector $\boldsymbol{x}$ and $\boldsymbol{b}$, respectively. Then the weighted sum is given as $\boldsymbol{z} = W \cdot \boldsymbol{x} + \boldsymbol{b}$ and the output of the whole layer can be written as

$$\boldsymbol{a} = \phi(\boldsymbol{z}) = \phi(W \cdot \boldsymbol{x} + \boldsymbol{b})\,. \tag{4.133}$$

The activation function is applied element-wise.

Note that a simple neural network can already be assembled entirely by connecting a few dense layers in series.

Convolutional Layer

A convolutional layer is an alternative to fully connected layers and is often used for image data, because it can implement various image recognition tasks, for example Gaussian filtering, edge detection or detection of other features.

In practice, for two-dimensional image data, a third dimension is introduced, which initially might be used for different color channels of the input data, but within the network it is used for different filters, which is explained below.

The calculation is based on the convolution of the input data $I_{i,j,k}$ with a typically small kernel $K_{m,n,k}$ [150]

$$S_{i,j} = \sum_{m,n,k} I_{i-m,j-n,k} K_{m,n,k}\,. \tag{4.134}$$

Usually, a convolutional layer has several kernels, which are also called the “filters”. For each filter the layer produces a two-dimensional output, so that the filters correspond to the third dimension. After the convolution, a bias is added and a nonlinear activation function is applied, similarly as for dense layers.

Convolutional layers are often combined with pooling layers, which aggregate the results over a small region. For example, by choosing the maximum activation of the region ("max pooling"). This can cause invariance to small translations of input values.

Since the weights of the kernel are reused for different input pixels, the number of parameters is greatly reduced. The pooling layers also reduce the output size of the layer and possibly the size of the subsequent layers. Sometimes the convolution is not calculated over all indices of the input image, but a "stride" s is used, which means that only every s-th index is used.

4.6.3 Supervised Learning

For the learning process one defines a loss function, which is minimized by adjusting the parameters of the model. The most straightforward strategy to train a neural network is to use supervised learning. It requires a training set, which consists of an input vector and a vector of the desired outputs $\boldsymbol{\theta}$, which are called the labels. Then the loss function is calculated by comparing the output $\boldsymbol{y}$ of the neural network with the labels. A typical loss function, which is suitable for function approximations, is the mean squared error

$$J_{\text{mse}} = \frac{1}{N} \left| \boldsymbol{y} - \boldsymbol{\theta} \right|^2 , \tag{4.135}$$

where N is the number of datapoints in the training set.

Stochastic Gradient Descent A neural network consists of linear matrix operations and nonlinear activation functions, which are all differentiable[6]. That means that the whole function, which the neural network represents, is also differentiable by its parameters, i.e. its weights and biases. If this can be efficiently calculated, the training process can be realized using a gradient descent technique. Note that typically the gradient is not calculated over the whole training data, which would be challenging for large datasets. Instead, for each training step the gradient is calculated only over a randomly selected "mini-batch", i.e. a subset of the training data and the algorithm is then called "stochastic gradient descent" [158].

In principle, one expects that in the high dimensional parameter space several local minima are possible which work similarly well. Therefore, one does not necessarily need to worry about finding the global optimum for the parameters.

Backpropagation In order to calculate the gradient of the loss function, one can use backpropagation. It is an algorithm which starts at the output of the network and constructs the gradient by successively applying the chain rule of differentiation until the beginning of the network is reached. I want to present this procedure using the physicist's way of handling partial differentials, to keep the notation more simple and to focus on the iterative nature of backpropagation.

We consider a neural network consisting of L dense layers connected in series. For each layer, described by index $l \in \{1, \dots, L\}$, weighted sum, output, weight matrix and bias vector are denoted as $\boldsymbol{z}^{(l)}$, $\boldsymbol{a}^{(l)}$, $W^{(l)}$, $\boldsymbol{b}^{(l)}$, respectively.

The loss J of the network depends directly on the activation of the last layer of the network

$$\mathrm{d}J = \frac{\partial J}{\partial \boldsymbol{a}^{(L)}} \cdot \mathrm{d}\boldsymbol{a}^{(L)} . \tag{4.136}$$

[6] Strictly speaking, semi-differentiable if the ReLU activation function is used, which is not a problem in practice and e.g. $\phi'_{\text{ReLU}}(0) := 0$ is used.

The differential of the output of a layer is derived from the forward-propagation of the network, given in equation (4.133) for a dense layer,

$$\mathrm{d}\boldsymbol{a}^{(l)} = \frac{\partial \boldsymbol{a}^{(l)}}{\partial \boldsymbol{z}^{(l)}} \cdot \left[\mathrm{d}W^{(l)} \cdot \boldsymbol{a}^{(l-1)} + \mathrm{d}\boldsymbol{b}^{(l)} + W^{(l)} \cdot \mathrm{d}\boldsymbol{a}^{(l-1)}\right] . \tag{4.137}$$

This result allows the calculation of further differentials. Most interestingly, the partial differential of the loss with respect to the activation of a layer with index $l-1$ can be expressed by values connected to the succeeding layer with index l

$$\frac{\partial J}{\partial \boldsymbol{a}^{(l-1)}} = \frac{\partial J}{\partial \boldsymbol{a}^{(l)}} \cdot \frac{\partial \boldsymbol{a}^{(l)}}{\partial \boldsymbol{a}^{(l-1)}} = \frac{\partial J}{\partial \boldsymbol{a}^{(l)}} \cdot \left(\frac{\partial \boldsymbol{a}^{(l)}}{\partial \boldsymbol{z}^{(l)}} \cdot W^{(l)}\right) , \tag{4.138}$$

which is essentially the multiplication of the weight matrix from the right.

This reveals some similarity between the normal operation of a neural network, the forward-propagation, which involves left side multiplication of the weight matrices in ascending order of the layer index, and the back-propagation, because it involve right side multiplication of the matrices in descending order of the layer index.

When these partial differentials of the activations of the layers are calculated, equation (4.137) implies the partial differentials for the biases

$$\frac{\partial J}{\partial \boldsymbol{b}^{(l)}} = \frac{\partial J}{\partial \boldsymbol{a}^{(l)}} \cdot \frac{\partial \boldsymbol{a}^{(l)}}{\partial \boldsymbol{z}^{(l)}} \tag{4.139}$$

and weights

$$\frac{\partial J}{\partial W^{(l)}} = \frac{\partial J}{\partial \boldsymbol{a}^{(l)}} \cdot \frac{\partial \boldsymbol{a}^{(l)}}{\partial \boldsymbol{z}^{(l)}} \cdot dW^{(l)} \cdot \boldsymbol{a}^{(l-1)} , \tag{4.140}$$

from which the gradient can directly be constructed.

Example: Neural network as Function Approximator

As an example which demonstrates how a neural network can approximate functions, a small neural network is trained to approximate the function $f(x) = \sin(2\pi x)\exp(-2x)$. As a training set 200 datapoints are sampled, with 20 % noise on the labels. Figure 4.23 shows how the trained neural network approximates the function in comparison to a polynomial fit.

In this simple example, the neural network does not have an advantage over the polynomial fit, but it can more easily be extended to more complicated multidimensional data.

4.6.4 Unsupervised Learning

It is not always possible to produce high quality labels, which are required for supervised learning [150]. Unsupervised learning stands for alternative approaches, which do not require labels.

One strategy is the use of an autoencoder. The idea is to use the input vectors of the training themselves as labels. Consequently, the neural network is trained to learn the identity function. This means that the neural network has to pass the information from the input vector through the whole network, which is trivial if enough neurons are available. But if one layer of the neural network is reduced to only a few neurons, creating a bottleneck, the network is forced to find a compressed representation of the input data.

By analyzing the representation of the data at the bottleneck, it is possible to learn about clustering of the data or hidden features.

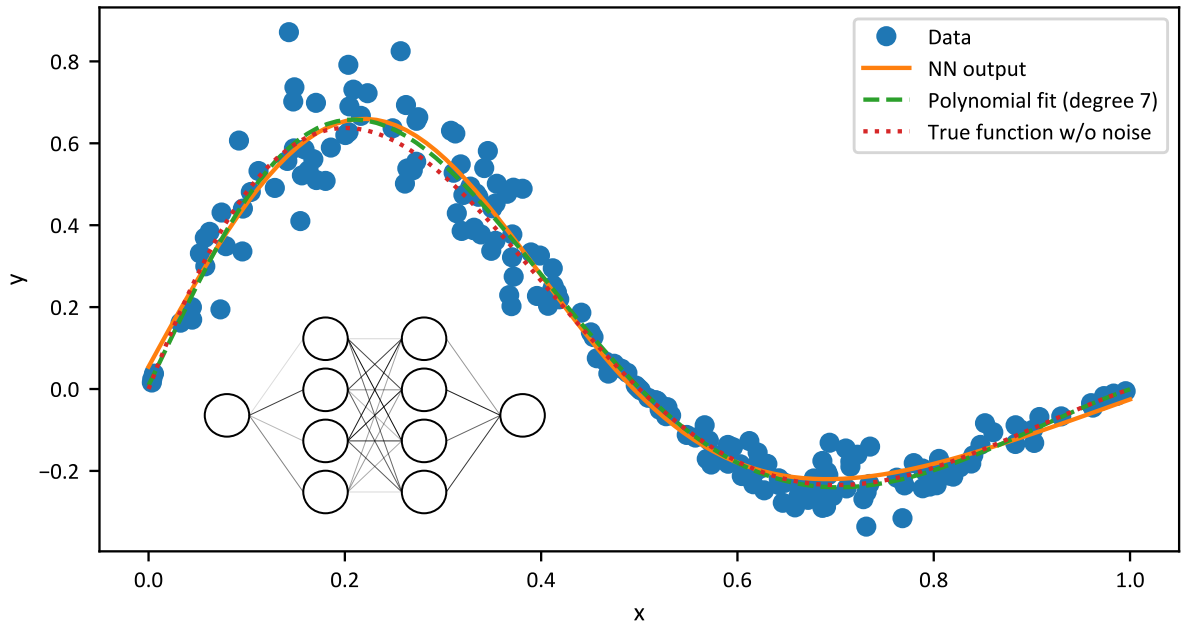

Figure 4.23: Function approximation with a neural network based on noisy training data The result is compared with a polynomial fit and the true function, which was used to generate the data is also shown. In the lower left an illustration of the employed neural network is shown. It consists of two hidden layers with tanh activation functions and four neurons each. The line strength is random and does not match the weights of the trained model.

5 Phase Diagram of BEC-BCS Crossover

This chapter presents an investigation of the phase diagram of a balanced strongly interacting Fermi gas in the BEC-BCS crossover by determining the critical temperature of the superfluid transition at different interactions. The detection of superfluidity is based on the rapid ramp technique. Additionally, it is detected from simple time-of-flight images by means of supervised and unsupervised machine learning, where the latter approach provides a completely independent measurement from the rapid ramp. Finally, the thermometry is explained and the difference of referencing the temperature to the Fermi energy of a harmonic trap or the local Fermi energy within LDA is worked out. This allows a meaningful comparison with theory and underlines shortcomings of previous measurements of the phase transition.

The detection of superfluidity described here has already been covered in ref. [98], but since then the thermometry and determination of Fermi energy have been improved and a better understanding of the influence of the trap potential has been reached.

5.1 Overview

Theoretical Predictions The most basic theoretical results for the critical temperature of the superfluid phase transition have already been discussed in section 2.4.3 for the homogeneous gas and in section 2.6.3 for the harmonically trapped gas. The former are presented together with more recent results in figure 5.1. Far on the BCS side, the critical temperature decays exponentially with the interaction parameter. The prefactor is known from a beyond mean-field calculation, the GMB correction [48]. On the BEC side, the value for an ideal gas $T_c/T_F \approx 21.8\,\%$ can be calculated from Bose statistics. At weak repulsive interactions, mean-field theory cannot predict a change of the critical temperature, but due to critical fluctuations near the phase transition an increase of the critical temperature with increasing interaction strength (i.e. decreasing $1/k_F a$) is expected [52]. Consequently, assuming a continuous curve of the critical temperature, the mathematical extreme value theorem implies that a maximum value of the critical temperature exists somewhere in the strongly interacting regime, because the increasing critical temperature must smoothly connect to the lower values on the BCS side. However, there is no agreement in the literature about the exact position of that maximum or its prominence.

In a harmonic trap deviations from the homogeneous critical temperature are expected. Far on the BEC side, the critical temperature approaches 52 % of the Fermi temperature (see section 2.6.3) instead of 21.8 % for the homogeneous gas. The upward trend of the critical temperature for increasing repulsive interaction, which is expected for the homogeneous gas, is suppressed by the trapping potential. Instead, there is a downward shift of the critical temperature due to the reduced central density in the trap center caused by repulsive interactions [52]. The BCS side is less affected by trap effects because the central density does barely change due to the Pauli exclusion principle.

Previous Measurements The phase transition has previously been measured based on the rapid ramp technique in ^{6}Li [29, 56] and ^{40}K [28] for a range of interactions. Additionally, the transition temperature at unitarity has been measured several times with various methods. The

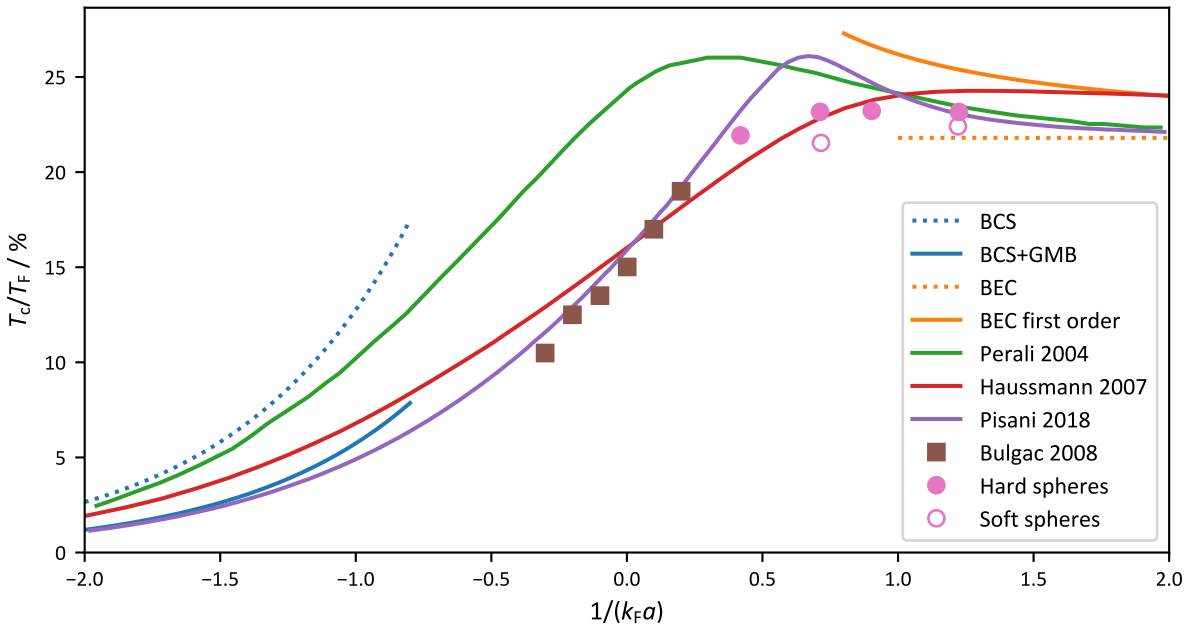

Figure 5.1: Theoretical predictions of the critical temperature for a homogeneous gas in the BEC-BCS crossover Shown are BCS theory [4] with GMB correction [48] on the BCS side, as well as the non-interacting BEC result and first order interaction correction [51, 160] on the BEC side. The prediction from ref. [47] ("Perali 2004") seems to overestimate the critical temperature because it converges to the BCS result rather than the GMB correction. Also shown are the prediction from ref. [53] ("Haussmann 2007") and the more recent result from ref. [54] ("Pisani 2018"). The latter agrees well with Monte-Carlo data from ref. [55] ("Bulgac 2008"), but predicts a more pronounced maximum as e.g. the hard and soft sphere calculation of ref. [161].

results are compared in figure 5.2. Note that in contrast to the theoretical results shown before, the experimental measurements are performed with a trapped gas and the critical temperature is referenced to the Fermi energy of a harmonic trap. For this case, theory predicts different values for the reduced critical temperature T_c/T_F, one reason being that the central density of the trap increases towards the BEC side, an effect which is not captured in the definition of the Fermi energy of a harmonically trapped gas.

For comparison, the experimental data is shown together with the theoretical predictions from refs. [47, 138] and the BCS prediction with GMB correction for a homogeneous gas. Note that although the corrected BCS prediction is for a homogeneous gas, it should also describe the harmonically trapped gas far on the BCS side appropriately because in that regime compression effects are suppressed by Pauli blocking. This indicates that the predictions from refs. [47, 138] are probably slightly overestimated, at least towards the BCS side.

The agreement on the BCS side between the early rapid ramp measurements (refs. [28, 29]) is quite reasonable and they also agree to the more recent measurements at unitarity (refs. [56, 60, 61]). But in the region from unitarity towards BEC side the behavior of the critical temperature deviates strongly from the trend predicted by theory.

Signatures of Superfluidity In principle, there are many experimental signatures which can indicate the presence of a superfluid, as is discussed in ref. [4].

For example, one can directly exploit the property of a superfluid that excitations are only possible above a critical velocity by stirring the gas with a laser beam, which has been demonstrated for Bose gases [162], Fermi gases [163] and has been extended by using a moving optical lattice [164].

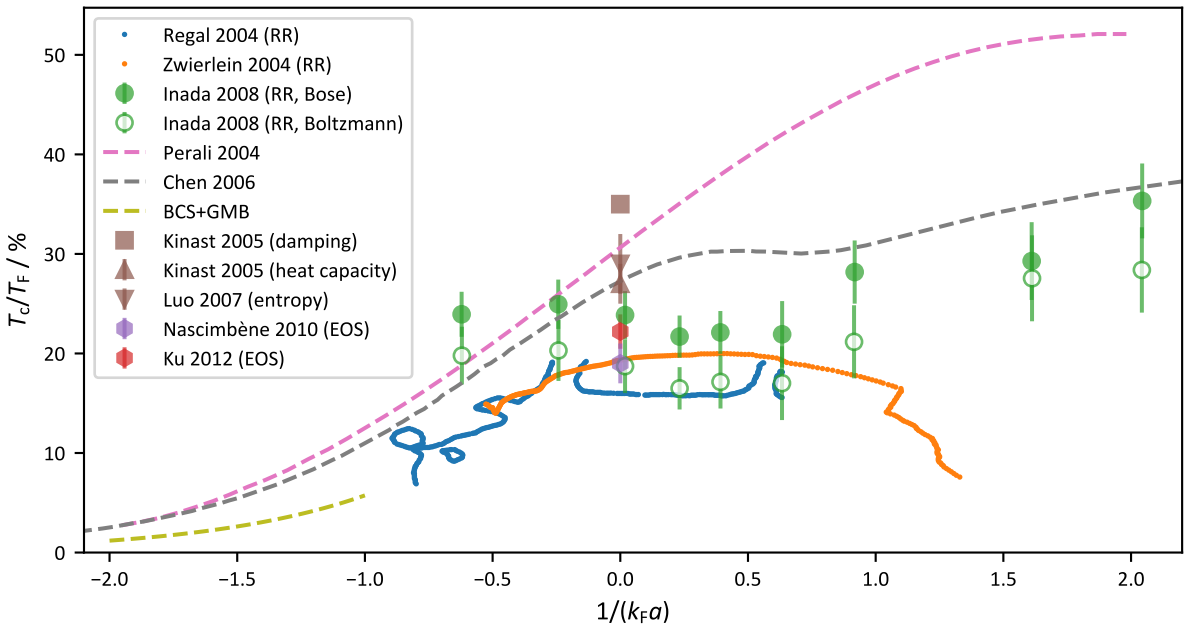

Figure 5.2: Comparison of measurements of the critical temperature of the superfluid transition in trapped gases For the early measurements based on the rapid ramp ("Zwierlein 2004" [29] and "Regal 2004" [28]) the lowest contour of the measured condensate fraction is shown and the x-axis is converted to the interaction parameter $1/(k_F a)$, using the provided information about magnetic field and Fermi energy. Ref. [56] ("Inada 2008") uses a more advanced thermometry, which either assumes a Bose or a Boltzmann gas (Two points are omitted, they measure about $T_c/T_F = 0.4(1)$ at $1/k_F a \approx 3.4$). These results are compared with measurements at unitarity, which detect the phase transition by finding kinks in the heat capacity or damping rate of the monopole mode [57, 58] ("Kinast 2005") or in the entropy [59] ("Luo 2007"). Measurements of the homogeneous equation-of-state within LDA of a trapped unitary gas also provide a value for the critical temperature ("Ku 2012" [61] and "Nascimbène 2010" [60]), which can be specified relative to the Fermi energy of the harmonically trapped gas by integration of the found equation-of-state over the trap potential as demonstrated in the latter reference. For comparison theoretical results for a harmonically trapped gas are shown ("Perali 2004" [47] and "Chen 2006" [138]).

Another property of a superfluid is the occurrence of long-lived vortices. Whereas vortices are in principle also possible in a normal fluid, the quantization of vortices [165] and occurrence of vortex lattices [166] can be attributed to superfluidity and has been exploited to detect the superfluid state throughout the BEC-BCS crossover [167].

The phase transition between normal and superfluid gas also leaves traces in the thermodynamic variables. For example, a kink in heat-capacity [58] and entropy [140] has been observed and similar behavior was seen when measuring the unitary equation-of-state [60, 61].

An obvious signature of superfluidity on the BEC side is the emergence of a bimodal distribution of pair momentum, which can be measured in time-of-flight. On the BCS side this is not directly possible because the Cooper pairs do not survive time-of-flight, but the bimodal distribution can still be recovered by first projecting the Cooper pairs onto molecules with the rapid ramp technique (see section 4.2), which has been applied in many experiments and has become the standard method to detect superfluidity in the BEC-BCS crossover.

But even without the application of a rapid ramp, momentum and density distributions across the BEC-BCS crossover are influenced by superfluidity. For example, a weakly interacting Bose gas has a different size associated with the condensate than for the thermal part of the cloud, and even for a unitary gas deviations from a Thomas-Fermi profile have been observed below

the critical temperature [4].

Neural Networks used for Detection of Phase Transitions Recently, machine learning techniques have been applied to problems in physics quite successfully and have also been used to characterize quantum phase transitions [168].

Based on simulated training data, it has been shown that neural networks trained via supervised learning can be used to detect the phase transition of the Ising model [63].

Additionally, unsupervised machine learning techniques have been developed to distinguish phase transitions, for example based on principle component analysis [169], but also using more versatile (non-linear) neural networks. For example, a classification task will yield a higher "confidence" if it was trained on labels matching to the phase transition, which allows to search for appropriate labels without knowing them beforehand [170, 171].

Unsupervised learning has also been applied to experimental data to find the phase transitions of the topological Haldane model [64].

Our Approach The detection of superfluidity is based on two different measurements. The first measurement is the application of the rapid ramp technique to extract the condensate fraction as explained in section 4.2. The second measurement consists of taking simple time-of-flight images, for which the exact signature of superfluidity is not known, but which can be analyzed with machine learning techniques. Here, the first approach is based on supervised machine learning for which a neural network is trained to associate time-of-flight images to condensate fraction values, determined by the rapid ramp technique at certain interactions and heating times. After training the network has to generalize to other interactions. The second approach is based on unsupervised machine learning and is completely decoupled from the rapid ramp technique because it only uses time-of-flight data to find a low-dimensional representation of the data. The idea is that a phase transition could influence how the data is arranged in that representation.

Equally important to the detection of the phase transition is a reliable thermometry, which is challenging for strongly interacting gases, as discussed in section 4.4. Here it is based on the density distribution at the edge of the cloud, but it is necessary to go beyond the approximation of the Boltzmann gas by including higher terms of a virial expansion in order to take quantum statistics and interaction effects into account.

Finally, the determined critical temperature is only meaningful compared to another temperature scale of the system, which is typically provided by the Fermi temperature. At the same time the Fermi momentum is needed to specify the interaction parameter $1/(k_\mathrm{F}a)$. For a harmonically trapped gas, the Fermi energy can simply be calculated from the atom number and trap frequencies with equation (2.70). Another method is to measure the density in the trap center which gives access to the Fermi energy calculated within LDA. Surprisingly, this leads to two different results for the Fermi energy because the former does not take into account that the density distribution of the gas is changed by interaction effects. The latter allows the comparison to the homogeneous gas for which a wider variety of theoretical results exists. Therefore, both energy scales are determined by taking in-trap images, which allows for the reconstruction of the central density.

5.2 Experimental Realization

A Fermi gas mixture of the lowest two ^{6}Li hyperfine states $|1\rangle$ and $|2\rangle$ is prepared at degenerate temperatures, as described in section 3.2.

Probing the phase diagram of the BEC-BCS crossover requires tuning of interaction and temperature. At first the interaction is set via the broad Feshbach resonance (see section 2.2.1) with an adiabatic sweep of the magnetic field. The sweep changes the magnetic field linearly and has a duration of 200 ms. Note that the initial temperature of the sample is also changed by the magnetic field sweep because the total energy of the gas changes according to the adiabatic sweep theorem of the contact, as discussed in section 2.5.4.

Next, the temperature is (further) varied by employing trap release heating, which has also been used in other experimental studies [58, 146]. The idea is to switch off the trap and to let the cloud expand for a variable heating time, until finally, the trap is switched back on. The process results in an increased potential energy, which leads to a higher temperature after a subsequent thermalization time. For this we fully switch off the vertical dipole beam, but keep the horizontal beam at half power to reduce atom loss. A thermalization time of 50 ms is chosen, which corresponds to several trap periods.

Finally, a measurement is performed which consist of measuring the optical density of the sample either in-trap, after 5 ms time-of-flight or after a rapid ramp. The in-trap measurement is used to extract temperature and Fermi energy, whereas time-of-flight and rapid ramp data are used for the detection of the phase transition. Since the measurements are destructive, the investigation relies on the ability of the experiment to prepare atomic samples with similar atom number and temperature with good repeatability. To reduce the effect of slow experimental drifts, different kinds of measurements at the same experimental parameters are taken in direct succession, so that they refer to very similar atomic clouds. The point of the phase transition will be referenced to a critical heating time, after which the superfluid vanishes. Therefore, the parameters of the measurement are generally varied randomly so that slow experimental drifts only cause statistical errors on the critical heating time.

5.2.1 Datasets

This investigation is based on two different datasets, with different kinds of data, as already mentioned: Rapid ramp measurements yield the condensate fraction, which is used as signature of superfluidity in section 5.3, but also as training-labels for the supervised machine learning in section 5.4. Time-of-flight images are the basis for the machine learning based detection of superfluidity in section 5.4 and section 5.5. Additionally, in-trap images are taken, which are used for the thermometry and extraction of the central density of the cloud in section 5.6 and section 5.7.

Machine Learning Dataset This dataset features time-of-flight images for all considered magnetic fields and heating times. Rapid ramp data for the training-labels and in-trap data for the thermometry are only taken for a subset of the magnetic fields. The main focus of this dataset is the detection of superfluidity with machine learning techniques. The central density cannot be determined for this dataset, because only low imaging intensity was used for the in-trap images, which does not produce a proper signal for the cloud center. For this investigation, the final trap frequencies are $\boldsymbol{\nu}_{\mathrm{trap}} = (168, 166, 238)$ Hz and the final atom number is typically 3×10^5 to 5×10^5, corresponding to Fermi energies of 1.1 µK to 1.3 µK.

Thermometry Dataset This dataset features rapid ramp data and in-trap images for all considered fields. The latter is taken at high imaging intensity to allow for the extraction of the central density. The main focus of this dataset is the thermometry and measurement of the central density, while time-of-flight data for the machine learning approaches was not taken.

The final trap uses exactly the same parameters as for the trap characterization in section 4.5, therefore the trap frequencies are $\boldsymbol{\nu}_{\mathrm{trap}} = (159(1), 196.8(2), 256(1))$ Hz. Since the previous

machine learning dataset was taken, the alignment of the dipole beams was reoptimized. Also the electric noise of the regulation was reduced, which caused a small change in the power set-points. This has slightly altered the trap geometry compared to the previous dataset. The atom number varies, mainly due to heating losses, between roughly 4×10^5 to 8×10^5 atoms, corresponding to Fermi energies of around 1.3 µK to 1.6 µK, which are evaluated for each measurement individually.

Atom Loss on BEC Side For both datasets, the atom number was reduced drastically towards the BEC side. This is not an artifact from imaging, because it was confirmed that the atom number is still lower after ramping back to higher magnetic fields. Also, the measured lifetime of the atoms is not lower on the BEC side, which means that the atom loss happens dynamically during the relatively slow magnetic field ramp.

The onset of this atom loss differs slightly between the two datasets, see figure 5.3. In the end it will turn out, that for this region of large atom losses the results deviate strongly from theoretical predictions. To account for the possibility that the measurement is disturbed by the atom losses, this region will be handled separately in the following. Reasons for the deviations could be, for example, a worse thermalization after the atom losses or a different imaging efficiency, which has been reported for the BEC side [129].

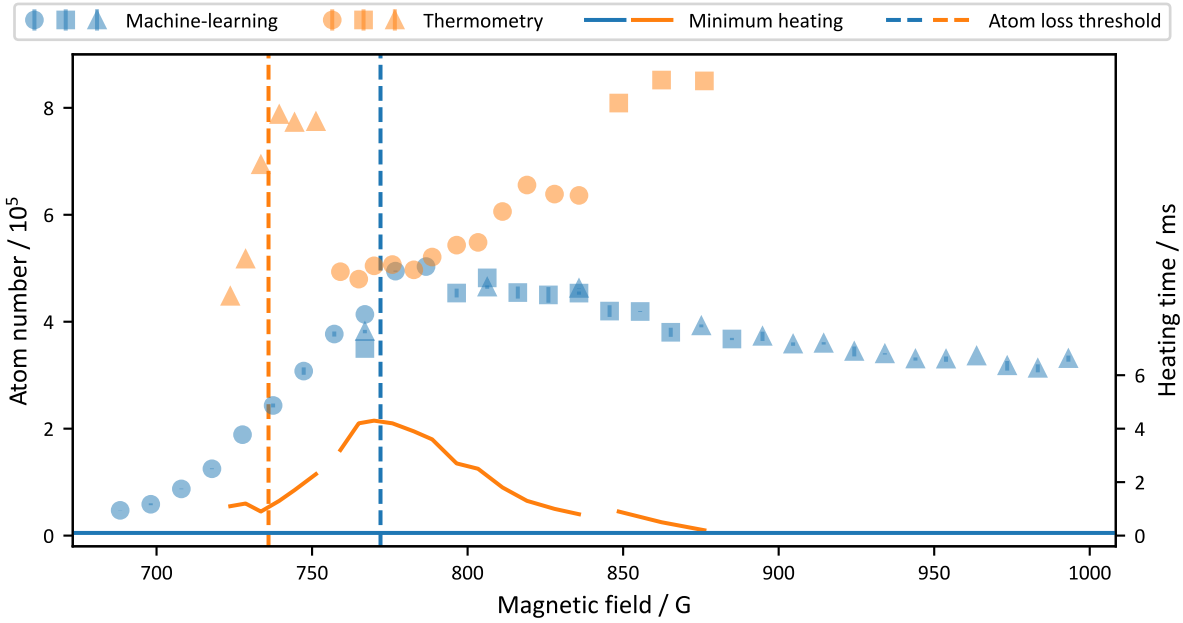

Figure 5.3: Atom number for *machine learning* and *thermometry* dataset Atom numbers are specified for the minimum heating time at each field, which is always 0.1 ms for the *machine learning* dataset, but varies for the *thermometry* dataset. Different markers indicate different measurement days. For the *thermometry* dataset the atom number changed for different measurement days, which is acceptable. Atom number changes during the same day can be explained by different minimum heating times. Towards the BEC side there is a strong reduction of the atom number, but the threshold magnetic field slightly differs for the two datasets.

5.3 Detection of Phase Transition via Rapid Ramp

This section briefly describes the conventional method to detect superfluidity based on the rapid ramp explained in section 4.2, which is similar to previous investigations [28, 29, 56].

However, a decisive difference lies in the more careful thermometry and determination of the energy scale from the central density, which is demonstrated later in section 5.6 and section 5.7. The measurements are based on the *thermometry* dataset defined in section 5.2.1.

5.3.1 Determine Critical Heating Time

The condensate fraction is determined via the rapid ramp for different heating times at various magnetic fields, as presented in figure 5.4. The heating time is only varied in a small region around the transition, which reduces the amount of data which is required. In this region the condensate fraction drops very linearly with heating time τ until it reaches zero. This enables the extraction of the transition point, characterized by the critical heating time τ_c, using a fit to the empiric piecewise linear-constant function

$$f(\tau) = \begin{cases} -\Gamma_{\text{heating}}(\tau - \tau_c) & \text{if } \tau < \tau_c, \\ 0 & \text{otherwise,} \end{cases} \tag{5.141}$$

with a second fit parameter Γ_{heating} describing the depletion rate of the condensate fraction during heating. The determined values for τ_c as a function of the magnetic field, also displayed in figure 5.4, already conclude the measurement of the phase transition given in experimental units. However, they still have to be referenced to temperature and Fermi energy, which will be done in section 5.6 and section 5.7.

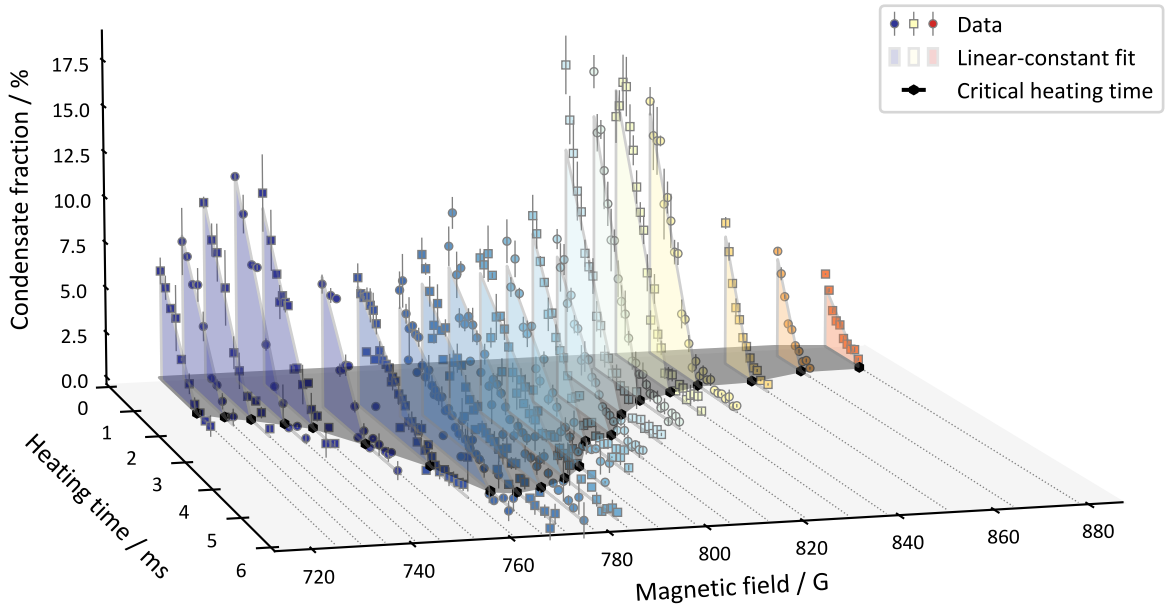

Figure 5.4: Identification of critical heating times The critical heating time is determined via a piecewise linear-constant fit (equation (5.141)) to the measured condensate fraction, which describes the data well for the measured range of heating times.

5.4 Detection of Phase Transition via Supervised Machine Learning

The measurements of this section are based on the *machine learning* dataset as defined in section 5.2.1. In a first step, a neural network is trained to predict the condensate fraction of a sample based on time-of-flight data, using the rapid ramp data as labels, which are available

for a subset of magnetic fields. In a second step, the trained network is applied to the full set of time-of-flight data, which allows for the detection of the superfluid at all considered magnetic fields. As an additional step, the training set is examined to get a sense for which features might be decisive for the predictions.

5.4.1 Training of Neural Network

The supervised training of the neural network is sketched in figure 5.5, showing examples of the training set and an illustration of the neural network architecture (See section 4.6 for an explanation of different types of layers). The training set for the neural network contains

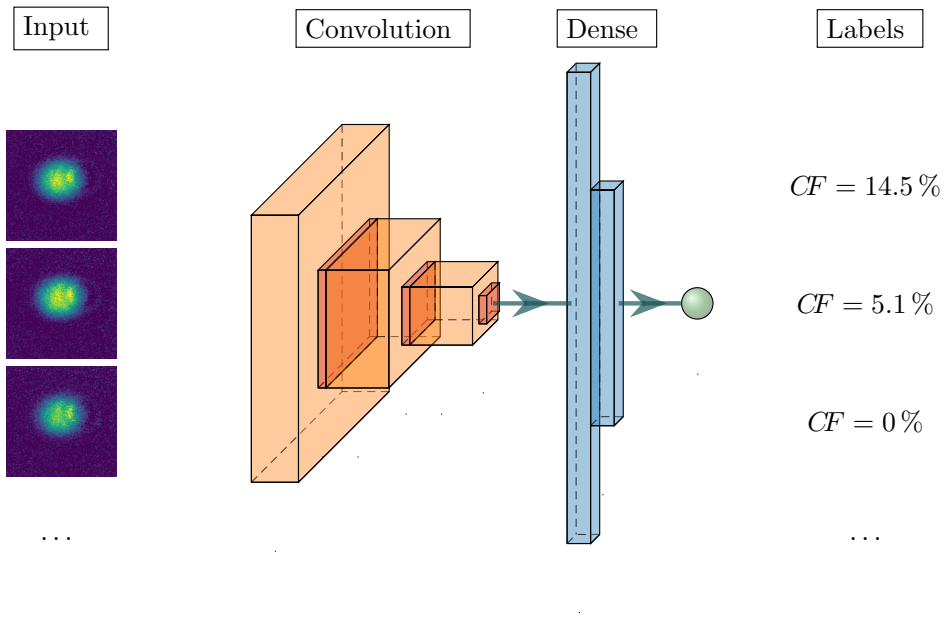

Figure 5.5: Visualization of the network architecture used for supervised learning Height and depth of the convolutional layers indicate the shape of the data and the width indicates the number of filters. Each convolutional layer is followed by a pooling layer. For the dense layers the height indicates the number of neurons. Some example residual images and corresponding condensate fractions from the training set are shown.

time-of-flight images as inputs and matching condensate fractions as labels, which have been measured with the rapid ramp. The images are centered and cropped to a region of interest with shape (150, 170). The region very close around the phase transition is masked out by removing all data with a condensate fraction below 5 %, unless the heating time is clearly above the phase transition in which case the data is kept and labeled as zero condensate fraction.

The training data has been taken at six different magentic fields. Table 5.1 details the number of datapoints for the different fields before and after the masking. 10 % of the data is used for validation.

The neural network consist of three convolutional layers, each combined with a max-pooling layer, and two fully connected (dense) layers, as sketched in figure 5.5. The exact parameters of the architecture are given in table 5.2. For the training the Adam optimizer is applied with a learning rate of 1.5×10^{-4} and with the mean-squared error as loss function. Dropout layers with a dropout rate of 0.5 are used to prevent overfitting. The network architecture is relatively robust and small changes have not a large effect on the training performance of the network.

The training and validation losses are shown in figure 5.6. The training is stopped after 10

Table 5.1: Number of datapoints in the training set at different magnetic fields The actual number used for the training is lower because data close to the phase transition is masked out, as described in the text. Some datapoints are also excluded from the total count if either a Gaussian fit to the time-of-flight image or the bimodal fit to the corresponding rapid ramp data leads to untypical parameters.

Magnetic field / G	Datapoints (total)	Datapoints (training)
728	654	443
757	1030	801
787	1042	474
836	1743	1130
895	732	490
914	604	373
Combined	5805	3711

Table 5.2: Neural network architecture for supervised learning The third dimension of the convolutional layers corresponds to the number of filters. Some other properties are given in the text.

Layer	Output shape	Parameter count	Properties	Activation
Convolution (2D)	150, 170, 30	300	Kernel: (3, 3)	ReLU
Max Pooling (2D)	75, 85, 30		Stride: (2, 2)	
Convolution (2D)	75, 85, 40	30040	Kernel: (5, 5)	ReLU
Max Pooling (2D)	37, 42, 40		Stride: (2, 2)	
Convolution (2D)	37, 42, 50	50050	Kernel: (5, 5)	ReLU
Max Pooling (2D)	18, 21, 50		Stride: (2, 2)	
Flatten	18900			
Dense	600	11340600		ReLU
Dropout	600			
Dense	300	180300		ReLU
Dropout	300			
Dense	1	301		ReLU

epochs because the validation loss plateaus while the training loss further decreases, which can be an indication for overfitting.

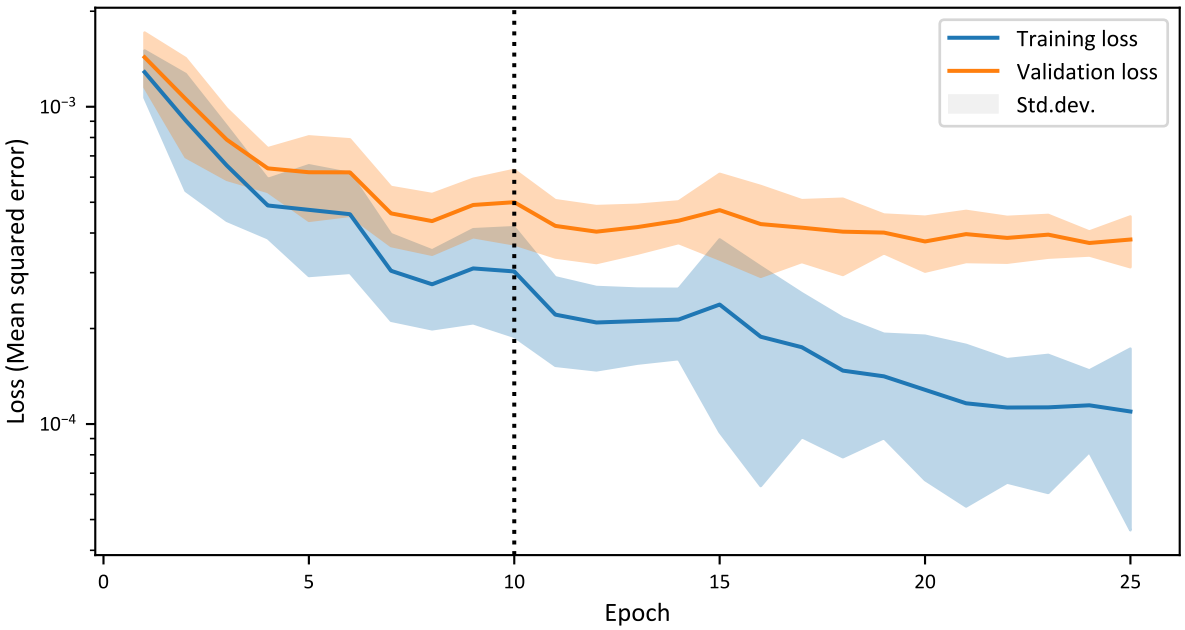

Figure 5.6: Training loss and validation loss during training The loss function is the mean squared error. Shown are mean and standard deviation of the loss for ten repetitions of the training process. The training loss is calculated without dropout to make the values more comparable. Already after a few epochs the validation loss levels off, while the training loss decreases further, so the training process is stopped after 10 epochs to prevent overfitting.

5.4.2 Detecting the Phase Transition

The trained neural network is applied to all available time-of-flight data, which yields predictions of the corresponding condensate fraction for the different magnetic fields and heating times. As before, the critical heating time τ_c is extracted by fitting the condensate fraction to the empiric piece-wise linear-constant function from equation (5.141), as presented in figure 5.7. Note that here the range of heating times is much larger than for the other dataset, which makes it necessary to restrict the fit to a small region around the transition, where the condensate fraction is below 20 %, because for higher condensate fractions a deviation from the linear behavior is observed.

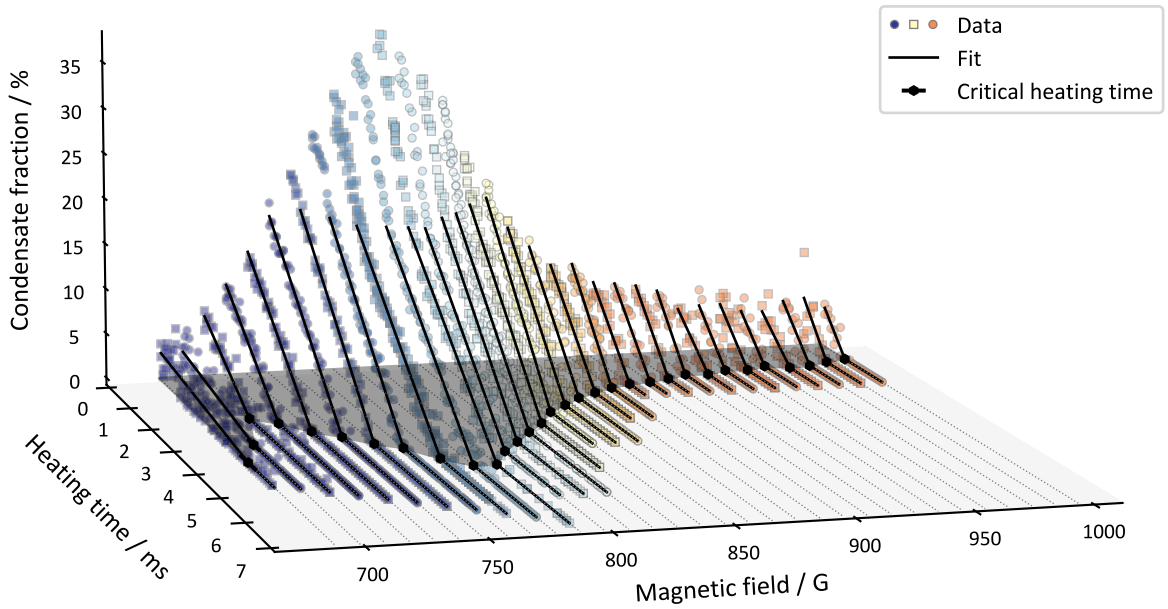

Figure 5.7: Identification of critical heating times for *machine learning* dataset The heating times are extracted via constant-linear fits. The fit range is restricted to values of low condensate fraction to avoid non-linear behavior at higher values.

Generalization The results are only usable if the neural network is able to generalize its predictions to interactions at which it has not been trained at. To test this, the condensate fraction is measured for another magnetic field at 983 G with the rapid ramp and compared to the predictions of the neural network, see figure 5.8. While the absolute value of the condensate fraction deviates slightly, the result for the critical heating time is indeed consistent. Note that also for the rapid ramp the absolute value of the condensate fraction is not necessarily comparable for different interactions, because the efficiency of the projection onto molecules can in principle depend on the initial interaction, and also on the specifics of the magnetic field ramp.

The generalization to another spin mixture is less convincing, which is also shown in figure 5.8. We also have observed that the predictions of the network do not generalize well to situations in which the trap frequencies change too much.

5.4.3 Examination of Dataset

In order to better understand what signals the neural network is sensitive to, a first approach can be to examine the dataset "manually" for any obvious features.

The time-of-flight images are typically fitted with a 2D Gaussian function to determine an estimate of the atom number. The main parameters are the amplitude and standard deviation of the Gaussian. Their dependence on magnetic field and heating time is examined in figure 5.9. It turns out that the datapoints separate quite well, which means that there is a mapping from the Gaussian parameters to magnetic field and heating time, which could in principle give the neural network a shortcut to learn the condensate fraction in a very indirect way.

Additionally, it is found that the central position of the fits deviates by a few pixel for parts of the training set, which could in principle provide a hint about which magnetic field was measured. But this information can be deleted easily by centering the images before feeding them to the neural network, which has been done as described above.

Making the information about the Gaussian parameters inaccessible to the neural network

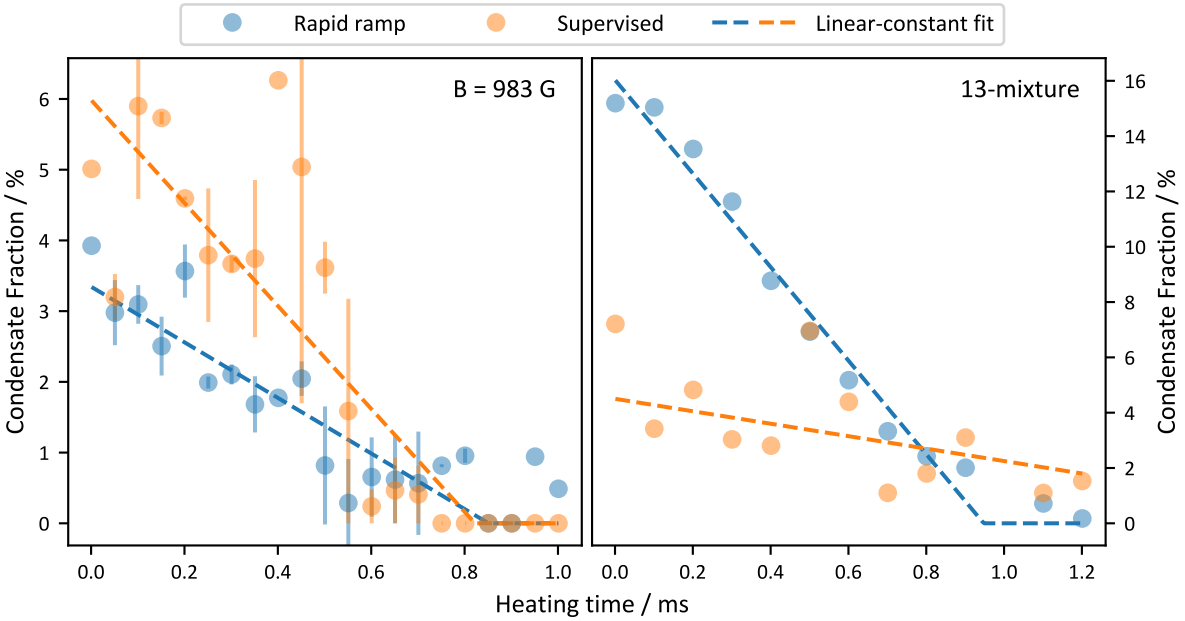

Figure 5.8: Generalization of the neural network To another magnetic field **(left)** and to another spin mixture **(right)**

is not easy. For example, scaling the optical density values in a way which always results in the same amplitude of a fitted Gaussian, also scales the noise level, leading to the noise level carrying information about the amplitude before the correction.

The important question now is if there are any other features available which could be exploited by the neural network. For this it can be useful to look at the residuals of the Gaussian fit to the data and indeed there is structure visible, which becomes more pronounced in regions with large condensate fraction. The residuals are shown in figure 5.10, but instead of a Gaussian fit a more appropriate Fermi gas fit, as described in ref. [4], is performed and the high intensity correction from section 4.1.2 is applied to make sure that this is not an artifact. At lower magnetic fields towards the BEC side, the residuals indicate an increased density in the trap center, which is what one would expect for a bosonic condensate. At unitarity a clear structure in the residuals persists, whereas the signal becomes unclear towards the BCS side.

This signal should also be accessible by the neural network and is closer connected to the presence of superfluidity, although interaction effects without superfluidity could also lead to structure in the residuals to a certain degree.

It is difficult to disentangle which of these features are considered by the neural network and whether there are still other features. Interestingly, the neural network can still be trained if the input images are replaced by the residuals or even by images of the best fits, although the latter leads to a slightly worse validation loss. This indicates that the original neural network does actually consider more information than just the Gaussian parameters.

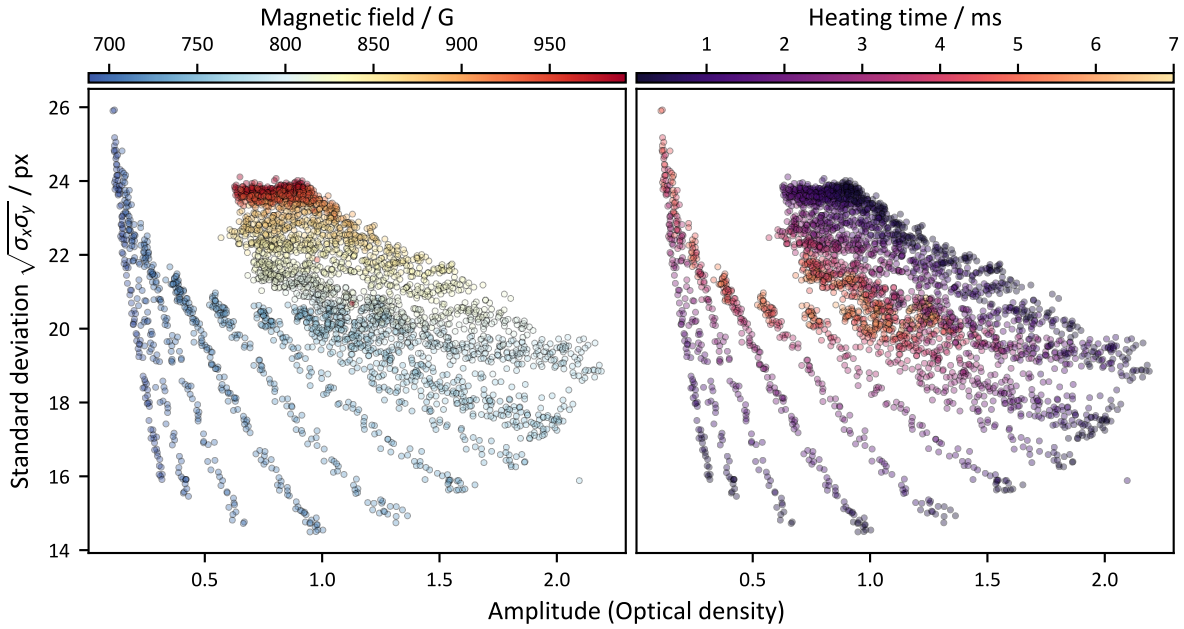

Figure 5.9: Amplitude and standard deviation of a Gaussian fit to the time-of-flight data The color shows the influence of the magnetic field **(left)** and the heating time **(right)**. Shown is the phase diagram data, which features more magnetic fields, but the training data behaves similarly.

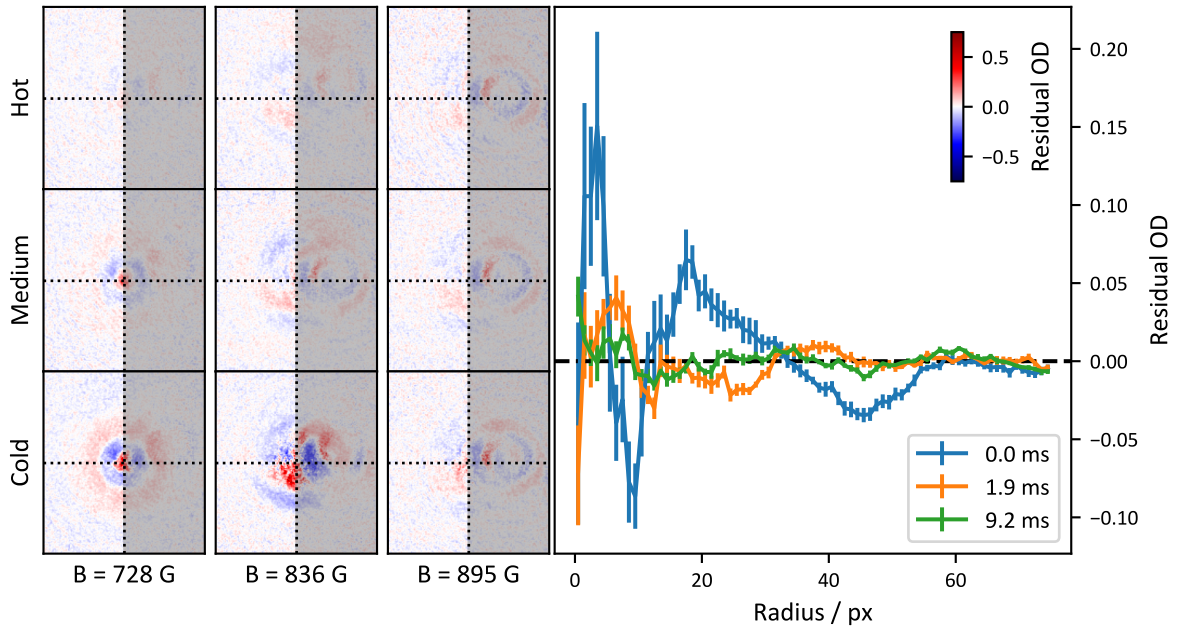

Figure 5.10: Residuals of Fermi gas fits to time-of-flight images The residuals are shown for some magnetic fields and heating times **(left)**, as well as radial averages of the residuals at $B = 836\,\mathrm{G}$ **(right)**. The data is averaged over 10 realizations with similar heating time. Fringes have a good visibility in the residual images, therefore only the left side of the images is used for the radial average to limit the effect of fringes which are more pronounced on the right side.

5.5 Detection of Phase Transition via Unsupervised Machine Learning

The supervised method to detect the condensate fraction in the previous chapter still depends on the rapid ramp labels of the training set. But by using unsupervised training methods, explained in section 4.6.4, it is possible to detect the phase transition independently, only relying on simple time-of-flight data.

This section is also based on the *machine learning* dataset introduced in section 5.2.1, but ignoring the rapid ramp data and using the phase diagram data as training set.

5.5.1 Training

The training set consists of 3002 unlabeled images which were taken at various magnetic fields and heating times. The neural network is implemented as an autoencoder as illustrated in figure 5.11 (See section 4.6 for an explanation of different types of layers and the concept of an autoencoder). The encoder consists of two convolutional layers in combination with max-

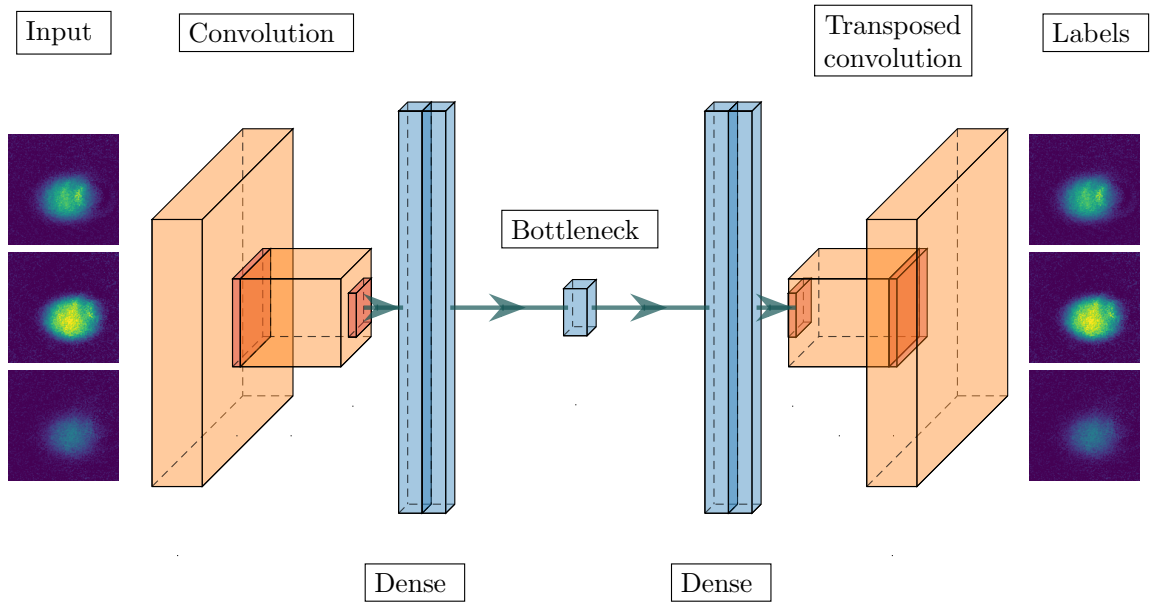

Figure 5.11: Visualization of the network architecture used for unsupervised learning Height and depth of the (transposed) convolutional layers indicate the shape of the data and the width indicates the number of filters. For the dense layers the height indicates the number of neurons. Some exemplary time-of-flight images are shown, which are used in identical form as input and label.

pooling layers, two dense layers and finally the bottleneck which consists of only 2 neurons. In this way the encoder maps the input images onto a two-dimensional representation in the latent space of the autoencoder. The decoder is built up symmetrically to the encoder and learns to reconstruct the images from the representation in the latent space. An L1 regularization with regularization strength $\lambda = 1 \times 10^{-4}$, applied to the bottleneck, speeds up the training process significantly. The training uses the Adam Optimizer with a learning rate of 5×10^{-4} and the mean squared error as loss function. The exact parameters of the network architecture are listed in table 5.3.

The losses during training, shown in figure 5.12, converge after a few epochs. The validation loss stays very similar to the training loss and a training with 15 epochs is chosen. Judging

Table 5.3: Neural network architecture for unsupervised learning The third dimension of the convolutional layers corresponds to the number of filters. While the model used for the analysis uses the Leaky ReLU activation function, I checked that at least during the training a normal ReLU activation has similar performance and would probably work equally well in this case.

Layer	Output shape	Parameter count	Properties	Activation
Convolution (2D)	150, 170, 32	320	Kernel: (3, 3)	Leaky ReLU
Max Pooling (2D)	75, 85, 32		Stride: (2, 2)	
Convolution (2D)	75, 85, 64	8256	Kernel: (2, 2)	Leaky ReLU
Max Pooling (2D)	15, 17, 64		Stride: (5, 5)	
Flatten	16320			
Dense	512	8356352		Leaky ReLU
Dense	512	262656		Leaky ReLU
Dense	2	1026		linear
Dense	512	1536		Leaky ReLU
Dense	512	262656		Leaky ReLU
Dense	16320	8372160		Leaky ReLU
Reshape	15, 17, 64			
Conv2DTranspose	75, 85, 64	102464		Leaky ReLU
Conv2DTranspose	150, 170, 32	8224		Leaky ReLU
Conv2DTranspose	150, 170, 1	289		Sigmoid

from the final validation loss, a bottleneck with only one neuron (“1D”) has worse performance, whereas more than two neurons have no clear advantage.

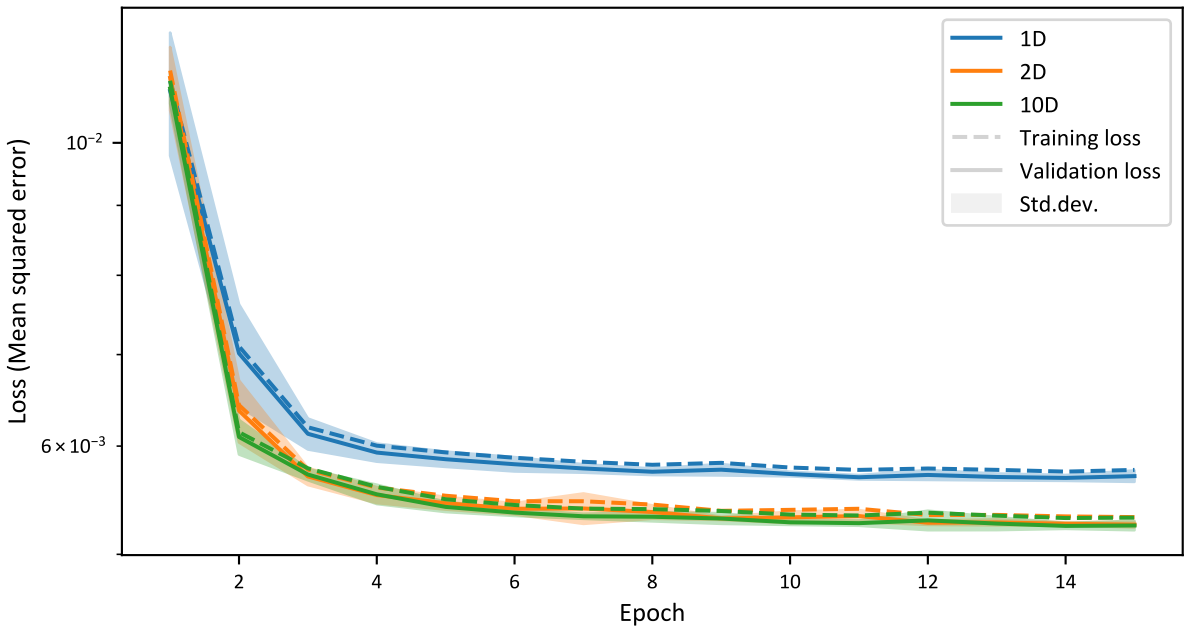

Figure 5.12: Mean squared error during the unsupervised training of the autoencoder Shown are the mean and standard deviation of 10 repetitions of the training process. The losses level off quickly, but training and validation loss stay very similar indicating no overfitting. With a one-dimensional bottleneck it is not possible to reach the same low level of loss as with a two-dimensional bottleneck, but an advantage of a higher dimensional latent space is not visible.

5.5.2 Results

In contrast to the results from the rapid ramp or the supervised machine learning, which directly reveal the superfluidity of the sample via the measured or predicted condensate fractions, the interpretation of the results from the unsupervised machine learning is more subtle. By applying only the encoder part of the neural network to the time-of-flight data, one obtains a compressed, low-dimensional representation of the data in the latent space. The question is whether the presence of a phase transition can be deduced from how the data is arranged in this space. The latent space representation of the data is shown in figure 5.13, highlighting its dependence on heating time and magnetic field.

In general, the data for different magnetic fields is distributed over the latent space, showing that the network can distinguish different interactions. Clouds with higher temperature are closer together, which is consistent with the expectation that thermal clouds stay more similar than cold clouds when the interaction is varied.

One observes that the datapoints are arranged along separate lines, which can be attributed to the different magnetic fields. Within one of these lines, the data is ordered by heating time. Interestingly, some of the lines feature a very clear kink, which means that at a certain critical heating time τ_c for a given magnetic field the properties of the sample change qualitatively. Such a qualitative change can be associated with a phase transition.

Extraction of the Kink Position The arrangement of the data in the latent space is well described with two lines intersecting at the kink position (x_c, y_c), which can be extracted with a fit to the piecewise linear function

$$f(x) = \begin{cases} m_1(x - x_c) + y_c & \text{if } x < x_c, \\ m_2(x - x_c) + y_c & \text{otherwise.} \end{cases} \tag{5.142}$$

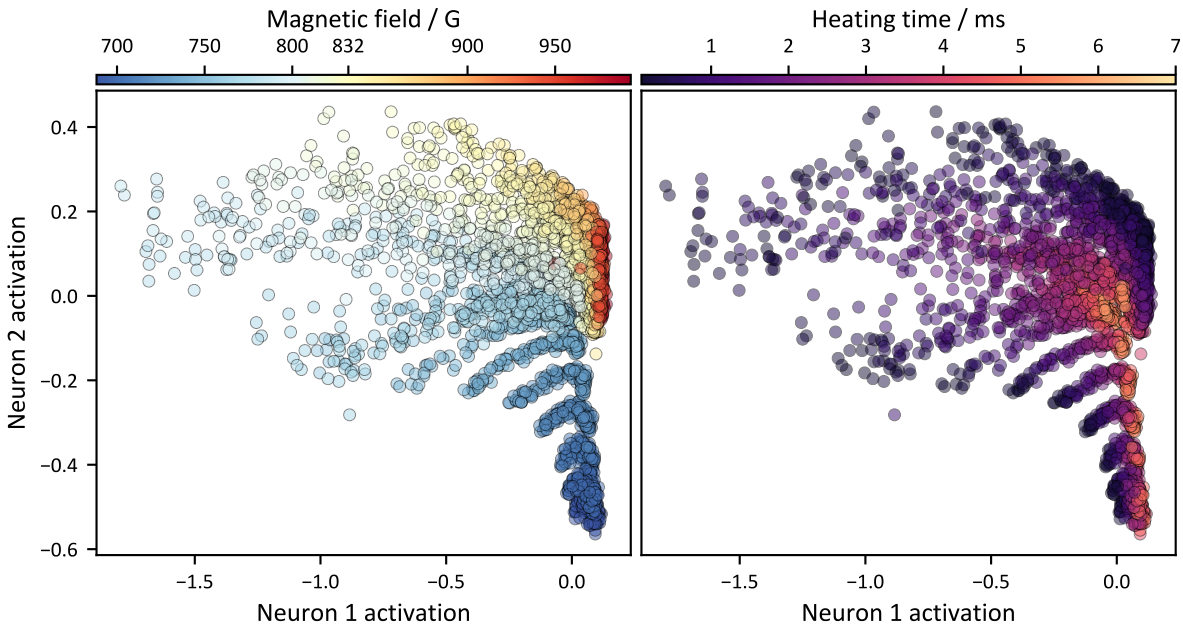

Figure 5.13: Arrangement of data in the latent space of the autoencoder Both plots show the same data but with either the magnetic fields **(left)** or heating time **(right)** visualized.

Note that the orientation of the data in the latent space has no special meaning and in practice one could also employ different fit strategies. If the training of the autoencoder is repeated, one usually obtains the same arrangement of the data, but the axes might be exchanged (neurons exchange role) or flipped (axes scaled by -1), depending on the random initialization of the neural network parameters before the training. Another thing to note is that the description of the latent space data (x, y) by a single-valued function $f : x \mapsto y$ is only possible for certain orientations of the data. Additionally, if the fit is based on minimizing the mean squared error along the y-axis, the orientation affects how deviations from the fit function are calculated.

Following these considerations, the most appropriate fit method would be to describe the data with two connected lines and to calculate the mean squared error from the euclidean distance between the datapoints and the lines. Unfortunately, my implementation of this method got stuck in local minima easily and manual inspection of the fits was not convincing.

An alternative approach, which is also independent of the orientation, is a parametric description of the data according to $f : \tau \mapsto (x, y)$, using the heating time τ as function argument. The advantage is that this does not only yield the position $(x_\mathrm{c}, y_\mathrm{c})$ in the latent space, corresponding to the transition point, but directly yields the critical heating time τ_c as a fit parameter. Another property is, that the fit is not only sensitive to the shape in the latent space, but also to the "speed" $\partial_\tau (x, y)$ with which the coordinates in latent space change with the heating time. This can be an advantage at some fields, for which the angle between the two line segments is very small, but it can also be a disadvantage, if the heating process is non-linear. For example, if the heating rate is not constant and suddenly changes above a certain point, one could misinterpret that as the transition point.

Finally, the best results have been achieved by performing piecewise-linear fits in a transformed coordinate system, for which the origin $(0, 0)$ is centered to the datapoints with minimum heating time and the point $(1, 0)$ is centered to the datapoints with maximum heating time. Then one calculates the transition point by transforming the fit result back to the original coordinate system of the latent space. The following analysis is based on the transition point determined by this fit method.

For the strategies which extract the transition point (x_c, y_c), the critical heating time τ_c is determined for every field by averaging the heating times in close distance to the transition point. For this dataset, considering the different densities of the data in the latent space representation, a reasonable choice is to average 10 % of the datapoints which are closest to the transition point.

The fit results for the different strategies are compared in figure 5.14. There are two magnetic

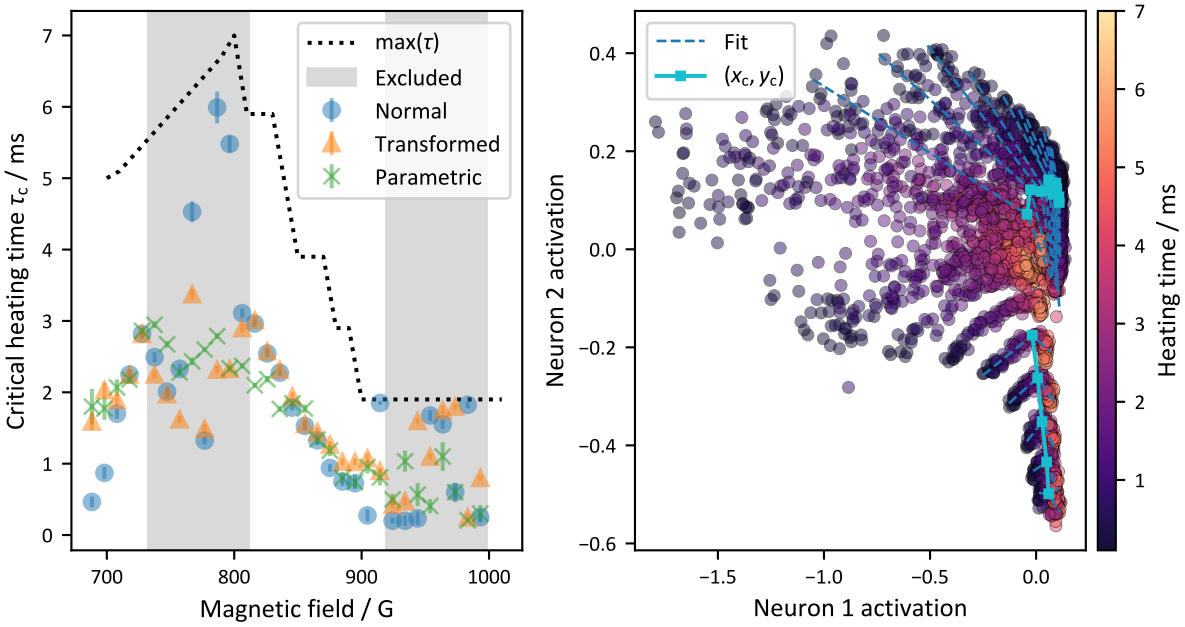

Figure 5.14: Extraction of critical heating time from latent space representation The results of different fit strategies are compared **(left)**. Two magnetic field intervals are excluded because the fits fail. For other fields the outcome of the different fit strategies is mostly consistent. Additionally, the phase boundary in latent space is shown **(right)**.

field intervals for which a clear kink is not visible. Hence, these are excluded in the further analysis. Figure 5.15 shows some examples of individual fits in regions where a good fit is possible and where it is not. It is interesting that the kink positions form a boundary within the latent space, which corresponds to the phase transition in that representation, as demonstrated in figure 5.14.

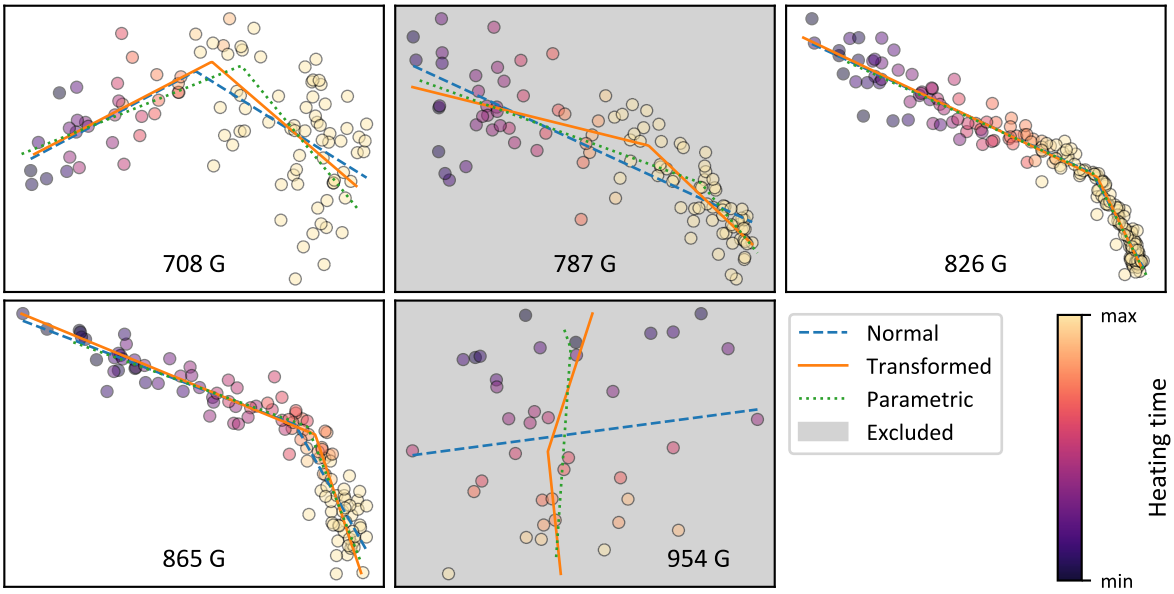

Figure 5.15: Example fits to data in latent space representation For sake of simplicity, the scales of the axes are omitted, because they do not have a direct physical significance. They would correspond to different activations of neuron 2 vs neuron 1, if needed please consult figure 5.14. The range of heating times differs for different fields. For some fields, the fits are not reliable because no clear kink is visible. The parametric fit can sometimes differ slightly, possibly due to non-linearities in the heating process, because it does not only depend on the position of the datapoints, but also on the associated heating times.

5.5.3 Comparison to Previous Results

The critical heating times for the two datasets and for the different detection methods are compared in figure 5.16. Note that the heating process might differ slightly for both datasets due to the different trap geometry. Therefore, the results cannot be compared directly at this point. But for the *machine learning* dataset the critical heating time has been determined with all three methods for some fields. In general, there is very good agreement between results from the rapid ramp and from the unsupervised machine learning, which is encouraging because these two methods are completely independent. Unfortunately, the unsupervised method only works reliably for certain ranges of the magnetic field. From the supervised machine learning, transition points for all measured fields can be determined, but there seem to be small deviations compared to the other two methods.

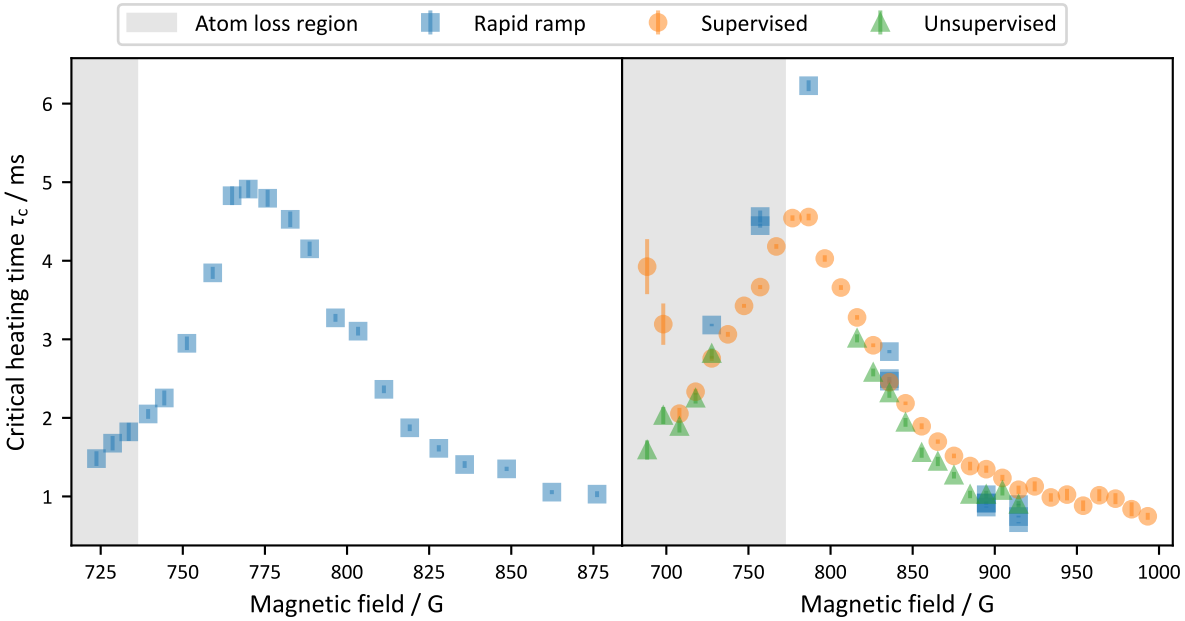

Figure 5.16: Summary of critical heating times For the *thermometry* dataset **(left)**, the *machine learning* dataset **(right)** and for the different detection methods of superfluidity

5.6 Thermometry

The thermometry is first explained for the *thermometry* dataset, which has in-trap images for all considered magnetic fields. Then the heating rate is examined for the *machine learning* dataset, for which a larger interval of heating times has been measured.

For different heating times, the in-trap density is measured to perform thermometry at the edge of the cloud with a third order virial fit as explained in section 4.4.4. To improve the signal-to-noise ratio, the data is empirically fitted to linear functions, in the region of the critical heating time τ_c as shown in figure 5.17. This is acceptable because it only involves datapoints in a small region around the phase transition where the temperature does not change much compared to the noise level. Note that the expectation for the second order phase transition is that the heat capacity has a jump [61], while the temperature remains continuous. Therefore, the linear fit will only lead to a minor systematic error.

Here, the temperature depends mainly on the magnetic field. The heating rate from the trap release heating is examined more closely in the following subsection, based on the other dataset which features a wider range of heating times.

As a byproduct, the thermometry fits produce estimates for the chemical potential μ_0, which are shown for the third order virial fit in figure 5.18. The value is not much affected by the heating, but reduces as expected towards the BEC side. The chemical potential used in the virial expansion is referenced to single fermions. Therefore, it takes negative values on the BEC side due to the presence of a bound state.

The same analysis can also be performed for different fit functions, considering the different possible density distributions described in section 2.5.1. This has an impact on the extracted critical temperature and critical chemical potential, which is compared in figure 5.19 and figure 5.20, respectively. First, considering the critical temperature, deviations between Boltzmann fit and ideal Bose or Fermi fit demonstrate that at the considered densities a Boltzmann fit is not valid anymore, especially towards the BEC side. Also it makes a big difference of more than a factor of two, whether an ideal Fermi or Bose fit is performed. The mean-field corrected

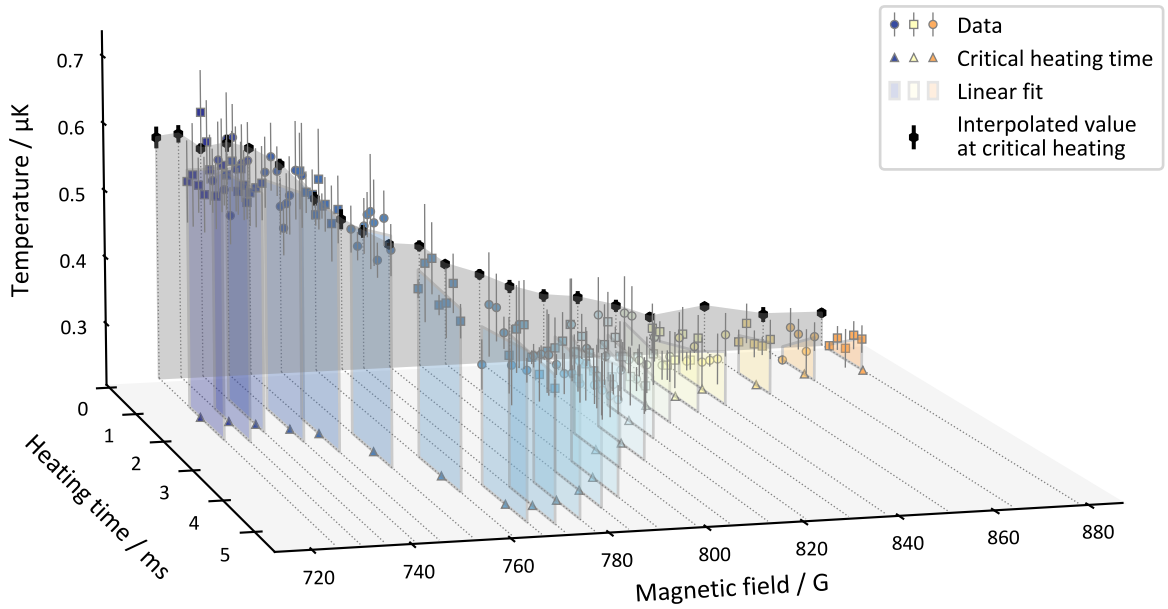

Figure 5.17: Extracted temperature near the phase transition from a third order virial fit to the density at the edge of the cloud The temperature at the critical heating time is determined with reduced statistical noise for each magnetic field by applying a linear fit and interpolating to the previously measured critical heating time.

Bose fit slightly bends down closer to the virial fit results, but towards stronger interactions this fit becomes unreliable. The result from the virial fits is consistent with the Bose fits far on the BEC side, yields lower temperatures in the strongly interacting regime, and seems to converge towards the result from the ideal Fermi fit towards the BCS side. Close to unitarity, a fit based on the known equation of state is employed, which yields a temperature consistent to the result of second and third order virial fit. This is an encouraging validation of the thermometry based on the virial fits.

Determining the chemical potential from the wings of the cloud is probably not very accurate. But here the fit results also show a consistent picture: The virial fits approach the values from the Fermi fit towards the BCS side, are consistent with the unitary fit and approach the values from the Bose fits towards the BEC side. Note that the chemical potential from the virial fits is referenced to single fermions, which quickly leads to large negative values on the BEC side due to the presence of the bound state, but can be compensated by subtracting half the (negative) bound state energy.

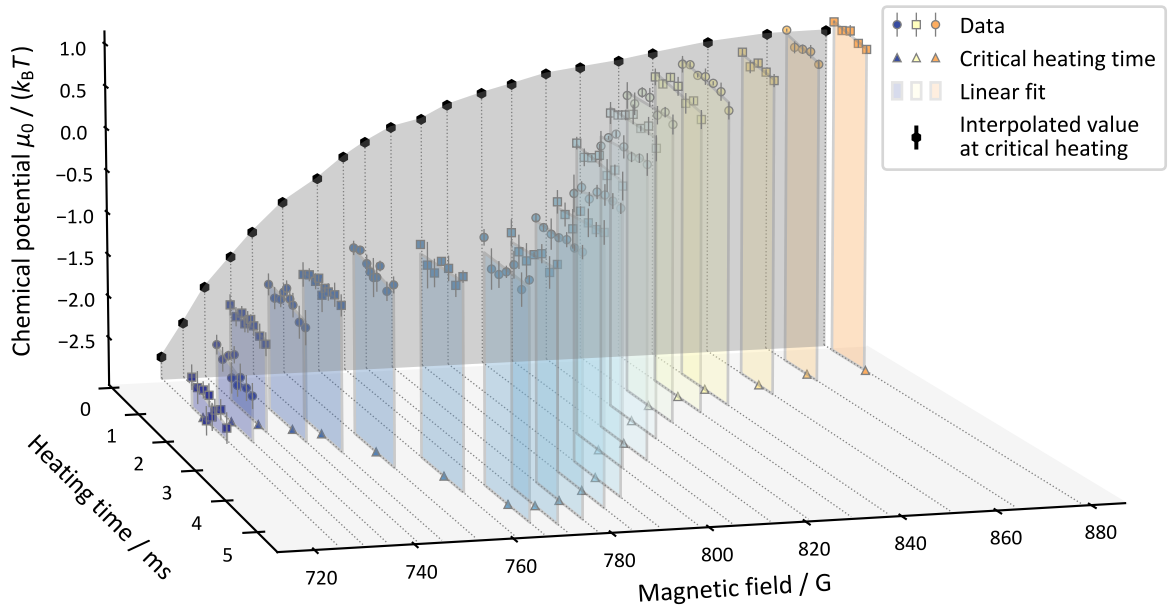

Figure 5.18: Chemical potential near the phase transition based on a third order virial fit
The value at the critical heating time is determined by applying a linear fit and interpolating to the previously measured critical heating time. The chemical potential is referenced to single fermions, which leads to negative values on the BEC side due to the existence of a bound state.

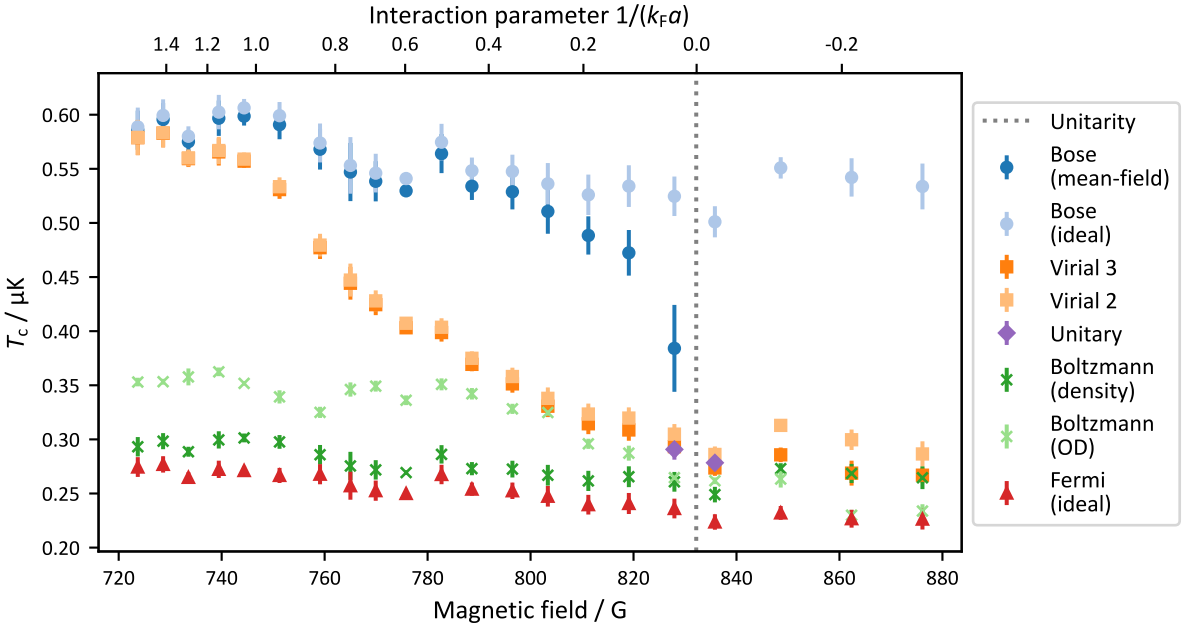

Figure 5.19: Critical temperature versus magnetic field compared for different fit functions
The interaction parameter is based on the corrected harmonic Fermi energy, which will be explained in section 5.7.

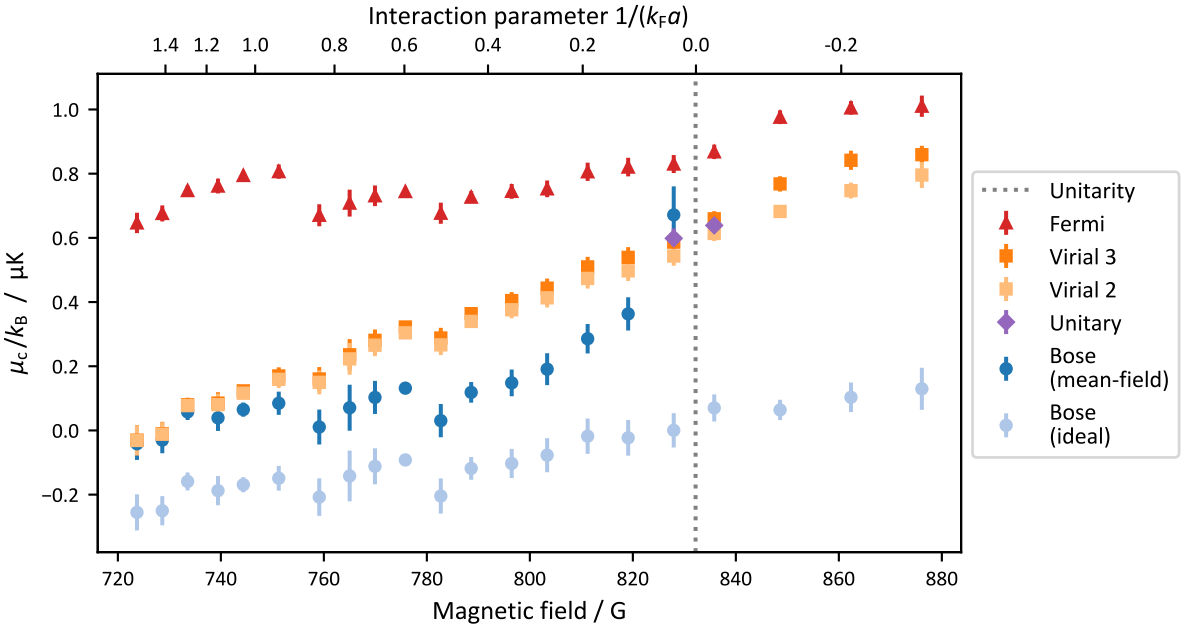

Figure 5.20: Critical chemical potential versus magnetic field compared for different fit functions Interaction parameter is based on corrected harmonic Fermi energy, which will be explained in section 5.7. The chemical potential μ_0 is always referenced to the single fermion. The bound state energy on the BEC side is not taken into account, except for the virial fits, for which that contribution is eliminated by subtracting half the (negative) bound state energy.

Reassessment of Fit Regions For the virial fits of the thermometry, it is essential to restrict the fit region to the virial regime $\beta\mu \ll 0$. However, beforehand it is not clear to which density or potential values this regime corresponds. After performing the fits, the condition for the

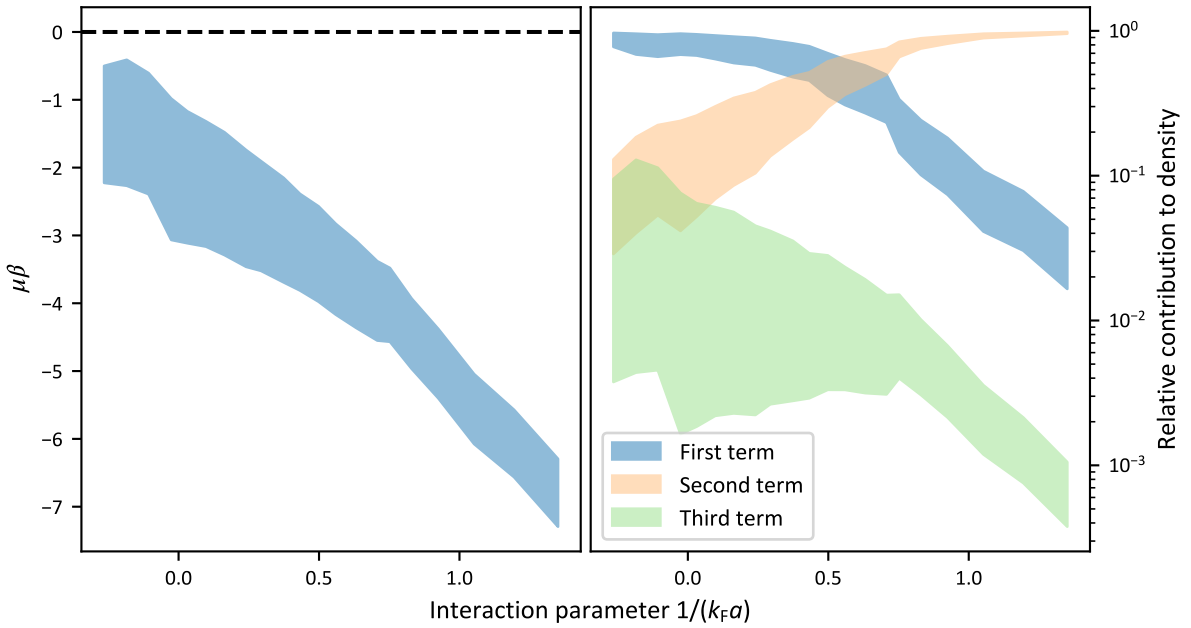

Figure 5.21: Condition for virial regime and contribution of different terms The fits are performed in the virial regime $\beta\mu \ll 0$ **(left)**, according to the values β and μ from a third order virial fit. The relative contribution to the calculated density is shown for the terms (monomials) of the virial expansion up to third order **(right)**. The plotted areas in both panels correspond to the full fit ranges from highest considered density (lowest potential) to lowest considered density (highest potential).

virial regime can be checked for consistency with the extracted values for chemical potential and temperature, as demonstrated in figure 5.21. Additionally, the contribution of the different terms in the virial expansion to the calculated density can be compared, in order to make sure that a reasonable convergence is reached. If this is not the case, the fit regions have to be adjusted and this step has to be reiterated.

Interestingly, the second order virial term becomes the dominant contribution on the BEC side, which emphasizes the importance of considering multiple terms of the expansion.

5.6.1 Heating Rate and Initial Temperature

While for the *thermometry* dataset only a short range of heating times around the transition have been measured, the *machine learning* dataset features in-trap data also for lower heating times, which allows the examination of the initial temperature and heating rate over a wider range, as shown in figure 5.22. The heating rate is not constant over the whole range, but is reduced for longer hold times. Therefore, the data is empirically well described with a piecewise linear function

$$f_1(t) = \begin{cases} m_1\,(t-\tau_0) + y_0 & \text{if } t < \tau_0, \\ m_2\,(t-\tau_0) + y_0 & \text{otherwise,} \end{cases} \tag{5.143}$$

or for the last two fields on the BCS side with a plain linear function $f_2(t) = m_1 t + y_0$.

Unfortunately, for this dataset the heating was only measured for a subset of magnetic fields, which requires interpolation to apply the thermometry to all measured fields. Specifically, all four parameters m_1, m_2, τ_0 and y_0, are linearly interpolated to the target magnetic field (and

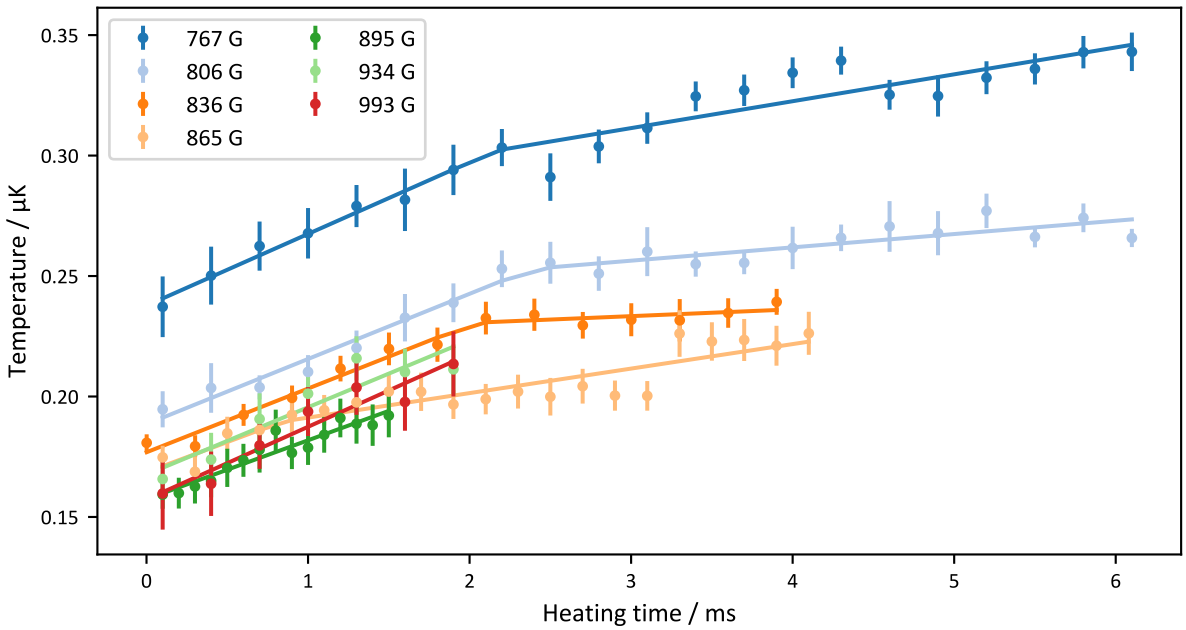

Figure 5.22: Trap release heating The temperature is determined with a second order virial fit. Heating rates and initial temperatures are empirically determined with piecewise linear fits as described in the text.

above 865 G f_2 is used instead of f_1). The goal is to provide a rough comparison to the newer results from the *thermometry* dataset. For that dataset enough thermometry data was taken, so that such an interpolation is not necessary.

5.7 Energy Scale and Central Density

Using in-trap absorption images, the 3D density distribution can be recovered with the inverse Abel transformation, as explained in section 4.3.1. Figure 5.23 shows an example of such a density distribution against the trap potential.

For the inverse Abel transformation the most central datapoints can become quite noisy and unreliable. This is a bit unfortunate because this is exactly the region of interest. Therefore, the most inner datapoints are removed and instead the density distribution is extrapolated linearly to the trap center. This can be justified with the assumption that the innermost density distribution is well described with a Thomas-Fermi density distribution which implies a linear relationship between density and potential [36]. The Thomas-Fermi approximation in the trap center is reliable at low temperatures, but close to the critical temperature the density can have a sharper increase [47], especially on the BEC side, which can lead to an underestimation of the central density. We still have to examine this effect more carefully.

Finally, this procedure is repeated for different interactions and heating times around the critical heating time, as shown in figure 5.24. To reduce noise, the value for the central density is interpolated to the critical heating time by using a linear fit, similarly as for the thermometry in the last section. Note that the observed reduction in central density with heating can partially be traced back to a reduction in atom number, but the main effect is thermal because we observe that the central density decreases faster, relatively, than the atom number (For pure atom loss at constant temperature, the cloud would shrink and the central density would decrease slower, relatively, than the atom number).

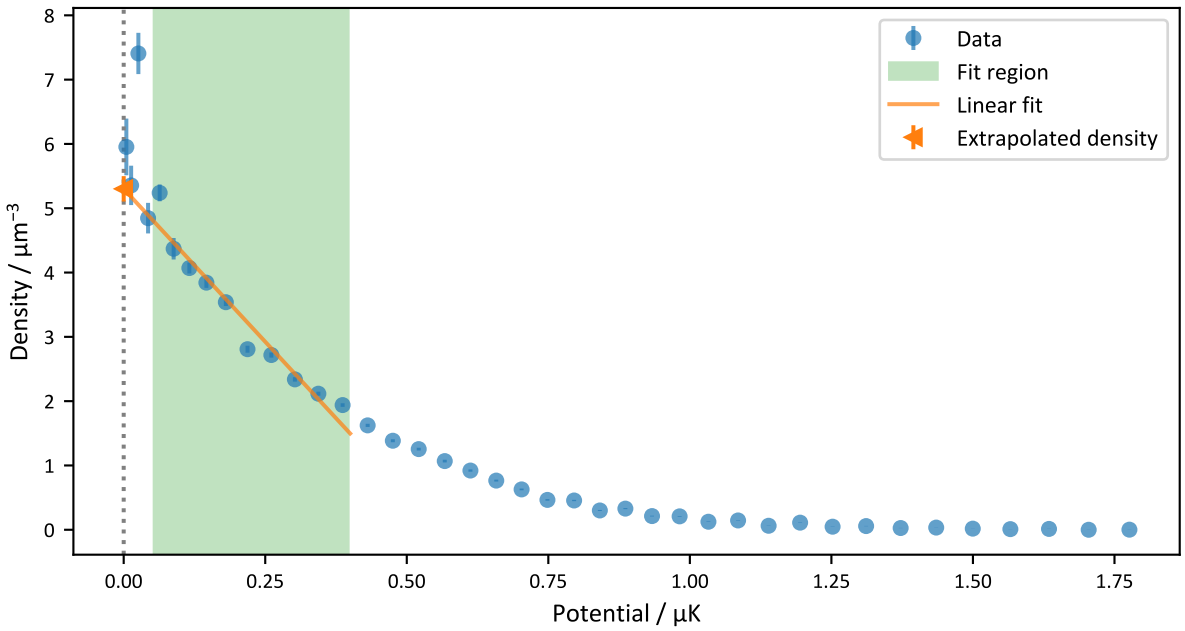

Figure 5.23: Measurement of the central density The datapoints are calculated from the inverse Abel transformation and averaged over bins of equal potential. The inverse Abel transformation becomes unreliable at the trap center. Therefore, the density is extrapolated to the center with a linear fit. The shown data is from a measurement close to unitarity for the lowest heating time.

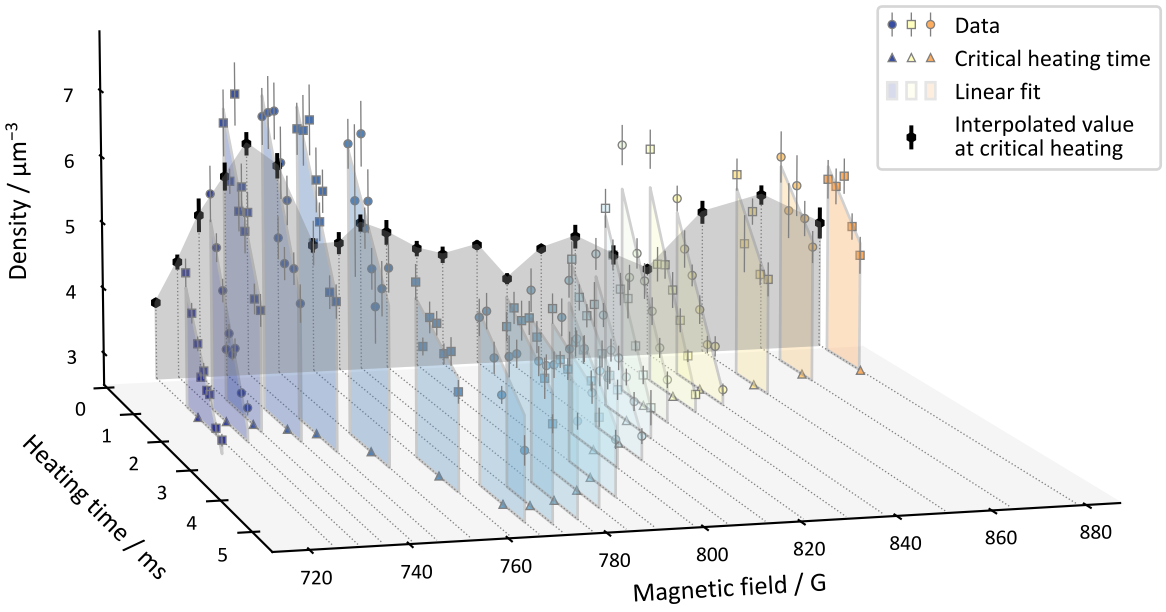

Figure 5.24: Extracted central densities of the cloud for different magnetic fields and heating times around the critical heating time The density clearly reduces with more heating and a linear fit is appropriate in the considered range to interpolate the data to the critical heating time for reduced statistical noise.

Local Fermi Energy The central density determines the central local Fermi energy within LDA, which is shown relative to the harmonic Fermi energy in figure 5.25 at the superfluid phase transition. The definition of the harmonic Fermi energy assumes the density distribution of a zero temperature ideal Fermi gas. In general, it is expected that the central density increases when the system is tuned from the BCS to the BEC side, because depending on the region it involves increasing attractive interaction, decreasing repulsive interaction or a change from fermionic to bosonic statistics.

The ratio is larger than the theoretically predicted density distributions at the critical temperature would suggest [47], but note that those results, compared with their predictions for the critical temperature, are not consistent with LDA, as also indicated in figure 5.25. For the considered interactions, the ratio of the Fermi energies agrees to a linear dependence on the interaction parameter. This trend should not continue further towards the BCS side, but instead, will bend towards a ratio of 1, when the limit of an ideal zero temperature Fermi gas is approached, but more data is needed to confirm this. Far on the BEC side, the ratio decreases suddenly, but this coincides with strong atom loss, which is why this range of data is excluded.

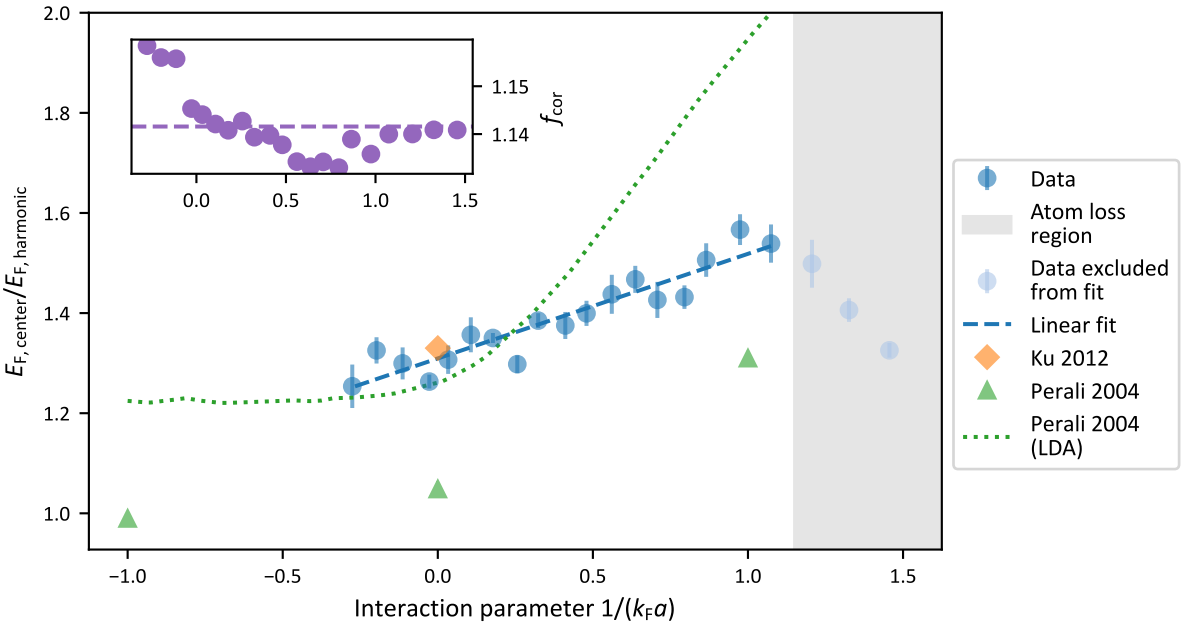

Figure 5.25: Ratio between central local Fermi energy within LDA and harmonic Fermi energy at critical temperature The data is compared to theoretical results from ref. [47] ("Perali 2004"): The datapoints are deduced from the central densities at T_c which are specified at interaction parameters $1/(k_F a) = 0, \pm 1$. The line is derived within LDA by considering a trapped gas at temperature $T_c^h = T_c^t$, which yields $E_{F,center}/E_{F,harmonic} = (T_c^t/T_F^t) \,/\, (T_c^h/T_F^h)$, which is calculated from the reduced critical temperatures provided by the reference. Note that the superscripts t and h in ref. [47] indicate the values for the trapped or homogeneous gas, respectively. The fact that these values do not agree, indicates that the result of ref. [47] is not consistent with LDA. The ratio is also derived from the unitary equation of state from ref. [61] ("Ku 2012"), which should be seen as a consistency check because it was used for the trap calibration before. Except for the far BEC side, the observed trend is consistent with a linear dependence over the measured range. The inset shows a correction factor f_{cor}, which has been applied to account for the anharmonicity of the trap, see text.

Correction of Fermi Energy in an Anharmonic Trap In a harmonic trap the Fermi energy derives from the atom number and the known trap frequencies. Within LDA, it coincides with

the local Fermi energy in the trap center for a zero temperature ideal Fermi gas. For finite temperature and interaction, the Fermi energy can still be a useful energy scale, but does not directly correspond to the local Fermi energy in the trap center anymore, which is generally increased by attractive interaction and reduced with temperature.

For an anharmonic trap, the relationship between atom number and Fermi energy has to be modified and can be calculated within LDA by considering the density distribution of a zero temperature ideal Fermi gas, as explained in section 2.6.2.

But here we are interested in a slightly different quantity. Given the slightly anharmonic trap $V(\boldsymbol{r})$ and a measured density profile $n_\sigma(V(\boldsymbol{r}))$ and assuming that within LDA the appropriate energy scale for the thermodynamics of the gas is the local Fermi energy, we want to know which Fermi energy the same gas (i.e. same temperature, chemical potential, interaction) would have, if it were in a perfect harmonic trap. But since we know the relationship between density and potential $n_\sigma(V(\boldsymbol{r}))$ from the measurement, this can be easily calculated: Assuming a dummy-harmonic potential $V_{\mathrm{dummy}}(\boldsymbol{r}) = 0.5m\omega_{\mathrm{dummy}}^2 r^2$, the atom number is given by

$$N_{\sigma,\mathrm{corrected}} = \int n_\sigma\big(V_{\mathrm{dummy}}(\boldsymbol{r})\big)\,\mathrm{d}^3\boldsymbol{r}\ , \tag{5.144}$$

which can be evaluated numerically and the corrected harmonic Fermi energy can then be calculated from equation (2.70), which cancels ω_{dummy}.

This correction $f_{\mathrm{cor}} := E_{\mathrm{F,harmonic,uncorrected}}/E_{\mathrm{F,harmonic}}$ is already included in figure 5.25, increasing the ratio $E_{\mathrm{F,center}}/E_{\mathrm{F,harmonic}}$ by roughly 14 %, as shown in the inset.

5.8 Results

5.8.1 Phase Boundary

Using the thermometry and measured central densities, the critical heating times can be converted to reduced temperatures $T_\mathrm{c}/T_\mathrm{F}$ and the magnetic fields can be properly converted to interaction parameters $1/(k_\mathrm{F}a)$, which results in the determination of the phase boundary as shown in figure 5.26. Shown are the two different choices for the Fermi energy: First, the corrected harmonic Fermi energy, and second, the local Fermi energy at the trap center within LDA, which allows a comparison to different theories.

The different methods to determine the phase transition are compared in figure 5.27. The deviation between the two results from the rapid ramp can be traced back as follows: For the *machine learning* dataset no high intensity in-trap images are available, which makes the trap calibration less precise and increases systematic errors of the thermometry. But without these deviations from the thermometry, a good agreement between the different methods can be seen, by only comparing the results of the *machine learning* dataset with each other.

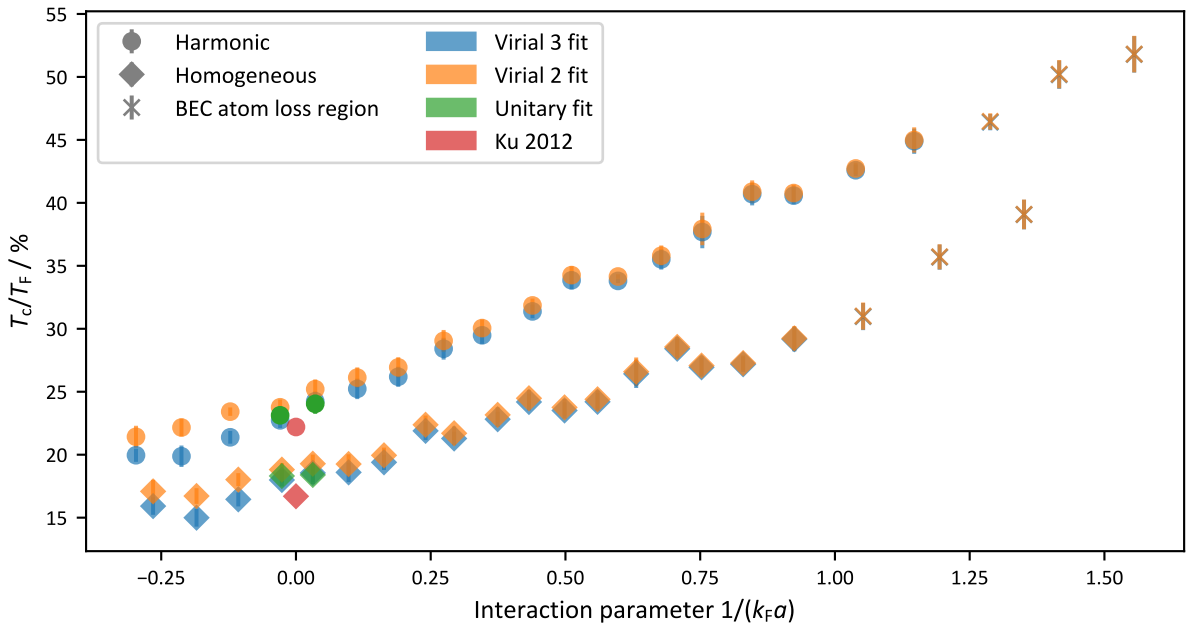

Figure 5.26: Superfluid phase transition of the BEC-BCS crossover based on the rapid ramp technique The third order virial theorem is the more accurate result, but is expected to slightly underestimate the temperature, as demonstrated by the fit to the full unitary equation of state. Also shown is the result from ref. [61] ("Ku 2012"), where the good agreement to the results from the third order virial fit should be considered as a check, because the equation of state from that reference was used for the trap calibration.

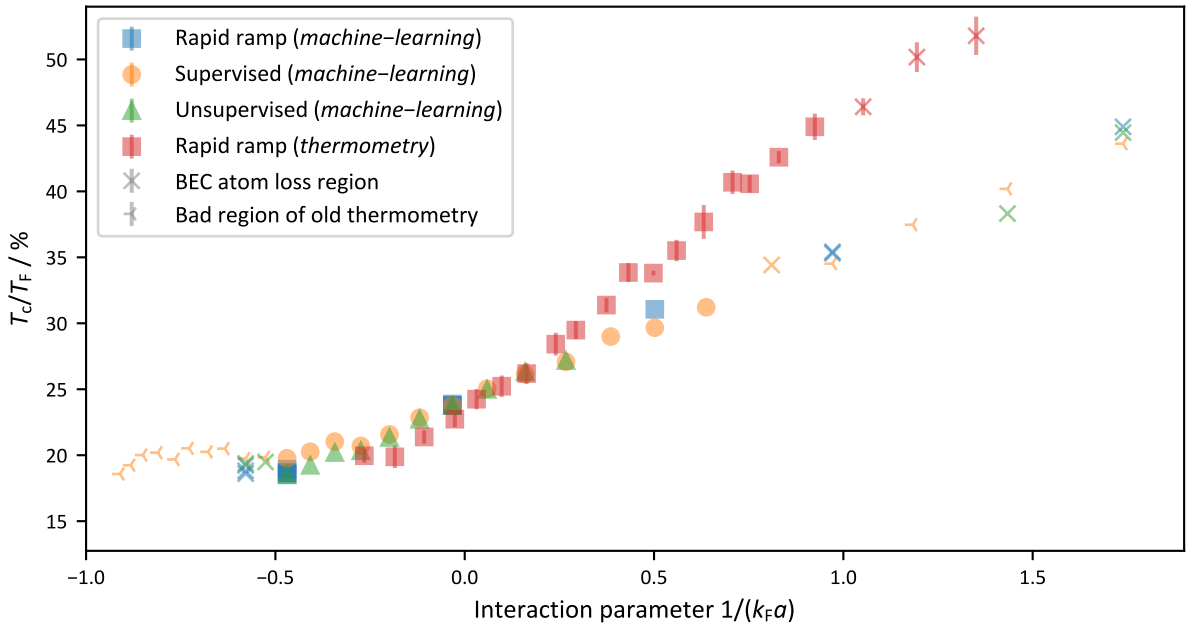

Figure 5.27: Comparison of results based on different detection methods for superfluidity The atom loss region and the unreliable region of the thermometry are indicated with different markers. The discrepancy between the datasets is attributed to the thermometry, see text.

5.8.2 Caveat of Boltzmann Thermometry

If the thermometry is naively performed only with Boltzmann fits, the temperature is systematically too low on the BEC side. This results in lower T_c values, which are close to the theory of homogeneous gases, as demonstrated in figure 5.28. However, this agreement is accidental.

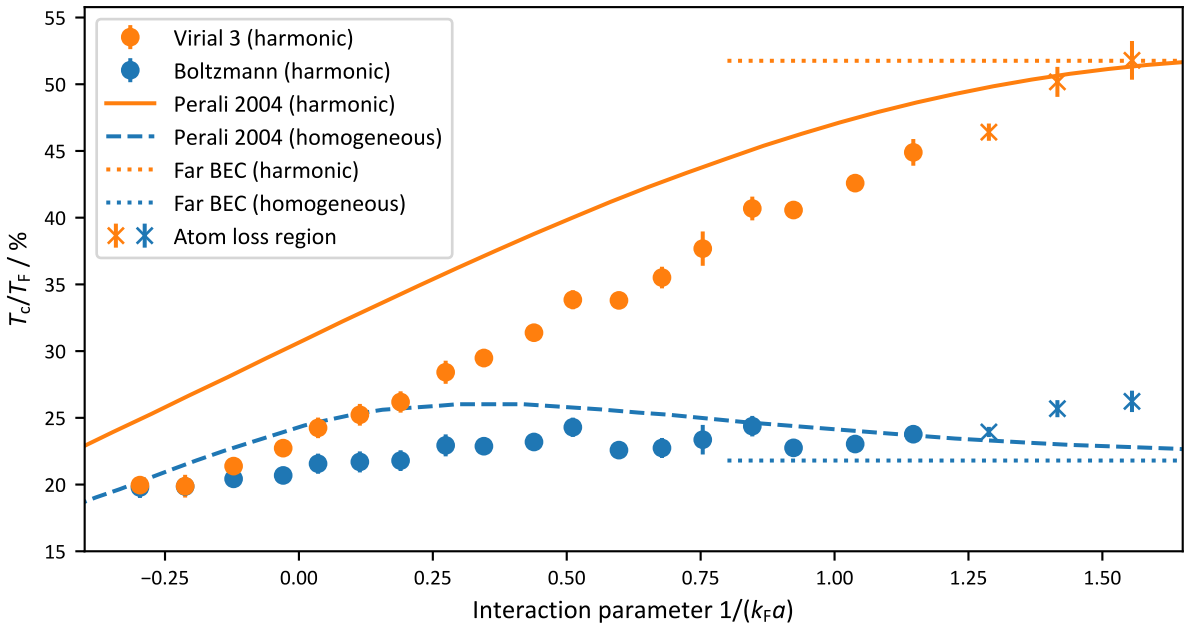

Figure 5.28: Comparison of results based on Boltzmann thermometry and on more careful thermometry using virial expansion Both fit results are referenced to the corrected harmonic Fermi energy. Compared with theory, Boltzmann thermometry of a harmonically trapped gas is more consistent with theory for homogeneous gases, because it systematically suggests too low temperatures on the BEC side.

Instead, higher order terms of the virial expansion should be used for thermometry. This approach is validated by the good agreement to Bose gas fits far on the BEC side, as demonstrated in section 5.6.

5.8.3 Comparison with Theory

A comparison of the results from the *thermometry* dataset, which should have lower systematic errors on temperature and Fermi energy, with different theoretical results for the critical temperature is given in figure 5.29.

The data referenced to the central local Fermi energy agrees well to the results from ref. [53] and ref. [54]. Unfortunately, the question of the position of the maximum cannot be answered yet.

The data referenced to the harmonic Fermi energy has the same trend as ref. [47], but has lower values. But note that this theory tends to overestimate the critical temperature, which can be seen from the homogeneous results from the same reference which agree to the BCS theory without GMB correction far on the BCS side, as was already discussed in the caption of figure 5.1.

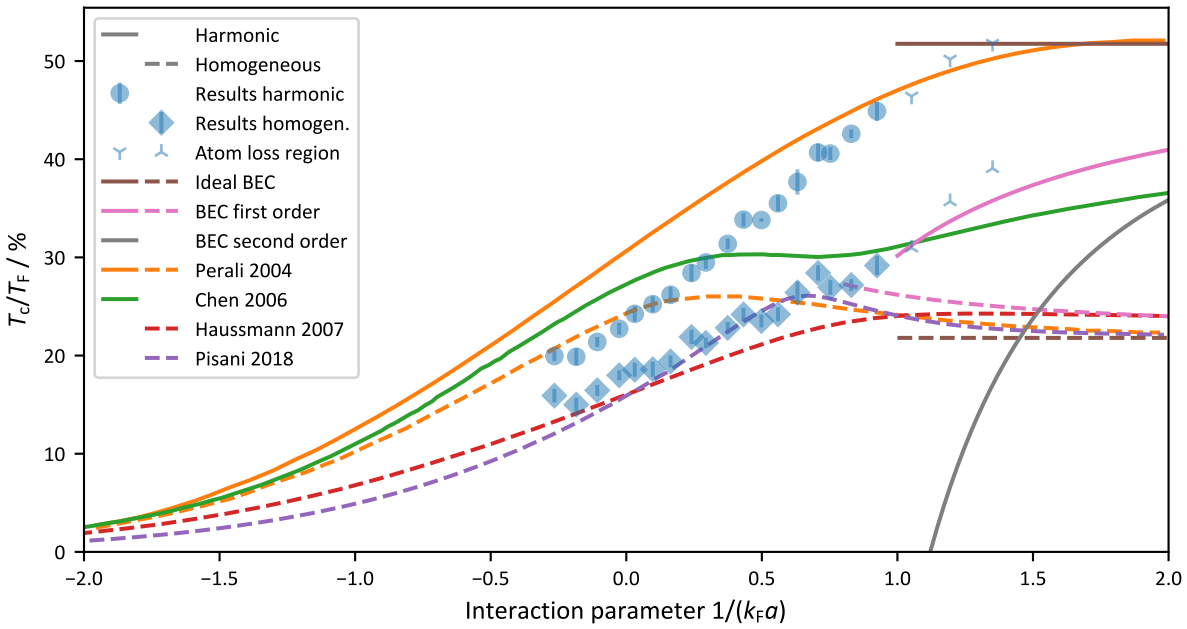

Figure 5.29: Comparison of measured phase boundary with theoretical predictions For a harmonically trapped gas (circles/solid lines, first column of legend) and for a homogeneous gas (diamonds/dashed lines, second column of legend); Shown are the results based on rapid ramp for the *thermometry* dataset. Ref. [47] ("Perali 2004") provides results for harmonically trapped and homogeneous gases and ref. [138] ("Chen 2006") only for the harmonically trapped gas, but a comparison with GMB corrected BCS theory (see figure 5.2) suggests that the critical temperature is overestimated towards the BCS side. Far on the BEC side the first order [51, 160] and for the trapped gas also the second order [50] interaction correction are shown. However, the latter clearly shows that it is not applicable for the considered interactions anymore. Agreement between the excluded homogeneous data and the first order trapped result is accidental. Last but not least, theoretical results for the homogeneous gas from ref. [53] ("Haussmann 2007") and ref. [54] ("Pisani 2018") are shown.

5.9 Conclusion

The superfluid phase transition of the BEC-BCS crossover has been detected with three different methods, using the standard rapid ramp technique but also two different machine learning methods, to extract the transition point from time-of-flight images.

With supervised machine learning a neural network is able to predict the condensate fraction from simple time-of-flight images. This approach still requires the rapid ramp to generate labeled training data, but the network is able to generalize to fields which are not part of the training set. A manual examination of the training data suggests that the output of the network could still be influenced by cloud size and atom number, but also reveals that the shape of the cloud changes for stronger interactions and lower temperatures. The expectation is that this effect is connected more closely to the presence of superfluidity.

By using an autoencoder for unsupervised machine learning, it is possible to detect the phase transition only based on the time-of-flight images without any dependence on the rapid ramp because no labels are required for the training. The result is very consistent to the rapid ramp measurements, but a reliable extraction of the transition point is only possible for a subset of the considered interactions.

Thermometry is based on the density distribution at the edge of the cloud. It is shown that the assumption of a Boltzmann gas at low densities would lead to significant systematic errors of the thermometry on the BEC side, which requires to consider higher terms of a virial

expansion.

The importance to distinguish between the harmonic Fermi energy and the central Fermi energy within LDA is pointed out, which leads to different results for the reduced critical temperature T_c/T_F. Then the experimental data has to be compared to matching theories for either the harmonically trapped or the homogeneous gas. Accessing the central Fermi energy within LDA is based on the measurement of the high density in the trap center, which requires calibrated high intensity imaging and the inverse Abel transformation.

The resulting phase boundaries for trapped and homogeneous gas match reasonably well to theory, which is in clear contrast to previous measurements of refs. [28, 29], for which the critical temperature beyond unitarity towards the BEC side is much lower than predicted for a harmonic trap.

The results from ref. [56] do show a higher critical temperature towards the BEC side. However, only much further on the BEC side. Our results contradict the almost constant critical temperature for $1/k_F|a| < 0.6$. One advantage of our thermometry is that we get an unambiguous result for each interaction, while in ref. [56] it is left open for which interactions their Bose fit or Boltzmann fit is appropriate.

Outlook The measurements presented here depend on a calibration of the trap geometry, which is based on the unitary equation of state. It is desirable to replace this with a calibration based on the ideal Fermi gas to achieve a completely independent measurement of the critical temperature at unitarity.

In principle, it is possible to extend the range of considered interactions further to the BCS side, but it might be necessary to use a trap geometry with lower trap frequencies than for the *thermometry* dataset to achieve the low temperatures required in this regime. Even more interesting is the extension of the data on the BEC side and maybe the identification of a point with maximum critical temperature. This requires to examine the atom loss region more carefully and to understand its impact on our temperature and density measurements.

Currently the data is retaken so that the detection of superfluidity with machine learning techniques can be combined with the enhanced thermometry. The quality of our imaging has improved and will allow a careful characterization of some systematic errors: The density in the trap center might be underestimated because the assumption of a distribution similar to a Thomas-Fermi profile, which is used to extrapolate the density to the trap center, might not be reliable anymore at T_c for the BEC side. Furthermore, the use of radial averages and of the inverse Abel transformation lead to systematic errors on central density and temperature measurements if there are deviations of the trap geometry from the assumed symmetries. Preliminary estimations indicate that this could affect the measured temperatures by around 10 % to 15 %.

Despite a few remaining points of possible refinements, the investigation already provides a valuable improvement to the experimental measurement of the critical temperature of the Fermi gas in the BEC-BCS crossover and a better understanding of the large deviations between experiment and theory in previous studies has been reached.

6 Interaction Quench

This chapter describes interaction quenches realized in two different ways. First, the interaction is effectively quenched by a fast population transfer from a strongly to a weakly interacting hyperfine state. The quench is considerably faster than the trap frequencies, but it is still slow compared to the Fermi time. Secondly, the quench is performed with a fast magnetic coil and is faster than the Fermi time.

6.1 Overview

Interaction quenches are one tool to study the nonequilibrium physics of quantum gases [65] and have lead to the observation of steady states, for example in a Bose gas quenched to unitarity [172]. Sometimes a nonequilibrium state can be long-lived if the quantum system lacks sufficient damping mechanisms, which was demonstrated for a one-dimensional Bose gas [173]. It is known that nonequilibrium states can lead to superfluidity even above the critical temperature of the original equilibrium state [174]. An example for this are light-induced superconductors [175].

Nonequilibrium can also be used to learn about the excitation spectrum of the system. For example, the collective modes of trapped quantum gases have been studied by a sudden change [66, 67] or modulation [176] of the trapping potential. The timescale of trap dynamics typically corresponds to a few milliseconds and is the slowest dynamics considered here.

For ultracold quantum gases, however, dynamics can also happen at quite different timescales, for example at the quasi-particle relaxation time $\tau_{\mathrm{qp}} = \hbar E_{\mathrm{F}}/\Delta^2$ [177]. Note that Δ describes how washed-out the Fermi surface is at low temperatures and is a measure for the amount of states which are available for scattering. This means that the relaxation time at higher temperatures is better described by $\tau_{\mathrm{R}} = \hbar E_{\mathrm{F}}/\left(k_{\mathrm{B}}T\right)^2$. At this timescale, for $\tau_{\mathrm{R}} \approx 0.5\,\mathrm{ms}$, the formation of a condensate has been observed [178].

The shortest timescale is constrained by the largest energy scale of the system, which is usually given by the Fermi energy E_{F} and results in the Fermi time $\tau_{\mathrm{F}} = \hbar/E_{\mathrm{F}}$, with typical values in our system ranging from 5 µs to 10 µs.

Pairing Dynamics As discussed in section 2.4.1, the symmetry breaking at the superfluid phase transition, which is connected to the phase of the order parameter, gives rise to massless phase modes [39, 40]. Additionally, the Higgs amplitude mode emerges, which is described as an oscillation of the amplitude of the order parameter with frequency $\omega_{\mathrm{H}} = 2\Delta/\hbar$. This constitutes dynamics on the order of the gap time $\tau_\Delta = \hbar/\Delta$, which can have the same order of magnitude as the Fermi time, depending on the interaction.

It has been suggested that a sudden quench of the interaction can lead to a steady-state with oscillations of the order parameter [68], which can be interpreted as the Higgs amplitude mode. Instead of a sudden quench, it has also been shown that a quench on a timescale similar to the Fermi time is sufficient for the excitation [179], consistent to the discussion above. Within BCS theory, it has been shown that the oscillations of the amplitude of the order parameter decay according to a power law proportional to $t^{-1/2}$ [180]. For the BEC side, this behavior changes to a power law with a different exponent $t^{-3/2}$ [181].

When performing an interaction quench, the observed behavior of the system depends on the initial and final interaction. In the theoretical study of ref. [182], different parameter ranges with qualitatively different behavior have been identified. These can be interpreted as dynamical phases and a corresponding phase diagram is shown in figure 6.1, with the qualitative behavior as a function of the initial and final equilibrium gap values, Δ_i and Δ_f, respectively. There

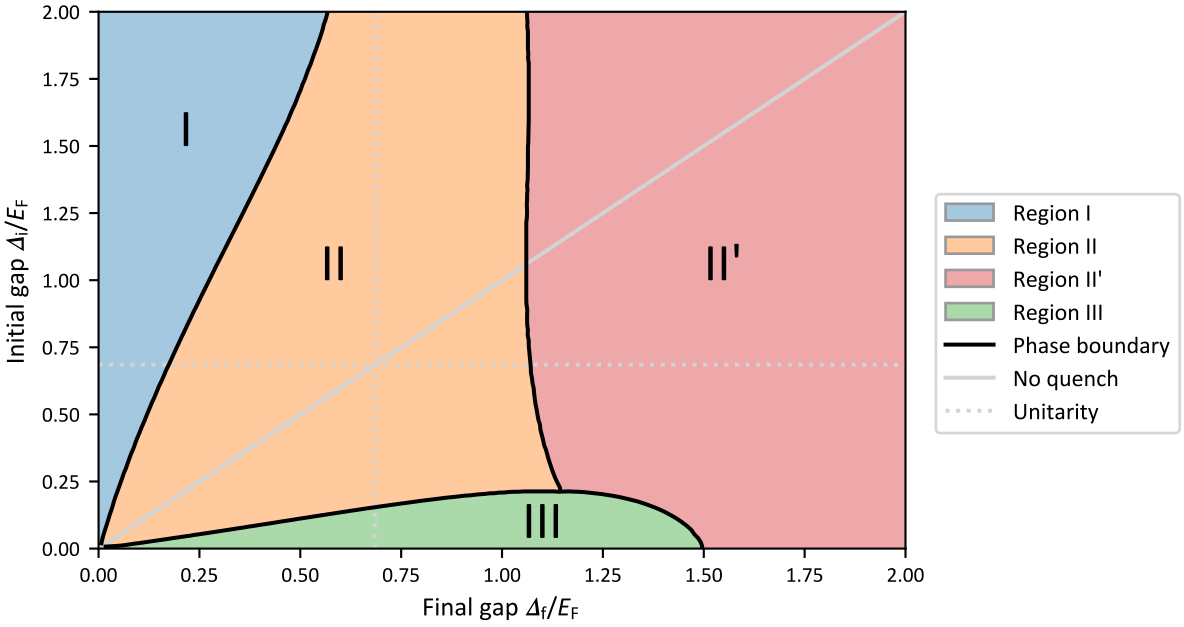

Figure 6.1: Dynamic phase diagram for interaction quenches in the BEC-BCS crossover Adapted from ref. [182]; For the equilibrium values of the gap Δ_i and Δ_f corresponding to the initial and final interaction of a quench, respectively, the theoretical study has identified regions with qualitatively different behavior of the superfluid order parameter: Exponential decay of the order parameter (region I), oscillations decaying with different power laws (region II and II') and persistent oscillations (region III).

are three different regions. Region I describes large quenches towards the BCS side and results in an exponential decay of the order parameter without oscillations. Region III describes large quenches towards the BEC side and results in persistent oscillations of the order parameter. For smaller quenches, oscillations which decay according to a power law are expected, with different exponents in region II and II'. The oscillation frequency $2\Delta_\infty$ in region II can, in principle, deviate from twice the initial gap $2\Delta_\mathrm{i}$ or twice the equilibrium value for the final interaction $2\Delta_\mathrm{f}$. This dynamic phase diagram will be used in the following sections to illustrate the parameters of the performed quenches, although only region II will be probed.

Previous Experimental Results Interestingly, the emergence of these modes is a universal phenomenon and can occur in other systems featuring a similar phase transition [41]. Besides the discovery in particle physics [39], the Higgs amplitude mode has been measured in superconductors [183–185], antiferromagnets [186] and in ^{3}He [41]. While weakly interacting Bose-Enstein condensates do not feature a stable Higgs mode [39], it has been observed in certain other systems of bosonic gases [187–190]. While most detection schemes rely on spectroscopic methods, I want to highlight the observation of the Higgs amplitude mode in the time domain for a superconductor in ref. [184] and for a supersolid coupled to cavities in ref. [190]. For the latter, a clear distinction between amplitude and phase mode was demonstrated by directly measuring the phase of the order parameter during the dynamics.

Strongly interacting Fermi gases in the BEC-BCS crossover provide a clean and easily tunable system, which is suitable to examine the Higgs amplitude mode. Particle-hole symmetry on the BCS side guarantees its stability [42] and it is coupled to the interaction, which can be directly controlled with Feshbach resonances. In this system the Higgs amplitude mode was excited spectroscopically using an RF modulation technique [46] and its precursor in a mesoscopic system in the quasi-2D regime was observed after modulating the interaction via the axial confinement [191].

For an interaction quench of a strongly interacting Fermi gas, the evolution of the contact has been examined [192], but no observation of the Higgs amplitude mode has been reported so far.

6.2 Radio-Frequency Quench

This section describes quenches from strong to weak attractive interaction towards the BCS side of the crossover. The quenches are realized with an RF transition, transferring the population from a strongly interacting to a weakly interacting state, which results in a significantly faster timescale compared to a magnetic field ramp using the Feshbach coils. It is still slower than the Fermi time of the system, but much faster than the trap frequencies. After the quench the monopole mode of the gas is excited, but also a faster initial response of the condensed part of the cloud is observed, which is comparable to or faster than the quasiparticle relaxation time.

This investigation has been published in ref. [1] and has already been described in refs. [98, 193]. Preliminary results can also be found in refs. [96, 97]. Therefore, I will only briefly describe the results with an experimental focus.

Experimental Methods An atomic cloud of the two lowest hyperfine states $|1\rangle$ and $|2\rangle$ of ^{6}Li at deeply degenerate temperatures is prepared, as described in section 3.2. The Fermi energy is $E_\mathrm{F}/h = 29(3)\,\mathrm{kHz}$ and the trap frequencies are $\boldsymbol{\nu}_\mathrm{trap} = (110, 151, 234)\,\mathrm{Hz}$. The initial interaction parameter $1/(k_\mathrm{F} a_\mathrm{i})$ is set to a value in the range of about -0.1 to -0.7, which corresponds to a magnetic field between 880 G and 1000 G.

At the given magnetic fields, a mixture of $|1\rangle$ and $|3\rangle$ state has a weaker interaction, with a parameter in the range of -1.14 to -1.31. Therefore, a fast population transfer from the $|2\rangle$ state to the $|3\rangle$ state effectively corresponds to a quench from strong to weak attractive interaction. This is realized by addressing the RF transition between the states at about 81 MHz. Any immediate change of the interaction energy is absorbed or supplied by the RF field, which causes an interaction shift of the RF transition [4, 194].

Figure 6.2 shows the interaction parameter for the 12-mixture and the 13-mixture over the considered range of magnetic fields, which defines the start and end points of the quenches. A comparison with the dynamic phase diagram above shows that such a quench would be in the region II, but the quench might be too slow to observe damped oscillations of the order parameter.

The RF transition is characterized by measuring Rabi oscillations, as shown in figure 6.3. For strong interactions close to unitarity, the efficiency of the π-pulse drops and the quenches are restricted to the region where the efficiency is at least 88 %. In this region a π-pulse time of 26 µs to 28 µs is achieved, during which a full transfer from $|2\rangle$ to $|3\rangle$ state takes place.

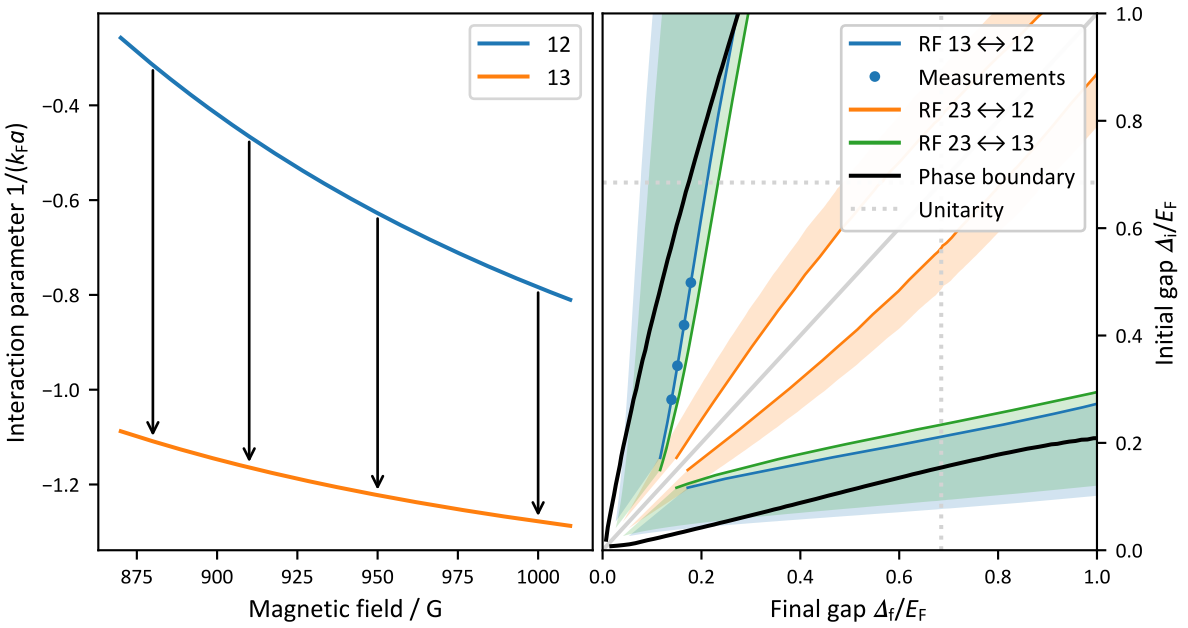

Figure 6.2: Initial and final interaction of RF quenches The values for initial and final interaction parameter are constrained by the Feshbach resonances of lithium for a given atom number. The performed quenches are indicated by arrows **(left)**. Lines in the dynamic phase diagram from figure 6.1 show the quenches which can be realized with this method by the transfer between different state mixtures **(right)**. The shaded areas indicate possible quenches if the atom number is decreased within a reasonable range. Note that the RF transition from a 12 to a 23 mixture is forbidden, but can be realized by applying multiple RF frequencies [96].

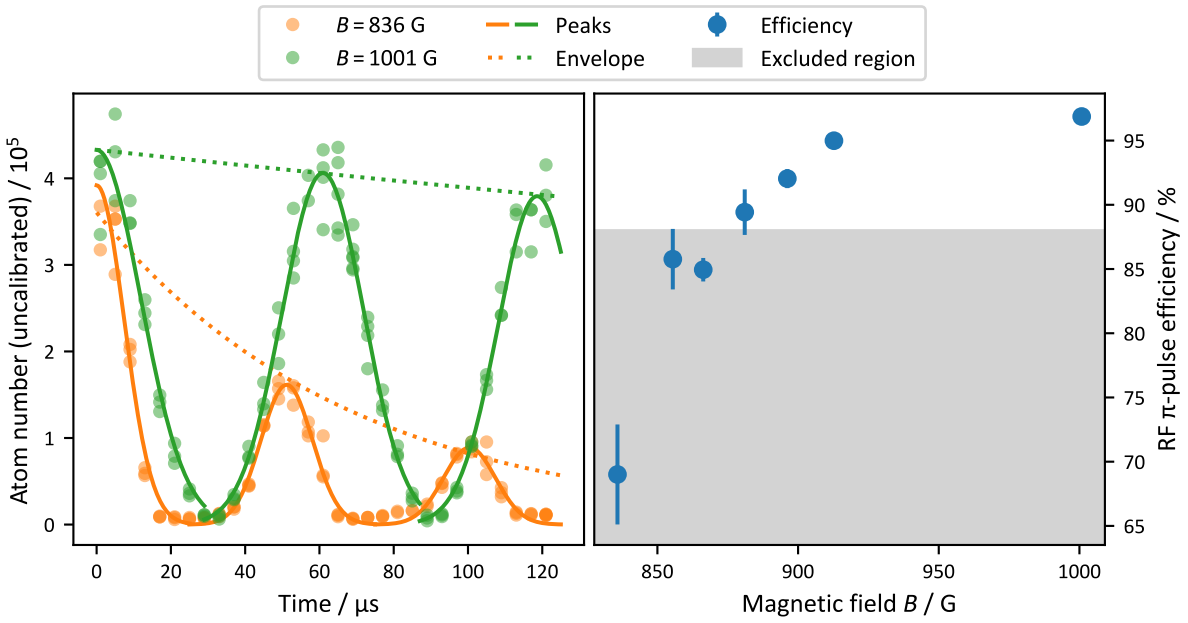

Figure 6.3: Characterization of RF transfer via resonant Rabi oscillations As an example, an efficient RF transfer on the BCS side and a transfer to unitarity with strong losses are shown **(left)**. The data is fitted with Gaussians to determine the π-pulse time, and the efficiency is determined with an exponential fit to the peak atom numbers. The efficiencies are shown for different interactions **(right)** and efficiencies below 88 % are excluded.

Measured Quantities For varying hold time after the interaction quench, the rapid ramp technique is used to measure the condensate fraction. This time, special attention is also directed to the shape of the condensate and the shape of the thermal cloud after time-of-flight. Determining the condensate fraction from bimodal fits is usually very reliable, especially when the fit parameters are restricted to the typical range of values. This is only possible, however, if the size of the condensate is significantly smaller than the thermal cloud. Otherwise, the fit routine often fails to distinguish the thermal part from the condensate and expands it to the full size of the cloud. Here the size of the condensate expands during the measurements, preventing reliable fits with our standard fit routine.

Instead, in a first step, the center of the cloud is masked out, so that only the thermal fraction is fitted with a Gaussian. The mask is chosen large enough to cover the condensate but small enough to allow a reliable fit of the thermal fraction. In a second step, the remaining signal of the condensate is fitted again with a Gaussian. The two Gaussian fits measure the atom numbers of thermal and condensed part of the cloud and consequently the condensate fraction. Additionally, they reveal the widths of thermal and condensed part. Figure 6.4 shows an exemplary measurement and demonstrates how condensate fraction and width typically behave for variable hold time after the quench.

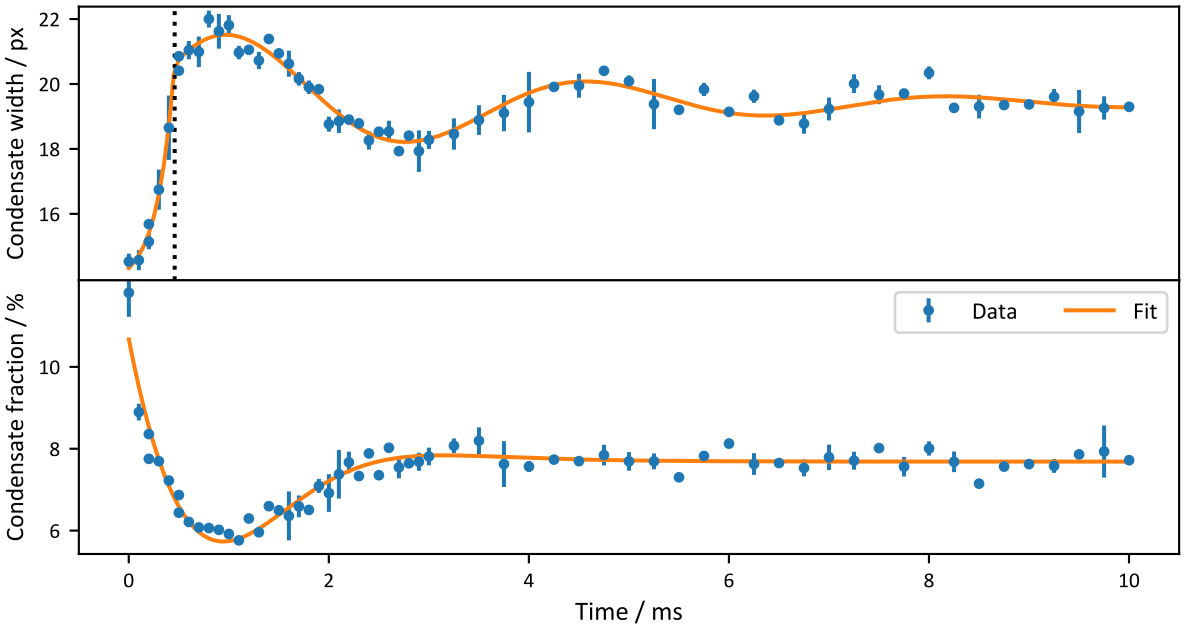

Figure 6.4: Evolution of condensate width and condensate fraction The width features a fast initial rise and a subsequent slower damped oscillation **(upper)**. The condensate fraction shows an initial decay to a minimum value, but then recovers to a higher value **(lower)**.

The width of condensate fraction has a quick initial broadening followed by a slow damped oscillation, which is identified as the monopole breathing mode. The timescale of initial broadening τ_{width} and the mode frequency ν_{mode} are extracted by modeling the data initially for $t < t_{\text{thr}}$ as an exponential growth and later as a damped oscillation[1]

$$f_1(t) = \begin{cases} w_0 + w_1 e^{t/\tau_{\text{width}}} & \text{if } t < t_{\text{thr}}, \\ w_2 e^{-t/\tau_{\text{mode}}} \sin(2\pi\nu_{\text{mode}} t + \phi_0) + w_0' & \text{otherwise.} \end{cases} \tag{6.145}$$

The threshold time t_{thr} can in practice be a fit parameter if the offset w_0' is chosen in a way which guarantees a continuous function.

[1] In ref. [1] this was modeled with two separate functions.

The condensate fraction features a fast decay and a subsequent revival. The behavior is empirically fit with an exponential decay plus a stretched exponential function for the revival

$$f_2(t) = A \exp\left[-t/\tau_{\text{decay}}\right] + B\left(1 - \exp\left[-\left(t/\tau_{\text{revival}}\right)^{\gamma}\right]\right) , \tag{6.146}$$

with the timescale τ_{decay} for the condensate fraction decay, τ_{revival} for the condensate fraction revival and the exponent γ describing the stretching.

Results Figure 6.5 compares the different extracted timescales with the relevant theoretical timescales. The period of the damped oscillation $1/\nu_{\text{mode}}$ is consistent with the expected monopole frequency. The revival of the condensate is surprisingly slow, with a larger timescale than the quasi-particle relaxation time. In contrast, the decay of the condensate and the initial broadening of the condensate width are roughly comparable with the quasi-particle relaxation time, with the former generally slower and the latter generally faster than the relaxation time.

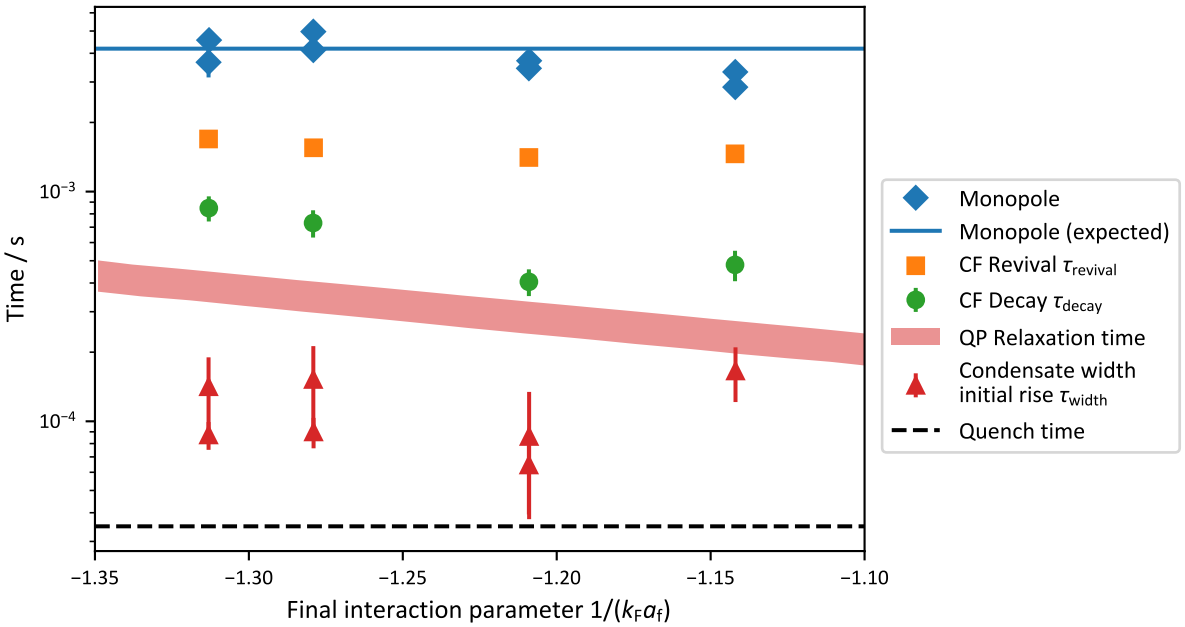

Figure 6.5: Extracted timescales from the dynamics after the interaction quench Adapted from ref. [1]; The period of the excited monopole mode agrees with our expectation. The initial decay and broadening of the condensate are comparable to the quasi-particle relaxation time, while the timescale of the revival is slower.

Theoretical Model The experiment is compared theoretically with a one-dimensional zero temperature attractive Hubbard model. A low filling is chosen to remove lattice effects. All three relevant states are considered and an additional term of the Hamiltonian explicitly models the RF transition. The time evolution is calculated numerically and compared with the experimental results.

Initially, the spread of the pair correlation momentum distribution increases quickly, which can be related to the fast increase of the condensate width in the experiment. The pair coherence, which relates to the experimental condensate fraction, shows a fast initial decrease. For longer evolution times, an influence of the monopole mode on the pair coherence is visible. This can explain why the revival of the condensate fraction is quite slow and closer to the timescale of trap dynamics than the quasi-particle relaxation time.

Conclusion With the RF quench, it is possible to observe fast dynamics of the condensate, which agree qualitatively with the theoretical model. Additionally, the monopole mode of the trapped gas is excited. The revival time of the condensate fraction from its minimum value to the final static value has been observed to be relatively slow in comparison to the quasi-particle relaxation time.

6.3 Fast Magnetic Quench

We have seen in the previous section that the interaction quenches based on RF state transfer are slower than the Fermi time. Therefore, a new dedicated quench coil has been constructed, which allows sufficiently fast interaction quenches on a timescale of 3 µs. It is described in detail in section 3.3. As a trade-off, the current through the quench coil is limited to at most 40 A to prevent over-heating, which also limits the amplitude of possible quenches. To counteract this limitation, the gas is prepared in a mixture of hyperfine states $|1\rangle$ and $|3\rangle$, which has the narrowest of the broad Feshbach resonances of ^{6}Li and therefore enables a change of the interaction by a significant amount. Note that the quench coil only creates an additional offset field which is added to the magnetic field of the regular Feshbach coils, i.e. only the magnetic field difference between initial and final point of the quench is provided by the quench coil.

In contrast to the RF quench, for which initial and final interaction are constrained by the Feshbach resonances and for which the efficiency of Rabi oscillation is only high for a certain region of interactions, this method allows to choose the initial and final interaction freely within a range limited by the maximum current of the quench coil, as illustrated in figure 6.6.

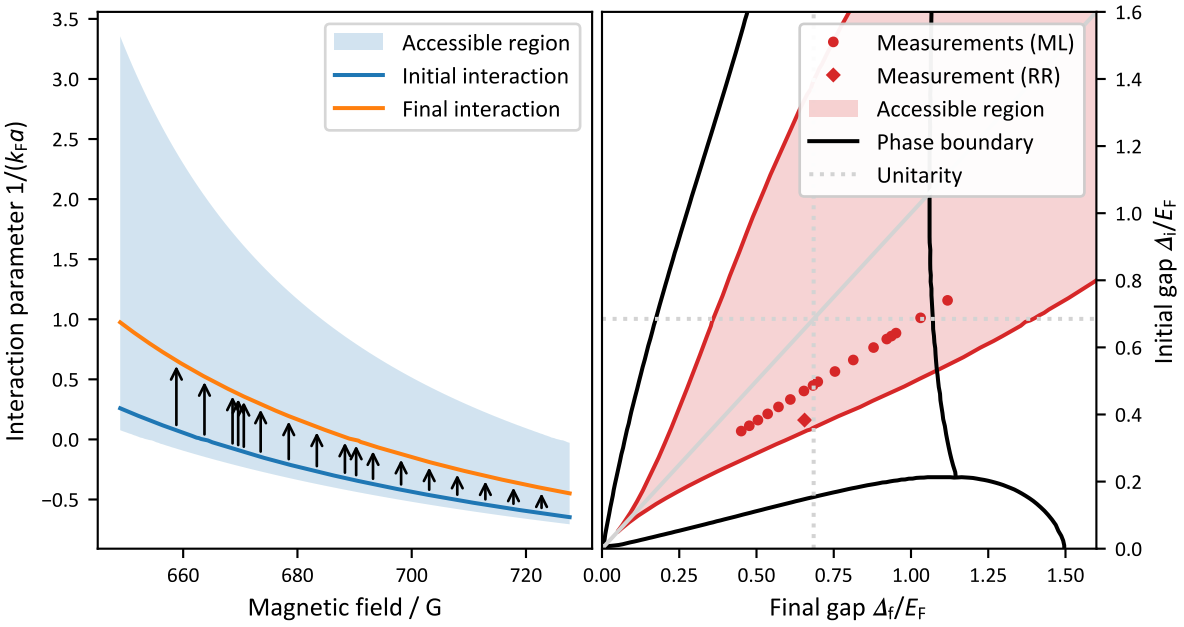

Figure 6.6: Initial and final interaction of fast magnetic interaction quenches The final interaction is set by the magnetic field of the Feshbach coils **(left)** and the additional magnetic field of the quench coil gives access to a certain range for the initial interaction. The actually performed quenches in section 6.3.1 are indicated with arrows. Additionally, these quenches ("Measurements (ML)") are compared to the dynamical phase diagram from figure 6.1 **(right)**. Finally, also the quench from section 6.3.2 is displayed ("Measurement (RR)").

Detection Methods After a variable hold time the condensate fraction is measured, which is closely related to the amplitude of the superfluid order parameter. Previously, this has been done with the rapid ramp technique. However, the results were not conclusive and technical problems have been identified, which become only relevant when very small signals are measured and the hold time before the rapid ramp is varied with a very fine temporal resolution. Instead, for the presented investigation in section 6.3.1 the condensate fraction is extracted from normal time-of-flight images using an artificial neural network trained on rapid ramp data of equilibrated samples, as described in section 6.3.1. This technique avoids the mentioned technical problems, but suffers from a rather low signal-to-noise ratio.

In section 6.3.2 the technical problems of the rapid ramp are discussed and how they can be avoided. Also, the first result of a new investigation based on the rapid ramp is presented.

6.3.1 Detection via Machine Learning Methods

Here, the condensate fraction is predicted by a neural network from time-of-flight images, using the same supervised machine learning approach as in section 5.4.

Indeed, using this method, fast oscillations close to the expected frequency of the Higgs mode are observed, but with a relatively low signal-to-noise ratio and an identification was not possible in all datasets. This leads to the question how reliable the results are and whether the oscillations could also be explained by pure statistical fluctuations of the measured condensate fraction. Therefore, a statistical hypothesis test is employed, which examines whether a background-only description of the data is adequate or whether it should be rejected in favor of oscillations close to the theoretically predicted frequencies.

Experimental Details A balanced mixture of degenerate ^{6}Li in the hyperfine states $|1\rangle$ and $|3\rangle$ is prepared in a harmonic crossed dipole trap, with trap frequencies of $\boldsymbol{\nu}_{\mathrm{trap}} = (108, 142, 199)$ Hz, as described in section 3.2. The atom number is typically 3×10^5 per spin state, which results in a Fermi energy of $E_{\mathrm{F}} = (6N_\sigma)^{1/3} h\bar{\nu}_{\mathrm{trap}} \approx h \times 18\,\mathrm{kHz}$ and a Fermi time of $\tau_{\mathrm{F}} = \hbar/E_{\mathrm{F}} \approx 9\,\mu\mathrm{s}$.

While the quench coil is still off, the magnetic field from the Feshbach coils is adiabatically ramped to the final magnetic field of the quench in the range of 657 G to 720 G, which corresponds to an interaction parameter $1/(k_{\mathrm{F}}a_{\mathrm{f}})$ of -0.5 to 0.9. Then the quench coil is adiabatically ramped up and increases the magnetic field further by 29 G (not the maximum possible value) to the initial value of the quench at an interaction $1/(k_{\mathrm{F}}a_{\mathrm{i}})$ of -0.8 to 0.1. After an initial holdtime, for further thermalization of the inital state, the quench coil is suddenly switched off, removing its contribution to the magnetic field within $\sim$3 µs (timespan during which that magnetic field contribution changes from 90 % to 10 % of its initial value).

Datasets

During this investigation, 32 datasets at different interactions have been taken with more than 30 (typically around 60) repetitions per hold time. The sampling interval of the hold times varies, but typically 41 different hold times in random order have been measured.

Figure 6.7 shows one dataset as an example. The quench excites a monopole mode, which leads to a slow oscillation of the condensate fraction on a millisecond timescale. It is sufficient to model this background as a linear function for hold times below 300 µs or as a quadratic function for some of the datasets with longer hold times. Additionally, the data is fitted to a sine function to describe fast oscillations of the condensate fraction. This is relatively well pronounced for the displayed dataset in figure 6.7, but overall it was not possible to consistently produce good quality fits, requiring a more careful statistical analysis to determine the significance of the observed effect.

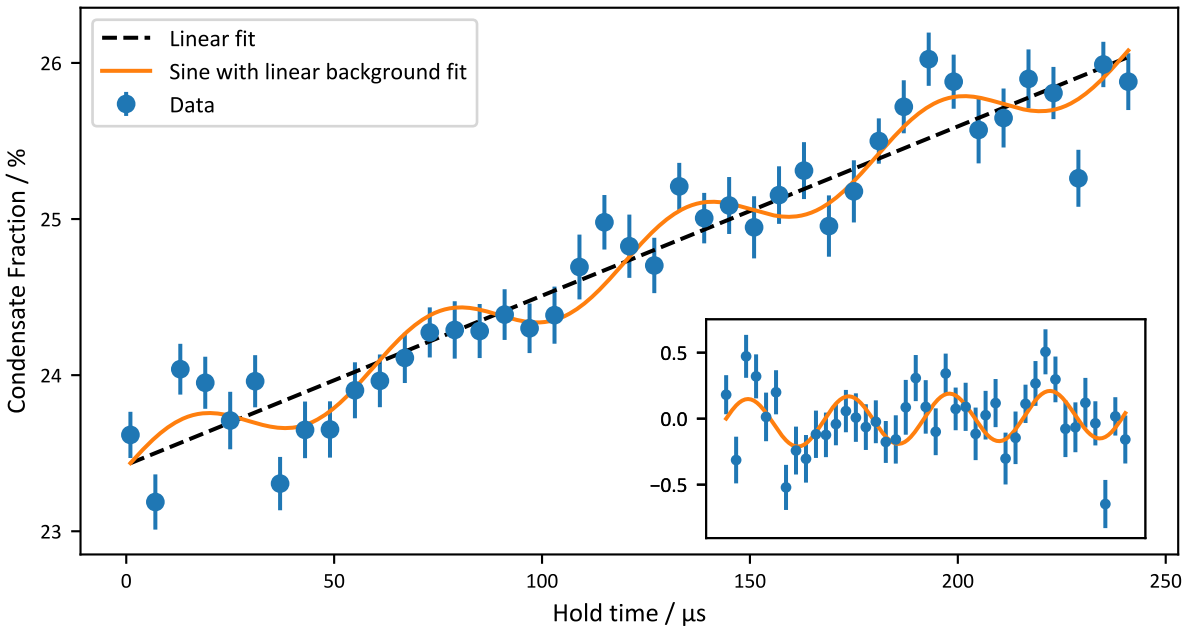

Figure 6.7: Fast oscillation of the condensate fraction during a variable hold time after an interaction quench For the inset, the linear part of the fit has been subtracted. It has the same scales for both axes as the main plot, and the same range for the x-axis, which is omitted. The data is based on a quench from $1/(k_F a_i) = 0.44$ to unitarity

Definition of Hypotheses and Simulation Details

The **hypothesis** is that there are oscillations of the condensate fraction at twice the value of the gap, and the **null-hypothesis** is that the measured condensate fraction emerges purely from the linear or quadratic background and from statistical fluctuations. In order to estimate the significance of the measured data, the quality of the fits is compared to simulated data in a background-only scenario.

Simulation of Background

The accurate background simulation of a dataset requires knowledge of the number of datapoints at each hold time, as well as the background condensate fraction and the noise characteristic, which are extracted for each dataset from the measured data. The noise level is well described by a normal distribution, as demonstrated in figure 6.8.

For some datasets, a weak dependence of the noise level on the background condensate fraction is observed, as shown in figure 6.9. This is attributed to an increased relative error in the detection of small condensate fractions. The dependence is well described as linear and is taken into account. Artificial correlation between neighboring datapoints from experimental drifts is avoided by sampling the hold times in random order during the measurements.

This information allows us to simulate each dataset by generating random numbers with the same noise characteristics and with the same amount of data per hold time. The simulation is repeated 1000 times and analyzed in exactly the same way as the measured data.

I want to mention that multiprocessing is used to speed up the analysis of the simulated data and I want to point out that this requires special care to avoid correlations between random numbers generated by different processes. The random numbers for the simulation are generated by the "PCG64" generator of the *numpy python* library and the recommended seeding method for parallel applications is used.

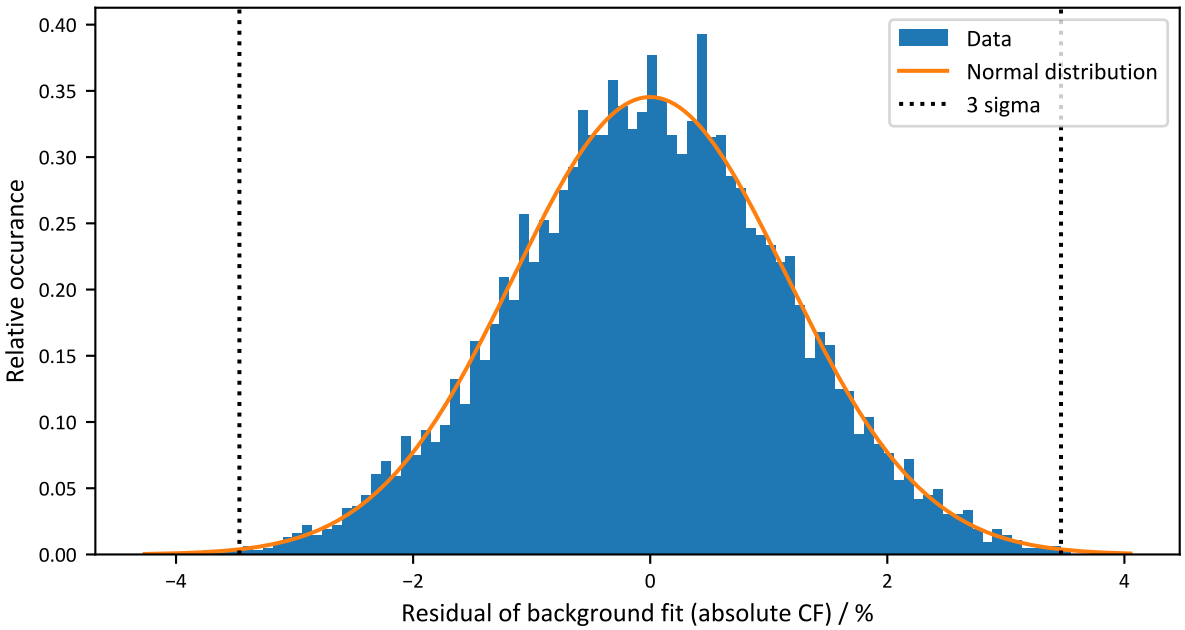

Figure 6.8: Fluctuation of measured condensate fraction around background model The data is based on a measurement for a quench from $1/(k_\mathrm{F}a_\mathrm{i}) = -0.65$ to $1/(k_\mathrm{F}a_\mathrm{i}) = -0.28$, which was selected because for this dataset, each datapoint was repeated 180 times instead of the typical 60 times.

Analysis

For the analysis, it is essential that exactly the same steps are performed for the datasets as for the simulated data. Also, the analysis should be automated as much as possible, to avoid manual choices which could have an effect on the outcome.

At first an outlier removal algorithm is used, which removes datapoints at each hold time until only datapoints within 3σ standard deviation remain. The reason for this is that the experimental data can sometimes contain "bad-shots" if there was e.g. a technical problem during one experimental sequence. This threshold typically only removes 0.2 % of the measured datapoints[2].

Then the data is fitted to the background model of a quadratic function

$$f(t) = at^2 + bt + c \tag{6.147}$$

or, if a dataset has only short hold times, a linear function with $a = 0$. Finally, it is fitted to the signal model

$$g(t) = A\sin(2\pi\nu t + \varphi_0) + f(t)\,, \tag{6.148}$$

with oscillations at a frequency ν and with initial phase φ_0. This frequency ν is restricted to a range of $\pm 20\,\%$ of the expected frequency of twice the theoretical value of the gap based on ref. [53] during fitting. The fit is only sensible if the sampling matches the considered frequencies, so datasets are discarded if they have less than 5 datapoints per oscillation or if their hold times do not span at least 2 full oscillations. According to this rule, we have to remove five datasets because the sampling was not appropriate for the frequencies expected from theory so that 27 datasets with appropriate sampling remain.

[2]The outliers are removed before estimating the noise level for the simulations, which is acceptable because only so few datapoints are removed. Then for the simulations themselves, the same outlier removal algorithm is applied.

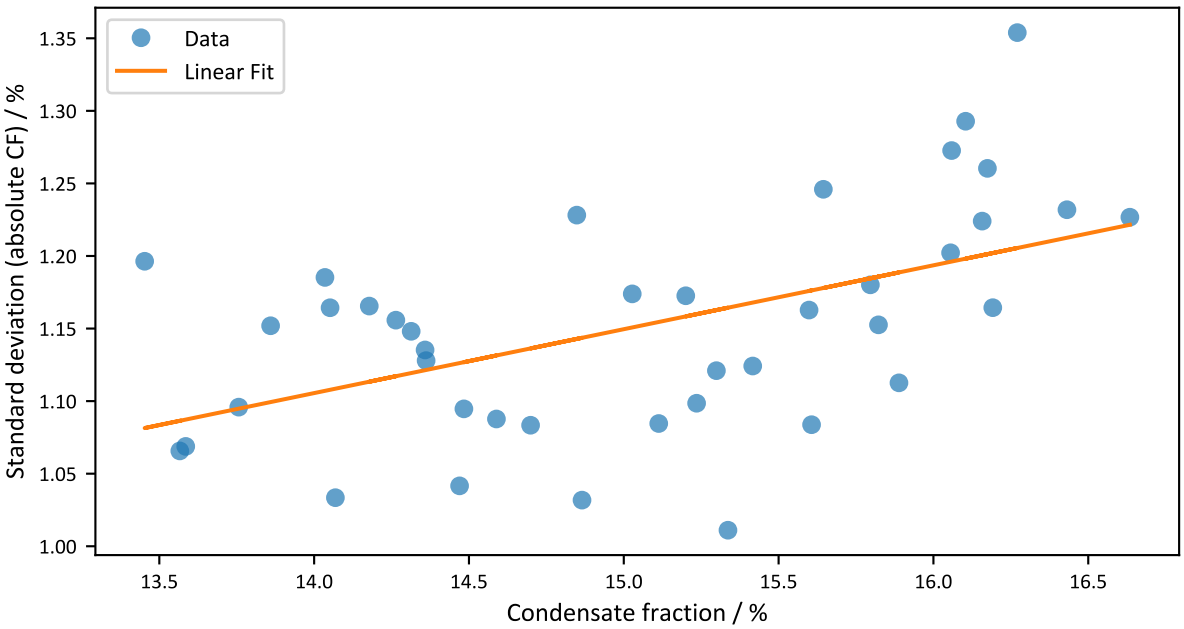

Figure 6.9: Dependence of noise level on condensate fraction Based on the same measurement as figure 6.8, for each hold time, the standard deviation of predicted condensate fractions is calculated as a measure for the noise level and plotted against the mean value. The noise level shows a weak dependence on the condensate fraction, which can be well described as linear (but not proportional) and is taken into account for the simulation of the background.

Fitting the signal model is sensitive to the initial values, so performing the actual fit is preceded by an automatic search for good initial values for ν and φ_0. As illustrated in figure 6.10, several fits with fixed frequency and three different initial values for the phase are performed and the reduced chi-squared value χ^2_r is calculated. Note that for the calculation of χ^2_r, the frequency is counted as a free parameter, so that the result can be compared with the reduced chi-squared of the final fit.

The **quality of a single dataset** q is judged by the reduction of the reduced chi-squared value of the signal model relative to the background model

$$q := 1 - \chi^2_{\mathrm{r,signal}} / \chi^2_{\mathrm{r,background}} \,. \tag{6.149}$$

Figure 6.11 shows the fitted frequencies versus the final interaction of the quench and the quality of each dataset is visualized.

As an **overall merit** of the datasets, the number of "accepted" datasets $n_\mathrm{acc}(q_\mathrm{thr})$ with a quality q above a certain threshold q_thr is considered. On the one hand, the threshold q_thr should not be chosen too small. Otherwise, good and bad fits cannot be discriminated. On the other hand, a too large threshold would cut away signal. Therefore, an intermediate value for q_thr seems reasonable. Indeed, the number of remaining datasets is significantly larger compared to the simulations for a certain range of thresholds between around 4 % and 7 %, as shown in figure 6.12, which considers a range of choices for q_thr.

Still, choosing a particular value for the threshold q_thr would be a decisive manual choice, which should be avoided. Instead, the threshold which generates the largest relative deviation from the average simulated data is chosen. The relative deviation is introduced as

$$d(q_\mathrm{thr}) := \left[n_\mathrm{acc}(q_\mathrm{thr}) - \mu(q_\mathrm{thr}) \right] / \sigma(q_\mathrm{thr}) \,, \tag{6.150}$$

with mean $\mu(q_\mathrm{thr})$ and standard deviation $\sigma(q_\mathrm{thr})$ of the number of accepted fits of the simulated data. The largest relative deviation d_max is selected within a range for q_thr from 0 % to 15 %. It

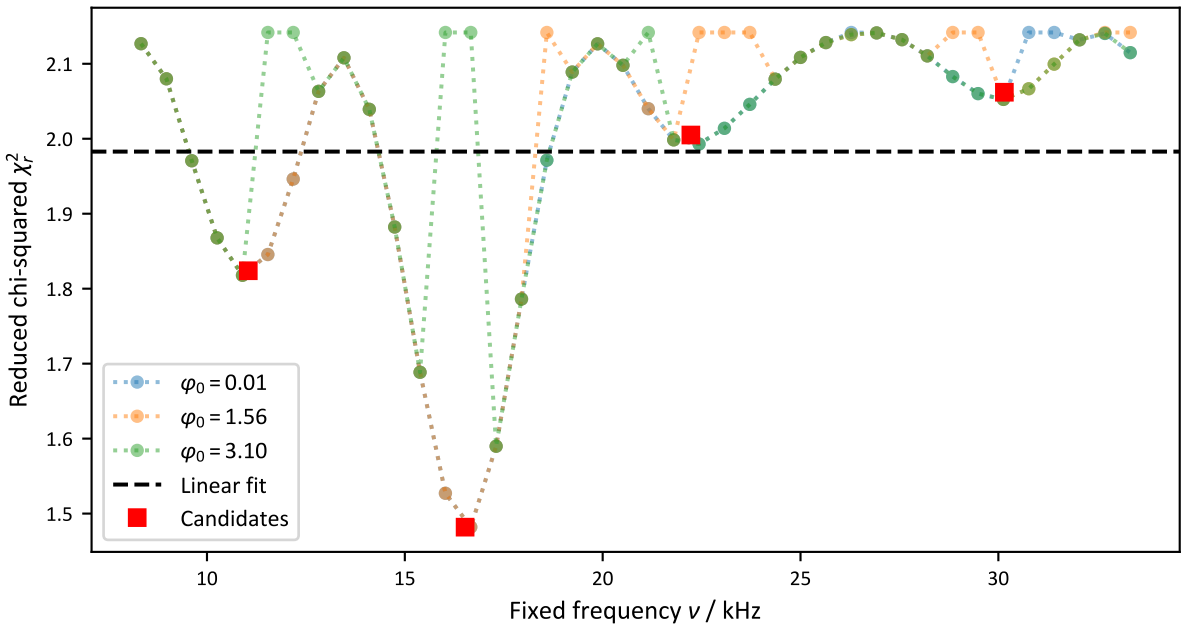

Figure 6.10: Automatic search for good initial values Shown are the reduced chi-squared values of fits, which are performed for a range of fixed frequencies and different initial values of the phase. At local minima, fits with variable frequency are performed and shown as fit candidates. Note that in both cases, the frequency is counted as a free parameter of the fit model, so that the reduced chi-squared values are comparable. Finally, the fit candidate with lowest reduced chi-squared is selected for the further analysis.

should be stressed, that this step must be repeated for simulated datasets in the same way as for the measured data, i.e. also for each simulation the relative deviations $d(q_{\mathrm{thr}})$ are calculated and the largest relative deviation d_{max} is selected.

The distribution of d_{max} for the simulations is shown in figure 6.13 and compared with the real datasets. The measured data yields a larger value for d_{max} than 98.5 % of the simulated datasets, which can be interpreted as a p-value of 1.5 % and implies the rejection of the null-hypothesis.

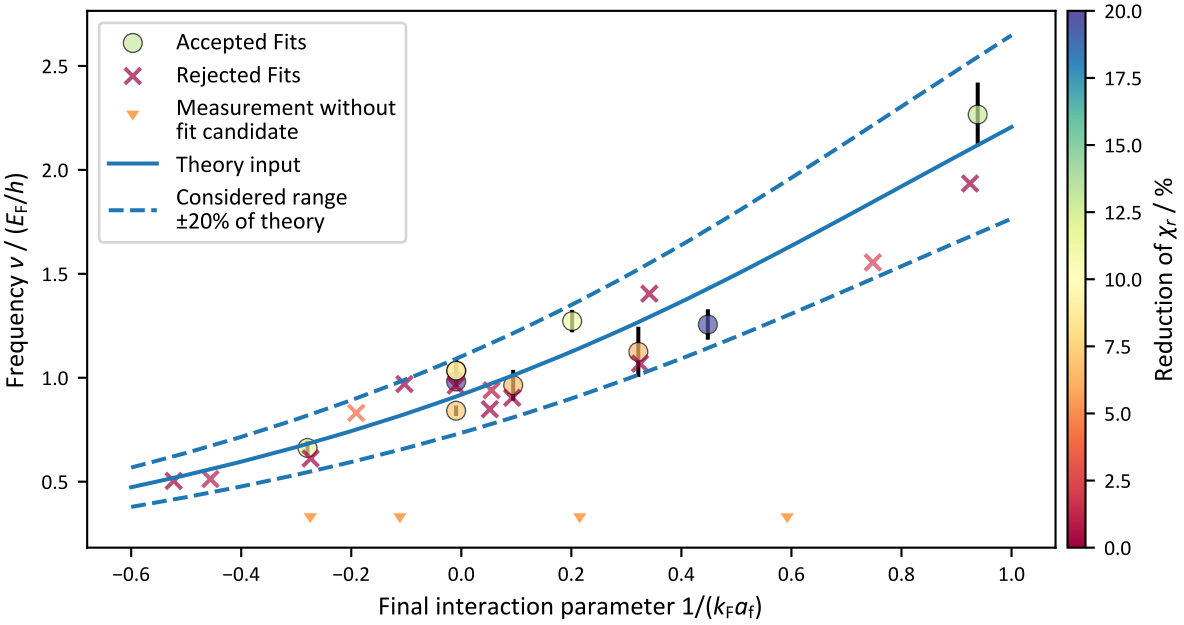

Figure 6.11: Overview of fitted frequencies to experimental data for different interactions Only fits close to the theoretical expectation are allowed within a range of $\pm 20\,\%$. The markers indicate whether the quality of the fits is above a threshold of $q_{\mathrm{thr}} = 5\,\%$, below the threshold, or whether no fit was performed (which is the case if the automatic search for initial values does not produce a fit candidate). Additionally, the quality q of the fits is visualized by the color of the markers. At unitarity, there are four accepted fits, which is not recognizable in the plot due to overlapping datapoints.

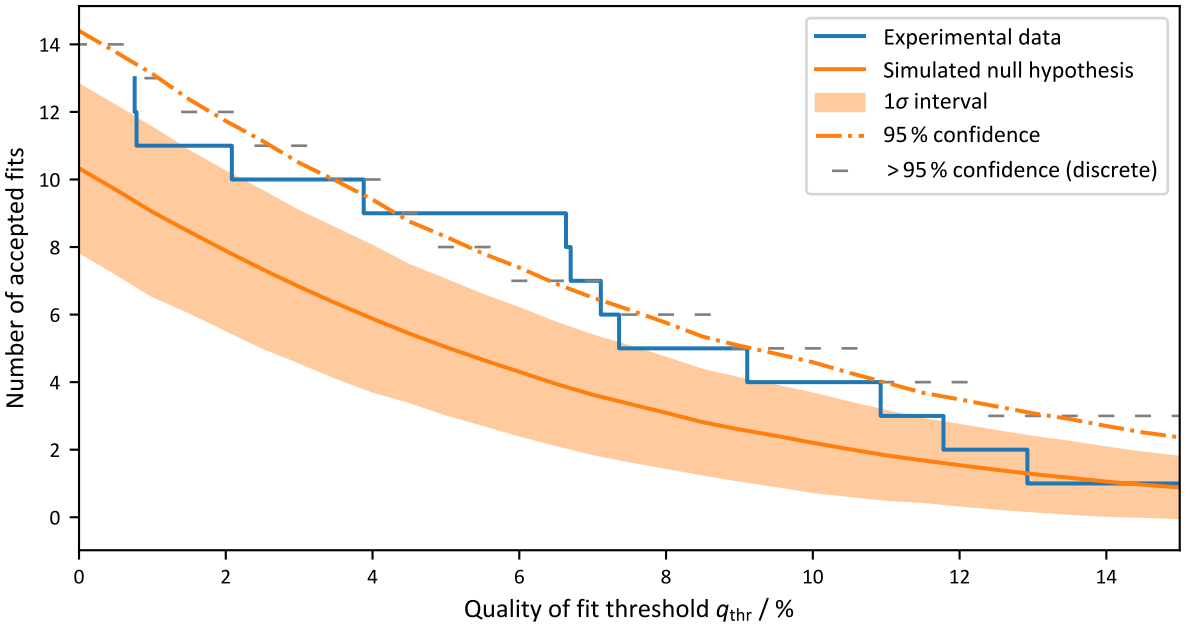

Figure 6.12: Number of accepted fits for different selected thresholds The result for the measured datasets is compared to the average result for the background simulations. For the simulations, the 1σ region and the one-tailed 95 % significance level are also shown. These regions are calculated by assuming a normal distribution of the accepted fits, which matches the actual distribution well, but neglects the discrete nature of the number of accepted fits. Therefore, for several thresholds an upper bound of the 95 % confidence level is additionally determined, without any assumption on the distribution, by counting the number of simulations with less accepted fits. Note that while for a single threshold q_{thr}, only 5 % of the simulations have a larger number of accepted fits than the 95 % confidence level, this is not necessarily true for the whole range of considered thresholds.

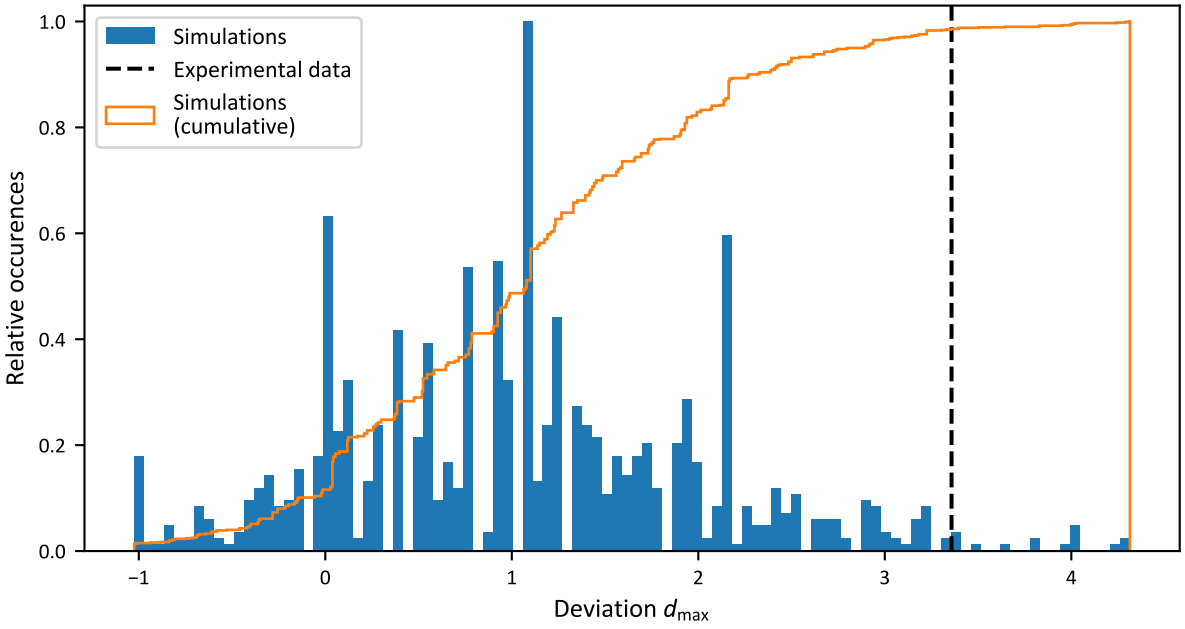

Figure 6.13: Simulated distribution of the maximum deviation compared to the result from experimental data The maximum deviation d_{max} of the experimental data is larger than for 98.5 % of the simulations.

Discussion

Robustness against Choice of Permitted Frequency Range The hypothesis test yields a low p-value for the null hypothesis because the data fits better to the expected Higgs frequencies than fluctuations can explain. The expected Higgs frequencies were supplied by theory as a function of the interaction parameter. To probe the consistency between the data and the theory, the expected frequencies are multiplied by a correction factor α, before they are fed into the hypothesis test. If there is a high consistency between the data and the theory, the hypothesis test should only yield a high confidence around $\alpha = 1$.

Additionally, it might be interesting to change the permitted frequency ranges which are considered for the fits. In general, a wider range of permitted frequencies should reduce the resulting confidence because this provides more opportunity for the simulations to generate fits. However, if the range becomes too narrow, too many datasets are rejected and the confidence also drops.

It is important to state, that changing these two parameters is not used to optimize the result of the hypothesis test but only to examine the robustness of the result.

The robustness against different permitted frequency ranges and different correction factors α is demonstrated in figure 6.14. The plateau around $\alpha = 1$, which is present for all shown frequency ranges, proves that the analysis is robust on the selected frequency range and that the data is consistent with the theory. For different values of α, the confidence is not consistently

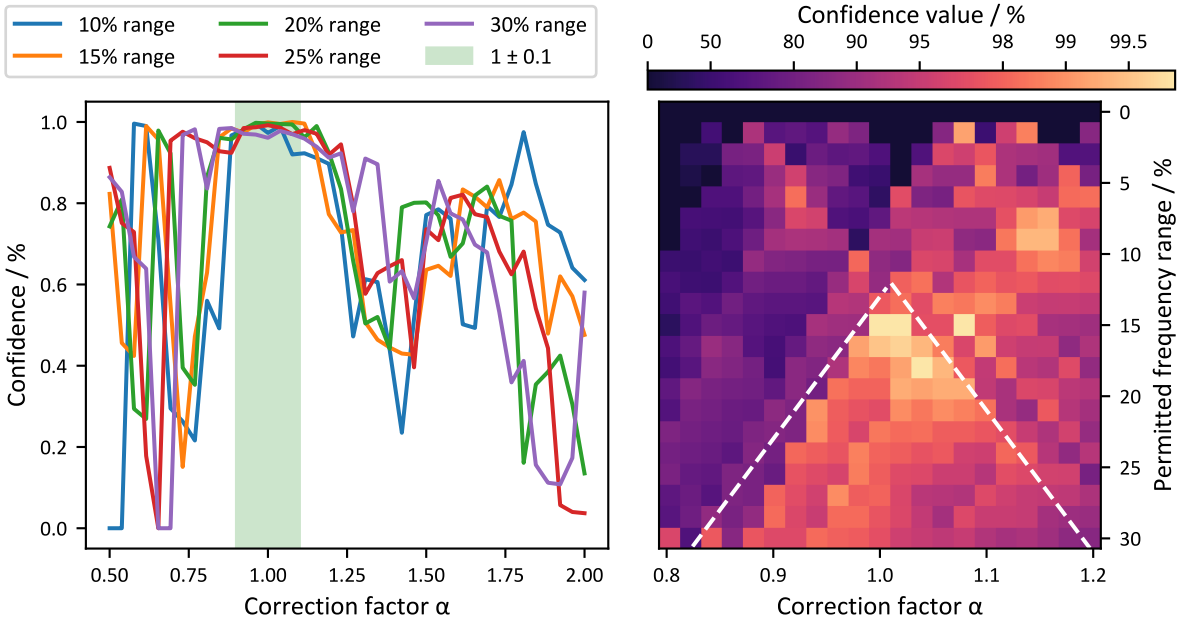

Figure 6.14: Confidence levels for different correction factors and permitted frequency ranges The confidence level has a plateau for the actually expected frequencies around $\alpha = 1$ **(left)**. This behavior is seen for several ranges of permitted frequencies. The same data is also shown as a density plot with a better resolution of different permitted frequency ranges **(right)**.

high for the different permitted frequency ranges.

To make this even more clear, the confidence is also shown in a density plot as a function of the permitted frequency range and α. The white dashed lines (with slope ± 1 and manually chosen offset) indicate a plateau, i.e. a region of good confidence around the expected frequency. As argued above, the confidence increases if a more narrow range of permitted frequencies is chosen because this reduces the possibilities for the simulated data to produce fits with a good quality. Below a frequency range of about 15 % the confidence is reduced. Possible reasons are

a small mismatch between the theory and the actual frequencies (e.g. caused by temperature effects) or experimental imperfection (e.g. systematic error on the atom number).

Previously, the theoretically calculated Higgs frequency was only an input for the investigation, providing the frequency ranges within which fits are performed. But the fact that the confidence level drops considerably when the expected frequencies are multiplied by the correction factor $\alpha \neq 1$ confirms the consistency between the data and the theoretically predicted Higgs frequency.

BCS vs BEC Side The analysis can be performed separately for quenches to the BEC side ($1/(k_\mathrm{F}a_\mathrm{f}) < -.05$), to the BCS side ($0.05 < 1/(k_\mathrm{F}a_\mathrm{f})$) and to unitarity ($|1/(k_\mathrm{F}a_\mathrm{f})| < 0.05$). The results are summarized in table 6.1.

Table 6.1: Results of hypothesis tests when applied to subsets of the measurements

Regime	Number of datasets	d_max	Confidence
All interactions	27	3.4	98.5 %
Unitarity	5	4.4	98.6 %
BCS (excluding unitarity)	8	0.76	38.7 %
BEC (excluding unitarity)	14	2.2	86.1 %
BCS (including unitarity)	13	2.7	93.3 %
BEC (including unitarity)	19	4	99.6 %

For the quenches to the BCS side, the confidence is considerably lower (38.7 %) than for the BEC side (86.1 %) and unitarity (98.6 %). Note that in general, it is expected that the confidence is lower for a reduced number of datasets. If only the quenches to the BEC side and unitarity are kept, the confidence increases to 99.6 %. This is surprising because the Higgs mode should be stable on the BCS side, being protected by particle-hole symmetry, while for the BEC side a faster decay is predicted, although this might be counteracted by slower oscillation times on the BCS side. A possible explanation is that the amplitude of the excited oscillation might be smaller on the BCS side. Also, the interaction quenches which we perform are for technical reasons smaller towards the BCS side than towards the BEC side, which could increase that effect.

About Weak Signal Strength The relatively low signal-to-noise ratio of the datasets implies that the observed peak-to-peak amplitude of the oscillations is below 2 % relative to the background condensate fraction. From theory, a relative amplitude of gap oscillations of roughly 13 % for a larger and instantaneous interaction quench of $1/(k_F a)$ from 0.5 to 0 was expected [69] and a relative amplitude of 1 % for a smaller finite-time quench from 0.55 to 0.6 [195], in both cases for a gas with harmonic confinement along one dimension but homogeneous confinement along the other two dimensions.

A problem of time-of-flight based measurements, like the rapid ramp technique or the extraction of the condensate fraction via a neural network from normal time-of-flight images, is that the observation takes place several milliseconds after the end of the hold time. In principle, one can imagine that the dynamics of the order parameter continue in the initial phase of the time-of-flight (compare to ref. [167], where it was shown that superfluidity can survive the initial phase of time-of-flight). Depending on the duration of these additional dynamics, the oscillations are damped for a longer time, which could explain the low observed signal-to-noise ratio.

6.3.2 Detection via Rapid Ramp

An earlier investigation of interaction quenches based on a detection of the condensate fraction via the rapid ramp technique did not lead to conclusive results. However, we have identified a technical problem of the rapid ramp, which led to a slight variation of its efficiency if the hold time is varied in steps which are not multiples of 100 µs. The reason for this is that analog setpoints were changed during the rapid ramp by using analog channels although they lacked the sufficient temporal resolution. While this effect is rather weak, because the exact curve of the rapid magnetic ramp depends mainly on the digital switching of IGBTs, as discussed in section 4.2, it can have a decisive impact on the measurements if small signals are measured.

Recently, after fixing this problem with a digitally controlled circuit which toggles between two analog setpoints, the first data of a new investigation has been measured and is discussed here.

Experimental Details Similar to the investigation of section 6.3.1, a degenerate 13-mixture of ^{6}Li is prepared but with different parameters. The trap frequencies are $\boldsymbol{\nu}_{\mathrm{trap}} = (138, 154, 184)$ Hz and the atom number is roughly 1.8×10^5 per spin state, which corresponds to a Fermi energy of $E_{\mathrm{F}} \approx h \times 16\,\mathrm{kHz}$ and a Fermi time of $\tau_{\mathrm{F}} \approx 10\,\mu\mathrm{s}$. So far only a single quench has been performed from an initial interaction on the BCS side of the resonance with $1/k_{\mathrm{F}}a_{\mathrm{i}} = -0.54$ to an interaction close to unitarity $1/k_{\mathrm{F}}a_{\mathrm{f}} = -0.05$. Measurements for 76 different hold times have been repeated typically 79 times.

Results The measurement is shown in figure 6.15 and shows a clear oscillation with damping. The data is empirically fit with an exponentially damped sine function with linear background

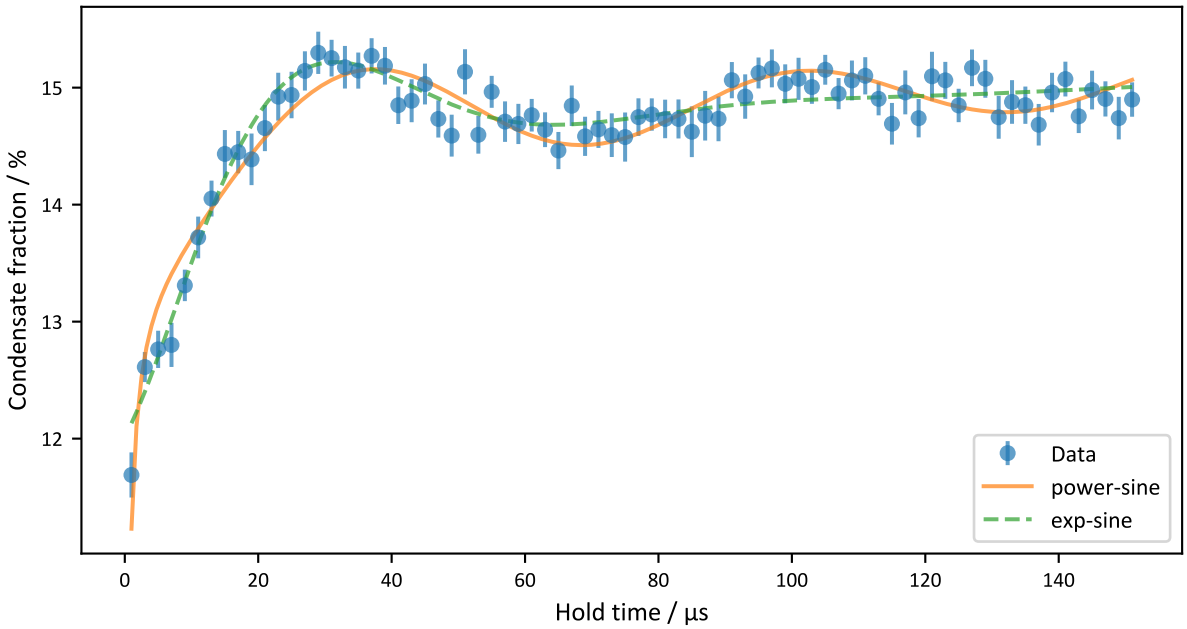

Figure 6.15: Condensate Fraction from Rapid Ramp after Interaction Quench The interaction is quenched from $1/k_{\mathrm{F}}a_{\mathrm{i}} = -0.54$ to $1/k_{\mathrm{F}}a_{\mathrm{f}} = -0.05$. The dynamics is fitted to the functions f_{pow} ("power-sine") and f_{exp} ("exp-sine"), defined in the text, and results in a reduced chi squared value of 1.37 and 0.99, respectively.

$$f_{\mathrm{exp}}(t) = y_0 + mt + A\sin\left(2\pi t\sqrt{\nu^2 - (2\pi\tau)^{-2}} + \varphi_0\right)e^{-t/\tau}\,, \tag{6.151}$$

with oscillation frequency ν, decay time τ and further fit parameters y_0, m, A and φ_0. Additionally, a fit function is employed which captures the theoretically predicted power law damping

$$f_{\mathrm{pow}}(t) = y_0 + mt + At^{\gamma} \sin(2\pi\nu t + \varphi_0)\,, \tag{6.152}$$

with oscillation frequency ν, damping exponent γ and further fit parameters y_0, m, A and φ_0.

The empiric fit with exponential damping yields $\nu = 16(1)\,\mathrm{kHz}$ and $\tau = 21(2)\,\mathrm{ms}$ and the fit motivated by theory yields $\nu = 15.7(4)\,\mathrm{kHz}$ and $\gamma = -0.61(5)$. This matches well to theoretically predicted frequency of $\nu_{\mathrm{Higgs}} = 2\Delta/h \approx 14.1\,\mathrm{kHz}$, based on the gap value of the final interaction according to ref. [53]. The value of the damping exponent γ is also very close to the theoretical expectation $\gamma = -1/2$ for the BCS side [180].

The measurement was repeated a second time with very similar parameters and clearly confirmed the behavior for hold times up to 50 µs, including the negative slope of the oscillation after the first maximum. That measurement was not extended to larger hold times ($t > 50\,\mu\mathrm{s}$) though, so a reasonable fit is not possible and the data is not shown here.

In ref. [195] the evolution of the Higgs amplitude mode in the BEC-BCS crossover for a trapped gas is examined and they find a transition from the BCS value of the damping exponent $\gamma = -1/2$ towards the BEC value of $\gamma = -3/2$. Our current measurement is on one end of the considered range of interactions and agrees well to the theoretical results, as shown in figure 6.16.

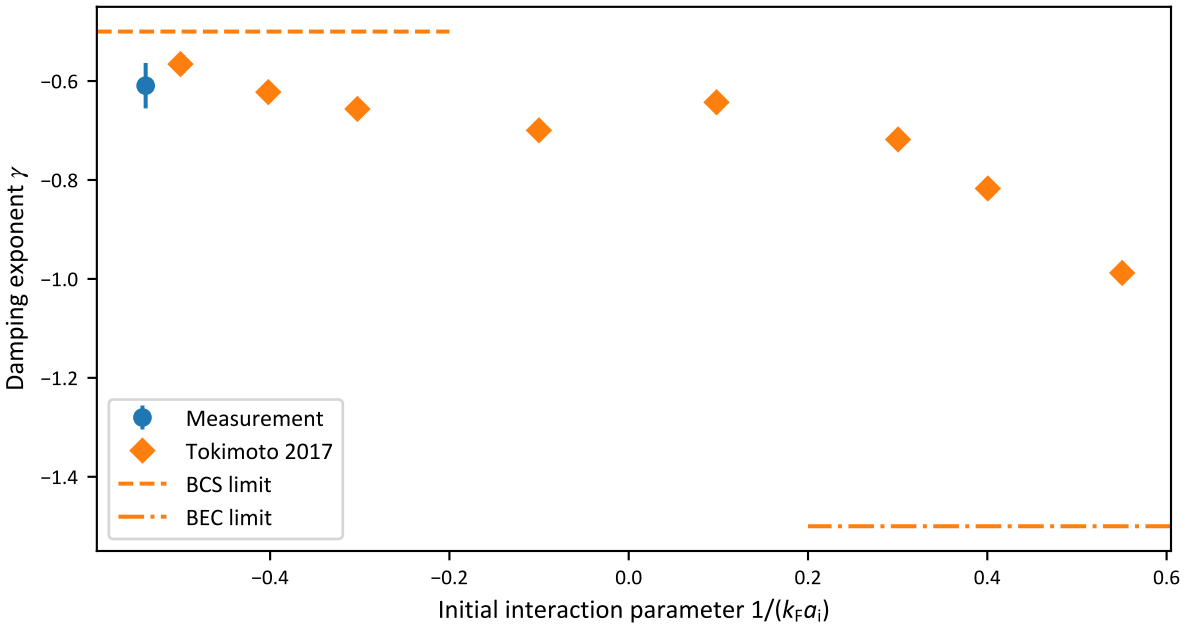

Figure 6.16: Damping Exponent Theoretical results are taken from ref. [195] ("Tokimoto 2017"). Predicted is a non-monotonic transition from the BCS value of $\gamma = -1/2$ towards the BEC value of $\gamma = -1/2$ as function of the initial interaction parameter $1/k_{\mathrm{F}}a_{\mathrm{i}}$. The measured data is consistent to the first theoretically considered quench.

6.3.3 Conclusion

After a magnetic interaction quench which is faster than the Fermi time of the system, an oscillating signal in the condensate fraction has been observed. Due to technical issues and a previous inconclusive investigation based on the rapid ramp, the extraction of the condensate fraction is based on the machine learning techniques of chapter 5. The data quality is not

good enough to extract interesting features like e.g. the exponent of a power law decay. But a hypothesis test has shown with a confidence of 98.5 % that the oscillations cannot be explained only by statistical fluctuations of the background. Additionally, it has been shown that the results are consistent with the theoretical expectations of the Higgs frequency, whereas changing the theory by a factor would lead to a considerably lower confidence.

Recently, the mentioned technical issues have been solved and a first measurement based on the rapid ramp has been performed. The achieved signal-to-noise ratio is sufficient to describe the data with an oscillation, which is damped by a power-law. The oscillation frequency and damping exponent match to the theoretical expectations of the Higgs amplitude mode and this measurement paves the way to verify theoretical predictions about the change of the damping exponent towards the BEC side.

7 Interaction Modulation

This chapter explores how magnetic interaction modulation [70] can be used to examine pairing phenomena in a strongly interacting Fermi gas. The technique constitutes a spectroscopic probe for Feshbach molecules on the BEC side, but also many-body pairing in the superfluid can be probed. Additionally, the excitation method has been proposed as an excitation scheme of the Higgs amplitude mode [69].

In a first investigation the bound state energy of Feshbach molecules close to unitarity is measured, which is a reproduction of an earlier measurement [70]. Additionally, a new detail is found: For small modulation frequencies at unitarity and even on the BCS side, where no Feshbach molecules exist, a finite onset frequency of excitations is measured. This is interpreted as a remnant of the gapped energy spectrum of the superfluid state, which is only partially washed out by the inhomogeneous density distribution of the trap.

In a second investigation a spectral feature is found, which can be identified as the Higgs amplitude mode of the superfluid. The upper bound on the spectral width of this mode at unitarity can be decreased substantially compared to previous studies [46].

7.1 Overview

In a Fermi gas, a modulation of the magnetic field can lead to a modulation of the interaction via Feshbach resonances (see section 2.2.1). It does neither directly act on individual fermions nor transfer momentum. Magnetic interaction modulation has been used to excite collective trap modes and the onset frequency of Feshbach molecule dissociation on the BEC side and a broad pair breaking spectrum for the whole crossover have been measured [70]. For Feshbach molecules also the reverse process, i.e. association of molecules, has been demonstrated [196].

Changing the magnetic field with a reasonable amplitude at a frequency of several tens of kilohertz can be challenging for typical inductances of the coils in the experiment, but is made possible with the new coil built for the quench experiments and a newly built current amplifier, as detailed in section 3.3.4.

Additionally, it has been proposed that a modulation of the interaction enables the excitation of the Higgs mode, i.e. the amplitude mode of the superfluid order parameter [69], which is difficult to excite by other means. An experimental realization of this scheme based on a magnetic modulation of the interaction has not yet been reported.

The Higgs amplitude mode has been measured in a Bose gas in an optical lattice near the superfluid-Mott transition [188]. Here the interaction can be modulated via the lattice depth, i.e. the power of the lattice laser. For a strongly interacting gas in the BEC-BCS crossover, the Higgs amplitude mode has also been measured with an RF dressing method [46], which exploits Rabi oscillation to a third hyperfine state with different interaction properties. In ref. [191] the precursor of the Higgs amplitude mode in a mesoscopic two-dimensional system has been excited by modulating the axial confinement, which influences the two-dimensional scattering length.

The Higgs amplitude mode has also been measured in superconductors. Here, the challenge is that the Higgs amplitude mode has no electric charge and does not directly couple to probes based on electromagnetic fields [41]. An exception are superconductors with a charge-density

wave, for which the Higgs amplitude mode can be detected in a Raman scattering experiment [183]. Recently, it has been shown that the Higgs amplitude mode can still couple to an electromagnetic field in a higher nonlinear order and can be measured with THz pump-probe spectroscopy [184].

A phase transition which features symmetry breaking is usually accompanied with Goldstone modes, which describe fluctuations of the phase of the order parameter, and with the Higgs amplitude mode [39]. However, it is not guaranteed that it is possible to observe a stable Higgs amplitude mode because this requires additional symmetries preventing a fast decay to the phase modes. In particle physics such a symmetry is given by Lorentz invariance, but for a BCS superfluid the particle-hole symmetry can have a similar effect [42]. For superconductors, which feature a superfluid of charged particles, a decay to Goldstone modes is prevented by the Anderson-Higgs mechanism, according to which the Goldstone modes are elevated in energy by coupling to the eletromagnetic field [41].

Still, for the Higgs amplitude mode of a neutral BCS gas, an oscillation of the order parameter at a frequency of $\omega_{\mathrm{H}} = 2\Delta/\hbar$ and a power law decay with exponent of $-1/2$ is predicted [180], which changes to $-3/2$ on the BEC side [181].

Therefore, it would be interesting to characterize the decay properties of the Higgs amplitude mode. While the time-domain signal in chapter 6 is too weak to determine the type of the decay directly, an alternative route is the measurement of the spectral width of the mode. In ref. [46] the Higgs amplitude mode is already measured spectroscopically, but the excitation method has a relatively broad frequency response with a momentum state dependent modulation frequency. This is not a limitation of the interaction modulation via the magnetic field, which should have a much more narrow spectral resolution, as will be discussed in section 7.2.

Comparison to Previous Study Based on Magnetic Interaction Modulation Since the excitation method used in this chapter is very similar to a previous experiment [70], where also an ultracold gas in the BEC-BCS crossover is examined, it makes sense to briefly showcase the results of that experiment and to motivate why, beyond reproduction of the previous results, there was hope to find an additional mode. As can be seen in figure 7.1, the modulation frequency is varied over a large range from 200 Hz to 200 kHz, starting close to the trap frequencies to observe the coupling of the interaction modulation to the breathing mode of the trapped gas. On the BCS side, pair breaking is observed even at very low modulation frequencies. This seems intuitive because the pair breaking should be related to the superfluid gap Δ, which can be arbitrarily small locally in the low density regions of the trap. A different behavior is seen on the BEC side, where a bound state exists, the Feshbach molecule, and leads to a finite onset frequency of excitations which can be identified as the binding energy of the Feshbach molecules.

In our investigation we are interested in the spectrum around the Higgs frequency, but this frequency range was not sufficiently sampled yet by ref. [70]. To make this clear, the frequency range around the expected Higgs frequency is marked in figure 7.1. While the shown data is well sampled logarithmically in their measurement range, there are, indeed, only a few datapoints around the expected Higgs frequency, which provides the motivation to investigate this region in more detail.

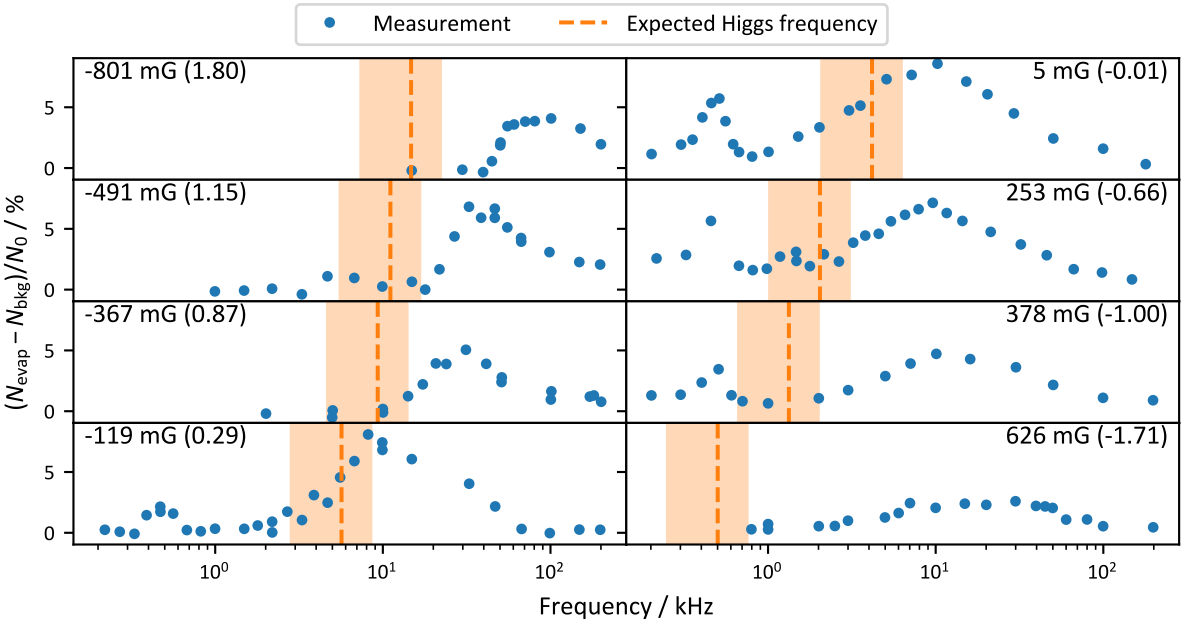

Figure 7.1: Excitation spectra based on magnetic interaction modulation adapted from ref. [70] Based on the stated Fermi energy and theoretical values of the gap Δ [53], the expected Higgs frequency $\nu_{\mathrm{H,\,expected}} = 2\Delta$ is overlayed together with a shaded interval from $0.5\nu_{\mathrm{H,\,expected}}$ to $2\nu_{\mathrm{H,\,expected}}$. This also required to convert the magnetic field values to the interaction parameters, shown in parentheses behind the magnetic field detunings, using the known parameters of the Feshbach resonance for ^{40}K [130, 197]. The panel illustrates that the region around the expected Higgs frequency is not yet sampled very densely, because this was not the objective of that investigation.

7.2 Shape of Modulation and Spectral Resolution

The modulation of the magnetic field at the modulation frequency ν_{mod} and with amplitude A has the form

$$f(t) = \begin{cases} A\sin(2\pi\nu_{\mathrm{mod}}t) & \text{if } 0 < t < t_{\mathrm{mod}}, \\ 0 & \text{otherwise,} \end{cases} \tag{7.153}$$

where the modulation duration $t_{\mathrm{mod}} = n_{\mathrm{mod}}/\nu_{\mathrm{mod}}$ depends on the number of modulations n_{mod}, which is chosen to be an integer value to prevent a discontinuity at the end of the modulation.

When varying the frequency, one strategy is to keep the number of modulations constant at e.g. $n_{\mathrm{mod}} = 50$, which consequently leads to a smaller modulation time for larger frequencies. But in this case it is important to add a wait time $t_{\mathrm{wait}} = t_{\mathrm{wait},0} - t_{\mathrm{mod}}$ after the modulation, keeping the time $t_{\mathrm{wait},0}$ between the start of the modulation and the measurement constant. This guarantees that additional effects like general heating in the trap are the same for all measurements. The effect of a shorter modulation time is understood and is explained in the next section.

A second strategy is to keep the modulation time constant. This requires to choose the modulation frequencies carefully so that n_{mod} is always integer. For relatively long modulation times of around $t_{\mathrm{mod}} = 100\,\mathrm{ms}$ there are many possible values for the modulation frequency so that this constraint is not difficult to fulfill ($\nu_{\mathrm{mod}} = n \cdot 0.01\,\mathrm{kHz}$ with $n \in \mathbb{N}$ for $t_{\mathrm{mod}} = 100\,\mathrm{ms}$).

Currently we do not shape the envelope of the modulation, because the number of modulations is sufficiently large. For shorter modulation times this might become necessary, e.g. by using a haversine function as in ref. [70]. The spectral width of the excitation function f can

be estimated from its Fourier transformation[1]

$$\left|\tilde{f}\left(\omega\right)\right| = A\sqrt{\frac{2}{\pi}}\frac{\sin(n_{\mathrm{mod}}\pi\omega/\omega_{\mathrm{mod}})}{-1+k^2} \tag{7.154}$$

and is shown in figure 7.2, which justifies to use

$$\Delta\nu = 1/t_{\mathrm{mod}} = \nu_{\mathrm{mod}}/n_{\mathrm{mod}} \tag{7.155}$$

or equivalently $\Delta\omega = \omega_{\mathrm{mod}}/n_{\mathrm{mod}}$ as a rough estimation for the spectral width. As mentioned above, typically either a constant $n_{\mathrm{mod}} = 50$ is used, which leads to $\Delta\nu/\nu_{\mathrm{mod}} = 2\,\%$ or a constant $t_{\mathrm{mod}} = 100\,\mathrm{ms}$ for a spectral resolution of $\Delta\nu = 10\,\mathrm{Hz}$ is used. In both cases the resolution is much more narrow than the features which are observed and described in this chapter.

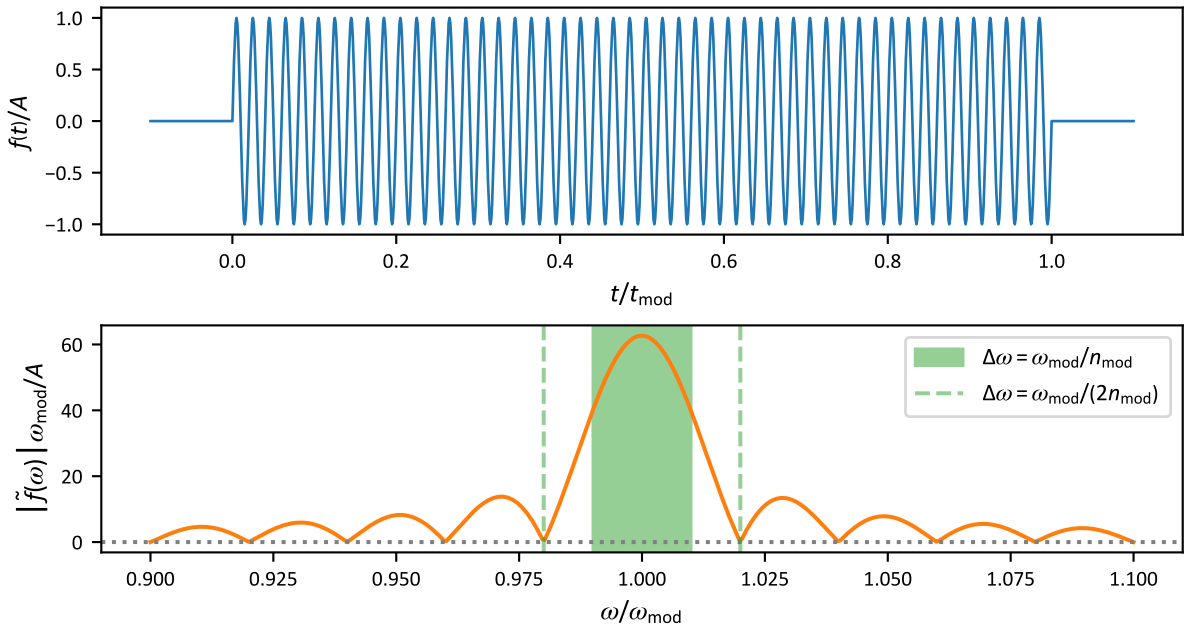

Figure 7.2: Modulation function and its Fourier transform A typical value of $n_{\mathrm{mod}} = 50$ is assumed. The estimation $\Delta\omega = \omega_{\mathrm{mod}}/n_{\mathrm{mod}}$ for the spectral width covers the main spectral weight of the excitation and only slightly underestimates the FWHM.

7.3 Experimental Realization and Description of Investigations

As before, a degenerate Fermi gas is prepared in a balanced mixture of the hyperfine states $|1\rangle$ and $|3\rangle$ as described in section 3.2. While a broad Feshbach resonance is important to stay in the universal regime of the strongly interacting BEC-BCS crossover (discussed in section 2.2.1), the resonance of the chosen mixture is still broad but spans over a more narrow interval of magnetic fields compared to the 1,2-mixture. This makes it technically easier to perform an interaction modulation with a significant amplitude.

After the preparation an interaction modulation is performed, as described in the previous section. The modulation is realized by using the fast magnetic "quench coil" in combination with the dedicated current amplifier, as detailed in section 3.3.4.

[1] Result was obtained by shifting $t \to t - t_{\mathrm{mod}}/2$, which results in a pure imaginary Fourier transformation from which the imaginary unit is omitted to obtain the absolute value.

For all measurements, the atom number is roughly 3.6×10^5 and the trap frequencies are $\boldsymbol{\nu}_{\mathrm{trap}} = (109(1), 158(4), 294(3))$ Hz, which results in a Fermi energy of $E_{\mathrm{F}} \approx 1.1\,\mu\mathrm{K}$. But the parameters of the modulation, including the considered frequency ranges and the considered interactions, change for the different investigation of this chapter. The first investigations are focused on the bound state energy of Feshbach molecules on the BEC side and are denoted as *Boundstate-1* and *Boundstate-2*. The other investigations examine the spectral features around the expected Higgs frequency and are denoted as *Higgs-1* and *Higgs-2*. In both cases, the first investigation is performed with a larger modulation amplitude and a shorter modulation time with constant n_{mod}, while the second investigation is performed with a smaller modulation amplitude and longer constant modulation time.

The parameters for the investigations are detailed in table 7.1 and they will be referenced by their names in the following sections. The goal was to keep the amplitude of the modulation

Table 7.1: Investigation parameters For the measurements either n_{mod} or t_{mod} is kept constant and listed here, while the other parameter is varied and given by $t_{\mathrm{mod}} = n_{\mathrm{mod}}/\nu_{\mathrm{mod}}$.

Name of investigation	Amplitude / G	n_{mod}	t_{mod}/ms
Boundstate-1	2 ... 2.2	50	
Boundstate-2	0.31 ... 0.36		100
Higgs-1	1.4 ... 1.8	50	
Higgs-2	0.3		100

constant, but initially the correct calibration of current amplifier and coil was not known yet so that the amplitude varies slightly for different ν_{mod}. Fortunately, the actual amplitude can be calculated from the final calibration and its influence on the measurement is understood as explained in the next section.

7.4 Observable: Depletion of Condensate Fraction

The measured signal after the magnetic field modulation is the reduction of condensate fraction. This requires to measure the background value of the condensate fraction without performing modulation, for each experimental setting. It is observed empirically that the reduction of the condensate fraction can be described as an exponential decay, which depends on the modulation time and the squared modulation amplitude: $CF \propto \exp(-\Gamma A^2 t_{\mathrm{mod}})$. Here Γ is the variable of interest, which characterizes the response of the system without a remaining dependence on the modulation amplitude A and modulation time t_{mod}. It describes the initial relative depletion rate of the condensate fraction normalized to the squared modulation amplitude[2] and will be called "CF depletion rate" in the following. In ref. [70] a similar response is observed, which is proportional to $A^2 t_{\mathrm{mod}}$. However, without the exponential dependence, which is only seen here because we measure the condensate fraction instead of a signal based on the number of evaporated atoms. This also agrees with theoretical considerations for this excitation method [198].

As a demonstration, figure 7.3 shows the exponential behavior, which is not influenced if the modulation amplitude changes within the considered range. Consequently the CF depletion rate is calculated from the background condensate fraction CF_{B} and signal condensate fraction

[2] Note that the condensate fraction decays exponentially with the modulation time t_{mod} and has a decay constant of ΓA^2, which would be the unnormalized decay constant. The decay constant λ of an exponential decay $A_0 e^{-\lambda t}$ corresponds to the initial relative rate of change, since $\lim_{t\to 0} \partial_t A_0 e^{-\lambda t} = -\lambda A_0$.

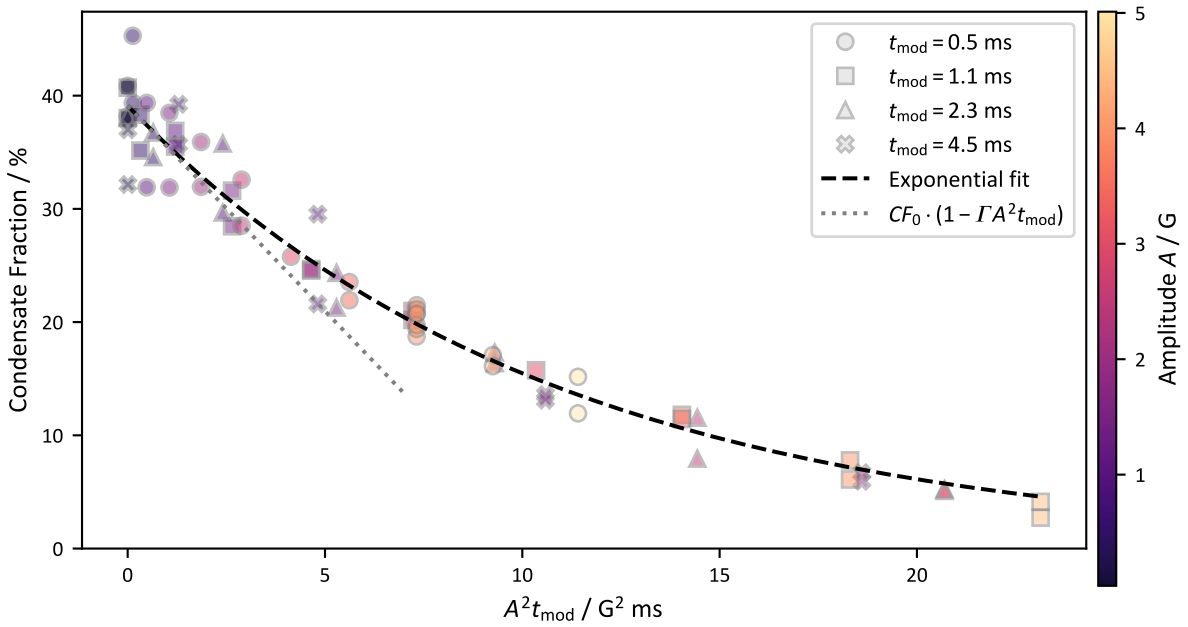

Figure 7.3: Exponential decay of condensate fraction during modulation The datapoints form a single exponential curve versus $A^2 t_{\mathrm{mod}}$, although modulation time t_{mod} and amplitude A are varied. The actual decay constant Γ depends on the experimental parameters (except for t_{mod} and A). For the shown example a magnetic field of 693 G and a modulation frequency of 22 kHz are applied. The interpretation of Γ as initial relative depletion rate of the condensate fraction is also visualized.

CF_{S} as

$$\Gamma = \frac{-\ln(CF_{\mathrm{S}}/CF_{\mathrm{B}})}{A^2 t_{\mathrm{mod}}} \,. \tag{7.156}$$

The result for Γ does not depend on which modulation parameters A and t_{mod} were used, within reasonable bounds. This justifies the usage of different parameters for the measurements, including a slightly varying modulation amplitude.

Measuring the condensate fraction should be more sensitive and easier to implement than the detection of evaporated atoms. One disadvantage is of course that this measurement is only possible at low temperatures, where a reasonable condensate fraction is present, but this is acceptable for the current investigation.

7.5 Molecular Bound State Energy

At first the measurement of a finite onset frequency from unitarity to the BEC side, corresponding to the molecular bound state, is reproduced. While this is successful on the BEC side, at small frequencies and close to the Feshbach resonance deviations from the behavior reported in ref. [70] are observed.

The modulation is performed for different interactions on the BEC side and figure 7.4 shows the measured excitation rates for one of the investigations. Indeed, as one would expect for finite boundstate energies, the CF depletion rate Γ is consistent with zero up to an onset frequency ν_{onset}. For higher frequency the excitation rate increases and fits well to a linear function in the considered frequency range. Overall, the dependence can be modeled with a

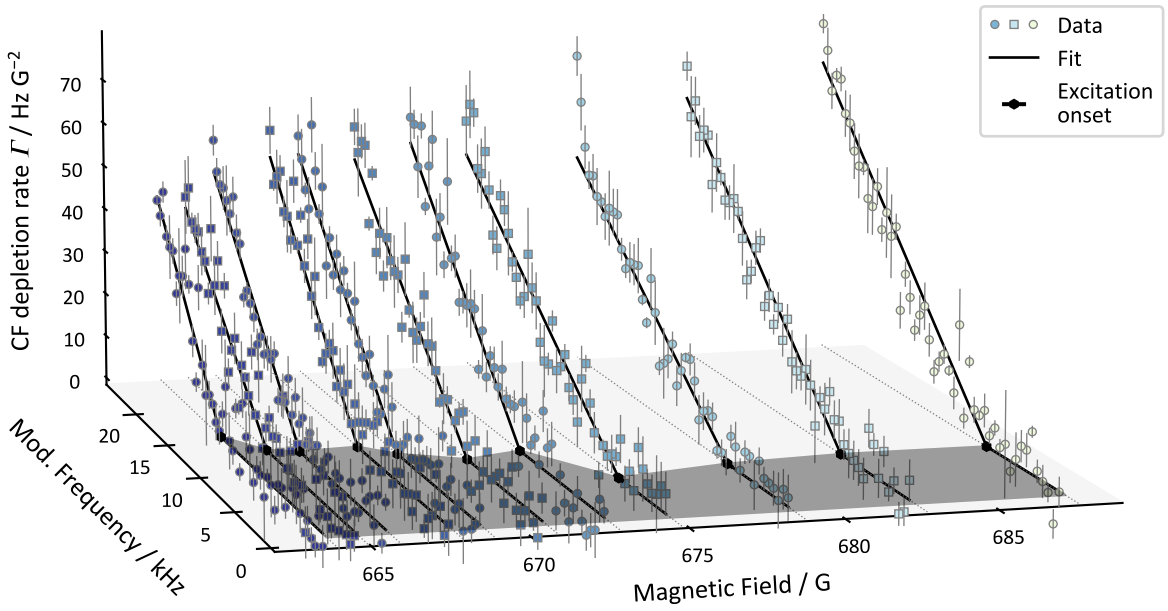

Figure 7.4: CF depletion rate versus modulation frequency for various fields on the BEC side close to unitarity The onset of excitations is determined via piecewise constant-linear fits. The data is based on the *Boundstate-2* investigation (results for *Boundstate-1* are similar).

piecewise constant-linear function of the form

$$\Gamma(\nu_{\mathrm{mod}}) = \begin{cases} \alpha\,(\nu_{\mathrm{mod}} - \nu_{\mathrm{onset}}) & \text{if } \nu_{\mathrm{mod}} > \nu_{\mathrm{onset}}, \\ 0 & \text{otherwise.} \end{cases} \tag{7.157}$$

This allows the extraction of the onset frequencies shown in figure 7.5. The expectation is that the onset frequency corresponds to the binding energy of a molecule given by equation (2.14) $\epsilon_{\mathrm{B}} = -\hbar^2/(ma^2)$, because this is the minimum energy required to break a molecule. A quadratic fit to the data on the BEC side matches very well to the calculation of ϵ_{B}, but it is obvious that the datapoints close to unitarity, where the bound state should vanish, cannot be explained in this way.

To demonstrate the validity of the performed fits, they are shown for the lowest and highest magnetic field in more detail in figure 7.6. Indeed, the onset is very sharp, even for the field very close to unitarity, and the observed deviation cannot be attributed to a bad fit. Note that any technical imperfections, like a too large excitation amplitude or noise in the excitation signal, would probably lead to excitations below a finite onset frequency but do not explain an increased onset frequency. On the BEC side molecules can be broken in all parts of the trap. On the BCS side the interaction modulation is expected to have only a small effect on unbound fermions in the thermal density of the gas, while mainly the breaking of Cooper pairs in the superfluid part of the cloud should contribute to the heating. Although the required energy of 2Δ to break a Cooper pair is arbitrarily small close to the edge of the superfluid, most Cooper pairs are further to the center of the trap and require a finite energy to break. This motivates the hypothesis, that one still gets a finite onset frequency on the BCS side, which might be only slightly washed-out by the trap inhomogeneity.

At unitarity and for small positive interaction parameters, one still expects a vanishing small onset frequency corresponding to the molecular bound state. The bound state is described by two-particle physics and the description should be valid in the thermal parts of the cloud. But in the condensed part of the cloud many-body physics must be considered and the pairing energy

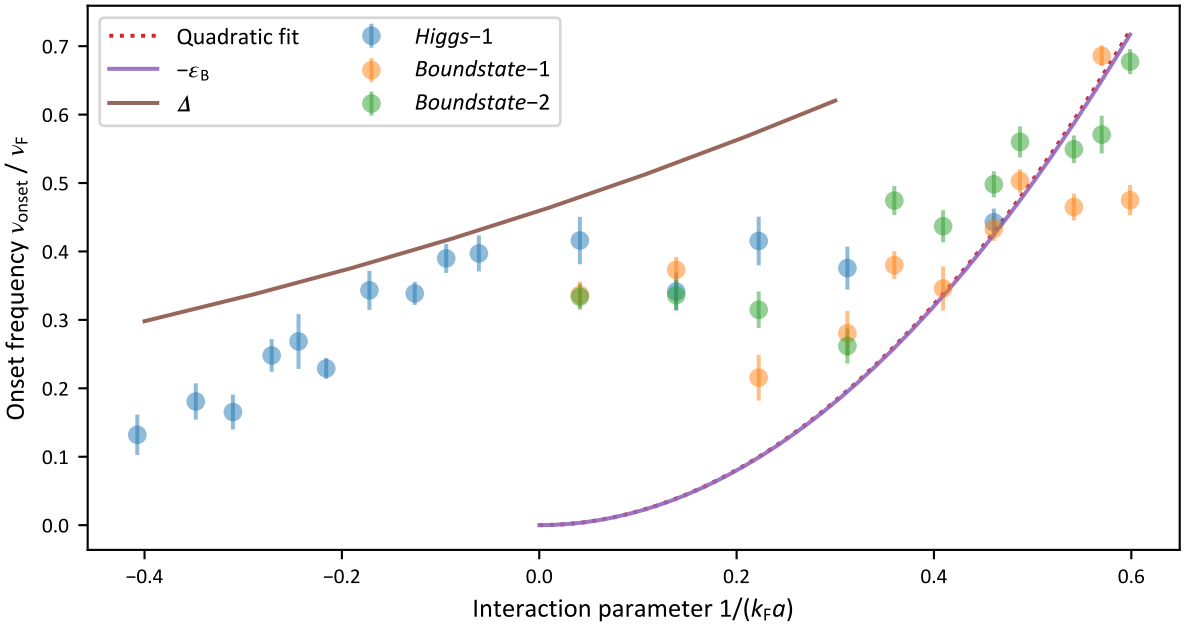

Figure 7.5: Onset frequency of excitations for different interactions in comparison to the expected Feshbach molecule bound state energies Due to the finite onset frequencies close to unitarity, the data from the *Boundstate* investigations are complemented with data from the *Higgs-1* investigation measured on the BCS side. Also shown is the value of the gap from ref. [53], which could be related to the observed finite onset frequency at unitarity and the BCS side.

is still connected to the gap Δ, which is valid as long as $\mu > 0$, i.e. roughly for $1/(k_F a) < 0.5$ [4]. In principle both excitation modes, excitation of the two-particle bound state, as well as of the many-body pairing, are possible but the pair excitations might be dominant closer to unitarity. There is also the possibility, depending on the interaction, that pair correlations already become relevant in the non-condensed parts of the cloud [199].

The measurement of a finite onset frequency seems to contradict the results reported in ref. [70], where excitations on the BCS side for arbitrarily small frequencies are reported. But note that the onset frequency which is measured here would correspond to roughly 1.5 kHz for their Fermi energy. This is already close to their parametric heating frequency $2\nu_{\mathrm{trap,r}} = 690\,\mathrm{Hz}$ and would be therefore difficult to measure for their experimental parameters.

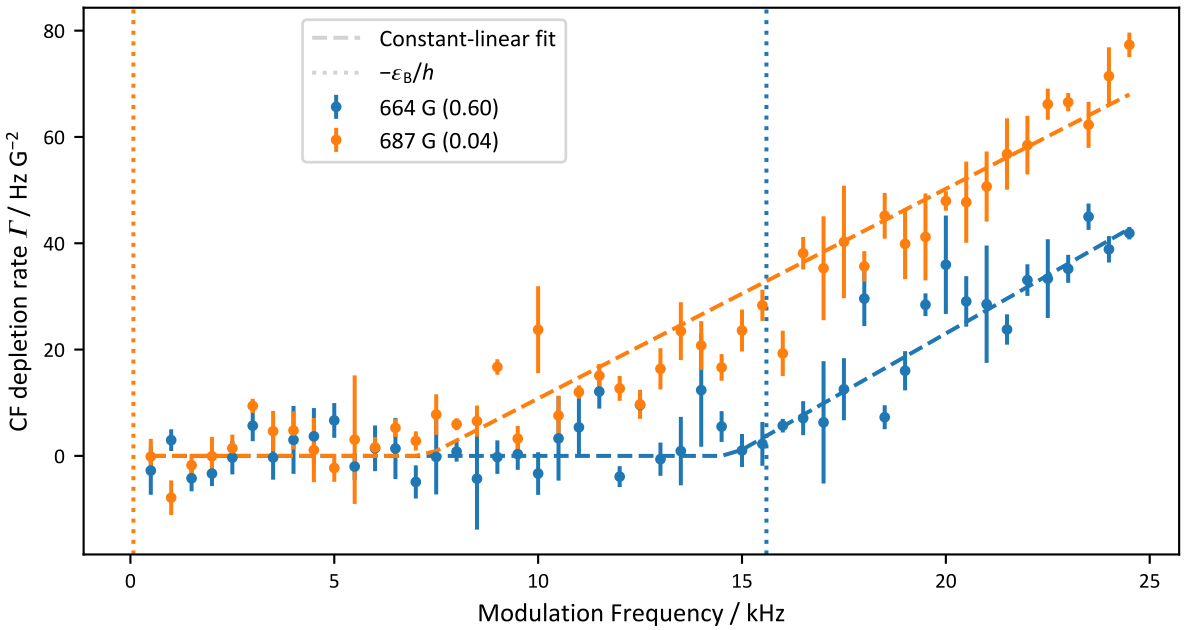

Figure 7.6: Examples for finite onset frequencies A finite onset is observed even at 687 G, very close to unitarity. The interaction parameters $1/(k_F a)$ are given in the legend in parentheses behind the magnetic field and the calculated bound state energies are shown for comparison. The data is from the *Boundstate-2* investigation (behavior for *Boundstate-1* is similar).

Simple Model for Finite Onset Frequency at Unitarity To support the hypothesis that even in a harmonically trapped strongly interacting gas a finite onset frequency can be observed without the presence of a feshbach molecule, a very simple model is developed for the zero temperature unitary gas. Here the bound state energy has vanished and the gas can be described with a very simple equation of state.

The excitation rate of Cooper pairs is assumed to be proportional to the density of pairs, which at unitarity and at zero temperature is proportional to the total density of the gas and can be described with a Thomas-Fermi profile, as discussed in section 2.6.1,

$$n_\sigma(\boldsymbol{r}) = \frac{8}{\pi^2}\frac{N_\sigma}{R_x R_y R_z}\left[1 - \frac{x^2}{R_x^2} - \frac{y^2}{R_y^2} - \frac{z^2}{R_z^2}\right]^{3/2}, \tag{7.158}$$

with the rescaled unitary Thomas-Fermi radii in direction $i \in \{x, y, z\}$

$$R_i = \xi^{1/4} a_{\mathrm{ho}} (48 N_\sigma)^{1/6} \bar{\omega}/\omega_i \,. \tag{7.159}$$

For simplicity, we assume $R_x = R_y = R_z$ and to better exploit the radial symmetry of the trap, we will consider the "Shell density" in the following, i.e. the density of the cloud integrated over a sphere with radius r, which reads $n_{\mathrm{shell}}(r) = 4\pi r^2 n(r)$.

To excite a cooper pair, a minimum energy of $\nu_{\mathrm{mod}} h \geq 2\Delta$ is required. Any additional energy $\nu_{\mathrm{mod}} h - 2\Delta$ is converted into kinetic energy and contributes to heating and depletion of the condensate fraction.

These considerations already allow for an analysis of the heating of the trapped gas. This can be explained with figure 7.7, which shows all relevant quantities. While the density of the gas has its maximum in the trap center, the shell density, which considers the 3D geometry of the trap and better reflects the relative contributions of different parts of the trap to the heating process, has its maximum further outside. Closely related to the density is the local Fermi energy, which is also proportional to the local gap.

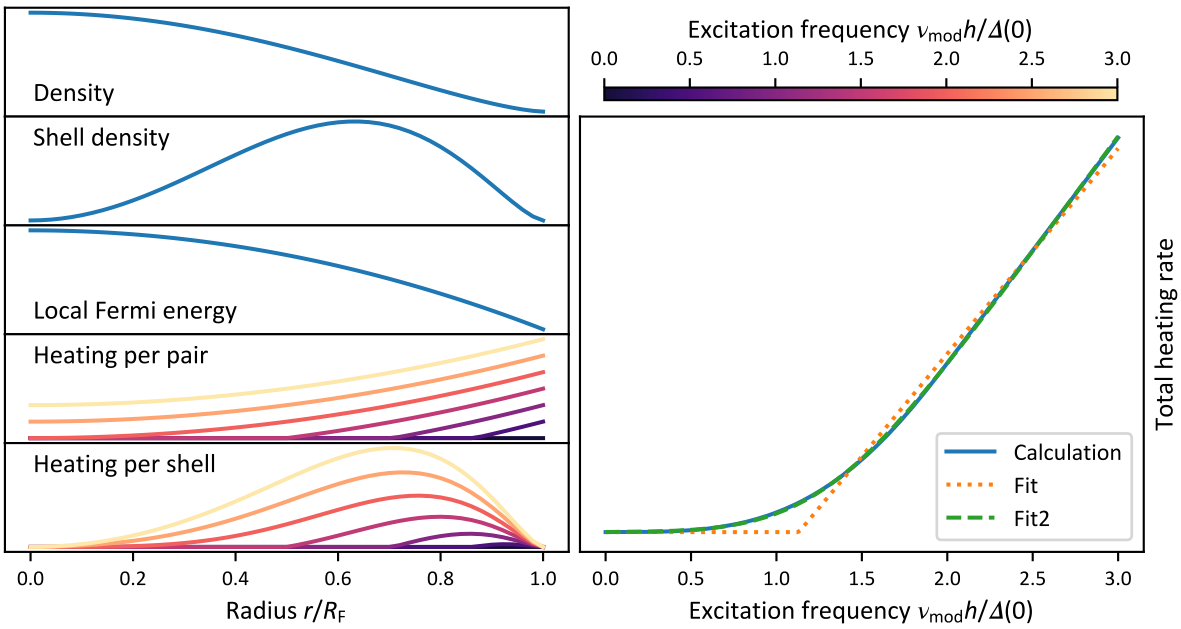

Figure 7.7: Simple model for the heating rate caused by interaction modulation All quantities are normalized to the corresponding maximum value because the model is not able to predict an absolute value for the heating rate. Consequently, the (linear) y-axis scale is omitted. The modulation frequency is given in units of the central value of the local gap $\Delta(0)$.

At low modulation frequencies only Cooper pairs at the edge of the cloud can be excited, while for larger frequencies more and more locations of the trap show excitation of Cooper pairs. Here the heating energy per Cooper pair is considered and also the more relevant heating energy per shell.

Finally, the contributions of heating can be integrated over the whole trap, which gives the total heating rate. Intuitively, one can argue that the shell density provides a certain range of modulation frequencies over which many Cooper pairs start to contribute to the heating rate. This leads to a curvature in the total heating rate versus modulation frequency. But below and above this range the deviation from a constant-linear function is not very large, until the slope becomes truly linear for modulation frequencies above $2\Delta/h$. A fit yields an onset frequency of roughly $1.1\Delta/h$, which is only slightly above the actually measured onset frequencies in figure 7.5.

As a fit function, which can also describe the washed-out region of the apparent onset frequency, one can convolute the constant-linear function with a Gaussian function with standard deviation σ, yielding

$$f_\mathrm{b}(\nu_\mathrm{mod}) = \frac{m\sigma}{\sqrt{2\pi}} e^{-(\nu_\mathrm{mod}-\nu_\mathrm{onset})^2/(2\sigma^2)} + \frac{1}{2} m \left(\nu_\mathrm{mod} - \nu_\mathrm{onset}\right) \left[1 + \mathrm{erf}\left(\frac{\nu_\mathrm{mod} - \nu_\mathrm{onset}}{\sqrt{2}\sigma}\right)\right] , \quad (7.160)$$

for slope m and apparent onset frequency ν_onset. As demonstrated in figure 7.7, the function fits well and will be used in the next section to describe the onset of pair excitations.

Note that this model neglects any temperature effects, which would e.g. modify the density distribution of pairs. Towards the BEC side the situation becomes more complicated, because additionally the excitation of Feshbach molecules has to be considered.

Simple Model for Finite Onset Frequency at Different Interactions Away from unitarity, gap and chemical potential are not proportional to the local Fermi energy (for constant a).

Instead, they can be calculated from BCS theory. For negative scattering length $a < 0$, the lowest excitation is pair breaking at an energy of 2Δ. If the chemical potential at the trap center is negative, the lowest excitation has the character of Feshbach molecule dissociation at an energy of $2\sqrt{\mu^2 + \Delta^2}$ (as discussed in section 2.4.1). In between these two regimes, both excitations can be the lowest excitation at different positions of the trap and this region is not considered for this simple model. Additionally, compression effects are neglected and for simplicity the density distribution of an ideal Fermi gas is assumed.

Then the onset frequency can be determined in the same way as for the previous model for the unitary gas. The results are shown in figure 7.8 and demonstrate qualitatively similar

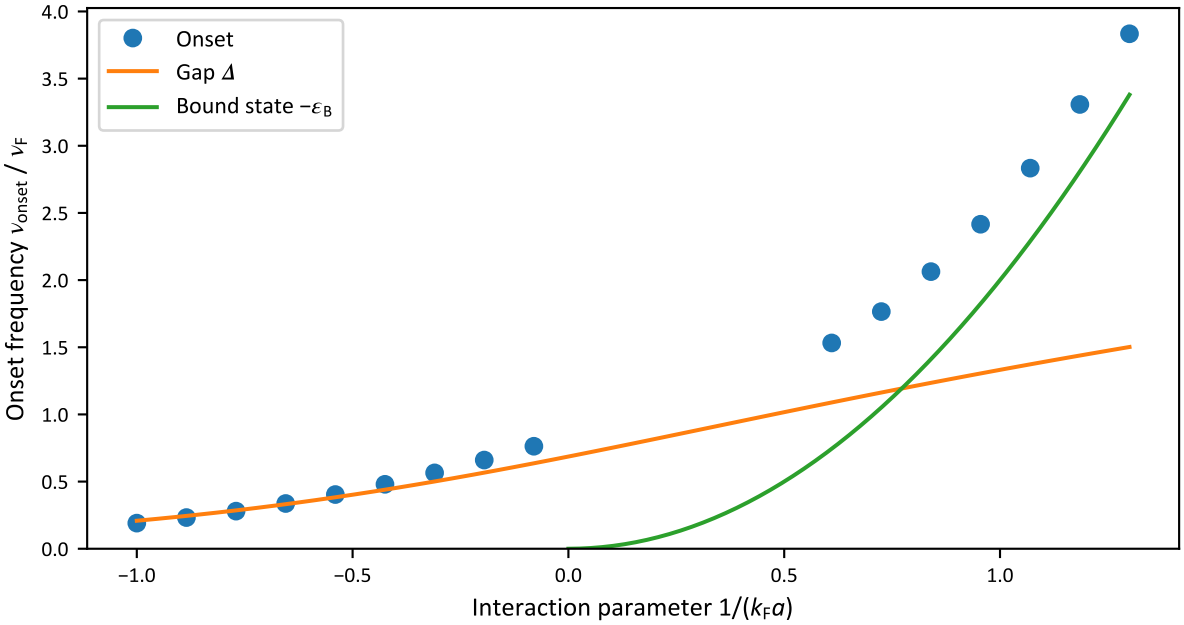

Figure 7.8: Onset frequencies of interaction modulation for a trapped gas based on BCS theory The result is compared with gap at the trap center and with the energy of Feshbach molecules on the BEC side. For small positive $1/(k_F a)$, data is excluded because both, Feshbach molecule dissociation and pair breaking, are relevant which requires a more complicated model.

behavior as the measured results in figure 7.5.

7.6 Spectroscopy near the Higgs Amplitude Mode

In the *Higgs-1* investigation (larger amplitude, shorter t_{mod}, constant n_{mod}), the excitation is measured in a wide range around the expected Higgs frequency for various magnetic fields in the strongly interacting regime. This section will at first focus on this investigation and later the results will be complemented with more measurements from the *Higgs-2* investigation (smaller amplitude, longer constant t_{mod}) in a narrower region around the observed features.

Figure 7.9 shows the remaining condensate fraction versus modulation frequency. As before, the reduction of the condensate fraction is converted into the CF depletion rate Γ in figure 7.10 according to equation (7.156).

7.6.1 Caveat: Artificial Prominent Minima

The comparison of the measured condensate fraction with the calibrated CF depletion rate in figure 7.11 reveals that the clear minimum in the condensate fractions becomes a much fainter

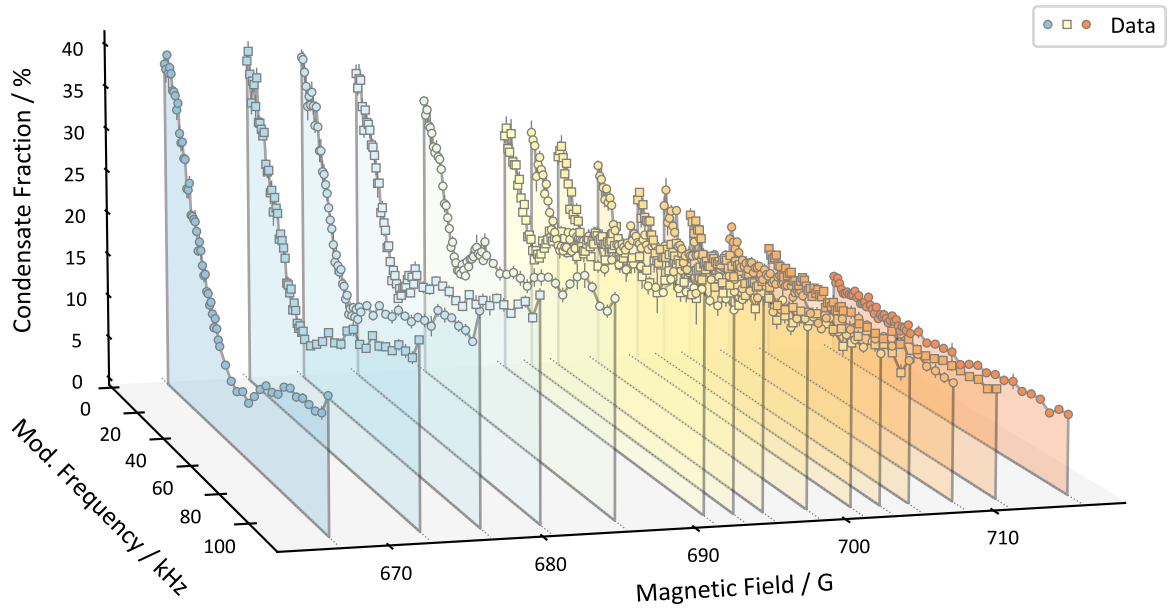

Figure 7.9: Remaining condensate fraction versus modulation frequency for various magnetic fields On the BEC side a prominent minimum is visible, but this is partially an artifact, as explained in the main text.

feature in the calibrated data. The reason why the bump in the calibrated data gets more prominent in the uncalibrated data is an interplay between generally larger CF depletion rates at higher frequencies and shorter modulation times $t_{\mathrm{mod}} \propto 1/\nu_{\mathrm{mod}}$, which are used for the *Higgs-1* investigation. The applied modulation time t_{mod} is known very precisely, which means that the remaining bump in the data is a real effect, although it might be more challenging to evaluate than the clear minimum in the uncalibrated data.

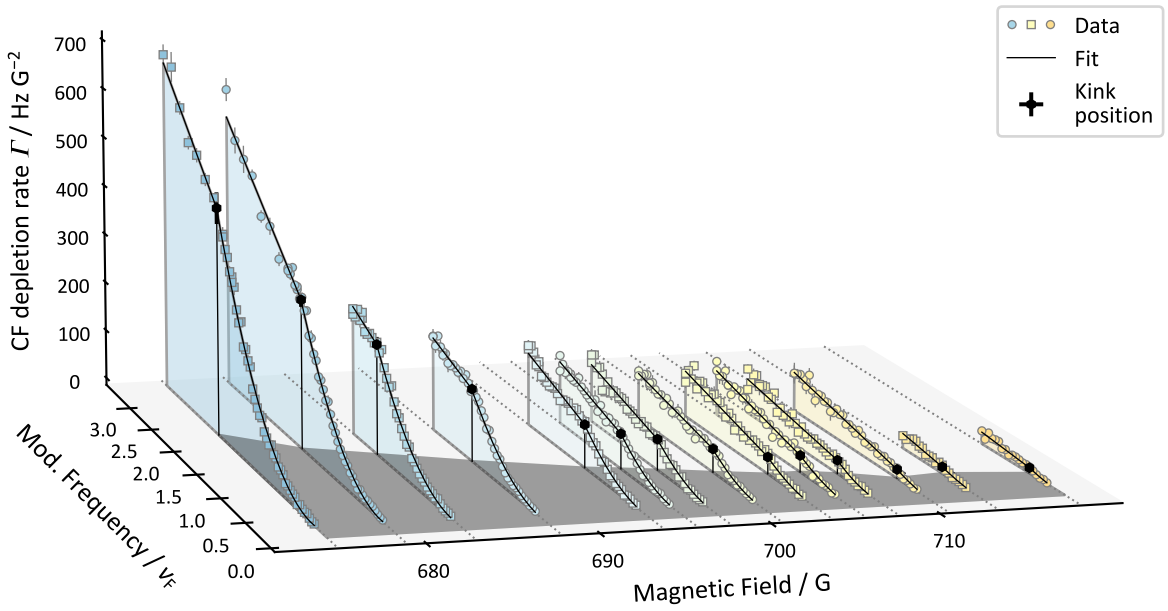

Figure 7.10: Excitation rate versus modulation frequency for various magnetic fields An empiric is used to determine the position of the kink. Due to the lower signal-to-noise ratio on the BCS side, the considered modulation frequencies are restricted to a smaller range around the kink position.

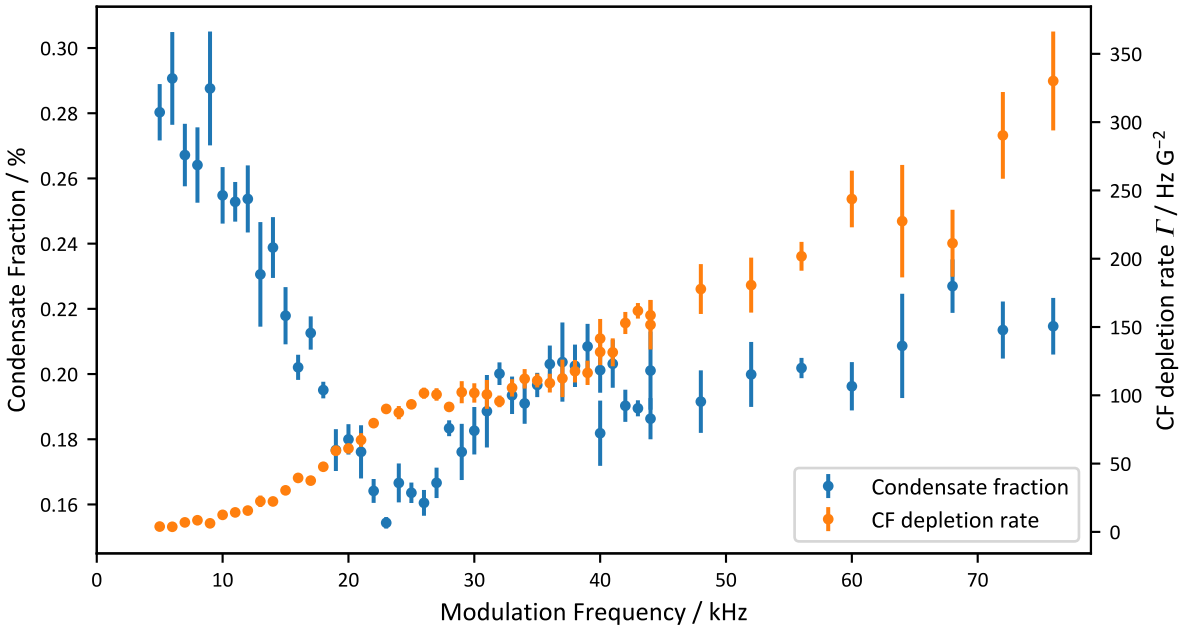

Figure 7.11: Comparison between raw data (Condensate fraction) and calibrated CF depletion rate Shown is the measurement at 693 G of the *Higgs-1* investigation.

7.6.2 Interpretation of Observed Features

Empiric Model The observed behavior is that the CF depletion rate increases towards higher modulation frequencies in the considered range, but there is a clear kink at a certain frequency, which shifts with different interactions. At first the data is fit to an empiric model to extract the kink positions: For low modulation frequencies a quadratic dependence is assumed and above the frequency corresponding to the kink a linear dependence is assumed

$$f(\nu_{\mathrm{mod}}) = \begin{cases} a\,(\nu_{\mathrm{mod}} - \nu_{\mathrm{offset}})^2 & \text{if } \nu_{\mathrm{mod}} < \nu_{\mathrm{kink}}, \\ \Gamma_{\mathrm{kink}} + b\,(\nu_{\mathrm{mod}} - \nu_{\mathrm{kink}}) & \text{otherwise,} \end{cases} \tag{7.161}$$

where $\Gamma_{\mathrm{kink}} = a\,(\nu_{\mathrm{kink}} - \nu_{\mathrm{offset}})^2$ is chosen to get a continuous function and a, b and ν_{offset} are further fit parameters. Figure 7.12 demonstrates for some exemplary magnetic fields that this model fits the data reasonably well. Therefore, the kink positions are extracted without putting too much interpretation into the model. Note that in order to get good fits for all considered

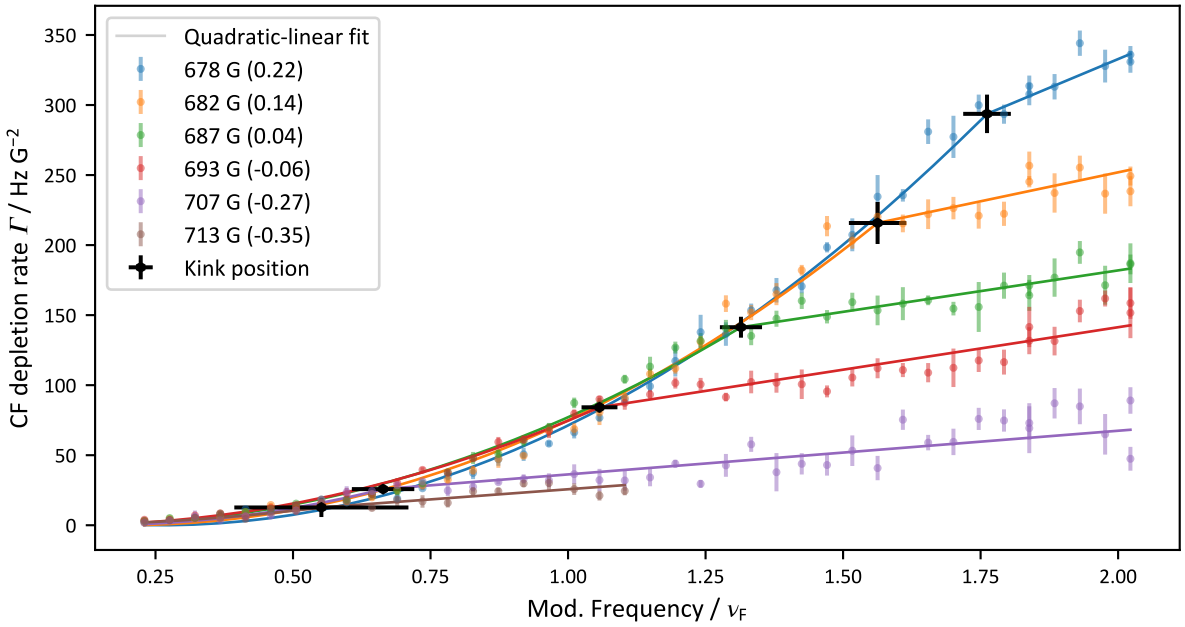

Figure 7.12: Empiric quadratic-linear fit to the CF depletion rates for a selection of fields Interaction parameters $1/(k_{\mathrm{F}}a)$ are given in the legend in parentheses behind each magnetic field.

interactions, data for frequencies much higher than the kink position are omitted.

Signal-Background Model As another approach, the possibility is explored to interpret the feature at the kink position as a peak, which also requires an appropriate model for the background. For this purpose the data around the kink position is masked in a relative interval of $\pm 40\,\%$ around ν_{kink} and it is tested how well several functions can describe the data, as illustrated in figure 7.13. A linear background fits well on the BCS side, but leads to large deviations on the BEC side. A quadratic function can also fit the background on the BEC side and would be a suitable fit function for the background.

It would be nice to have a physical understanding of the background and it is not so clear why a quadratic function would be the right choice: We already know that on the BCS side the excitation at low frequencies can be well described with a constant-linear function, which is slightly washed out by trap effects as given in equation (7.160). On the BEC side, additionally,

Feshbach molecules can be dissociated, which also leads to a constant-linear function. In a simple picture, that function is not washed out in this case, because the bound state energy only depends on the scattering length and not on the density of the gas.

For the measured interactions, the onset of the Feshbach molecules should occur at lower frequencies than the pair excitations, which is consistent with the behavior in figure 7.5. By combining these two background functions, one gets the fit function denoted as "Linear-linear" in figure 7.13. This function fits the background equally well than the quadratic function, but is more convincing and will be used to describe the background on the BEC side, while on the BCS side only a linear function is used.

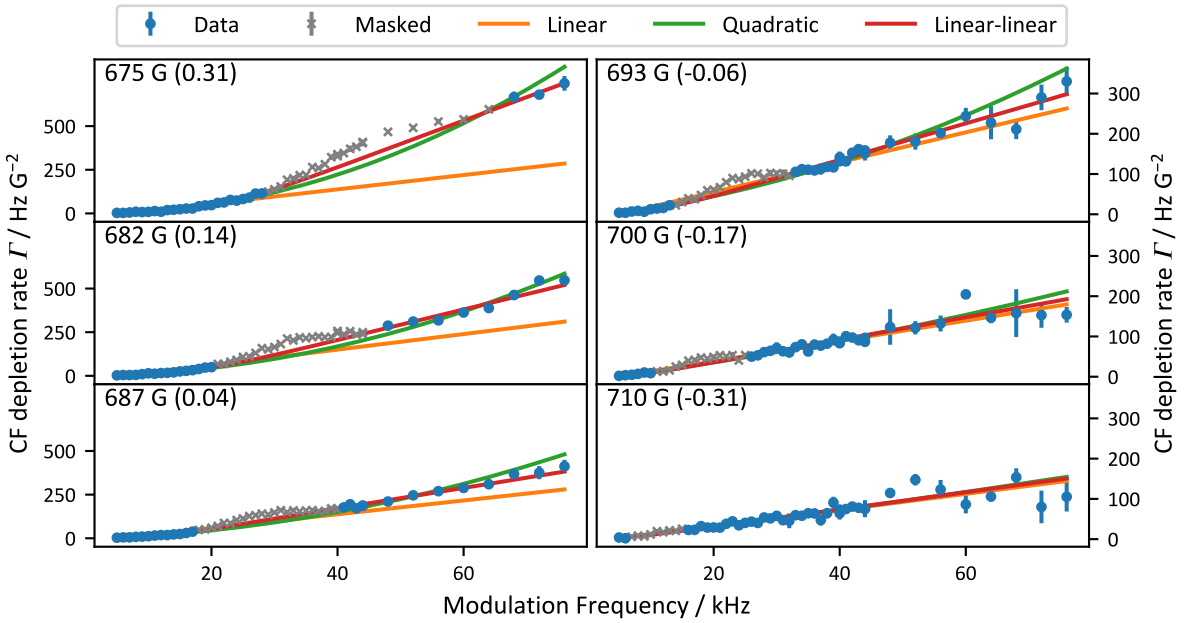

Figure 7.13: Comparison of background models After masking the data around the kink position, the background can be described with a linear function on the BCS side and a quadratic or linear-linear function on the BEC side. Each panel is annotated with the magnetic field and the interaction parameter in parentheses.

As an example, figure 7.14 compares the fit functions again and shows the residual of the fits. Quadratic and linear-linear fits both describe the data quite well, but the former slightly overestimates the data systematically at high modulation frequencies. Therefore, the linear-linear function is chosen. Another reason is that the linear-linear model is consistent with the physical understanding of the excitation process.

Note that a deviation from the linear dependencies of the background at high frequencies is expected if compared to the results from ref. [70]. However, apparently we do not probe that regime yet because we use a higher Fermi energy but a lower range of modulation frequencies.

The remaining datapoints around the kink position form a peak structure and are well described by a Gaussian function

$$f_{\mathrm{s}}(\nu) = \frac{A_{\mathrm{s}}}{\sigma_{\mathrm{s}}\sqrt{2\pi}} e^{-(\nu-\nu_{\mathrm{peak}})^2/(2\sigma_{\mathrm{s}}^2)}, \tag{7.162}$$

with amplitude A_{s}, standard deviation σ_{s} and peak position ν_{peak}. The performed fits of the combined signal and background functions are shown for several fields in figure 7.15.

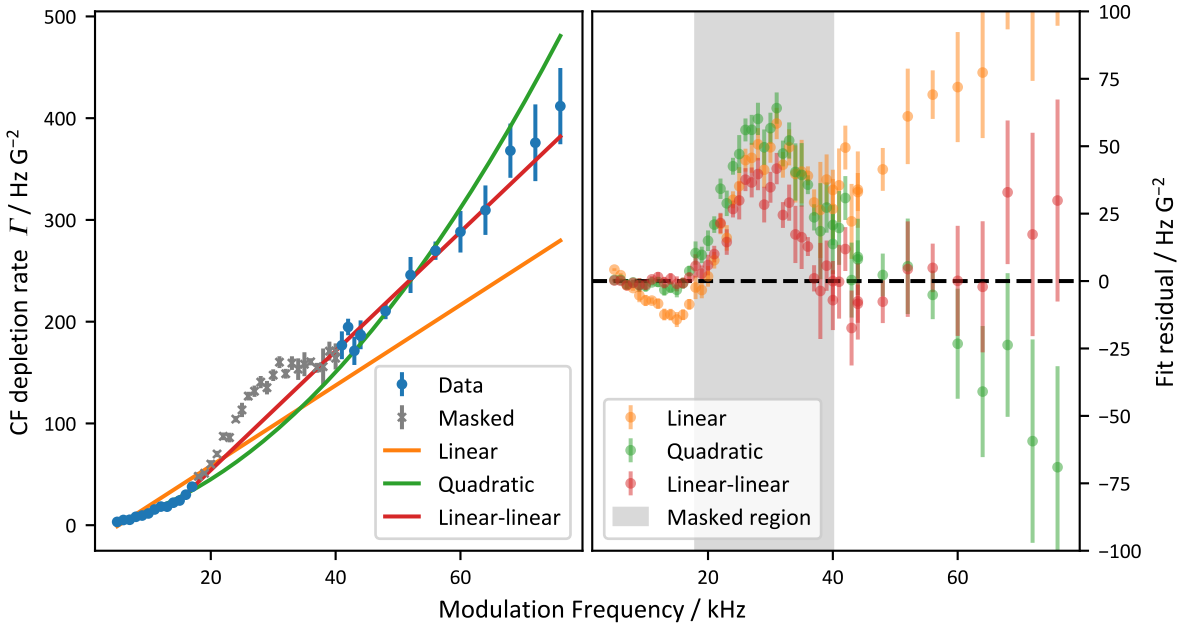

Figure 7.14: Exemplary background fits with three different functions and their residuals The data **(left)** is taken at a magnetic field of 687 G, which is on the BEC side of the resonance where a linear fit to the background is not sufficient. Instead, a quadratic or linear-linear fit is more appropriate. This is elucidated by showing the corresponding residuals **(right)**, which are more convincing for the linear-linear than for the quadratic model.

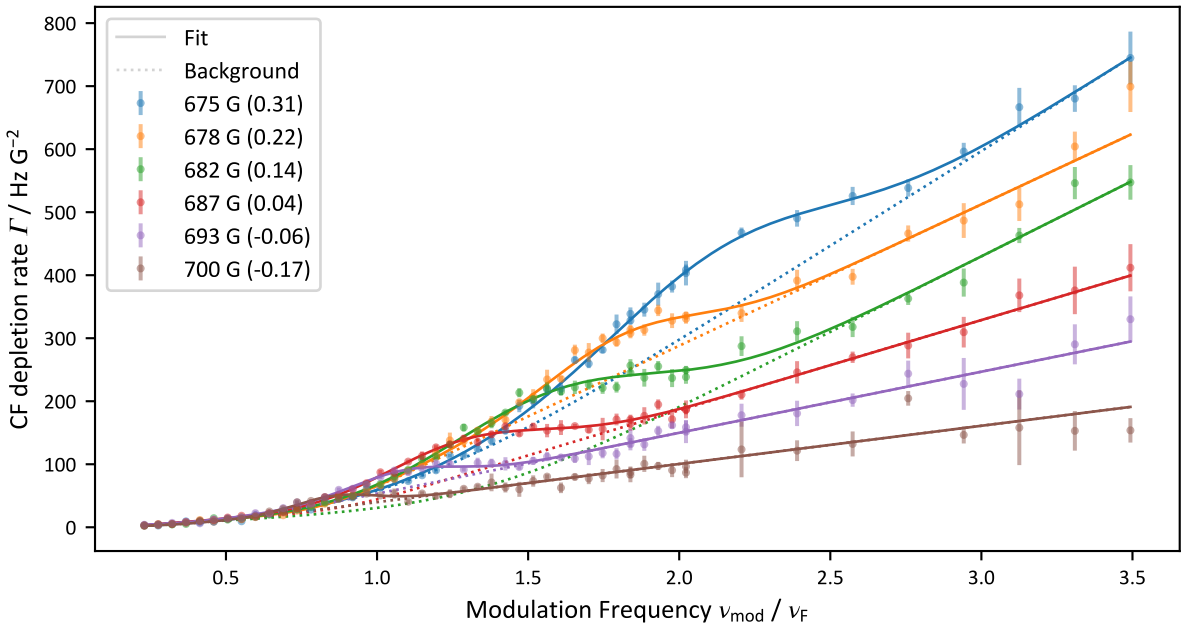

Figure 7.15: Signal-background fit to the excitation rates for several magnetic fields Interaction parameters $1/(k_F a)$ are given in the legend in parentheses behind each magnetic field. The background part of the fit is also shown (not a separate fit). Note that the background fit for the magnetic field of 682 G looks somewhat unsatisfying because it seems to bend down too much, but for most fields this does not happen and the influence on the peak position or width is small.

Result from Second Investigation The *Higgs-2* investigation uses measurements with a lower modulation amplitude of 0.3 G and a constant modulation time of 100 ms. The data is shown in figure 7.16: Only a few magnetic fields were measured and a smaller frequency range has been used, which makes it more difficult to fit the background properly. On the other hand, the observed features are more pronounced and narrow. The data is fitted to a linear background plus a Gaussian peak, as in equation (7.162), to extract position, width and amplitude of the resonances.

At an interaction close to unitarity ($1/(k_\mathrm{F}a) = -0.06$) four measurements are taken and presented in the inset of figure 7.16. The data was taken at different days, so for example slight variations in the atom number could explain the slightly displaced peak positions at this interaction, but the shape of the peaks is quite reproducible.

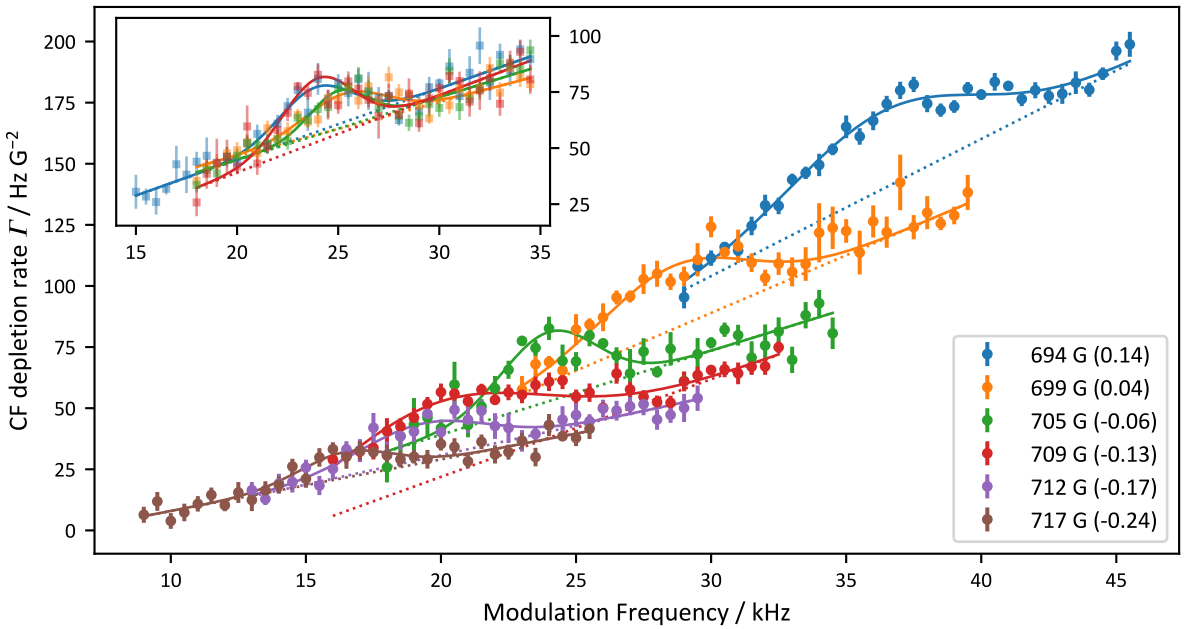

Figure 7.16: Signal-background fits to data from *Higgs-2* investigation The legend provides the magnetic field and interaction parameter in parentheses. The inset shows four measurements close to unitarity ($1/(k_\mathrm{F}a) = -0.06$), which were taken at different days. The inset axes are the same as for the main plot. The measurement at 709 G is an example for insufficient range of the background, which can lead to a strong correlation between A_s and σ_s and probably an overestimation of the latter.

7.6.3 Spectral Weight

Figure 7.17 presents the spectral weight A_s of the fitted peaks (proportional to its height and its width). The signal is quite strong on the BEC side but gets attenuated roughly exponentially towards the BCS side. This leads to larger error bars on the fit parameters on the BCS side in the following.

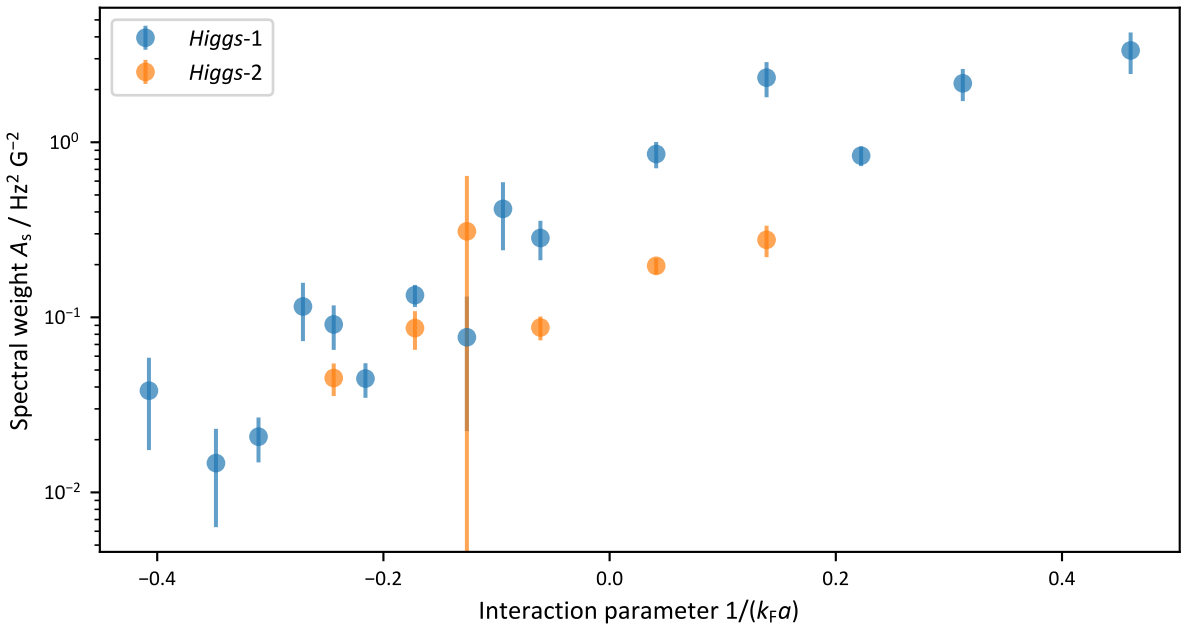

Figure 7.17: Spectral weight of measured resonances A roughly exponential attenuation towards the BCS side is observed.

7.6.4 Resonance Position

The fitted peak positions versus interaction are shown in figure 7.18. The result agrees reasonably well with the previous measurement of the Higgs amplitude mode based on RF dressing [46]. On the BCS side it also agrees well with theoretical values for Δ from ref. [53], assuming $\omega_H = 2\Delta/\hbar$, but at unitarity and towards the BEC side a deviation from theory towards higher frequencies is observed. At some point the measured frequency even exceeds the BCS prediction for 2Δ, even though the BCS result is expected to overestimate the gap.

It has been theoretically predicted that the loss of particle-hole symmetry towards the BEC side and the broadening of the Higgs amplitude mode coincide with an increased Higgs frequency [200].

Another reason for this might be an increased central density of the cloud caused by the trap potential, an effect which was also discussed in section 5.7 but at a higher temperature (around T_c). On the BCS side and at unitarity the central density is still expected to be very similar to the density of an ideal Fermi gas, but towards the BEC side, the central density at low temperatures increases significantly, which leads within LDA to a higher Fermi energy at the center of the trap, which could also shift the frequency of the gap and of the Higgs mode upwards. To get a better impression of this effect, figure 7.19 shows the ratio between the theoretical value of 2Δ and the measured peak positions.

This ratio is compared with the expected increase in local Fermi energy at unitarity, which has similar values. For $T = T_c$ this increase is derived from the equation of state and for $T = 0$ from the Bertsch parameter, both based on the results from ref. [61]. Following instructions in ref. [36], this is also compared to first order corrections for a weakly interacting Fermi or Bose gas in the inset. The BEC result does not match quantitatively because we are too far in the strongly interacting regime, but it shows that qualitatively the central density can be increased significantly towards the BEC side. Note that far on the BEC side the universal dependence of the physics on the interaction parameter $1/(k_F a)$ is lost and an additional dependence on the atom number is obtained. In the limit of an ideal gas, the central density scales linearly with the atom number for a Bose gas but proportional to $\sqrt{N_\sigma}$ for a Fermi gas.

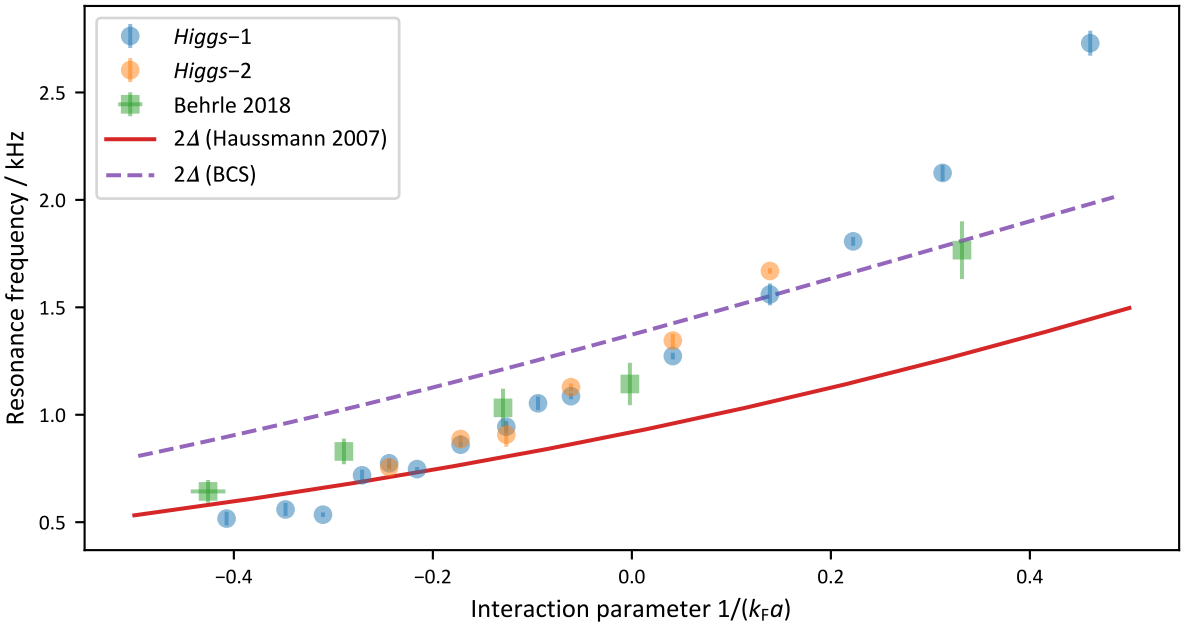

Figure 7.18: Measured resonance positions The results are compared to the previous measurement of the Higgs amplitude mode in ref. [46] ("Behrle 2018") and to theoretical predictions for the gap based on BCS theory and on ref. [53] ("Haussmann 2007").

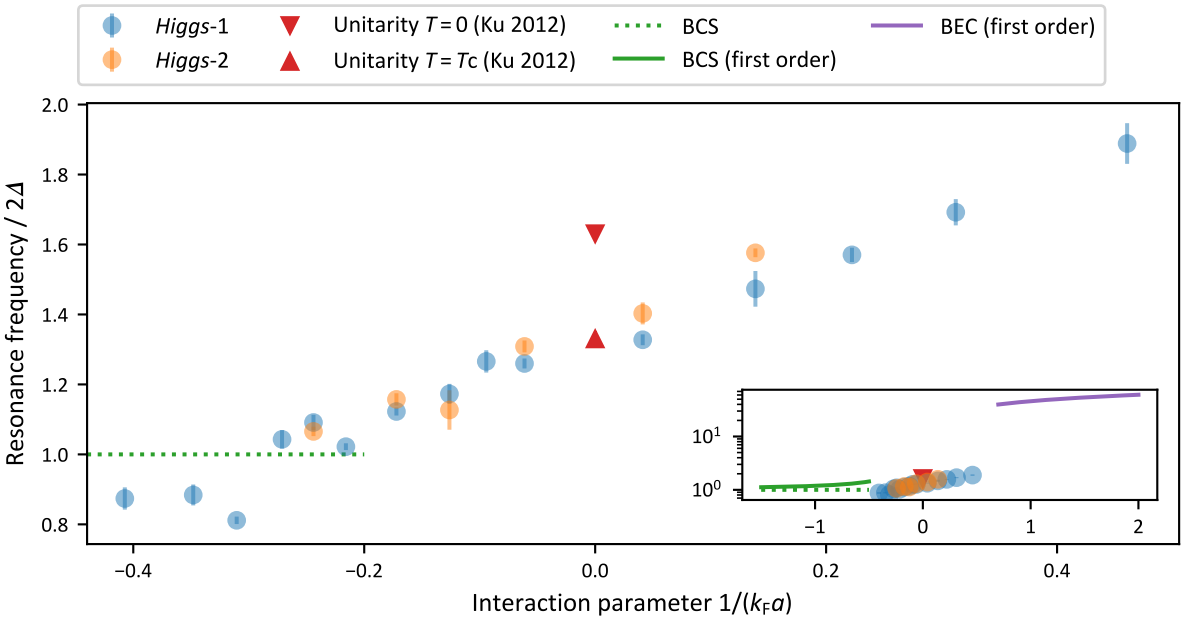

Figure 7.19: Ratio between measured resonance frequencies and theoretical values for twice the gap The theoretical value for the gap is from ref. [53]. The data is compared to estimates for the increase of the local Fermi energy in the trap center at unitarity based on results from ref. [61] ("Ku 2012"). The inset demonstrates the qualitative expectation towards weak interaction [36] and uses the same axes, except for the logarithmic scale of the y-axis.

7.6.5 Resonance Width

The width of the observed peaks can reveal information about the stability of the observed mode. Shorter lifetimes lead to broader spectral features. The expectation for the Higgs amplitude mode is that it is stable on the BCS side, whereas the loss of particle-hole symmetry towards the BEC side leads to a fast decay into Goldstone modes [42]. Based on BCS theory a power-law decay with exponent $-1/2$ on the BCS side and $-3/2$ on the BEC side is predicted [181]. The measured peak widths are presented in figure 7.20. Indeed the data suggests a weak

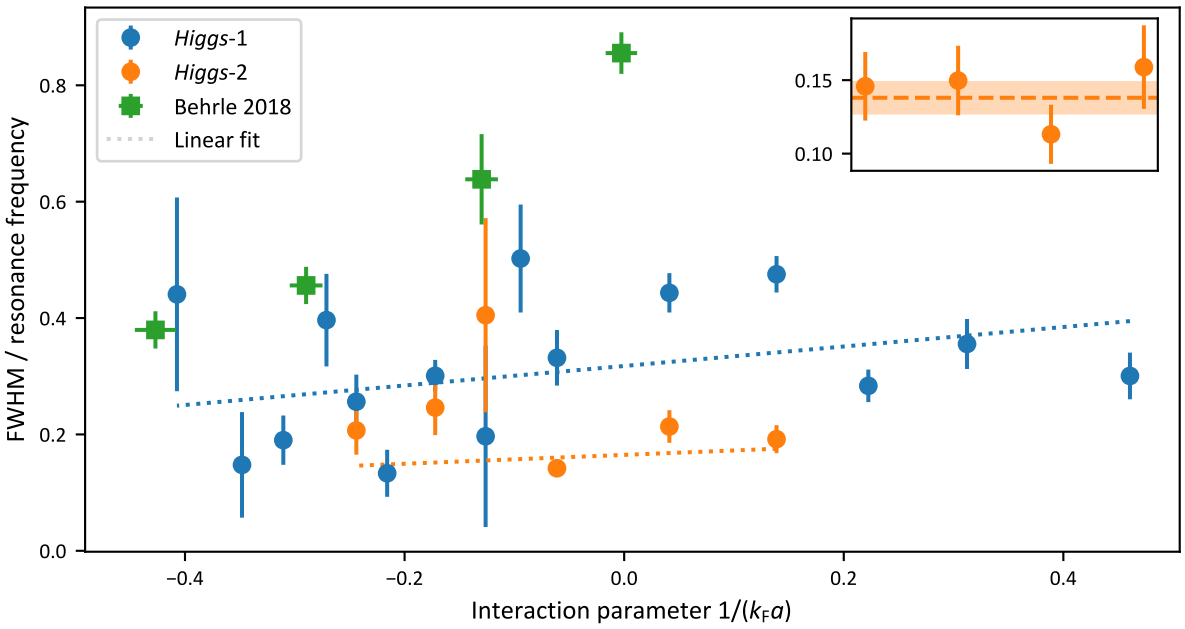

Figure 7.20: Relative peak width versus interaction The data is compared to the result from ref. [46] ("Behrle 2018"). The inset shows the four different measurements close to unitarity ($1/(k_\mathrm{F}a) = -0.06$), together with the mean and its standard error. These measurements show a very consistent narrow width and are combined to a single datapoint in the main plot. The x-axis of the inset has no special meaning and is omitted.

trend of increasing spectral width towards the BEC side. The measured width is smaller than for the previous measurement based on RF dressing [46], for which the smallest measured FWHM was 0.38(3) of the resonance frequency, while the new measurements find a ratio of 0.14(1) close to unitarity. But the fact that the width is even narrower for the second investigation shows that the resonance is still broadened by the measurement and should be considered as an upper bound.

Note that this result is much broader than the Fourier limit of the excitation, which was calculated in section 7.2. Reasons for a broadening could be a too large modulation amplitude or a too large modulation time, which could in principle reduce the gap during modulation (this effect has been seen in the simulations of ref. [69]). Also, an insufficient signal-to-noise ratio or an insufficient data range for the background model are possible.

7.7 Distinction of Molecules and Pairs

For the *Higgs-1* investigation (larger amplitude, shorter t_mod, constant n_mod) it was necessary to consider three different contributions in order to get an appropriate model describing the whole spectrum on the BEC side: The onset of the pair breaking continuum, the onset of the dissociation of Feshbach molecules and a peak for the Higgs amplitude mode. In section 7.5

contributions from pair breaking and from molecule dissociation have both been observed, but with a simple constant-linear function it was not possible to separate the two effects on the BEC side. After a full model for all three excitations has been developed in the last section one can revisit this problem and figure 7.21 shows the fit results for the pairing onset and for the molecular dissociation onset. While the result for the gap onset shows some inconsistency

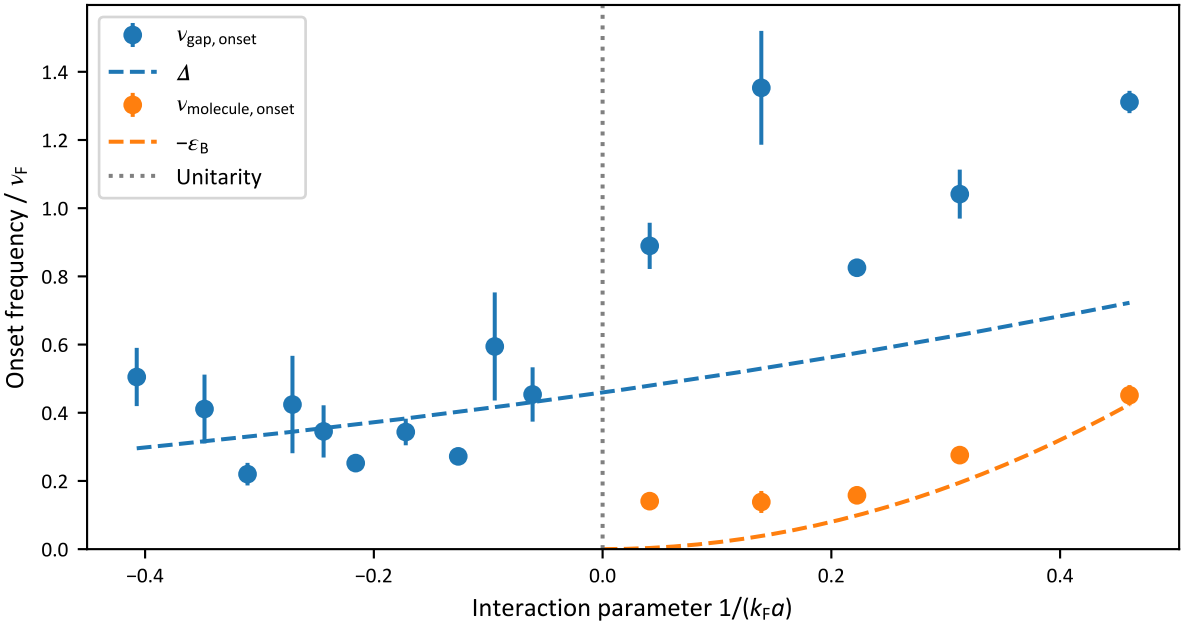

Figure 7.21: Fit results for the onset frequency of pair breaking and molecule dissociation Note that below and above unitarity different fit functions are used because on the BCS side no molecule dissociation is considered. The value of the gap is based on ref. [53].

between the values on the BEC and BCS side of the resonance, which could be caused by unwanted correlations between the fit parameters for the three different excitation processes, there is a general agreement to an excitation onset close to the calculated bound state energy and a second excitation onset close to the value of the calculated gap. This can be seen as an improvement compared to the result in figure 7.5. Note that the frequency sampling of this investigation is not good at low frequencies, which can probably explain the poor agreement at very low molecule dissociation frequencies.

Far on the BEC side, where the global chemical potential μ_0 becomes negative, it is predicted that Δ is not directly connected to quasi-particle excitations anymore, but instead $\Delta^2/|\mu_0|$ becomes important [4]. But for the current measurement, that region has not yet been probed.

Excitation Rates Another interesting parameter, which can be different for pair breaking and molecule dissociation, is the slope of the CF depletion rate above the onset frequency. The CF depletion rate Γ is a measure for the heating. Under the assumption that the amount of heating is proportional to the rate of excitations K and proportional to the kinetic energy released per excitation $h\,(\nu_{\text{mod}} - \nu_{\text{onset}})$, one can conclude that the slope $\partial\Gamma/\partial\nu_{\text{mod}}$ is proportional to the rate of excitations, i.e. $\Gamma \propto K\,(\nu_{\text{mod}} - \nu_{\text{onset}}) \Rightarrow \partial\Gamma/\partial\nu_{\text{mod}} \propto K$.

Therefore, on the BCS side the slope of the background m_{gap} is connected to the rate of pair breaking. On the BEC side the background additionally contains the slope m_{molecule} connected to the rate of Feshbach molecule dissociation, which can be separated due to the different onset frequency.

Figure 7.22 shows this excitation rate for molecules and pairs. A very basic explanation

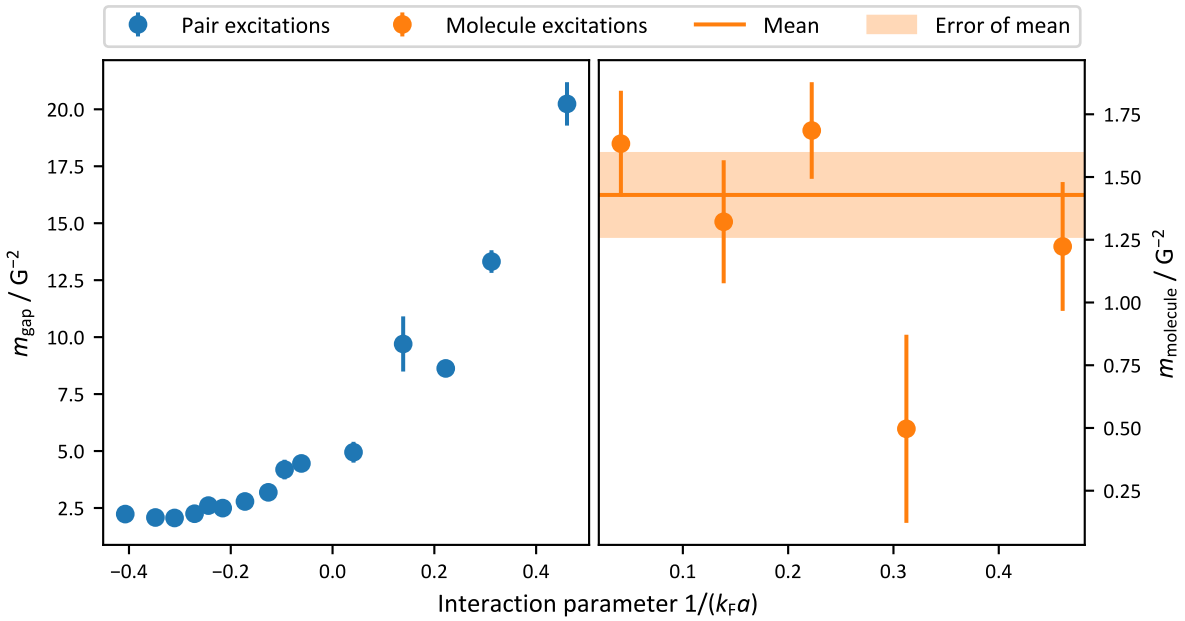

Figure 7.22: Excitation rates of pair breaking and molecule dissociation The rate of pair breaking is proportional to m_{gap} **(left)** and the rate of molecule dissociation is proportional to m_{molecule} **(right)**, as discussed in the text. The contributions m_{gap} and m_{molecule} are separated by fits to the full signal-background model, where m_{molecule} is dominant for lower frequencies and m_{gap} is an additional slope at higher frequencies.

attempt could be based on Fermi's golden rule: Apart from the probability for the excitation itself, the excitation rate will depend on the number of available pairs and on the number of available final states. This is consistent with the increased excitation rate of the pairs towards the BEC side because larger condensate fractions are expected there and because on the BCS side Pauli blocking could play a role and suppress the number of available final states. For the molecules no significant change of the excitation rate is measured.

7.8 Conclusion

In this chapter interaction modulation via the magnetic field has been performed to examine pairing in the BEC-BCS crossover.

First, the bound state energy of Feshbach molecules on the BEC side is measured, which matches to calculated values. Additionally, a finite onset frequency even at unitarity and towards the BCS side is observed, which has not been reported before for a trapped gas. This could be a many-body effect caused by the energetically gapped excitation of Cooper pairs in the superfluid, although the inhomogeneous density distribution of the trap makes the interpretation more subtle. Simple models have been developed which support this perspective.

The main result of this chapter is the observation of a spectral feature at roughly twice the superfluid gap, which can be identified as the Higgs amplitude mode, standing out on top of the background of individual pair-breaking excitations. The frequency agrees well to theory on the BCS side and on unitarity, but is shifted towards higher frequencies on the BEC side, which is most likely a trap effect caused by an increased central density. An increased density is generally related to a larger Fermi energy and therefore also an increased gap and Higgs frequency.

An advantage of this excitation scheme is a relatively narrow excitation frequency, which

is momentum state independent. The data gives a hint of an increased mode width towards the BEC side, but also a dependence on the experimental parameters has been observed. At unitarity it was possible to decrease the upper bound on the spectral width of the mode to 14(1) % of the mode center frequency.

Outlook In the future, a next step would be to carefully characterize the dependence of the mode width on the experimental parameters, considering modulation amplitude and duration, while ensuring a good signal-to-noise ratio and sufficient data-range for the background. This should enable a better measurement of the mode width and possibly a clearer observation of the expected change of the decay from BCS to BEC side.

In section 5.7 it was already explored how to measure the central density of the gas. It should be possible to apply the same method to this investigation, for which the gas is at temperatures further below the critical temperature. This would allow to characterize the increase of central density towards the BEC side and to verify whether this effect explains the shift of the Higgs amplitude mode to higher frequencies or whether an additional effect is present.

8 Conclusion

Phase Diagram of BEC-BCS Crossover As discussed in chapter 5, there is no consensus in theoretical studies about the exact behavior of the critical temperature across the whole BEC-BCS crossover. For example, there are different predictions for the position and prominence of a maximum critical temperature towards the BEC side for the homogeneous gas. Previous experimental studies for a trapped gas show large deviations to theoretical predictions, especially towards the BEC side. The deviations can be traced back to an inappropriate thermometry. Another challenge arises from the determination of the Fermi energy of the trapped gas, which does not consider compression effects, i.e. the increase of the density in the trap center towards the BEC side.

In the presented investigation these two points have been addressed. The temperature is derived from the density profile at the edge of the cloud and a virial expansion is used to be more resilient against interaction effects. The density in the trap center is determined from high intensity absorption images via the inverse Abel transformation. This allows a comparison of the results with theory for the homogeneous gas, in addition to theory for a harmonically trapped gas, for which the Fermi energy is determined from the atom number instead of the central density.

The superfluid transition point is determined for several interactions with the rapid ramp technique, similar to previous studies. Additionally, it is demonstrated that it is possible to deduce this transition point from simple time-of-flight images by using machine learning. A first approach based on supervised machine learning initially still requires the rapid ramp to generate labels for the training set. A second approach based on unsupervised machine learning can even find the transition point completely independent of the rapid ramp, but this was only possible for certain interactions. The superfluid transition points determined by these methods are consistent with the results based on the rapid ramp and the unsupervised machine learning can be used as an independent validation of the result.

Currently data is retaken in order to combine the detection of the superfluid state based on machine learning techniques with the enhanced thermometry. This also allows to address some possible refinements of the current investigation. Improvements in the quality of the imaging should allow for a better understanding of systematic errors which are caused by deviations from the assumed symmetries of the trap potential when applying the inverse Abel transformation. The measurement of the central density far on the BEC side requires a more careful examination, on one hand, because deviations of the density from a Thomas-Fermi profile near the critical temperature might be relevant, on the other hand, it has been reported that the imaging efficiency in this region can be reduced [129].

The final result for the critical temperature curve in the BEC-BCS crossover has a reasonable agreement to theoretical predictions, although the question about the exact location of a maximum critical temperature for the homogeneous gas cannot be answered yet.

This investigation leads to a better understanding of the large deviations of experimental results from theoretical prediction in previous studies [28, 29] and realizes an unambiguous thermometry in contrast to another study [56].

Interaction Quenches In chapter 6 the dynamics of a strongly interacting Fermi gas induced by interaction quenches on different timescales has been examined.

At first an interaction quench based on a population transfer via RF from a strongly to a weakly interacting state faster than trap dynamics and faster than the quasi-particle relaxation time is performed. As a fast response of the system, comparable to the quasi-particle relaxation time, the condensate fraction decays initially and the width of the condensate (in time-of-flight) increases. Additionally, the monopole mode of the trap is excited and a revival of the condensate fraction is seen, which is closer to the trap dynamics than the quasi-particle relaxation time. This is consistent to the theoretical modeling, which finds an influence of the monopole mode on pair coherence.

For interaction quenches, which are fast compared to the Fermi time of the system, oscillations of the order parameter are predicted, which are interpreted as the Higgs amplitude mode. In order to perform quenches on this timescale, a new fast magnetic coil has been constructed.

To avoid technical issues connected to our application of the rapid ramp to dynamics on short timescales, the condensate fraction is instead predicted from time-of-flight images, employing the neural network which has already been used for the measurement of the superfluid phase diagram. Indeed, small oscillations of the measured condensate fraction are observed, but the signal-to-noise ratio is quite low. Considering the possibility that statistical fluctuations of the data are interpreted as oscillations, a statistical hypothesis test is performed. By repeating the analysis on simulated data in a background-only scenario, it is shown with a confidence of 98.5 %, that the observed oscillations close to the predicted frequencies cannot be explained by statistical fluctuations.

Finally, it was possible to eliminate the mentioned technical issues of the rapid ramp. First measurements show an improved signal-to-noise ratio, which enables the extraction of the Higgs frequency and the damping exponent. The result is consistent with theoretical predictions at the measured interaction and further measurements should be able to check the predicted change of the damping in the BEC-BCS crossover.

Interaction Modulation As an alternative excitation scheme for the Higgs amplitude mode, apart from interaction quenches, theoretical studies have suggested a spectroscopic method based on interaction modulation. The new magnetic coil, which has also been used for the magnetic interaction quenches, enables the modulation of the interaction at the required frequencies. Additionally, this method leads to excitations corresponding to the dissociation of Feshbach molecules and to breaking of pairs which are part of the superfluid many-body state.

In this investigation, as described in chapter 7, it has been possible to observe these three excitations and to separate them. The pair breaking leads to a linear background of the measured signal above an onset frequency, which is connected to the superfluid gap. Interestingly, this onset is only partially washed-out by trap effects. On the BEC side, the dissociation of molecules leads to an additional signal, which has a similar shape but with different onset frequency and slope.

On top of the background from pair breaking and molecule dissociation, a resonance peak is identified as the Higgs amplitude mode. The resonance frequency is consistent to theoretical predictions on the BCS side, but deviates towards higher frequencies on the BEC side. An explanation for this might be the increase of the central density of the trapped gas towards the BEC side, which is connected to a larger local Fermi energy and gap. But there are also theoretical predictions for an increased Higgs frequency in connection to the damping on the BEC side [200]. In principle, the influence of compression effects can be checked by measuring the central density, similar as in chapter 5, in order to evaluate if an additional effect is present, which would be an interesting future measurement.

The magnetic interaction modulation has a good frequency resolution, which can be used to examine the width of the Higgs amplitude mode in order to get information about its

stability. At unitarity, the performed measurements found a FWHM of 14(1) % relative to the resonance frequency of the mode. This is seen as an upper bound for the mode width because a dependence of the observed width on the modulation parameters has been found, which still has to be examined more carefully.

Outlook Some future steps, which are closely connected to the investigations presented in this thesis, have already been mentioned above. For example, the improved rapid ramp enables a characterization of the Higgs amplitude mode in the BEC-BCS crossover in the time-domain after an interaction quench. Similarly, for the interaction modulation, an optimization of the parameters should allow a better characterization of the spectral width of the Higgs amplitude mode.

One of the main challenges was to take the inhomogeneous density distribution of a trapped gas into account. For the measurement of the superfluid phase diagram, it was necessary to use the inverse Abel transformation, which increases the noise for the central density and can introduce systematic errors if there are deviations of the assumed elliptic symmetry of the trap potential. For the interaction modulation, the inhomogeneous density complicates the interpretation of the data because the nature of pairing depends on the local interaction and reduced temperature. For both investigations, compression effects influence the measured quantities, i.e. the reduced critical temperature and the Higgs frequency.

As mentioned in section 3.2.6, the implementation of a gas in a homogeneous potential has already been prepared. This would be a good opportunity to repeat the described measurements, in order to compare them directly to theoretical results for a homogeneous gas, but also to have a direct comparison between a trapped and a homogeneous system. Of course, a homogeneous gas will have its own challenges, for example the thermometry has to be modified because it relies on a known potential gradient.

Additionally, a strong confinement in one direction has already been implemented and the preparation of a gas in a quasi-two-dimensional regime has been demonstrated. It would be interesting to study the fate of the Higgs amplitude mode in the crossover from three to two dimensions, because in two dimensions the superfluid transition is replaced by the Berezinskii-Kosterlitz-Thouless transition, which is a superfluid state without long range order and without symmetry-breaking [201]. Nevertheless, there are theoretical predictions for the existence of a Higgs amplitude mode in this regime [202].

Bibliography

[1] T. Harrison, M. Link, A. Behrle, K. Gao, A. Kell, J. Kombe, J.-S. Bernier, C. Kollath, and M. Köhl, *Decay and revival of a transient trapped Fermi condensate*, Phys. Rev. Research **3**, 023205 (2021), (cit. on pp. iv, 125, 127, 128).

[2] A. Kell, M. Link, M. Breyer, A. Hoffmann, M. Köhl, and K. Gao, *A compact and fast magnetic coil for the manipulation of quantum gases with Feshbach resonances*, Review of Scientific Instruments **92**, 093202 (2021), (cit. on pp. iv, 39).

[3] R. J. Donnelly, *The Discovery of Superfluidity*, Physics Today **48**, 30–36 (1995), (cit. on p. 1).

[4] W. Ketterle and M. W. Zwierlein, *Making, probing and understanding ultracold Fermi gases*, Riv. del Nuovo Cim, 247–422 (2008) (cit. on pp. 1, 4, 8–10, 12–14, 17–20, 22, 23, 69, 92, 94, 102, 125, 150, 163).

[5] J. F. Allen and A. D. Misener, *Flow of Liquid Helium II*, Nature **141**, 75–75 (1938), (cit. on p. 1).

[6] P. Kapitza, *Viscosity of Liquid Helium below the λ-Point*, Nature **141**, 74–74 (1938), (cit. on p. 1).

[7] F. London, *The λ-Phenomenon of Liquid Helium and the Bose-Einstein Degeneracy*, Nature **141**, 643–644 (1938), (cit. on p. 1).

[8] A. Einstein, *Plancks Gesetz und Lichtquantenhypothese*, Z. Physik **26**, 178–181 (1924), (cit. on pp. 1, 183).

[9] N. Bogoliubov, *On the theory of superfluidity*, J. Phys **11** (1947) (cit. on p. 1).

[10] J. Bardeen, L. N. Cooper, and J. R. Schrieffer, *Microscopic Theory of Superconductivity*, Phys. Rev. **106**, 162–164 (1957), (cit. on pp. 1, 14, 183).

[11] J. Bardeen, L. N. Cooper, and J. R. Schrieffer, *Theory of Superconductivity*, Phys. Rev. **108**, 1175–1204 (1957), (cit. on pp. 1, 14, 183).

[12] D. M. Eagles, *Possible Pairing without Superconductivity at Low Carrier Concentrations in Bulk and Thin-Film Superconducting Semiconductors*, Phys. Rev. **186**, 456–463 (1969), (cit. on p. 1).

[13] A. J. Leggett, *Diatomic molecules and cooper pairs*, in *Modern Trends in the Theory of Condensed Matter*, Vol. 115, edited by A. Pękalski and J. A. Przystawa, (Springer Berlin Heidelberg, Berlin, Heidelberg, 1980), pp. 13–27, (visited on 03/26/2022) (cit. on p. 1).

[14] T. Hänsch and A. Schawlow, *Cooling of gases by laser radiation*, Optics Communications **13**, 68–69 (1975), (cit. on p. 1).

[15] W. D. Phillips, *Nobel Lecture: Laser cooling and trapping of neutral atoms*, Rev. Mod. Phys. **70**, 721–741 (1998), (cit. on p. 1).

[16] C. N. Cohen-Tannoudji, *Nobel Lecture: Manipulating atoms with photons*, Rev. Mod. Phys. **70**, 707–719 (1998), (cit. on p. 1).

[17] S. Chu, *Nobel Lecture: The manipulation of neutral particles*, Rev. Mod. Phys. **70**, 685–706 (1998), (cit. on p. 1).

[18] M. H. Anderson, J. R. Ensher, M. R. Matthews, C. E. Wieman, and E. A. Cornell, *Observation of Bose-Einstein Condensation in a Dilute Atomic Vapor*, Science **269**, 198–201 (1995), (cit. on p. 1).

[19] C. C. Bradley, C. A. Sackett, J. J. Tollett, and R. G. Hulet, *Evidence of Bose-Einstein Condensation in an Atomic Gas with Attractive Interactions*, Phys. Rev. Lett. **75**, 1687–1690 (1995), (cit. on p. 1).

[20] K. B. Davis, M. .-. Mewes, M. R. Andrews, N. J. van Druten, D. S. Durfee, D. M. Kurn, and W. Ketterle, *Bose-Einstein Condensation in a Gas of Sodium Atoms*, Phys. Rev. Lett. **75**, 3969–3973 (1995), (cit. on p. 1).

[21] S. Inouye, M. R. Andrews, J. Stenger, H.-J. Miesner, D. M. Stamper-Kurn, and W. Ketterle, *Observation of Feshbach resonances in a Bose–Einstein condensate*, Nature **392**, 151–154 (1998), (cit. on p. 1).

[22] P. Courteille, R. S. Freeland, D. J. Heinzen, F. A. van Abeelen, and B. J. Verhaar, *Observation of a Feshbach Resonance in Cold Atom Scattering*, Phys. Rev. Lett. **81**, 69–72 (1998), (cit. on p. 1).

[23] J. Cubizolles, T. Bourdel, S. J. J. M. F. Kokkelmans, G. V. Shlyapnikov, and C. Salomon, *Production of Long-Lived Ultracold Li_2 Molecules from a Fermi Gas*, Phys. Rev. Lett. **91**, 240401 (2003), (cit. on p. 1).

[24] C. A. Regal, C. Ticknor, J. L. Bohn, and D. S. Jin, *Creation of ultracold molecules from a Fermi gas of atoms*, Nature **424**, 47–50 (2003), (cit. on p. 1).

[25] S. Jochim, *Bose-Einstein Condensation of Molecules*, Science **302**, 2101–2103 (2003), (cit. on p. 1).

[26] M. Greiner, C. A. Regal, and D. S. Jin, *Emergence of a molecular Bose–Einstein condensate from a Fermi gas*, Nature **426**, 537–540 (2003), (cit. on p. 1).

[27] M. W. Zwierlein, C. A. Stan, C. H. Schunck, S. M. F. Raupach, S. Gupta, Z. Hadzibabic, and W. Ketterle, *Observation of Bose-Einstein Condensation of Molecules*, Phys. Rev. Lett. **91**, 250401 (2003), (cit. on p. 1).

[28] C. A. Regal, M. Greiner, and D. S. Jin, *Observation of Resonance Condensation of Fermionic Atom Pairs*, Physical Review Letters **92**, 10.1103/PhysRevLett.92.040403 (2004), (cit. on pp. 2, 3, 63, 91–93, 96, 122, 167).

[29] M. W. Zwierlein, C. A. Stan, C. H. Schunck, S. M. F. Raupach, A. J. Kerman, and W. Ketterle, *Condensation of pairs of fermionic atoms near a Feshbach resonance*, Physical Review Letters **92**, 120403–1 (2004) (cit. on pp. 2, 3, 63, 91–93, 96, 122, 167).

[30] M. Randeria and E. Taylor, *Crossover from Bardeen-Cooper-Schrieffer to Bose-Einstein Condensation and the Unitary Fermi Gas*, Annual Review of Condensed Matter Physics **5**, 209–232 (2014), (cit. on pp. 2, 12, 13).

[31] E. Braaten, *Universal Relations for Fermions with Large Scattering Length*, in *The BCS-BEC Crossover and the Unitary Fermi Gas*, Vol. 836, edited by W. Zwerger, (Springer Berlin Heidelberg, Berlin, Heidelberg, 2012), pp. 193–231, (visited on 03/27/2022) (cit. on p. 2).

[32] T.-L. Ho, *Universal Thermodynamics of Degenerate Quantum Gases in the Unitarity Limit*, Physical Review Letters **92**, 10.1103/PhysRevLett.92.090402 (2004), (cit. on pp. 2, 13, 23).

[33] T.-L. Ho and Q. Zhou, *Obtaining the phase diagram and thermodynamic quantities of bulk systems from the densities of trapped gases*, Nature Phys **6**, 131–134 (2010), (cit. on pp. 2, 23, 65, 70).

[34] D. T. Son, *Vanishing Bulk Viscosities and Conformal Invariance of the Unitary Fermi Gas*, Phys. Rev. Lett. **98**, 020604 (2007), (cit. on p. 2).

[35] A. Gezerlis and J. Carlson, *Strongly paired fermions: Cold atoms and neutron matter*, Phys. Rev. C **77**, 032801 (2008), (cit. on p. 2).

[36] S. Giorgini, L. P. Pitaevskii, and S. Stringari, *Theory of ultracold atomic Fermi gases*, Reviews of Modern Physics **80**, 1215–1274 (2008) (cit. on pp. 2, 7, 9, 12, 20, 23, 27, 115, 160, 161).

[37] P. A. Fleury, *Phase Transitions, Critical Phenomena, and Instabilities*, Science **211**, 125–131 (1981), (cit. on p. 2).

[38] V. L. Ginzburg, *On Superconductivity and Superfluidity: A Scientific Autobiography* (Springer Berlin Heidelberg, Berlin, Heidelberg, 2009), http://link.springer.com/10.1007/978-3-540-68008-6 (visited on 03/30/2022) (cit. on p. 2).

[39] D. Pekker and C. M. Varma, *Amplitude / Higgs Modes in Condensed Matter Physics*, Annual Review of Condensed Matter Physics **6**, 269–269 (2014), (cit. on pp. 2, 19, 123, 124, 144).

[40] J. Goldstone, A. Salam, and S. Weinberg, *Broken Symmetries*, Phys. Rev. **127**, 965–970 (1962), (cit. on pp. 2, 19, 123).

[41] R. Shimano and N. Tsuji, *Higgs Mode in Superconductors*, Annu. Rev. Condens. Matter Phys. **11**, annurev–conmatphys–031119–050813 (2019), (cit. on pp. 2, 124, 143, 144).

[42] X. Han, B. Liu, and J. Hu, *Observability of Higgs mode in a system without Lorentz invariance*, Physical Review A **94**, 10.1103/PhysRevA.94.033608 (2016), (cit. on pp. 2, 125, 144, 162).

[43] W. Weimer, K. Morgener, V. P. Singh, J. Siegl, K. Hueck, N. Luick, L. Mathey, and H. Moritz, *Critical Velocity in the BEC-BCS Crossover*, Physical Review Letters **114**, 10.1103/PhysRevLett.114.095301 (2015), (cit. on p. 3).

[44] S. Hoinka, P. Dyke, M. G. Lingham, J. J. Kinnunen, G. M. Bruun, and C. J. Vale, *Goldstone mode and pair-breaking excitations in atomic Fermi superfluids*, Nature Phys **13**, 943–946 (2017), (cit. on pp. 3, 19).

[45] H. Biss, L. Sobirey, N. Luick, M. Bohlen, J. J. Kinnunen, G. M. Bruun, T. Lompe, and H. Moritz, *Excitation Spectrum and Superfluid Gap of an Ultracold Fermi Gas*, arXiv:2105.09820 [cond-mat], (2021), (cit. on p. 3).

[46] A. Behrle, T. Harrison, J. Kombe, K. Gao, M. Link, J.-S. Bernier, C. Kollath, and M. Köhl, *Higgs mode in a strongly interacting fermionic superfluid*, Nature Physics, 10.1038/s41567-018-0128-6 (2018), (cit. on pp. 3, 5, 125, 143, 144, 160–162).

[47] A. Perali, P. Pieri, L. Pisani, and G. C. Strinati, *BCS-BEC Crossover at Finite Temperature for Superfluid Trapped Fermi Atoms*, Phys. Rev. Lett. **92**, 220404 (2004), (cit. on pp. 4, 13, 92, 93, 115, 117, 120, 121).

[48] L. P. Gor'kov and T. K. Melik-Barkhudarov, *Contribution to the Theory of Superfluidity in an Imperfect Fermi Gas*, Sov, Phys. JETP **40**, 5 (1961) (cit. on pp. 3, 17, 91, 92, 183).

[49] S. Giorgini, L. P. Pitaevskii, and S. Stringari, *Condensate fraction and critical temperature of a trapped interacting Bose gas*, Phys. Rev. A **54**, R4633–R4636 (1996), (cit. on pp. 3, 28).

[50] P. Arnold and B. Tomášik, *T_c For trapped dilute Bose gases: A second-order result*, Phys. Rev. A **64**, 053609 (2001), (cit. on pp. 3, 28, 121).

[51] P. Arnold and G. Moore, *BEC Transition Temperature of a Dilute Homogeneous Imperfect Bose Gas*, Phys. Rev. Lett. **87**, 120401 (2001), (cit. on pp. 3, 92, 121).

[52] F. Gerbier, J. H. Thywissen, S. Richard, M. Hugbart, P. Bouyer, and A. Aspect, *Critical Temperature of a Trapped, Weakly Interacting Bose Gas*, Phys. Rev. Lett. **92**, 030405 (2004), (cit. on pp. 3, 20, 91).

[53] R. Haussmann, W. Rantner, S. Cerrito, and W. Zwerger, *Thermodynamics of the BCS-BEC crossover*, Phys. Rev. A **75**, 023610 (2007), (cit. on pp. 3, 10, 92, 120, 121, 132, 140, 145, 150, 160, 161, 163).

[54] L. Pisani, A. Perali, P. Pieri, and G. C. Strinati, *Entanglement between pairing and screening in the Gorkov-Melik-Barkhudarov correction to the critical temperature throughout the BCS-BEC crossover*, Phys. Rev. B **97**, 014528 (2018), (cit. on pp. 3, 92, 120, 121).

[55] A. Bulgac, J. E. Drut, and P. Magierski, *Quantum Monte Carlo simulations of the BCS-BEC crossover at finite temperature*, Phys. Rev. A **78**, 023625 (2008), (cit. on pp. 3, 92).

[56] Y. Inada, M. Horikoshi, S. Nakajima, M. Kuwata-Gonokami, M. Ueda, and T. Mukaiyama, *Critical Temperature and Condensate Fraction of a Fermion Pair Condensate*, Phys. Rev. Lett. **101**, 180406 (2008), (cit. on pp. 4, 69, 91–93, 96, 122, 167).

[57] J. Kinast, A. Turlapov, and J. E. Thomas, *Damping of a Unitary Fermi Gas*, Phys. Rev. Lett. **94**, 170404 (2005), (cit. on pp. 4, 28, 93).

[58] J. Kinast, *Heat Capacity of a Strongly Interacting Fermi Gas*, Science **307**, 1296–1299 (2005), (cit. on pp. 4, 69, 93, 95).

[59] L. Luo, B. Clancy, J. Joseph, J. Kinast, and J. E. Thomas, *Measurement of the Entropy and Critical Temperature of a Strongly Interacting Fermi Gas*, Phys. Rev. Lett. **98**, 080402 (2007), (cit. on pp. 4, 93).

[60] S. Nascimbène, N. Navon, K. J. Jiang, F. Chevy, and C. Salomon, *Exploring the thermodynamics of a universal Fermi gas*, Nature **463**, 1057–1060 (2010), (cit. on pp. 4, 69, 70, 92, 93).

[61] M. J. H. Ku, A. T. Sommer, L. W. Cheuk, and M. W. Zwierlein, *Revealing the Superfluid Lambda Transition in the Universal Thermodynamics of a Unitary Fermi Gas*, Science **335**, 563–567 (2012), (cit. on pp. 4, 23, 27, 65, 66, 81, 83, 92, 93, 110, 117, 119, 160, 161).

[62] X.-J. Liu, *Virial expansion for a strongly correlated Fermi system and its application to ultracold atomic Fermi gases*, Physics Reports **524**, 37–83 (2013), (cit. on pp. 4, 12, 23, 26).

[63] J. Carrasquilla and R. G. Melko, *Machine learning phases of matter*, Nature Phys **13**, 431–434 (2017), (cit. on pp. 4, 94).

[64] N. Käming, A. Dawid, K. Kottmann, M. Lewenstein, K. Sengstock, A. Dauphin, and C. Weitenberg, *Unsupervised machine learning of topological phase transitions from experimental data*, arXiv:2101.05712 [cond-mat, physics:quant-ph], (2021), (cit. on pp. 4, 94).

[65] A. Polkovnikov, K. Sengupta, A. Silva, and M. Vengalattore, *Colloquium : Nonequilibrium dynamics of closed interacting quantum systems*, Rev. Mod. Phys. **83**, 863–883 (2011), (cit. on pp. 4, 123).

[66] S. Riedl, E. R. Sánchez Guajardo, C. Kohstall, A. Altmeyer, M. J. Wright, J. H. Denschlag, R. Grimm, G. M. Bruun, and H. Smith, *Collective oscillations of a Fermi gas in the unitarity limit: Temperature effects and the role of pair correlations*, Phys. Rev. A **78**, 053609 (2008), (cit. on pp. 5, 77, 123).

[67] A. Altmeyer, S. Riedl, M. J. Wright, C. Kohstall, J. H. Denschlag, and R. Grimm, *Dynamics of a strongly interacting Fermi gas: The radial quadrupole mode*, Phys. Rev. A **76**, 033610 (2007), (cit. on pp. 5, 28, 123).

[68] G. L. Warner and A. J. Leggett, *Quench dynamics of a superfluid Fermi gas*, Physical Review B - Condensed Matter and Materials Physics **71**, 1–10 (2005) (cit. on pp. 5, 123).

[69] R. G. Scott, F. Dalfovo, L. P. Pitaevskii, and S. Stringari, *Rapid ramps across the BEC-BCS crossover: A route to measuring the superfluid gap*, Phys. Rev. A **86**, 1–6 (2012) (cit. on pp. 5, 138, 143, 162).

[70] M. Greiner, C. A. Regal, and D. S. Jin, *Probing the Excitation Spectrum of a Fermi Gas in the BCS-BEC Crossover Regime*, Physical Review Letters **94**, 10.1103/PhysRevLett.94.070403 (2005), (cit. on pp. 5, 143–145, 147, 148, 150, 157).

[71] C. Chin, R. Grimm, P. Julienne, and E. Tiesinga, *Feshbach resonances in ultracold gases*, Rev. Mod. Phys. **82**, 1225–1286 (2010), (cit. on pp. 8, 10, 11, 13).

[72] Z.-C. Yan, J. F. Babb, A. Dalgarno, and G. W. F. Drake, *Variational calculations of dispersion coefficients for interactions among H, He, and Li atoms*, Phys. Rev. A **54**, 2824–2833 (1996), (cit. on p. 8).

[73] K. Huang and C. N. Yang, *Quantum-Mechanical Many-Body Problem with Hard-Sphere Interaction*, Phys. Rev. **105**, 767–775 (1957), (cit. on p. 10).

[74] M. Marini, F. Pistolesi, and G. Strinati, *Evolution from BCS superconductivity to Bose condensation: analytic results for the crossover in three dimensions*, Eur. Phys. J. B **1**, 151–159 (1998), (cit. on pp. 10, 17, 185).

[75] A. J. Moerdijk, B. J. Verhaar, and A. Axelsson, *Resonances in ultracold collisions of ^{6}Li, ^{7}Li, and ^{2}3Na*, Phys. Rev. A **51**, 4852–4861 (1995), (cit. on p. 10).

[76] G. Zürn, T. Lompe, A. N. Wenz, S. Jochim, P. S. Julienne, and J. M. Hutson, *Precise Characterization of ^{6}Li Feshbach Resonances Using Trap-Sideband-Resolved RF Spectroscopy of Weakly Bound Molecules*, Physical Review Letters **110**, 10.1103/PhysRevLett.110.135301 (2013), (cit. on p. 12).

[77] K. E. Strecker, G. B. Partridge, and R. G. Hulet, *Conversion of an Atomic Fermi Gas to a Long-Lived Molecular Bose Gas*, Phys. Rev. Lett. **91**, 080406 (2003), (cit. on p. 12).

[78] J. Zhang, E. G. M. van Kempen, T. Bourdel, L. Khaykovich, J. Cubizolles, F. Chevy, M. Teichmann, L. Tarruell, S. J. J. M. F. Kokkelmans, and C. Salomon, *P-wave Feshbach resonances of ultracold ^{6}Li*, Phys. Rev. A **70**, 030702 (2004), (cit. on p. 12).

[79] G. B. Partridge, K. E. Strecker, R. I. Kamar, M. W. Jack, and R. G. Hulet, *Molecular Probe of Pairing in the BEC-BCS Crossover*, Phys. Rev. Lett. **95**, 020404 (2005), (cit. on p. 12).

[80] C. J. Pethick and H. Smith, *Bose–Einstein Condensation in Dilute Gases*, (Cambridge University Press, Cambridge, 2008), http://ebooks.cambridge.org/ref/id/CBO9780511802850 (visited on 11/22/2017) (cit. on pp. 19, 20, 22).

[81] L. Salasnich, N. Manini, and A. Parola, *Condensate fraction of a Fermi gas in the BCS-BEC crossover*, Phys. Rev. A **72**, 023621 (2005), (cit. on p. 19).

[82] K. Huang, *Statistical mechanics*, (Wiley, New York, 1987) (cit. on p. 21).

[83] A. L. Fetter and J. D. Walecka, *Quantum theory of many-particle systems* (Dover Publications, Mineola, N.Y, 2003) (cit. on pp. 21, 22).

[84] L. P. Pitaevskiĭ and S. Stringari, *Bose-Einstein condensation and superfluidity*, International series of monographs on physics 164, (Oxford University Press, Oxford, United Kingdom, 2016) (cit. on pp. 21, 22).

[85] N. Gemelke, X. Zhang, C.-L. Hung, and C. Chin, *In situ observation of incompressible Mott-insulating domains in ultracold atomic gases*, Nature **460**, 995–998 (2009), (cit. on p. 23).

[86] E. Beth and G. E. Uhlenbeck, *The quantum theory of the non-ideal gas. II. Behaviour at low temperatures*, Physica **4**, 915–924 (1937), (cit. on pp. 23–26).

[87] X.-J. Liu, H. Hu, and P. D. Drummond, *Virial Expansion for a Strongly Correlated Fermi Gas*, Phys. Rev. Lett. **102**, 160401 (2009), (cit. on pp. 24, 25).

[88] Y. Hou and J. E. Drut, *Fourth- and Fifth-Order Virial Coefficients from Weak Coupling to Unitarity*, Phys. Rev. Lett. **125**, 050403 (2020), (cit. on pp. 24–26).

[89] D. Lee and T. Schäfer, *Cold dilute neutron matter on the lattice. I. Lattice virial coefficients and large scattering lengths*, Phys. Rev. C **73**, 015201 (2006), (cit. on p. 24).

[90] X. Leyronas, *Virial expansion with Feynman diagrams*, Phys. Rev. A **84**, 053633 (2011), (cit. on pp. 25, 26).

[91] S. Tan, *Energetics of a strongly correlated Fermi gas*, Annals of Physics **323**, 2952–2970 (2008), (cit. on p. 26).

[92] V. Romero-Rochin, *The thermodynamic origin of the Contact and its relation to the gap in the BEC-BCS crossover*, arXiv:1012.0236 [cond-mat], (2010), (cit. on p. 26).

[93] S. Tan, *Large momentum part of fermions with large scattering length*, Annals of Physics **323**, 2971–2986 (2008), (cit. on pp. 26, 69).

[94] S. Jensen, C. N. Gilbreth, and Y. Alhassid, *Contact in the Unitary Fermi Gas across the Superfluid Phase Transition*, Phys. Rev. Lett. **125**, 043402 (2020), (cit. on p. 27).

[95] M. J. Wright, S. Riedl, A. Altmeyer, C. Kohstall, E. R. S. Guajardo, J. H. Denschlag, and R. Grimm, *Finite-Temperature Collective Dynamics of a Fermi Gas in the BEC-BCS Crossover*, Physical Review Letters **99**, 10.1103/PhysRevLett.99.150403 (2007), (cit. on p. 28).

[96] T. J. Harrison, *Measuring the Gap and Investigating Non-equilibrium in the BEC-BCS Crossover*, PhD Thesis (Bonn, 2017), https://nbn-resolving.org/urn:nbn:de:hbz:5n-48182 (cit. on pp. 29, 34, 35, 37, 38, 57, 59, 72, 125, 126).

[97] A. Behrle, *Driving a Strongly Interacting Superfluid out of Equilibrium*, PhD Thesis (Bonn, 2017), https://nbn-resolving.org/urn:nbn:de:hbz:5n-50076 (cit. on pp. 29, 33, 35, 36, 38, 57, 125).

[98] M. Link, *Exploring Non-Equilibrium in Ultracold Fermi Gases and Machine Learning in Physics*, PhD Thesis (Bonn, 2021), https://nbn-resolving.org/urn:nbn:de:hbz:5-62382 (cit. on pp. 29, 57, 62, 70, 85, 91, 125).

[99] C. Linse, *Construction of a ^{6}Li spectroscopy cell and Doppler-free spectroscopy*, Bachelor Thesis (Bonn, 2014) (cit. on p. 29).

[100] D. Eberz, *Design and Construction of a Multi-Species Effusive Atomic Oven for Lithium and Sodium*, Master thesis (Bonn, Nov. 2020) (cit. on pp. 29, 34, 35).

[101] M. J. Zawierucha, *Design and Construction of a Sodium Spectroscopy Cell and a Lock-in Amplifier for Frequency Locking a Laser*, Bachelor Thesis (Bonn, 2015) (cit. on p. 29).

[102] J. Andrijauskas, *Optical dipole trap laser setup in a new quantum gas experiment*, Master thesis (Bonn, 2015) (cit. on p. 29).

[103] A. Kell, *Optical Trap for Ultracold 2D Fermi Gas*, Master thesis (Bonn, Nov. 2017) (cit. on pp. 29, 38).

[104] V. Jonas, *Acousto-Optic Sculpturing of Optical Potential Landscapes for Ultracold Fermions*, Master thesis (Bonn, 2021) (cit. on pp. 29, 38).

[105] M. E. Gehm, *Preparation of an optically-trapped degenerate fermi gas of ^{6}Li: Finding the route to degeneracy*, PhD Thesis (Duke University, 2003) (cit. on pp. 30, 58, 61, 62).

[106] D. A. Steck, *Sodium D Line Data*, `https://steck.us/alkalidata` (visited on 02/24/2022) (cit. on p. 30).

[107] R. Grimm, M. Weidemüller, and Y. B. Ovchinnikov, *Optical Dipole Traps for Neutral Atoms*, in *Advances In Atomic, Molecular, and Optical Physics*, Vol. 42 (Elsevier, 2000), pp. 95–170, (visited on 10/04/2017) (cit. on pp. 31, 74).

[108] Z. Hadzibabic, S. Gupta, C. A. Stan, C. H. Schunck, M. W. Zwierlein, K. Dieckmann, and W. Ketterle, *Fiftyfold Improvement in the Number of Quantum Degenerate Fermionic Atoms*, Phys. Rev. Lett. **91**, 160401 (2003), (cit. on pp. 32, 36, 37).

[109] C. A. Stan and W. Ketterle, *Multiple species atom source for laser-cooling experiments*, Review of Scientific Instruments **76**, 063113 (2005), (cit. on p. 33).

[110] S. C. Bell, M. Junker, M. Jasperse, L. D. Turner, Y.-J. Lin, I. B. Spielman, and R. E. Scholten, *A slow atom source using a collimated effusive oven and a single-layer variable pitch coil Zeeman slower*, Review of Scientific Instruments **81**, 013105 (2010), (cit. on p. 34).

[111] C. J. Foot, *Atomic Physics* (Oxford University Press, Oxford, 2005) (cit. on pp. 35–37, 57, 60, 61).

[112] W. Ketterle, K. B. Davis, M. A. Joffe, A. Martin, and D. E. Pritchard, *High densities of cold atoms in a dark spontaneous-force optical trap*, Phys. Rev. Lett. **70**, 2253–2256 (1993), (cit. on p. 36).

[113] M.-O. Mewes, G. Ferrari, F. Schreck, A. Sinatra, and C. Salomon, *Simultaneous magneto-optical trapping of two lithium isotopes*, Phys. Rev. A **61**, 011403 (1999), (cit. on p. 36).

[114] M. Okano, H. Hara, M. Muramatsu, K. Doi, S. Uetake, Y. Takasu, and Y. Takahashi, *Simultaneous magneto-optical trapping of lithium and ytterbium atoms towards production of ultracold polar molecules*, Appl. Phys. B **98**, 691–696 (2010), (cit. on p. 36).

[115] C.-L. Hung, X. Zhang, N. Gemelke, and C. Chin, *Accelerating evaporative cooling of atoms into Bose-Einstein condensation in optical traps*, Physical Review A **78**, `10.1103/PhysRevA.78.011604` (2008), (cit. on p. 38).

[116] N. L. Smith, W. H. Heathcote, G. Hechenblaikner, E. Nugent, and C. J. Foot, *Quasi-2D confinement of a BEC in a combined optical and magnetic potential*, Journal of Physics B: Atomic, Molecular and Optical Physics **38**, 223–235 (2005), (cit. on p. 38).

[117] T. P. Meyrath, F. Schreck, J. L. Hanssen, C. S. Chuu, and M. G. Raizen, *Bose-Einstein condensate in a box*, Physical Review A - Atomic, Molecular, and Optical Physics **71**, 1–4 (2005) (cit. on p. 38).

[118] P. Dyke, K. Fenech, T. Peppler, M. G. Lingham, S. Hoinka, W. Zhang, S. G. Peng, B. Mulkerin, H. Hu, X. J. Liu, and C. J. Vale, *Criteria for two-dimensional kinematics in an interacting Fermi gas*, Physical Review A **93**, 1–10 (2016) (cit. on p. 38).

[119] K. Hueck, N. Luick, L. Sobirey, J. Siegl, T. Lompe, and H. Moritz, *Two-Dimensional Homogeneous Fermi Gases*, Phys. Rev. Lett. **120**, 060402 (2018), (cit. on p. 38).

[120] H. Nagaoka, *The Inductance Coefficients of Solenoids*, Journal of the college of science, Imperial university Tokyo (1909), (cit. on pp. 40, 45, 185).

[121] J. D. Jackson, *Classical electrodynamics*, (Wiley, New York, 1999) (cit. on pp. 40, 42, 49).

[122] J. Lunt, *Large-scale production, properties and commercial applications of polylactic acid polymers*, Polymer Degradation and Stability **59**, 145–152 (1998), (cit. on p. 41).

[123] R. Weaver, *Numerical Methods for Inductance Calculation*, `http://electronbunker.ca/eb/CalcMethods.html` (visited on 02/25/2022) (cit. on p. 45).

[124] D. O. Sabulsky, C. V. Parker, N. D. Gemelke, and C. Chin, *Efficient continuous-duty Bitter-type electromagnets for cold atom experiments*, Review of Scientific Instruments **84**, 104706 (2013), (cit. on p. 48).

[125] E. Hecht, *Optics*, (Pearson, Harlow, 2016) (cit. on p. 55).

[126] I. T. Young, R. Zagers, L. J. van Vliet, J. Mullikin, F. Boddeke, and H. Netten, *Depth-of-Focus in Microscopy*, in Proceedings of the 8th Scandinavian Conference on Image Analysis (1993), pp. 493–498 (cit. on pp. 55, 62).

[127] G. Reinaudi, T. Lahaye, Z. Wang, and D. Guéry-Odelin, *Strong saturation absorption imaging of dense clouds of ultracold atoms*, Opt. Lett. **32**, 3143 (2007), (cit. on pp. 57, 58).

[128] K. Hueck, N. Luick, L. Sobirey, J. Siegl, T. Lompe, H. Moritz, L. W. Clark, and C. Chin, *Calibrating high intensity absorption imaging of ultracold atoms*, Optics Express **25**, 8670 (2017), (cit. on pp. 57, 60).

[129] M. G. Ries, A. N. Wenz, G. Zürn, L. Bayha, I. Boettcher, D. Kedar, P. A. Murthy, M. Neidig, T. Lompe, and S. Jochim, *Observation of Pair Condensation in the Quasi-2D BEC-BCS Crossover*, Physical Review Letters **114**, 1–5 (2015) (cit. on pp. 57, 96, 167).

[130] E. Cocchi, *Analogue Qantum Simulation of the Two-Dimensional Hubbard Model with Ultracold Fermions by Eugenio Cocchi*, PhD Thesis (Cambridge, 2016) (cit. on pp. 57, 58, 145).

[131] L. A. Miller, *Ultracold Fermions in Two-Dimensional Optical Lattices: Quantum Simulation of the Hubbard Model*, PhD Thesis (Cambridge, 2016) (cit. on p. 57).

[132] L. Chomaz, *Coherence and superfluidity of Bose gases in reduced dimensions: from harmonic traps to uniform fluids*, PhD Thesis (Paris, 2014), `https://tel.archives-ouvertes.fr/tel-01302847` (cit. on pp. 57, 59).

[133] J. Drewes, *Thermodynamics and correlations of ultracold fermions in a two-dimensional optical lattice*, PhD Thesis (Bonn, 2020) (cit. on pp. 61, 62).

[134] M. Horikoshi, A. Ito, T. Ikemachi, Y. Aratake, M. Kuwata-Gonokami, and M. Koashi, *Appropriate probe condition for absorption imaging of ultracold ^{6}Li atoms*, Journal of the Physical Society of Japan **86**, 104301 (2017), (cit. on pp. 61, 62).

[135] P. A. Murthy, D. Kedar, T. Lompe, M. Neidig, M. G. Ries, A. N. Wenz, G. Zürn, and S. Jochim, *Matter-wave Fourier optics with a strongly interacting two-dimensional Fermi gas*, Physical Review A **90**, `10.1103/PhysRevA.90.043611` (2014), (cit. on pp. 64, 69).

[136] M. J.-H. Ku, *Thermodynamics and Solitonic Excitations of a Strongly-Interacting Fermi Gas*, PhD Thesis (MIT, June 2015), http://hdl.handle.net/1721.1/99309 (cit. on p. 66).

[137] H. Hu, X.-J. Liu, and P. D. Drummond, *Temperature of a trapped unitary Fermi gas at finite entropy*, Phys. Rev. A **73**, 023617 (2006), (cit. on pp. 69, 70).

[138] Q. Chen, C. A. Regal, M. Greiner, D. S. Jin, and K. Levin, *Understanding the superfluid phase diagram in trapped Fermi gases*, Physical Review A **73**, 10.1103/PhysRevA.73.041601 (2006), (cit. on pp. 69, 92, 93, 121).

[139] F. M. Spiegelhalder, A. Trenkwalder, D. Naik, G. Hendl, F. Schreck, and R. Grimm, *Collisional Stability of ^{4}0K Immersed in a Strongly Interacting Fermi Gas of ^{6}Li*, Phys. Rev. Lett. **103**, 223203 (2009), (cit. on pp. 69, 70).

[140] L. Luo and J. E. Thomas, *Thermodynamic Measurements in a Strongly Interacting Fermi Gas*, J Low Temp Phys **154**, 1–29 (2009), (cit. on pp. 69, 93).

[141] Y.-i. Shin, C. H. Schunck, A. Schirotzek, and W. Ketterle, *Phase diagram of a two-component Fermi gas with resonant interactions*, Nature **451**, 689–693 (2008), (cit. on p. 69).

[142] J. E. Thomas, J. Kinast, and A. Turlapov, *Virial Theorem and Universality in a Unitary Fermi Gas*, Phys. Rev. Lett. **95**, 120402 (2005), (cit. on p. 69).

[143] Q. Chen, J. Stajic, and K. Levin, *Thermodynamics of Interacting Fermions in Atomic Traps*, Phys. Rev. Lett. **95**, 260405 (2005), (cit. on p. 70).

[144] L. D. Carr, G. V. Shlyapnikov, and Y. Castin, *Achieving a BCS Transition in an Atomic Fermi Gas*, Phys. Rev. Lett. **92**, 150404 (2004), (cit. on p. 70).

[145] J. T. Stewart, J. P. Gaebler, T. E. Drake, and D. S. Jin, *Verification of Universal Relations in a Strongly Interacting Fermi Gas*, Physical Review Letters **104**, 10.1103/PhysRevLett.104.235301 (2010), (cit. on p. 70).

[146] E. D. Kuhnle, S. Hoinka, P. Dyke, H. Hu, P. Hannaford, and C. J. Vale, *Temperature Dependence of the Universal Contact Parameter in a Unitary Fermi Gas*, Physical Review Letters **106**, 10.1103/PhysRevLett.106.170402 (2011), (cit. on pp. 70, 95).

[147] B. Mukherjee, P. B. Patel, Z. Yan, R. J. Fletcher, J. Struck, and M. W. Zwierlein, *Spectral Response and Contact of the Unitary Fermi Gas*, Physical Review Letters **122**, 10.1103/PhysRevLett.122.203402 (2019), (cit. on p. 70).

[148] R. S. Lous, I. Fritsche, M. Jag, B. Huang, and R. Grimm, *Thermometry of a deeply degenerate Fermi gas with a Bose-Einstein condensate*, Physical Review A **95**, 10.1103/PhysRevA.95.053627 (2017), (cit. on p. 70).

[149] T. Paintner, D. K. Hoffmann, M. Jäger, W. Limmer, W. Schoch, B. Deissler, M. Pini, P. Pieri, G. Calvanese Strinati, C. Chin, and J. Hecker Denschlag, *Pair fraction in a finite-temperature Fermi gas on the BEC side of the BCS-BEC crossover*, Phys. Rev. A **99**, 053617 (2019), (cit. on p. 71).

[150] I. Goodfellow, Y. Bengio, and A. Courville, *Deep Learning* (MIT Press, 2016), https://www.deeplearningbook.org/ (visited on 11/11/2021) (cit. on pp. 85, 86, 88).

[151] Y. LeCun, Y. Bengio, and G. Hinton, *Deep learning*, Nature **521**, 436–444 (2015), (cit. on p. 85).

[152] D. Kriesel, *A Brief Introduction to Neural Networks* (2007), http://www.dkriesel.com (visited on 03/10/2022) (cit. on p. 85).

[153] W. S. McCulloch and W. Pitts, *A logical calculus of the ideas immanent in nervous activity*, Bulletin of Mathematical Biophysics **5**, 115–133 (1943), (cit. on p. 85).

[154] F. Rosenblatt, *The Perceptron - A Perceiving and Recognizing Automaton*, tech. rep. (1957) (cit. on p. 85).

[155] M. Minsky and S. A. Papert, *Perceptrons: an introduction to computational geometry*, (The MIT Press, Cambridge/Mass., 1972) (cit. on p. 85).

[156] D. E. Rumelhart, G. E. Hinton, and R. J. Williams, *Learning representations by back-propagating errors*, Nature **323**, 533–536 (1986), (cit. on p. 85).

[157] A. Krizhevsky, I. Sutskever, and G. E. Hinton, *ImageNet classification with deep convolutional neural networks*, Commun. ACM **60**, 84–90 (2017), (cit. on p. 85).

[158] F. Emmert-Streib, Z. Yang, H. Feng, S. Tripathi, and M. Dehmer, *An Introductory Review of Deep Learning for Prediction Models With Big Data*, Front. Artif. Intell. **3**, 4 (2020), (cit. on pp. 85, 87).

[159] J. Schmidhuber, *Deep learning in neural networks: An overview*, Neural Networks **61**, 85–117 (2015), (cit. on p. 85).

[160] G. Baym, J.-P. Blaizot, M. Holzmann, F. Laloë, and D. Vautherin, *The Transition Temperature of the Dilute Interacting Bose Gas*, Phys. Rev. Lett. **83**, 1703–1706 (1999), (cit. on pp. 92, 121).

[161] S. Pilati, S. Giorgini, and N. Prokof'ev, *Critical Temperature of Interacting Bose Gases in Two and Three Dimensions*, Phys. Rev. Lett. **100**, 140405 (2008), (cit. on p. 92).

[162] C. Raman, M. Köhl, R. Onofrio, D. S. Durfee, C. E. Kuklewicz, Z. Hadzibabic, and W. Ketterle, *Evidence for a Critical Velocity in a Bose-Einstein Condensed Gas*, Physical Review Letters **83**, 2502–2505 (1999), (cit. on p. 92).

[163] V. P. Singh, W. Weimer, K. Morgener, J. Siegl, K. Hueck, N. Luick, H. Moritz, and L. Mathey, *Probing superfluidity of Bose-Einstein condensates via laser stirring*, Physical Review A **93**, 10.1103/PhysRevA.93.023634 (2016), (cit. on p. 92).

[164] L. Sobirey, N. Luick, M. Bohlen, H. Biss, H. Moritz, and T. Lompe, *Observation of superfluidity in a strongly correlated two-dimensional Fermi gas*, arXiv:2005.07607 [cond-mat], (2020), (cit. on p. 92).

[165] K. W. Madison, F. Chevy, W. Wohlleben, and J. Dalibard, *Vortex Formation in a Stirred Bose-Einstein Condensate*, Phys. Rev. Lett. **84**, 806–809 (2000), (cit. on p. 93).

[166] J. R. Abo-Shaeer, C. Raman, J. M. Vogels, and W. Ketterle, *Observation of Vortex Lattices in Bose-Einstein Condensates*, Science **292**, 476–479 (2001), (cit. on p. 93).

[167] C. H. Schunck, M. W. Zwierlein, A. Schirotzek, and W. Ketterle, *Superfluid Expansion of a Rotating Fermi Gas*, Phys. Rev. Lett. **98**, 050404 (2007), (cit. on pp. 93, 138).

[168] G. Carleo, I. Cirac, K. Cranmer, L. Daudet, M. Schuld, N. Tishby, L. Vogt-Maranto, and L. Zdeborová, *Machine learning and the physical sciences*, Rev. Mod. Phys. **91**, 045002 (2019), (cit. on p. 94).

[169] L. Wang, *Discovering phase transitions with unsupervised learning*, Physical Review B **94**, 10.1103/PhysRevB.94.195105 (2016), (cit. on p. 94).

[170] E. P. L. van Nieuwenburg, Y.-H. Liu, and S. D. Huber, *Learning phase transitions by confusion*, Nature Phys **13**, 435–439 (2017), (cit. on p. 94).

[171] P. Broecker, F. F. Assaad, and S. Trebst, *Quantum phase recognition via unsupervised machine learning*, arXiv:1707.00663 [cond-mat], (2017), (cit. on p. 94).

[172] C. Eigen, J. A. P. Glidden, R. Lopes, E. A. Cornell, R. P. Smith, and Z. Hadzibabic, *Universal prethermal dynamics of Bose gases quenched to unitarity*, Nature **563**, 221–224 (2018), (cit. on p. 123).

[173] T. Kinoshita, T. Wenger, and D. S. Weiss, *A quantum Newton's cradle*, Nature **440**, 900–903 (2006), (cit. on p. 123).

[174] A. Robertson and V. M. Galitski, *Nonequilibrium enhancement of Cooper pairing in cold fermion systems*, Phys. Rev. A **80**, 063609 (2009), (cit. on p. 123).

[175] D. Fausti, R. I. Tobey, N. Dean, S. Kaiser, A. Dienst, M. C. Hoffmann, S. Pyon, T. Takayama, H. Takagi, and A. Cavalleri, *Light-Induced Superconductivity in a Stripe-Ordered Cuprate*, Science **331**, 189–191 (2011), (cit. on p. 123).

[176] M. K. Tey, L. A. Sidorenkov, E. R. S. Guajardo, R. Grimm, M. J. H. Ku, M. W. Zwierlein, Y.-H. Hou, L. Pitaevskii, and S. Stringari, *Collective Modes in a Unitary Fermi Gas across the Superfluid Phase Transition*, Physical Review Letters **110**, 10.1103/PhysRevLett.110.055303 (2013), (cit. on p. 123).

[177] R. A. Barankov and L. S. Levitov, *Synchronization in the BCS Pairing Dynamics as a Critical Phenomenon*, Physical Review Letters **96**, 10.1103/PhysRevLett.96.230403 (2006), (cit. on p. 123).

[178] M. W. Zwierlein, C. H. Schunck, C. A. Stan, S. M. F. Raupach, and W. Ketterle, *Formation Dynamics of a Fermion Pair Condensate*, Physical Review Letters **94**, 10.1103/PhysRevLett.94.180401 (2005), (cit. on p. 123).

[179] R. G. Scott, F. Dalfovo, L. P. Pitaevskii, and S. Stringari, *Dynamics of Dark Solitons in a Trapped Superfluid Fermi Gas*, Phys. Rev. Lett. **106**, 185301 (2011), (cit. on p. 123).

[180] A. F. Volkov and S. M. Kogan, *Collisionless relaxation of the energy gap in superconductors*, Sov. Phys.-JETP **38**, 4 (1973) (cit. on pp. 123, 140, 144).

[181] V. Gurarie, *Nonequilibrium Dynamics of Weakly and Strongly Paired Superconductors*, Phys. Rev. Lett. **103**, 075301 (2009), (cit. on pp. 123, 144, 162).

[182] E. A. Yuzbashyan, M. Dzero, V. Gurarie, and M. S. Foster, *Quantum quench phase diagrams of an s-wave BCS-BEC condensate*, Physical Review A - Atomic, Molecular, and Optical Physics **91**, 10.1103/PhysRevA.91.033628 (2015) (cit. on p. 124).

[183] R. Sooryakumar and M. V. Klein, *Raman Scattering by Superconducting-Gap Excitations and Their Coupling to Charge-Density Waves*, Phys. Rev. Lett. **45**, 660–662 (1980), (cit. on pp. 124, 144).

[184] R. Matsunaga, Y. I. Hamada, K. Makise, Y. Uzawa, H. Terai, Z. Wang, and R. Shimano, *Higgs Amplitude Mode in the BCS Superconductors $Nb_{1-x}Ti_xN$ Induced by Terahertz Pulse Excitation*, Phys. Rev. Lett. **111**, 057002 (2013), (cit. on pp. 124, 144).

[185] D. Sherman, U. S. Pracht, B. Gorshunov, S. Poran, J. Jesudasan, M. Chand, P. Raychaudhuri, M. Swanson, N. Trivedi, A. Auerbach, M. Scheffler, A. Frydman, and M. Dressel, *The Higgs Mode in Disordered Superconductors Close to a Quantum Phase Transition*, Nature Phys **11**, 188–192 (2015), (cit. on p. 124).

[186] C. Rüegg, B. Normand, M. Matsumoto, A. Furrer, D. F. McMorrow, K. W. Krämer, H. .-. Güdel, S. N. Gvasaliya, H. Mutka, and M. Boehm, *Quantum Magnets under Pressure: Controlling Elementary Excitations in $TlCuCl_3$*, Phys. Rev. Lett. **100**, 205701 (2008), (cit. on p. 124).

[187] U. Bissbort, S. Götze, Y. Li, J. Heinze, J. S. Krauser, M. Weinberg, C. Becker, K. Sengstock, and W. Hofstetter, *Detecting the Amplitude Mode of Strongly Interacting Lattice Bosons by Bragg Scattering*, Phys. Rev. Lett. **106**, 205303 (2011), (cit. on p. 124).

[188] M. Endres, T. Fukuhara, D. Pekker, M. Cheneau, P. Schauβ, C. Gross, E. Demler, S. Kuhr, and I. Bloch, *The 'Higgs' amplitude mode at the two-dimensional superfluid/Mott insulator transition*, Nature **487**, 454–458 (2012), (cit. on pp. 124, 143).

[189] T. M. Hoang, H. M. Bharath, M. J. Boguslawski, M. Anquez, B. A. Robbins, and M. S. Chapman, *Adiabatic quenches and characterization of amplitude excitations in a continuous quantum phase transition*, Proc Natl Acad Sci USA **113**, 9475–9479 (2016), (cit. on p. 124).

[190] J. Léonard, A. Morales, P. Zupancic, T. Donner, and T. Esslinger, *Monitoring and manipulating Higgs and Goldstone modes in a supersolid quantum gas*, Science **358**, 1415–1418 (2017), (cit. on p. 124).

[191] L. Bayha, M. Holten, R. Klemt, K. Subramanian, J. Bjerlin, S. M. Reimann, G. M. Bruun, P. M. Preiss, and S. Jochim, *Observing the emergence of a quantum phase transition – shell by shell*, arXiv:2004.14761 [cond-mat], (2020), (cit. on pp. 125, 143).

[192] P. Dyke, A. Hogan, I. Herrera, C. C. N. Kuhn, S. Hoinka, and C. J. Vale, *Condensation dynamics in a quenched unitary Fermi gas*, arXiv:2103.07033 [cond-mat], (2021), (cit. on p. 125).

[193] J. A. Kombe, *Nonequilibrium Dynamics of Correlated Fermi Gases*, PhD Thesis (Bonn, 2020), https://nbn-resolving.org/urn:nbn:de:hbz:5-59946 (cit. on p. 125).

[194] S. Gupta, Z. Hadzibabic, M. W. Zwierlein, C. A. Stan, K. Dieckmann, C. H. Schunck, E. G. M. van Kempen, B. J. Verhaar, and W. Ketterle, *Radio-Frequency Spectroscopy of Ultracold Fermions*, Science **300**, 1723–1726 (2003), (cit. on p. 125).

[195] J. Tokimoto, S. Tsuchiya, and T. Nikuni, *Higgs Mode in a Trapped Superfluid Fermi Gas*, J Low Temp Phys **187**, 765–770 (2017), (cit. on pp. 138, 140).

[196] S. T. Thompson, E. Hodby, and C. E. Wieman, *Ultracold Molecule Production via a Resonant Oscillating Magnetic Field*, Phys. Rev. Lett. **95**, 190404 (2005), (cit. on p. 143).

[197] J. S. Krauser, J. Heinze, S. Götze, M. Langbecker, N. Fläschner, L. Cook, T. M. Hanna, E. Tiesinga, K. Sengstock, and C. Becker, *Investigation of Feshbach resonances in ultracold ^{40K} spin mixtures*, Phys. Rev. A **95**, 042701 (2017), (cit. on p. 145).

[198] J. Plata, *Magnetic-modulation spectroscopy of an atomic Fermi gas in the BCS-BEC crossover: Dissociation spectra in the Bose-Einstein condensate regime*, Physical Review A **74**, 10.1103/PhysRevA.74.013603 (2006), (cit. on p. 147).

[199] A. Richie-Halford, J. E. Drut, and A. Bulgac, *Emergence of a Pseudogap in the BCS-BEC Crossover*, Phys. Rev. Lett. **125**, 060403 (2020), (cit. on p. 150).

[200] B. Liu, H. Zhai, and S. Zhang, *Evolution of the Higgs mode in a fermion superfluid with tunable interactions*, Phys. Rev. A **93**, 033641 (2016), (cit. on pp. 160, 168).

[201] V. L. Berezinskii, *Destruction of long-range order in one-dimensional and two-dimensional systems having a continuous symmetry group I. Classical systems.* Sov. Phys. JETP **32**, 493–500 (1971) (cit. on p. 169).

[202] A. Rançon and N. Dupuis, *Higgs amplitude mode in the vicinity of a $(2+1)$-dimensional quantum critical point*, Phys. Rev. B **89**, 180501 (2014), (cit. on p. 169).

Acronyms

AC Alternating Current 31
AOM Acousto-Optic Modulator 58
BCS Bardeen, Cooper and Schrieffer [10, 11] iii
BEC Bose-Einstein Condensate [8] iii
CAD Computer-Aided Design 32
CAS Computer Algebra System 66
CCD Charge-Coupled Device 55
CF Condensate Fraction 147
CMOT Compressed Magneto-Optical Trap 33
DC Direct Current 48
DMM Digital Multimeter 48
FWHM Full Width Half Maximum 146
GMB Gor'kov and Melik-Barkhudarov [48] 17
IGBT Insulated-Gate Bipolar Transistor 38
LDA Local Density Approximation 23
MOSFET Metal-Oxide-Semiconductor Field-Effect Transistor 39
MOT Magneto-Optical Trap 9
NA Numerical Aperture 40
PLA Polylactic Acid 41
ReLU Rectified Linear Unit 85
RF Radio-Frequency 3
TEM Transverse Electromagnetic Mode 38
XOR Exclusive OR 85

Tools

Most analysis is performed in *python*, based mainly on the libraries *numpy*, *scipy*, *pandas*, *matplotlib*, *lmfit* and *tensorflow*. Additionally, *Wolfram Mathematica* is employed. *WebPlot-Digitizer* by Ankit Rohatgi is used to extract data from plots. CAD designs are based on *Autodesk Inventor*. Circuits are designed with *Eagle* by Autodesk and simulated with *LTSpice* by Analog Devices. The thesis is written in LaTeX and the bibliography is created with *Zotero*.

A Appendix

A.1 Elliptic Integrals

The thesis uses the following definitions for the complete elliptic integral of the first kind

$$K(m) := \int_0^{\pi/2} \frac{\mathrm{d}t}{\sqrt{1 - m\sin(t)^2}} \tag{A.163}$$

and the complete elliptic integral of the second kind

$$E(m) := \int_0^{\pi/2} \sqrt{1 - m\sin(t)^2}\,\mathrm{d}t \ , \tag{A.164}$$

which matches the convention of Mathematica and of the python library scipy.

But note that some references [74, 120] use a different convention, where the argument of the functions is $\kappa := \sqrt{m}$.